Deep Inelastic Scattering

A M Cooper-Sarkar, R C E Devenish and A T Doyle

Draft Chapters Jan 2002

Preface

The book gives an introduction to the ideas behind, and the results of, deep inelastic scattering in high energy particle physics. As an experimental technique, deep inelastic scattering can trace its lineage back to the very discovery of the nucleus by Rutherford using the scattering data from Geiger and Marsden. More recently deep inelastic scattering was crucial to the emergence of the quark-parton model and the development of Quantum Chromodynamics (QCD) as the theory of the strong interaction. Both fixed target and more recent collider experiments are covered. The advances in the understanding of QCD made possible by deep inelastic experiments, particularly those at the HERA collider are explained. Prospects for electroweak physics at large momentum transfer are explored. Particular attention is paid to a clear exposition of the formalism required to analyse the high luminosity, high momentum transfer data from the HERAII ep collider. The importance of accurate parton distribution functions for advances in hadron collider physics at the Tevatron and LHC is outlined. The book is intended for graduate students and others new to the field.

Thanks to...

Contents

1 Introduction

The basic idea of scattering experiments as a probe of spatial structure. Relation between the spatial distribution of the target and the Fourier transform or momentum space 'form factor' or 'structure function'. Illustrated by the example of spinless non-relativistic scattering of a point-like particle from a fixed potential. Momentum transfer and spatial resolution. Brief discussion of the experiments by Hofstadter on nuclei, including smearing of the quasi-elastic electron-nucleon peak in high-resolution electron-nucleus scattering. An historical route into the structure of the book is provided via a description of the SLAC (quarks) and Gargamelle (neutral current) experiments which introduces some of the key ideas.

2

The quark-parton model

This chapter introduces the quark-parton model (QPM), in which deep inelastic scattering is seen as the incoherent sum of point-like *elastic* scattering of spin-$\frac{1}{2}$ nucleon constituents (the partons). The necessary cross-section expressions for elastic electron-quark and quasi-elastic neutrino-quark scattering are developed. The full cross-section for lepton-nucleon deep inelastic scattering is constructed by folding the point-like elastic cross-sections with parton momentum densities. This then leads to expressions for the electromagnetic and neutrino nucleon structure functions in terms of parton density functions. The QPM structure functions exhibit Bjorken scaling, that is they are approximately independent of momentum transfer from the probe to the nucleon. This is a direct consequence of the underlying elastic scattering. An outline of other elementary tests of the quark-parton model then follows and the chapter ends with a discussion of sum rules.

Written Summer 2001, revised Xmas 2001.

2.1 The essential idea of the parton model

The quark-parton model is developed by considering its application to the lepton-hadron scattering process. The commonly used Lorentz invariants will be defined for the basic process

$$lN \to l'X$$

where l, l' represent leptons (lepton is taken to include antileptons, unless it is necessary to distinguish them), N represents a nucleon and X represents the hadronic final state particles.
The associated four vectors are k, k' for the incoming and outgoing leptons respectively, and p for the target (or incoming) nucleon. The process is mediated by the exchange of a virtual vector boson, $V^*(\gamma, W$ or $Z)$, see Fig. 2.1. This boson has four momentum given by

$$q = k - k'$$

and the four vector p_X of the hadronic final state system X is given by

$$p_X = p + q.$$

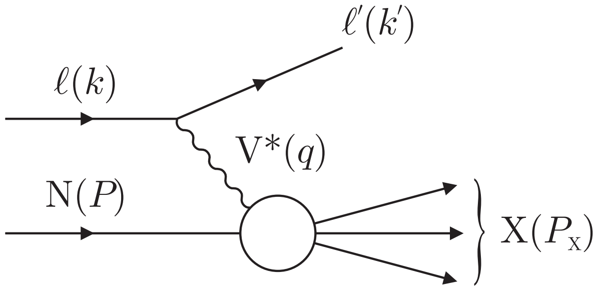

Fig. 2.1 Schematic diagram of lepton-hadron scattering via Vector-Boson Exchange

Various Lorentz invariants are useful in the description of the kinematics of the process:

$$s = (p + k)^2$$

the centre of mass energy squared for the lp interaction,

$$Q^2 = -q^2$$

the (negative of) the invariant mass squared of the virtual exchanged boson,

$$x = Q^2/2p.q$$

the Bjorken x variable, which will be interpreted in the quark-parton model as the fraction of the momentum of the incoming nucleon taken by the struck quark, and

$$y = p.q/p.k$$

which gives a measure of the amount of energy transferred between the lepton and the hadron systems. Note that (ignoring masses),

$$Q^2 = sxy,$$

so that only two of these quantities are independent.

The quark-parton model (QPM) grew out of the attempt by Feynman [Fey69] to provide a simple physical picture of the scaling that had been predicted by Bjorken [Bjo69] and observed in the first high energy deep inelastic electron scattering experiments at SLAC [Fri91], where F_2 was observed to be independent of Q^2 for x values around $x \sim 0.25$. The model states that the nucleon is full of point-like non-interacting scattering centres known as partons. The lepton-hadron reaction cross-section is then approximated by an incoherent sum of elastic lepton-parton scatters via an exchanged vector current, see Fig. 2.2.

It turns out that only spin $\frac{1}{2}$ partons (quarks or antiquarks) interact directly with the current, and for centre of mass energies much less than M_W, M_Z, the relevant current is the electromagnetic current. Thus the electromagnetic scattering of two spin $\frac{1}{2}$ point-like particles is the underlying fundamental process to be considered.

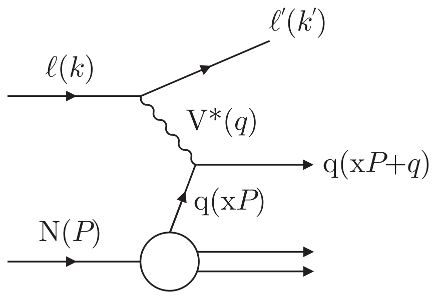

Fig. 2.2 Schematic diagram of lepton-hadron scattering in the quark-parton model

2.1.1 Elastic electron-muon scattering

Electron-muon scattering provides an example of such a process which can only proceed via the t channel diagram of Fig. 2.3. The Feynman rules for

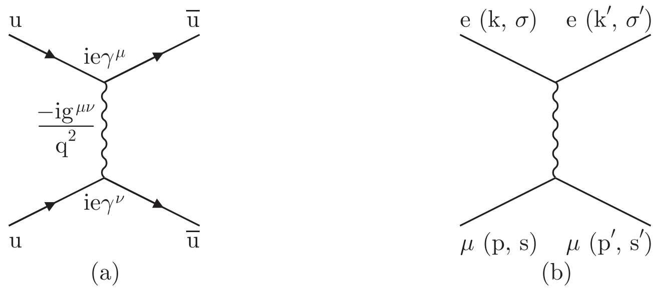

Fig. 2.3 Feynman diagram for $e\mu$ scattering

this process are summarized on the external particle lines, internal propagator line and vertices of the left hand side of the figure. The 4-momenta and spin labels are given on the right hand side of the figure. (The Feynman rules for all relevant processes are summarized in Appendix B). Putting the external lines together with the vertex factors, the electron and muon currents

$$j_e^\nu = ie\bar{u}(k',\sigma')\gamma^\nu u(k,\sigma) \tag{2.1}$$

$$j_{muon}^\mu = ie'\bar{u}(p',s')\gamma^\mu u(p,s) \tag{2.2}$$

are obtained. The matrix element for the process is then obtained by sandwiching the propagator, $-\frac{ig_{\mu\nu}}{q^2}$, between these currents, yielding

$$M = -\frac{ee'}{q^2}\left[\bar{u}(k',\sigma')\gamma_\mu u(k,\sigma)\right]\left[\bar{u}(p',s')\gamma^\mu u(p,s)\right] \tag{2.3}$$

Note that the charge on the muon current e' has been distinguished from that on the electron current to allow the formalism to be used for eq scattering, where the charge of the quark is not the same as that of the electron.

The cross-section for the process is then obtained from $|M|^2$ by using the Fermi Golden Rule. For the unpolarised cross-section initial spin states must be averaged and the final spin states summed. This involves the contraction of two leptonic tensors

$$\frac{1}{4}\sum_{spins}|M|^2 = \frac{e^2 e'^2}{q^4} L_e^{\mu\nu} L_{\mu\nu}^{muon} \tag{2.4}$$

The spin summations are performed using the well established trace techniques of Dirac algebra (see Appendix A) to obtain

$$L_e^{\mu\nu} = 2(k'^{\mu}k^{\nu} + k'^{\nu}k^{\mu} - (k'.k)g^{\mu\nu}) \tag{2.5}$$

where the mass of the electron has been neglected, and

$$L_{\mu\nu}^{muon} = 2(p'_{\mu}p_{\nu} + p'_{\nu}p_{\mu} - (p'.p - m^2)g_{\mu\nu}) \tag{2.6}$$

where m is the mass of the muon. In the limit where all masses may be ignored the result is

$$\frac{1}{4}\sum_{spins}|M|^2 = \frac{e^2 e'^2}{Q^4} 2s^2[1 + (1-y)^2] \tag{2.7}$$

Note that for this simple process

$$(p+q)^2 = p'^2$$

so that

$$2p.q + q^2 = 0$$

and consequently

$$x = \frac{Q^2}{p.q} = 1$$

and

$$Q^2 = sy.$$

Putting the matrix element together with the phase space and the flux factor (as detailed in Appendix C) the Fermi Golden Rule gives the differential cross-section

$$\frac{d\sigma}{dy} = \frac{e^2 e'^2}{8\pi Q^4}[1 + (1-y)^2]s \tag{2.8}$$

and since $e' = e$ this may be written in the form

$$\frac{d\sigma}{dy} = \frac{2\pi\alpha^2}{Q^4}[1 + (1-y)^2]s \tag{2.9}$$

This derivation and useful equivalent forms for the cross-section are collected in Appendix D.

It is illuminating to follow a more heuristic approach to the derivation of this form by considering the spin directions of the electron and muon with respect to their directions of motion. There are two possibities: the incoming electron and muon may have the same handedness (RR or LL) or opposite handedness (RL or LR). If they have opposite handedness then there is net spin $J_z = +1(RL)$ or $J_z = -1(LR)$ along the beam direction. In the high energy limit handedness is conserved, hence $RL \to RL$ such that the amplitude for scattering at an angle θ is given by the rotation matrix $d^1_{11}(\theta) = \frac{1}{2}(1 + \cos\theta)$. For $LR \to LR$ the amplitude is the same since $d^1_{-1-1} = d^1_{11}$. This case is illustrated in Fig. 2.4. The same result is obtained by considering the rotation of spin $\frac{1}{2}$ through the angle θ for both the electron and the muon: $d_{++} = \cos(\frac{\theta}{2})$ each, giving a total amplitude $cos^2(\frac{\theta}{2})$ for $RL \to RL$. Similarly for $LR \to LR$, since $d_{--} = d_{++}$.

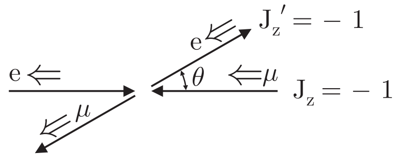

Fig. 2.4 $e\mu$ scattering with opposite handedness

If the leptons have the same handedness there is no net spin along the beam direction thus an isotropic distribution can ensue. This is most easily seen by considering the rotation of spin $\frac{1}{2}$ through the angle θ for each of the electron and the muon and realising that for overall $J_z = 0$ the transition $RR \to RR$ may also be achieved by the rotations $d_{+-} = \sin(\frac{\theta}{2})$, such that the total amplitude is $\cos^2(\frac{\theta}{2}) + \sin^2(\frac{\theta}{2})$. Similarly for $LL \to LL$ since $d_{-+} = -d_{+-}$. This case is illustrated in Fig. 2.5. Thus there are two distinguishable amplitudes: opposite handed $cos^2(\frac{\theta}{2}) = (1 - y)$ and same handed isotropic, giving a total cross-section with the dependence $1 + (1 - y)^2$.

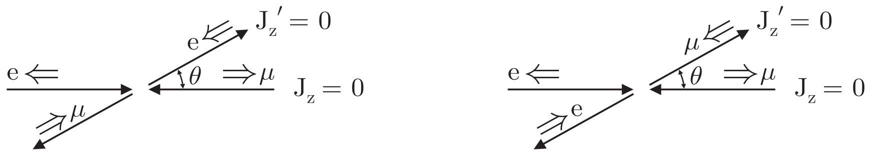

(a) (b)

Fig. 2.5 $e\mu$ scattering with same handedness

2.1.2 Elastic electron-quark scattering

The above formalism is now extended to electron-quark scattering in order to interpret lepton hadron scattering as an incoherent sum of lepton-parton scatters. Firstly, the charge of the quark may be $\frac{2}{3}e$ or $-\frac{1}{3}e$, which is written as $e' = e_i.e$ in general. Secondly the kinematic variables s,Q^2,y must be appropriate for electron quark scattering, where the quark takes only a fraction x' of the momentum of the parent hadron. Clearly Q^2 and y are unaffected, but $p \to x'p$, implies $s \to x's$, if s is the centre of mass energy of the electron-hadron system. Thus using the formalism which led to Eqn2.9 the cross-section for electron-quark scattering at a specific value of x' is given by

$$\frac{d\sigma}{dy} = \frac{2\pi\alpha^2}{Q^4}[1 + (1-y)^2]x'se_i^2. \tag{2.10}$$

The relationship $Q^2 = sy$ becomes $Q^2 = x'sy$ and this gives x' an identification in terms of the external kinematic variables such that $x' = x = Q^2/2p.q$.

To obtain a cross-section for electron-hadron scattering from this result a distribution function $q_i(x)$ which gives the probability that the struck quark i carries a fraction x of the hadron's momentum p must be defined. This gives the parton number, or density, distribution. It is also useful to define the momentum distribution $xq(x)$ (also called the momentum density), and this is what is meant by the term parton distribution function or PDF.

Thus the double differential cross-section for incoherent scattering off all possible types of quark with a specific value of x is

$$\frac{d^2\sigma}{dxdy} = \frac{2\pi\alpha^2}{Q^4}[1 + (1-y)^2]s\sum_i e_i^2 xq_i(x) \tag{2.11}$$

or equivalently

$$\frac{d^2\sigma}{dxdQ^2} = \frac{2\pi\alpha^2}{xQ^4}[1 + (1-y)^2]\sum_i e_i^2 xq_i(x) \tag{2.12}$$

2.2 Inelastic e- or μ-hadron scattering

To appreciate these parton model results they must be compared with the general formulae for inelastic lepton hadron scattering. The detailed formalism is given in Appendix D. It is necessary to consider the contraction of a leptonic and a hadronic tensor

$$d\sigma \sim L^e_{\mu\nu}W^{\mu\nu}$$

The hadronic tensor parametrizes our ignorance of the hadronic current, but it must have the general form

$$W^{\mu\nu} \quad = \quad -W_1 g^{\mu\nu} + \frac{W_2}{m^2} - i\epsilon^{\mu\nu\alpha\beta}p_\alpha q_\beta \frac{W_3}{2m^2} \tag{2.13}$$

$$+q^\mu q^\nu \frac{W_4}{m^2} + (p^\mu q^\nu + q^\mu p^\nu)\frac{W_5}{m^2} + i(p^\mu q^\nu - p^\nu q^\mu)\frac{W_6}{2m^2},$$

where m is the hadron mass and the W_i are real scalar functions (called structure functions) of two independent kinematic variables such as x, Q^2 or x, y. The expression for $W^{\mu\nu}$ can immediately be simplified since not all of these terms can contribute to the cross-section. The antisymmetric term W_6 will not contribute because the lepton tensor is symmetric and the W_3 term will not contribute since its contribution violates parity. Current conservation at the hadron vertex gives $q_\mu W^{\mu\nu} = q_\nu W^{\mu\nu} = 0$, so that

$$W_5 = -W_2 \frac{p.q}{q^2}$$

and

$$W_4 = W_2 (\frac{p.q}{q^2})^2 + W_1 \frac{m^2}{q^2}$$

Thus the hadronic tensor simplifies to

$$W^{\mu\nu} = W_1(-g^{\mu\nu} + \frac{q^\mu q^\nu}{q^2}) + \frac{W_2}{m^2}(p^\mu - \frac{p\cdot q}{q^2}q^\mu)(p^\nu - \frac{p\cdot q}{q^2}q^\nu) \tag{2.14}$$

The resulting differential cross-section expressed in terms of x, y, Q^2 is

$$\frac{d^2\sigma(lh)}{dxdy} = \frac{4\pi\alpha^2 s}{Q^4}\Big[xy^2 F_1^{lh}(x,y) + (1-y)F_2^{lh}(x,y)\Big], \tag{2.15}$$

where mass terms have been ignored and the structure functions are redefined such that $F_1 = W_1$ and $F_2 = \nu W_2/m^2$, where $\nu = p.q$. The longitudinal structure function is defined as $F_L = F_2 - 2xF_1$, so that the cross-section may also be written as

$$\frac{d^2\sigma(lh)}{dxdQ^2} = \frac{2\pi\alpha^2}{xQ^4}\Big[Y_+ F_2^{lh}(x,Q^2) - y^2 F_L^{lh}(x,Q^2)\Big], \tag{2.16}$$

where $Y_+ = 1 + (1-y)^2$. The structure functions F_1, F_2, F_L in these equations are labelled with the superscript lh to indicate that they are appropriate to the charged lepton-hadron process.

Comparing Eqn. 2.16 with the parton model result of Eqn. 2.12 implies that the parton model predicts

$$F_2^{lh}(x,Q^2) = \sum_i e_i^2 x q_i(x) \tag{2.17}$$

where the fractional momentum of the struck quark has again been identified with the kinematic variable $x = \dfrac{Q^2}{2p.q}$. Thus the parton model predicts Bjorken scaling, F_2 depends only on x not on Q^2.

The parton model also predicts,

$$F_L^{lh}(x, Q^2) = 0.$$

implying the Callan-Gross relationship, $2xF_1^{lh} = F_2^{lh}$, as a consequence for scattering from spin-$\frac{1}{2}$ partons.

The latter result may be understood by relating the structure functions to the cross-sections for the virtual photon-hadron subprocess. The detailed formalism is given in Appendix D. For Q^2 large enough to ignore mass terms, these cross=sections are given by

$$\sigma_T = \frac{4\pi^2\alpha}{Q^2(1-x)} 2xF_1$$

and

$$\sigma_T + \sigma_L = \frac{4\pi^2\alpha}{Q^2(1-x)} F_2$$

where σ_T, σ_L are the cross-sections for transverse and longitudinal virtual photon scattering. Real photons are transversely polarized, $\sigma_L = 0$, but this does not have to be true for virtual photons. It is the Callan-Gross relationship for spin $\frac{1}{2}$ partons which implies that $\sigma_L = \dfrac{4\pi^2\alpha}{Q^2} F_L = 0$ and measurements of $R = \sigma_L/\sigma_T$ in early SLAC data indicated that this is true (approximately). If partons were, for example, spin 0 a very different prediction would be obtained. In this case $\sigma_T = 0$ and $R \to \infty$, since a spin 0 parton cannot absorb a transverse photon with helicity ± 1. The formal derivation of this result is left as a problem.

At this point it is worth reviewing the derivation of the parton model results to make some of its limitations clear. (The detailed formalism is summarized in Appendix B). When calculating the cross-section for electron-muon scattering the two-body final state phase space must be evaluated. It is educational not to integrate out all the delta functions but to express the phase space as

$$\mathrm{dLips} = \frac{E' dE' d\Omega}{4(2\pi)^2} \delta(\nu - Q^2/2).$$

where $E,\ E'$ are the lab energies of the incident and scattered electron and $d\Omega$ is the solid angle at scattering angle θ. The delta function arises from overall 4-momentum conservation, $\delta^4(p + q - p')$, and thus

$$\delta(p'^2 - m^2) = \delta(q^2 + 2\nu) = \frac{1}{2}\delta(\nu - Q^2/2).$$

Hence the differential cross-section

$$\frac{d^2\sigma}{d\Omega dE'} = \frac{4\alpha^2}{Q^4} mE'^2 \left[\cos^2\frac{\theta}{2} + \frac{Q^2}{2m^2}\sin^2\frac{\theta}{2}\right] \delta(\nu - Q^2/2). \qquad (2.18)$$

is obtained in the lab frame.

In the derivation of the electron-hadron cross-section the equivalent form is

$$\frac{d^2\sigma}{d\Omega dE'} \quad = \quad \frac{4\alpha^2}{Q^4}\frac{E'^2}{m}\left[W_2\cos^2\frac{\theta}{2} + 2W_1\sin^2\frac{\theta}{2}\right] \tag{2.19}$$

where a delta function is not introduced since $p'^2 = p_X^2$ does not have to take a unique value. Comparing Eqns. 2.18 and 2.19 it is clear that for a pointlike 'hadron' of mass m and unit charge,

$$2W_1 = \frac{Q^2}{2}\delta(\nu - Q^2/2)$$

and

$$W_2 = m^2\delta(\nu - Q^2/2)$$

or equivalently

$$2W_1 = \frac{Q^2}{2\nu}\delta(1 - \frac{Q^2}{2\nu})$$

and

$$\frac{\nu W_2}{m^2} = \delta(1 - \frac{Q^2}{2\nu})$$

such that the structure functions $F_2 = \nu W_2/m^2$ and $F_1 = W_1$ are functions of the single dimensionless variable $x = Q^2/(2\nu)$ rather than of the variables ν, Q^2 separately.

In the parton model the target hadron is NOT pictured as pointlike but the supposition is that, if the probing virtual photon has sufficiently large Q^2, it may be able to resolve pointlike partons within the hadron. To make use of the results developed so far, it is necessary to be more specific about the relationship $p_{parton} = x'p_{hadron}$. The components of the parton 4-vector must be specified in terms of those of the hadron 4-vector, such that if p_{hadron} is given by $(E, p_L, \mathbf{p}_T = 0)$ then p_{parton} is given by $(x'E, x'p_L, \mathbf{p}_T = 0)$. This implies a mass for the parton $m = x'M$, where the mass of the hadron is now denoted as M to distinguish it from the mass of the parton. With these definitions the parton model structure functions for a single parton of unit charge are given by

$$W_1 = \frac{Q^2}{4\nu'}\delta(1 - \frac{Q^2}{2\nu'})$$

$$\frac{\nu' W_2}{m^2} = \delta(1 - \frac{Q^2}{2\nu'})$$

where the variable

$$\nu' = p_{parton}.q = x'p_{hadron}.q = x'\nu$$

(Note that this relationship would not hold if the parton were not collinear with the hadron). Hence for a parton of mass $x'M$ and charge $e_i.e$, inside a hadron of mass M, the contributions to the hadron structure functions are

$$\frac{W_1}{M} = e_i^2 \frac{Q^2}{4(xM)\nu'} \delta(1 - \frac{Q^2}{2\nu'})$$

and

$$\frac{\nu' W_2}{M} = e_i^2 (xM) \delta(1 - \frac{Q^2}{2\nu'}),$$

where the roles of the masses of the parton and the hadron are made manifest. Thus

$$F_1 = e_i^2 \frac{x}{2x'^2} \delta(1 - \frac{x}{x'})$$

and

$$F_2 = e_i^2 \delta(1 - \frac{x}{x'})$$

Summing these contributions for one parton incoherently over all the partons in the hadron gives

$$F_2 = \sum_i e_i^2 \int_0^1 dx q_i(x) x \delta(x' - x)$$

and

$$F_1 = \sum_i e_i^2 \int_0^1 dx q_i(x) \frac{x}{2x'^2} x \delta(x' - x),$$

by using the parton density functions. Hence the usual parton model results are recovered.

In this derivation the concept of a parton of mass $x'M$ has been introduced, so that both the parton energy and longitudinal momentum may be fractions x' of those of the hadron. This collinear approximation is only really possible in the infinite momentum frame, where all masses may be neglected. In this frame time dilation slows down the rate at which partons interact with each other, so that during the short time that the virtual photon interacts with the parton, the parton is essentially free. This jusitifies the incoherent addition of the probabilities to interact with each parton in the target. The interaction of the partons then happens over a much longer time-scale in which the struck parton must interact with the other partons in order to form colourless hadrons in the final state.

Such a picture can only really be valid at large Q^2, but suprisingly both Bjorken scaling and the Callan-Gross relationship were substantiated by the early SLAC data at Q^2 values in the range $1 - 10\,\mathrm{GeV}^2$. In Chap. 3 the early onset of scaling will be explored in the context of the theory of QCD. The remainder of this Chapter develops the evidence for the parton model further by considering the results from neutrino and antineutrino scattering.

2.3 Neutrino induced DIS

2.3.1 Elastic (anti-)neutrino-electron scattering

The Feynman diagram for elastic neutrino-electron scattering through the charged weak current is illustrated in Fig. 2.6. Instead of the the electro-

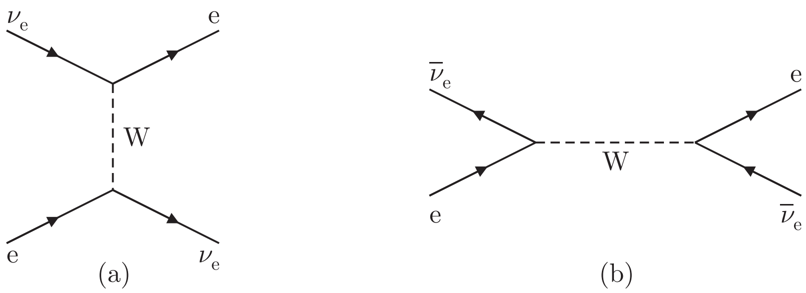

Fig. 2.6 νe scattering

magnetic current of Eqn. 2.1 is replaced by

$$j^\nu = -i\frac{g}{\sqrt{2}}\bar{u}(k',\sigma')\frac{1}{2}\gamma^\nu(1-\gamma^5)u(k,\sigma) \tag{2.20}$$

which has the $V-A$ form which projects out only left-handed particles and right-handed antiparticles. The weak coupling g has the value $g\sin(\theta_W) = e$ in electroweak unification. The propagator to be sandwiched between two currents of this form is now that of the masive W boson

$$-i\frac{(g_{\mu\nu} - p_\mu q_\nu/M_W^2)}{q^2 - M_W^2}$$

giving a matrix element

$$\begin{aligned} M &= \frac{g^2}{2}\frac{1}{M_W^2 - q^2}\left[\bar{u}(k',\sigma')\frac{1}{2}\gamma_\mu(1-\gamma^5)u(k,\sigma)\right] \\ &\quad \times \left[\bar{u}(p',s')\frac{1}{2}\gamma^\mu(1-\gamma^5)u(p,s)\right]. \end{aligned} \tag{2.21}$$

When $Q^2 = -q^2 \ll M_W^2$ this is usually written as

$$M = \frac{G}{\sqrt{2}}\left[\bar{u}(k',\sigma')\gamma_\mu(1-\gamma^5)u(k,\sigma)\right]\left[\bar{u}(p',s')\gamma^\mu(1-\gamma^5)u(p,s)\right] \tag{2.22}$$

where $\dfrac{G}{\sqrt{2}} = \dfrac{g^2}{8M_W^2}$ defines Fermi's weak coupling constant G.

Evaluating the spin averaged squared matrix element and the flux and phase space factors gives

$$\frac{d\sigma\ (\nu e)}{dy} = \frac{G^2}{\pi}s \tag{2.23}$$

as the equivalent cross-section to Eqn. 2.9 for neutrino electron scattering. The antineutrino electron cross-section is then obtained by crossing as

$$\frac{d\sigma(\bar{\nu}e)}{dy} = \frac{G^2}{\pi}(1-y)^2 s \tag{2.24}$$

The simple forms of these cross-sections can be readily understood by returning to the heuristic arguments based on handedness. Because of the $V-A$ form of the weak charged current, there are not many possibilities in spin averaging. The neutrino and electron are necessarily both left handed and thus for νe scattering the isotropic distribution appropriate for $LL \to LL$ is obtained. The antineutrino is right-handed and thus for $\bar{\nu}e$ scattering the $(1-y)^2$ distribution appropriate for $RL \to RL$ is obatined.

2.3.2 Elastic (anti-)neutrino-(anti-)quark scattering

These results may now be applied to (anti-)neutrino (anti-)quark scattering by defining an (anti-)quark charged weak current as a $V-A$ current of the same form as the leptonic charged weak current, with exactly the same weak charge g. Hence, since this current projects out left-handed quarks and right-handed antiquarks, the scattering cross-sections at a specific value of x are given by

$$\frac{d\sigma(\nu q)}{dy} = \frac{G^2}{\pi}xs$$

$$\frac{d\sigma(\bar{\nu} q)}{dy} = \frac{G^2}{\pi}(1-y)^2 xs$$

$$\frac{d\sigma(\nu \bar{q})}{dy} = \frac{G^2}{\pi}(1-y)^2 xs$$

$$\frac{d\sigma(\bar{\nu} \bar{q})}{dy} = \frac{G^2}{\pi}xs$$

Thus the parton model predictions for neutrino and antineutrino hadron scattering are,

$$\frac{d^2\sigma(\nu h)}{dxdy} = \frac{G^2 s}{\pi}\Sigma_i \left[xq_i(x) + (1-y)^2 x\bar{q}_i(x)\right] \tag{2.25}$$

and

$$\frac{d^2\sigma(\bar{\nu} h)}{dxdy} = \frac{G^2 s}{\pi}\Sigma_i \left[(1-y)^2 xq_i(x) + x\bar{q}_i(x)\right] \tag{2.26}$$

respectively, the same parton distribution functions introduced in Eqs. 2.11, 2.12 have been used. These cross-sections for ν, $\bar{\nu}$ scattering include antiquarks as well as quarks in the target nucleon. This is required to explain the results of ν, $\bar{\nu}$ scattering experiments. The reconciliation of the parton model for inelastic lepton-hadron scattering with the static quark model, which pictures nucleons as made of three constituent quarks which give them their flavour properties, is made by identifying the constituent quarks as 'valence' quarks, and considering the nucleon to be made of three such quarks and a 'sea' of quark antiquark pairs which have no overall flavour. Both the valence quarks and the sea quarks and antiquarks are identified as partons.

2.3.3 Inelastic (anti-)neutrino-hadron scattering

To fully interpret the parton model predictions of Eqs. 2.25 and 2.26 for (anti-)neutrino hadron scattering they should be compared with the general formulae which may be derived from the hadronic tensor already given in Eqn. 2.14. In the present case W_6 contributes in principle, and current conservation is not exact for the axial vector current such that there are residual terms from W_4 and W_5. However these contributions are all small terms of the order of the lepton mass. The only significant difference is that the parity violating contribution of W_3 cannot be omitted. The differential cross-sections which result are

$$\frac{d^2\sigma(\nu h)}{dxdy} = \frac{G^2 s}{2\pi}\Big[xy^2F_1^{\nu h}(x,y) + (1-y)F_2^{\nu h}(x,y) + y(1-\frac{y}{2})xF_3^{\nu h}(x,y)\Big], \tag{2.27}$$

and

$$\frac{d^2\sigma(\bar{\nu} h)}{dxdy} = \frac{G^2 s}{2\pi}\Big[xy^2F_1^{\bar{\nu} h}(x,y) + (1-y)F_2^{\bar{\nu} h}(x,y) - y(1-\frac{y}{2})xF_3^{\bar{\nu} h}(x,y)\Big], \tag{2.28}$$

where $\nu W_3/m^2 = F_3$. In terms of the longitudinal structure function F_L these become

$$\frac{d^2\sigma(\nu,\bar{\nu})}{dxdy} = \frac{G^2 s}{4\pi}\Big[Y_+F_2^{\nu,\bar{\nu}}(x,y) - y^2F_L^{\nu,\bar{\nu}}(x,y) \pm Y_-xF_3^{\nu,\bar{\nu}}(x,y)\Big], \tag{2.29}$$

where the plus sign applies for neutrino and the minus sign for antineutrino scattering, and $Y_- = 1-(1-y)^2$. Comparing this with the quark-parton model formluae Eqs. 2.25, 2.26 gives

$$F_L^{\nu,\bar{\nu}}(x,y) = 0$$

appropriate for scattering from only spin $\frac{1}{2}$ partons, and

$$F_2^{\nu,\bar{\nu}}(x,y) = 2\sum_i x(q_i(x) + \bar{q}_i(x))$$

$$xF_3^{\nu,\bar{\nu}}(x,y) = 2\sum_i x(q_i(x) - \bar{q}_i(x))$$

so that Bjorken scaling is obtained. The parity violating structure function xF_3 is non-zero because the couplings of q and $\bar{q}$ are different due to their different handedness. The neutrino and antineutrino structure functions are distinguished from each other by the flavour of quarks and antiquarks which may enter the sums, as detailed in the following Section.

2.4 Quark-Parton model tests

A powerful test of the quark-parton model can be made by comparing the structure functions obtained in charged lepton scattering with those obtained in (anti-)neutrino scattering, as follows. Consider charged lepton scattering from a proton target. Clearly the result of Eqn. 2.17 should be generalised to give

$$F_2(x, Q^2) = \Sigma_i e_i^2 * (xq_i(x) + x\bar{q}_i(x)), \tag{2.30}$$

and thus for a proton target

$$F_2^{lp}(x) = \frac{4}{9}x(u(x)+\bar{u}(x)+c(x)+\bar{c}(x))+\frac{1}{9}x(d(x)+\bar{d}(x)+s(x)+\bar{s}(x)) \tag{2.31}$$

Nucleon parton distribution functions are **defined** to be those for the proton. For a neutron target strong isospin swapping gives

$$F_2^{ln}(x) = \frac{4}{9}x(d(x)+\bar{d}(x)+c(x)+\bar{c}(x))+\frac{1}{9}x(u(x)+\bar{u}(x)+s(x)+\bar{s}(x)) \tag{2.32}$$

and an isoscalar target is treated as an average of these two

$$F_2^{lN} = \frac{5}{18}x(u(x)+\bar{u}(x)+d(x)+\bar{d}(x))+\frac{1}{9}x(s(x)+\bar{s}(x))+\frac{4}{9}x(c(x)+\bar{c}(x)) \tag{2.33}$$

It is assumed that there is no significant bottom or top quark content in the nucleon. (Note that not all authors define a parton distribution for a heavy quark such as the charm quark. The treatment of heavy quarks is discussed in Sec. 4.7)

Now consider charged current neutrino scattering from a proton target. Note that the W^+ weak current has to increase the charge of the parton by one unit. Hence it can only hit quarks of charge $-\frac{1}{3}e$ or antiquarks of charge $-\frac{2}{3}e$, hence

$$\begin{aligned} F_2^{\nu p} &= 2x(d(x)+s(x)+\bar{u}(x)+\bar{c}(x)), \\ xF_3^{\nu p} &= 2x(d(x)+s(x)-\bar{u}(x)-\bar{c}(x)) \end{aligned} \tag{2.34}$$

For antineutrino scattering on a proton target the W^- weak current must decrease the charge of the struck parton by one unit. Hence it can only hit quarks of charge $\frac{2}{3}e$ or antiquarks of charge $\frac{1}{3}e$, hence

$$\begin{aligned} F_2^{\bar{\nu} p} &= 2x(u(x)+c(x)+\bar{d}(x)+\bar{s}(x)), \\ xF_3^{\bar{\nu} p} &= 2x(u(x)+c(x)-\bar{d}(x)-\bar{s}(x)) \end{aligned} \tag{2.35}$$

Again it is assumed that there are no top or bottom quarks in the nucleon targets and that W^2 is above threshold for production of charmed quarks in the final state. (Below the charm threshold, d must be multiplied by $\cos^2\theta_c$ and s by $\sin^2\theta_c$ in Eq. 2.34 and $\bar{d}$ must be multiplied by $\cos^2\theta_c$ and $\bar{s}$ by $\sin^2\theta_c$ in Eq. 2.35, where θ_c is the Cabibbo mixing angle).

Strong isospin swapping gives the corresponding results for a neutron target, and thus the results appropriate to an isoscalar target are

$$F_2^{\nu N}(x) = x(u(x) + d(x) + \bar{u}(x) + \bar{d}(x) + 2s(x) + 2\bar{c}(x)) \quad (2.36)$$
$$F_2^{\bar{\nu} N}(x) = x(u(x) + d(x) + \bar{u}(x) + \bar{d}(x) + 2\bar{s}(x) + 2c(x)) \quad (2.37)$$

and

$$xF_3^{\nu N}(x) = x(u(x) + d(x) - \bar{u}(x) - \bar{d}(x) + 2s(x) - 2\bar{c}(x)) \quad (2.38)$$
$$xF_3^{\bar{\nu} N}(x) = x(u(x) + d(x) - \bar{u}(x) - \bar{d}(x) - 2\bar{s}(x) + 2c(x)) \quad (2.39)$$

Hence, assuming $s(x) = \bar{s}(x), c(x) = \bar{c}(x)$, the structure functions F_2 for lepton and neutrino scattering on isoscalar targets are related as follows

$$F_2^{lN} = \frac{5}{18}F_2^{\nu N} - \frac{1}{3}xs(x) + \frac{1}{3}xc(x) \quad (2.40)$$

Since the contributions of strange and charmed sea quarks are small (see below), this implies

$$F_2^{lN} \approx \frac{5}{18}F_2^{\nu N}$$

The observation that the charged lepton scattering and the neutrino scattering structure functions are indeed related by $\sim 5/18$, established the relationship of the parton scatterers to the quarks of the constituent quark model and thus established the quark-parton model.

The early (anti)neutrino data [Fis82] were also used to develop the model further by determining the approximate shapes of the sea and valence quark momentum distributions in the nucleon. Since antiquark distributions are purely sea distributions, whereas quark distributions have both valence and sea contributions,

$$xq(x) = xq_v(x) + xq_{sea}(x), \;\; x\bar{q}(x) = x\bar{q}_{sea}(x),$$

and it is assumed that

$$xq_{sea}(x) = x\bar{q}_{sea}(x).$$

Applying these relationships to the structure functions for (anti)neutrino scattering on isoscalar targets gives

$$xF_3^{\nu N} \approx xF_3^{\bar{\nu} N} \approx \frac{xF_3^{\nu N}(x) + xF_3^{\bar{\nu} N}(x)}{2} = x(u_v(x) + d_v(x)) = xV(x) \quad (2.41)$$

where $xV(x)$ represents a purely valence, or non-singlet, distribution consisting only of u and d valence quarks, as suggested by the constituent quark model. Similarly,

$$F_2^{\nu N}(x) = F_2^{\bar{\nu} N}(x) = x(u_v(x)+d_v(x)+2\bar{u}(x)+2\bar{d}(x)+2\bar{s}(x)+2\bar{c}(x)) \quad (2.42)$$

so that

$$F_2^{\nu N}(x) = xV(x) + xS(x) \quad (2.43)$$

represents a combination of valence and sea, which is a singlet distribution.[1]

Hence the shapes of the valence and sea distributions may be extracted from the data on ν,$\bar{\nu}$ structure functions. For large x, $F_2^{\nu N} = xF_3^{\nu N}$ and so both distributions must be purely valence. Thus the sea quarks are only significant at low momemtum fraction. At small x, $xF_3^{\nu N} \to 0$ and hence the valence distribution is now negligible. The valence and sea distributions extracted from the data are illustrated schematically in Fig **??** (*figure not yet prepared - Fig.6.3 gives an idea*). These results can be interpreted as follows. If the target hadron consisted of just three non-interacting valence quarks, then there would be no sea distribution and the valence distribution would be a delta function at $x = \frac{1}{3}$. Of course the three quarks are confined in a small size and thus there must be a sizeable uncertainty in their momentum (called Fermi motion) such that this delta function will be smeared. This begs the question of what is confining the quarks. Since they must be interacting they can redistribute momenta amongst themselves. In the theory of QCD (summarised in Chap. 3) quarks interact via the exchange of gluons, and these virtual gluons may also produce quark-antiquark pairs, which deplete the momentum of the valence quarks and produce a low momentum sea, as observed.

At moderate Q^2 the sea is responsible for $\sim$ 10% of the hadron's momentum, as may be deduced from the cross-section ratio, $\dfrac{\sigma(\nu N)}{\sigma(\bar{\nu} N} \sim 0.43$ (see problem 3). Since the sea is considered as made up from $q\bar{q}$ pairs emitted by gluons light $q\bar{q}$ pairs are more readily produced than than heavy $q\bar{q}$ pairs. This is why the strange and charmed quark contributions to the structure functions are small.

The charged lepton and ν, $\bar{\nu}$ DIS scattering data can be used to gain detailed information on the flavour decomposition of the valence and sea distributions. A lot of early phenomenology was done on the assumption of an SU(3) symmetric sea: $\bar{u} = u_{sea} = \bar{d} = d_{sea} = \bar{s} = s = K$, but $\bar{c} = c = 0$. This would give

$$\frac{F_2^{ep}}{F_2^{en}} = \frac{u_v + 4d_v + 4/3K}{4u_v + d_v + 4/3K} \quad (2.44)$$

The assumption of an SU(3) symmetric sea has been modified in the light of experience as explained in Chap. 6, however the above relationship remains approximately true for moderate Q^2 values. Experimental results on this quantity indicate that $F_2^{en}/F_2^{ep} \to 1$ at small x, corresponding to dominance of the sea, whereas $F_2^{en}/F_2^{ep} \ll 1$ at large x indicating

[1]The terminology singlet and non-singlet will be explained in context in Sec. 4.2, particularly following Eq. 4.30.

a dominance of u valence quarks. Since there is no sea at large x, the ratio $d_v/u_v = 1/2$, which is expected from the consituent quark model, would give $F_2^{en}/F_2^{ep} \to 2/3$. However, the experimental value is closer to $F_2^{en}/F_2^{ep} \to 1/4$, suggesting that, $d_v/u_v \to 0$ as $x \to 1$. Results on the ratio $F_2^{\nu p}/F_2^{\bar{\nu} p}$ confirm this (see problem 4). These results indicate that the d_v quark momentum distribution is softer than that of the u_v quark, at high x.

Further investigation of the use of DIS data to extract the detailed shapes of the parton distribution functions of different flavours is postponed until Chapter 6, because modern DIS data are so accurate that the corrections to the parton model emdbodied in QCD must first be considered.

2.5 Sum rules

To conclude this chapter the further support for the quark-parton model which comes from sum rules is considered. Since $q(x)$ gives the quark number distribution the number sum-rules

$$\int_0^1 dx u_v(x) = 2, \int_0^1 dx d_v(x) = 1 \tag{2.45}$$

are implied. Of course these relations cannot be directly verified, but their consequences can be, for example the Gross Llewelyn-Smith sum rule [Gro69]

$$\int_0^1 dx F_3^{\nu N} \approx \int_0^1 dx(u_v(x) + d_v(x)) = 3 \tag{2.46}$$

was verified in early neutrino data on isoscalar targets. Similarly, the Adler sum rule [Adl66]

$$\int_0^1 \frac{dx}{x}\left(F_2^{\bar{\nu} p} - F_2^{\nu p}\right) = 2\int_0^1 dx((u_v(x) - d_v(x)) = 2 \tag{2.47}$$

was verified using neutrino data on hydrogen targets.

Sum rules are a lot more general than this simple quark-parton model picture implies. They may be rigorously derived in QCD from current algebra, with the appropriate order α_s corrections.

A sum rule can also be applied to the sum over the momenta of all types of quarks and antiquarks in the nucleon. Denoting this distribution as the singlet $x\Sigma(x)$,

$$x\Sigma(x) = x(u(x) + \bar{u}(x) + d(x) + \bar{d}(x) + s(x) + \bar{s}(x) + c(x) + \bar{c}(x)) \tag{2.48}$$

the momentum sum-rule is expressed as

$$\int_0^1 dx x\Sigma(x) = 1 \tag{2.49}$$

if quarks and antiquarks carry all of the momentum of the nucleon. This momentum sum rule (MSR) can be checked experimentally, since

$$x\Sigma(x) = F_2^{\nu N}$$

and the result

$$\int_0^1 dx F_2^{\nu N} \sim 0.5 \tag{2.50}$$

implies that there is more momentum in the nucleon than that carried by the quarks and antiquarks. This gave impetus to the development of the theory of QCD in which the deficit in momentum is carried by the gluons.

2.6 Summary

This chapter has described the basic idea of the quark-parton model and provided the details for constructing the full deep inelastic cross-sections for electron and neutrino nucleon scattering. Crucial to the model are the parton momentum densities, which although they cannot be calculated within the model are assumed to be universal. The various test of the model described in the chapter show it to be succssful. However a number of paradoxes remain:

- the partons are assumed to be essentially free particles, but at the same time are confined inside the hadron;
- although Bjorken scaling is approximately satisfied, there is clear evidence for sclae breaking at large and small x;
- the failure to saturate the momentum sum rule with contributions from charged partons shows that there are other nucleon constituents.

These puzzles led to the development of QCD as the theory of the strong interactions. How it in turn resolves the difficulties of the simple quark-parton model will be taken up in Chapter 4 after the elements of QCD have been outlined in the next chapter.

2.7 Questions

1. Derive the relationship $x = \dfrac{Q^2}{2p.q}$ from the kinematics of Fig. 2.2 by neglect masses and insisting that struck quark and outgoing quark are on mass-shell.
2. Derive the equivalent equation to Eqn 2.18 for spin 0 quarks, by using the appropriate vertex factors (see Appendix B). Hence deduce that $\sigma_T = 0$ in this case.
3. Use equations 2.25,2.26 to calculate the total cross-sections $\sigma(\nu N)$ and $\sigma(\bar{\nu} N)$ in terms of the integrals $\int_0^1 dx x q(x) = Q$ and $\int_0^1 dx x \bar{q}(x) = \bar{Q}$. Hence prove that

$$\frac{\bar{Q}}{Q} = \frac{3R-1}{3-R},$$

where $R = \dfrac{\sigma(\nu N)}{\sigma(\bar{\nu}N}$

4. Consider Eqs 2.34, 2.35 for large x. Hence express the ratio $F_2^{\nu p}/F_2^{\bar{\nu}p}$ in terms of a ratio of valence quark distributions.
5. Experimental information on valence and sea distributions may also be obtained from charged lepton-nucleon scattering. Express F_2^{lN} for an isoscalar target as a combination of valence and sea distributions. The difference $F_2^{lp} - F_2^{ln}$ (which may be deduced experimentally from data on proton and deuterium targets) can be expresses purely in terms of valence distributions. Justify this statement and hence derive the result of the Gottfried sum-rule [Got67]

$$\int_0^1 \frac{dx}{x}(F_2^{lp} - F_2^{ln}) = \frac{1}{3}.$$

By examining the assumptions you made in the derivation, suggest why this sum-rule is violated.
6. Neutrino and antineutrino scattering data on proton and isoscalar targets potentially give a lot of information on the different parton flavour distributions. Suggest how the 4 cross-sections for the processes νp, $\bar{\nu}p$, νn, $\bar{\nu}n$, might be combined to extract the distributions u_v, d_v, $\bar{u}$, $\bar{d}$, assuming that $s = \bar{s} = 0$.
7. The momentum sum rule can also be checked from charged lepton hadron data. Define $\epsilon_u = \int_0^1 dxx(u+\bar{u})$, $\epsilon_d = \int_0^1 dxx(d+\bar{d})$ and hence express $\int_0^1 dxF_2^{ep}$ and $\int_0^1 dxF_2^{en}$ in terms of these integrals (again assuming $s = \bar{s} = 0$). Experimental results yield $\int_0^1 dxF_2^{ep} \sim 0.18$ and $\int_0^1 dxF_2^{en} \sim 0.12$. Deduce the fraction of nucleon momentum taken by gluons, ϵ_g.

3
QCD and formal methods

The chapter begins with a brief introduction to QCD. Full QCD calculations are not attempted, instead some key tree level diagrams are evaluated using the corresponding QED processes and QCD colour factors. The idea of renormalisation is then introduced, showing how it leads to the 'running coupling'. A brief discussion of the renormalisation group follows. The relation of DIS structure functions to the hadronic tensor $W_{\mu\nu}$ for virtual photon Compton scattering is explained and light cone and Sudakov variables are introduced. The chapter ends with an outline of the operator production expansion and how this may be used to provide the justification for the 'factorisation' of the DIS cross-section. None of the topics here are treated either with full rigour or in detail, the aim is to give an outline of some of the more formal approaches to DIS and to provide references for further study. At the end of the chapter are appendices containing useful formulae for cross-sections etc.

Do so some sections go into too much detail - better in appendices? Written 2000 and not revised.

3.1 QCD

Before outlining the mathematical structure of QCD it is worth recalling its important features. The idea that quarks carry a 3-fold 'colour' charge was introduced to allow baryon wavefunctions (e.g. the Δ^{++}) to have simultaneously the correct permutational symmetry and satisfy Fermi-Dirac statistics. The word 'colour' and the designation of the 3 varieties of charge as red (r), green(g), blue(b) are convenient shorthands but one should consider colour charge as very closely analogous to the 2-fold electric charge, as the mathematical structure of QCD will make clear. The theory also provides the basis for why only the 'colourless' qqq and $\mathrm{q\bar{q}}$ combinations form 'confined' hadronic bound states.[1] The strong force quanta – the spin-1 massless gluons – also carry colour charges and this is the major difference between QCD and QED. Consider a $\mathrm{q\bar{q}}$ meson and all the possible combinations of colour that a gluon exchanged between the q and $\mathrm{\bar{q}}$ might carry: naively (r,g,b)$\otimes$($\mathrm{\bar{r}, \bar{g}, \bar{b}}$) gives 9 combinations, however the $\mathrm{r\bar{r}}$,

[1]There is a nice account of why this is plausible with an SU(3) of colour, together with other QCD-based results on the static properties of hadrons in [Bow90,Ch.12].

$g\bar{g}$, $b\bar{b}$ 'neutral' combinations may be linearly combined to give three new states so that the 9 combinations are split into one totally symmetric colour state $(r\bar{r} + g\bar{g} + b\bar{b})/\sqrt{3}$ and 8 others: $r\bar{g}$, $r\bar{b}$, $g\bar{r}$, $g\bar{b}$, $b\bar{r}$, $b\bar{g}$, $(r\bar{r} - g\bar{g})/\sqrt{2}$, $(r\bar{r}+g\bar{g}-2b\bar{b})/\sqrt{6}$. In group theoretic language, this is the outcome of combining the 3 and $\bar{3}$ representations of SU(3): $3 \otimes \bar{3} = 8 \oplus 1$. It explains why there only 8 gluons, the totally symmetric colour singlet gluon would be unconfined and would couple equally to all colour charges – as the photon does to both charges in QED. The other two colour 'neutral' combinations are analogous to the electrically neutral members of strong isospin multiplets - they are not 'colourless'. The SU(3) symmetry of QCD is assumed to be exact.

3.1.1 The QCD Lagrangian

In QCD the strong force at short distances is assumed to have a similar space-time structure to QED. The SU(3) non-abelian gauge invariant coupling of the octet of gluons amongst themselves and with the triplet of quarks gives a much richer structure. Mathematically the group generators T^a satisfy

$$[T^a, T^b] = if^{abc}T^c \tag{3.1}$$

where f^{abc} are the SU(3) structure constants. The gluon field strength tensor is

$$F_a^{\mu\nu} = \partial^\mu A_a^\nu - \partial^\nu A_a^\mu + gf^{abc}A_b^\mu A_c^\nu, \tag{3.2}$$

where A_a $(a = 1, \ldots, 8)$ are the gluon fields. The quark spinor fields ψ_i transform as triplets under SU(3) with $i = 1, 2, 3$ running over the three colour indices. The Lagrangian density is given by

$$L_{QCD} = \sum_{flavours} \bar{\psi}_i(i\gamma_\mu D^\mu - m)_{ij}\psi_j - \frac{1}{4}F_a^{\mu\nu}F_{a\mu\nu} \tag{3.3}$$

where the covariant derivative is

$$D_{ij}^\mu = \delta_{ij}\partial^\mu - ig(t^a)_{ij}A_a^\mu \tag{3.4}$$

and $(t^a)_{ij}$ are 3×3 hermitian matrices, which for the fundamental triplet representation of SU(3) are $(\lambda^a)_{ij}/2$, where λ^a are the Gell-Mann matrices. The mass parameter, m, in the Lagrangian is only non-zero for the heavy flavours c, b, t. For the light quarks, mass is assumed to be generated by spontaneous symmetry breaking and m is set to zero. In any case since quarks cannot propagate freely the meaning of the parameter m will usually be context dependent.

Note that the same coupling constant g couples the gluon fields to themselves (in $F_a^{\mu\nu}$) and the gluon to the quark fields through the covariant derivative (D_{ij}^μ). The derivation of the Feynman rules from L_{QCD} and their use, even at the tree-level, is non-trivial as non-abelian gauge theories give rise to greater complications in handling quantisation and gauge invariance than QED. Briefly, in addition to the choice of gauge and gauge fixing term in the Lagrangian, to calculate with gauge invariance manifest requires the introduction of 'ghost' terms. The alternative is to give up manifest gauge invariance and ghost terms and work in a 'physical' or axial gauge in which the gluon fields satisfy $n_\mu A_a^\mu = 0$ where n_μ is a fixed space-like or null 4-vector. These complications will not be pursued here – the Feynman rules are given in the appendix at the end of chapter together with references to fuller derivations for the interested reader. Fortunately most of the tree-level results that are required later can be derived from the more familiar QED calculation with the addition of colour factors.

3.1.2 QCD colour factors

In QED the strength of the coupling of the photon to two point-like particles with charges e_1 and e_2 is given by $e_1 e_2 \alpha_{qed}$. In QCD the equivalent coupling strength for a gluon and two quarks with colour charges c_1 and c_2 is $\frac{1}{2}c_1 c_2 \alpha_S$ where $\alpha_S = g^2/4\pi$ and the $\frac{1}{2}$ is conventional. Usually one is interested in expressions for physical processes like cross-sections in which case powers of the factor $\frac{1}{2}c_1 c_2$ have to be summed or averaged over the states involved to give the overall factor by which the QED expression is modified (in addition to the change $\alpha_{qed} \to \alpha_S$). Consider the colour factor for gluon exchange between a q and a $\bar{\text{q}}$ in an overall colour singlet state $(\text{r}\bar{\text{r}} + \text{g}\bar{\text{g}} + \text{b}\bar{\text{b}})/\sqrt{3}$ – as would be the case in a meson.[2] The generic diagram is shown in Fig. 3.1 and start with the $\text{r}\bar{\text{r}}$ interactions, there are four gluons that can contribute: (a) $\text{r}\bar{\text{b}}$ for $\text{r}\bar{\text{r}} \to \text{b}\bar{\text{b}}$ (as shown) for which $c_1 c_2 = (+1)(-1) = -1$ (the sign of the colour charge is reversed for the $\bar{\text{q}}$); (b) similarly $\text{r}\bar{\text{g}}$ for $\text{r}\bar{\text{r}} \to \text{g}\bar{\text{g}}$ gives -1; (a) gluons $(\text{r}\bar{\text{r}} + \text{g}\bar{\text{g}} - 2\text{b}\bar{\text{b}})/\sqrt{6}$ and $(\text{r}\bar{\text{r}} - \text{g}\bar{\text{g}})/\sqrt{2}$ can both contribute to $\text{r}\bar{\text{r}} \to \text{r}\bar{\text{r}}$, the first gives $c_1 c_2 = (\frac{1}{\sqrt{6}})(-\frac{1}{\sqrt{6}}) = -\frac{1}{6}$ and the second $(\frac{1}{\sqrt{2}})(-\frac{1}{\sqrt{2}}) = -\frac{1}{2}$. Summing over the final states ($\text{b}\bar{\text{b}}$, $\text{g}\bar{\text{g}}$,$\text{r}\bar{\text{r}}$) gives $-1 - 1 - \frac{1}{6} - \frac{1}{2} = -\frac{8}{3}$. There are two more such factors to account for the $\text{b}\bar{\text{b}}$ and $\text{g}\bar{\text{g}}$ interactions and each is normalised by $\frac{1}{\sqrt{3}}\frac{1}{\sqrt{3}}$ from the totally symmetrised colour wavefunctions of the initial and final $\text{q}\bar{\text{q}}$ state – so the overall result remains $-\frac{8}{3}$ and the colour factor in this case is $\frac{4}{3}$ (remembering the conventional factor of 1/2).

An alternative method of calculating colour factors is to use the SU(3) group properties. Some useful properties of the T^a (adjoint, for gluons) and t^a (fundamental, for quarks) matrix representations of SU(N)) are:

$$[t^a, t^b] = i f^{abc} t^c, \ [T^a, T^b] = i f^{abc} T^c, \ (T^a)_{bc} = -i f^{abc}. \tag{3.5}$$

The t^a are normalised such that $\text{Tr}\,[t^a t^b] = T_F \delta^{ab}$, where $T_F = \frac{1}{2}$. The colour matrices then satisfy the following relations which define the constants C_F and C_A

[2]The treatment here follows [Hal84,Sec.2.15], but see also [Ren90,Sec.2.5.5].

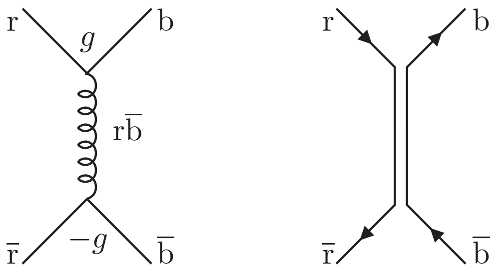

Fig. 3.1 The generic diagram for single gluon exchange between a q$\bar{\text{q}}$ pair and the corresponding colour flow. The labelling is for the exchange of an r$\bar{\text{b}}$ gluon producing a r$\bar{\text{r}}$ $\rightarrow$ b$\bar{\text{b}}$ interaction.

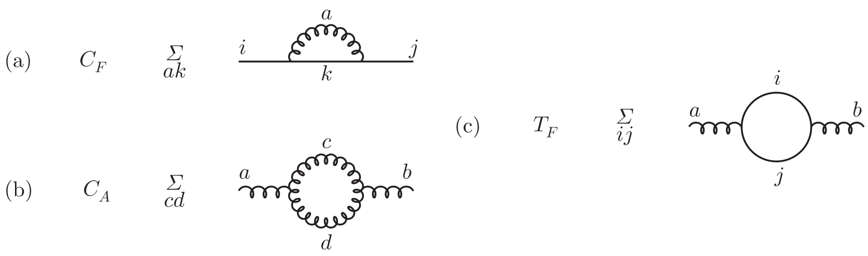

Fig. 3.2 Quark and gluon loop insertions associated with the colour factors: (a) C_F for the gluon loop on a quark line;(b) C_A for a gluon loop in a gluon line and (c) T_F for a quark loop in a gluon line.

$$\sum_a (t^a)_{ik}(t^a)_{kj} = C_F \delta_{ij}, \; C_F = \frac{N^2-1}{2N} \tag{3.6}$$

$$\mathrm{Tr}\,[T^a T^b] = \sum_{c,d} f^{acd} f^{bcd} = C_A \delta^{ab}, \; C_A = N. \tag{3.7}$$

C_F, C_A are the *Casimir operators* and, as they are group invariants, are used to label SU(3) representations (just as the eigenvalues of SU(2) I^2 are used to label isospin multiplets). C_F, C_A and T_F are the colour factors associated with the quark and gluon loop insertions as shown in Fig. 3.2. For SU(3) $C_F = \frac{4}{3}$ and $C_A = 3$. Quite often the colour factors are shown for SU(N) to make it clear what they are.

3.1.3 Some simple tree-level diagrams

Gluon bremsstrahlung and q$\bar{\text{q}}$ pair production processes will be considered. Both are important for $O(\alpha_S)$ improvements to the QPM and for large p_t jet production in DIS. The route followed here is to start with the equivalent

QED calculation and then modify the result by the appropriate colour factor. For those who want a more rigorous approach, the axial gauge is the simplest for elementary calculations and good accounts are to be found in [Lea96,Mut98,Ynd99].

The QCD Compton process $\gamma^* \mathrm{q} \to \mathrm{gq}$ is one of the most useful for understanding the essential physics of how QCD modifies the quark-parton model. The related QED process is $\gamma^* e \to \gamma e$ which is Compton scattering with one photon virtual. The tree-level diagrams are shown in Fig. 3.3 which also defines the 4-momenta of the particles involved.

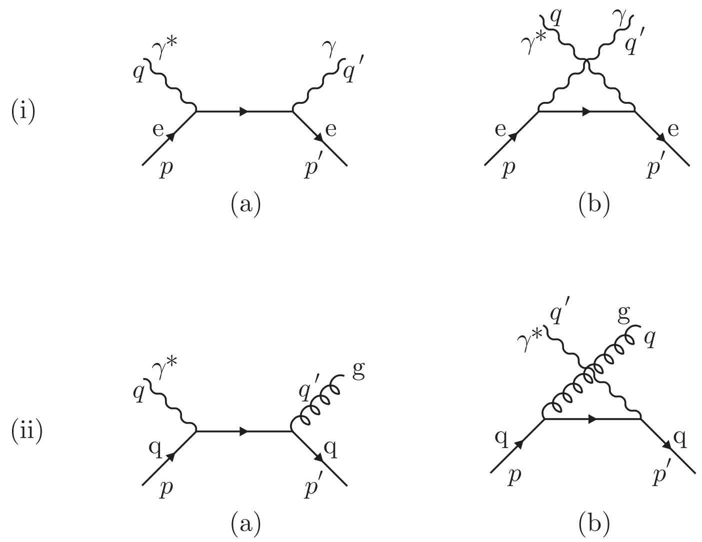

Fig. 3.3 (i) QED tree-level diagrams for $\gamma^* e \to \gamma e$, (a) s-channel, (b) u-channel; (ii) the equivalent diagrams for the QCD Compton process $\gamma^* \mathrm{q} \to \mathrm{gq}$.

The usual kinematic Lorentz invariants are:

$$\begin{aligned} s &= (q+p)^2 = (q'+p')^2 = 2q.p - Q^2 \\ t &= (q-q')^2 = (p'-p)^2 = -2p.p' \\ u &= (q-p')^2 = (q'-p)^2 = -2q'.p \end{aligned} \tag{3.8}$$

where all masses have been neglected except for the virtual photon with $q^2 = -Q^2$. Both of the diagrams shown in the figure are required for gauge invariance. Using the Feynman rules for QED, the amplitudes for the s and u channel processes are $M_a,\ M_b$ where:

$$M_a = e^2 \varepsilon'^*_\nu \varepsilon_\mu \bar{u}(p')\gamma^\nu(\not{q} + \not{p})\gamma^\mu u(p)/s \tag{3.9}$$

$$M_b = e^2 \varepsilon'^*_\nu \varepsilon_\mu \bar{u}(p')\gamma^\mu(\not{p} - \not{q}')\gamma^\nu u(p)/u,$$

where the symbols are defined in appendix A. For the unpolarised cross-section one needs $|M_a + M_b|^2$ summed over the final spin states and averaged over the initial spin states:

$$\frac{1}{4}\sum_{spins} |M_a + M_b|^2 = 2e^4 \left[-\frac{u}{s} - \frac{s}{u} + \frac{2tQ^2}{su} \right]. \tag{3.10}$$

The three terms on the RHS come from $|M_a|^2$, $|M_a|^2$ and the cross term $M_a M_b^*$ respectively. The calculations are explained in many texts (e.g. [Ait98,Bj064,Hal84]) and some details are discussed in the problems at the end of this chapter. To get from this result to the equivalent one for $\gamma^*\mathrm{q} \to \mathrm{gq}$ one needs to replace e^4 and introduce the relevant colour factor. For future reference e^2 is written in terms of α_{qed} (usually just written as α), so for a quark with charge $e_i e$

$$e^4 \to e^2 e_i^2 g^2 \to (4\pi)^2 \alpha \alpha_S e_i^2.$$

By looking at $|M_a|^2$ diagrammatically (Fig. 3.3(ii)a), it is clear that the colour factor comes from the gluon loop insertion on the quark line $C_F = \frac{4}{3}$ (as in Fig. 3.2a). The expression for the QCDC spin summed and averaged squared matrix element is

$$\overline{|M_{QCDC}|^2} = \frac{1}{4}\sum_{spins} |M_a + M_b|^2 = \frac{8}{3}(4\pi)^2 e_i^2 \alpha \alpha_S \left[-\frac{u}{s} - \frac{s}{u} + \frac{2tQ^2}{su} \right]. \tag{3.11}$$

$\overline{|M|^2}$ is related to the cross-section by[3]

$$\frac{d\sigma}{d\Omega} = \frac{1}{(8\pi)^2 s} \frac{k}{k'} \overline{|M|^2}, \tag{3.12}$$

where k, k' are the magnitudes of the initial and final state 3-momenta. QCDC involves a virtual photon in the initial state and this implies that a choice has to be made in defining the flux factor, $4k\sqrt{s}$. In this book the Hand convention is followed, which is that the initial state momentum factor is calculated as though the photon were real. Since the quarks are taken to be massless that means that $k = k' = \sqrt{s}/2$. Using this, the expression for the QCDC cross-section is

$$\frac{d\sigma}{d\Omega}|_{QCDC} = \frac{2}{3}\frac{e_i^2 \alpha \alpha_S}{s} \left[-\frac{u}{s} - \frac{s}{u} + \frac{2tQ^2}{su} \right]. \tag{3.13}$$

In the $\gamma^*\mathrm{q}$ CMS the invariant u is given by $u = -2kk'(1 - \cos\theta)$ where θ is the angle between the incoming γ^* and the outgoing scattered quark. Because the partons are taken to be massless $\frac{d\sigma}{d\Omega}|_{QCDC}$ is divergent as $\theta \to 0$. In any physical application these divergences will have to be regulated.

[3]See problem 2 at the end of the chapter.

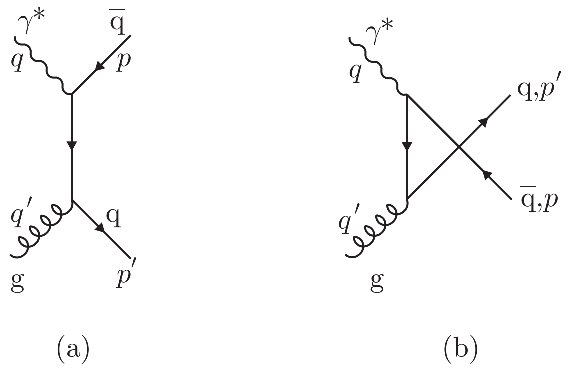

Fig. 3.4 The tree-level diagrams for the photon (or boson) gluon fusion process.

The second process that is important, particularly at low x and for heavy quark production, is the photon (or boson) gluon fusion process (BGF) for producing a q$\bar{\text{q}}$ pair. The tree-level diagrams are shown in Fig. 3.4. The corresponding QED process is the inverse of pair production ($e^+e^- \to \gamma^*\gamma$) in which one photon is virtual. The $\sum_{spins} |M(ee \to \gamma^*\gamma)|^2$ may be calculated directly or 'crossing symmetry' may be used to write down the result immediately from that for Compton scattering.[4] The latter gives

$$\sum_{spins} |M(ee \to \gamma * \gamma)|^2 = (-1) \sum_{spins} |M(\gamma^* e \to \gamma e)|^2 (s \leftrightarrow t, u \text{ unchanged})$$

Allowing for the different colour factor, in this case $\frac{1}{2}$ (T_F from the quark loop in the gluon line in the diagrams in $\overline{|M_{BGF}|^2}$), one then gets

$$\overline{|M_{BGF}|^2} = (4\pi)^2 e_i^2 \alpha \alpha_S \frac{1}{2} \left[\frac{u}{t} + \frac{t}{u} - \frac{2sQ^2}{tu} \right],$$

where the kinematic invariants are now: $s = (q+q')^2$; $t = (q-p)^2$; $u = (q-p')^2$. Using the Hand convention for the virtual photon flux, the expression for the BGF cross-section is

$$\frac{d\sigma}{d\Omega}|_{BGF} = \frac{1}{4} \frac{e_i^2 \alpha \alpha_S}{s} \left[\frac{u}{t} + \frac{t}{u} - \frac{2sQ^2}{tu} \right]. \tag{3.14}$$

In the $\gamma^* g$ CMS $t = -2kk'(1-\cos\theta)$ and $u = -2kk'(1+\cos\theta)$ where k, k' are the magnitudes of the initial and final state CM momenta and θ is the angle between the incoming γ^* and the outgoing $\bar{\text{q}}$. $\frac{d\sigma}{d\Omega}|_{BGF}$ is divergent both when $\theta \to 0$ and $\theta \to \pi$.

[4]See Appendix 13.3 for details.

3.2 Renormalisation, the running coupling

Quantum field theory is designed to allow calculation of processes in which particles are created and annihilated. For example, in QED quantum fluctuations introduce fermionic loops as higher corrections to the photon propagator – see Fig. 3.5. The loop graphs and other higher order diagrams generally are divergent because of the unrestricted integration over the momentum flowing around the loop. The way in which these divergences are regulated is known as renormalisation. Not all field theories are renormalisable, for example the Fermi theory of weak processes is not, but the gauge theories of the standard model are. A renormalisable field theory is one in which the renormalisation of a finite number of parameters ensures finite results for calculations to all orders of perturbation theory. Renormalisation also has the effect of making what appear to be constants in the Lagrangian (e.g. the coupling g and mass m) become dependent on the scale of the process under study. A full treatment of renormalisation beyond the scope of this book, however some appreciation of the consequences for QCD and how they are exploited is essential for understanding how QCD resolves the conundrum of the strong interaction. The crucial physical idea is that the quantum fluctuations of a charged particle may be thought of as polarising the vacuum which in turn then changes the effective charge of the original particle.

3.2.1 Charge renormalisation in QED

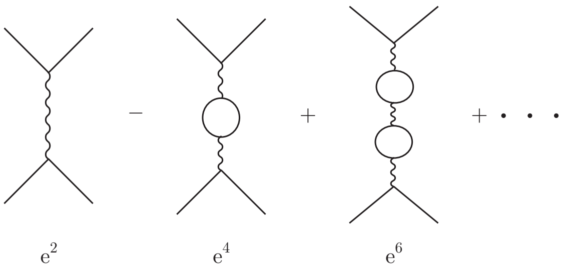

Fig. 3.5 Higher order loop corrections to the photon propagator for scattering between point like particles in QED.

Many of the ideas can be explored in QED.[5] Consider first how the infinities arising from the loop insertions in the photon propagator are regulated by renormalisation of the coupling constant (the electric charge). Fig. 3.5 shows the first few higher order loop diagrams for scattering between unlike point-like fermions at fixed CM energy (note the minus sign which arises from from each fermion loops). The amplitude depends only

[5]The heuristic approach taken here follows closely that in either [Hal84,Ch.7] or [Ait89,Chs6,9].

on the square of the 4-momentum transfer, q^2, and the modification of the photon propagator by a single fermion loop is

$$\frac{-ig_{\mu\nu}}{q^2} \to \frac{-ig_{\mu\nu}}{q^2} + \left(\frac{-ig_{\mu\alpha}}{q^2}\right)\Pi^{\alpha\beta}\left(\frac{-ig_{\beta\nu}}{q^2}\right).$$

$\Pi^{\alpha\beta}$ is the fermion loop term

$$\Pi^{\alpha\beta} = (-1)\int \frac{d^4k}{(2\pi)^4}\mathrm{Tr}\left[(ie\gamma^\alpha)\frac{i(\not{k}+m)}{k^2-m^2}(ie\gamma^\beta)\frac{i(\not{q}-\not{k}+m)}{(q-k)^2-m^2}\right],$$

where k is the internal loop momentum and m the fermion mass. $\Pi^{\alpha\beta}$ may be reduced to the form

$$\Pi_{\alpha\beta} = -ig_{\alpha\beta}q^2\Pi(q^2) + \ldots, \tag{3.15}$$

where the missing terms are proportional to $q_\alpha q_\beta$ and give zero when the propagator is coupled to external charges (since $q_\alpha\Pi^{\alpha\beta} = 0$) and

$$\Pi(q^2) = \frac{\alpha_0}{3\pi}\int_{m^2}^{\infty}\frac{dk^2}{k^2} - \frac{2\alpha_0}{\pi}\int_0^1 dz\, z(1-z)\ln(1-q^2z(1-z)/m^2),$$

where $\alpha_0 = e_0^2/4\pi$ is the bare coupling and e_0 is the charge appearing in the Lagrangian. Because the integral over the loop momentum runs to infinity the first term in the above expression diverges logarithmically. This is an example of a high mass (ultra-violet) logarithmic divergence, which has to be controlled either by a high mass cut off Λ^2 or dimensional regularisation. The details are to be found in the standard texts, e.g. [Bjo64,Jau76],[Wei95,Vol.I]. For large $Q^2 = -q^2$ the log factor in the second integrand may be approximated by $\ln(Q^2/m^2)$ and using the cut-off Λ^2 for the first integral gives

$$\Pi(Q^2) \approx \frac{\alpha_0}{3\pi}\left[\ln\left(\frac{\Lambda^2}{m^2}\right) - \ln\left(\frac{Q^2}{m^2}\right)\right].$$

The fermion mass then drops out of the leading high Q^2 term, which is

$$\Pi(Q^2) = \frac{\alpha_0}{3\pi}\ln\left(\frac{\Lambda^2}{Q^2}\right). \tag{3.16}$$

The form of the amplitude for the scattering process, including only the first loop correction, may be written

$$A_1(Q^2) = \alpha_0 A_0(Q^2)[1-\alpha_0\tilde{\Pi}(Q^2)], \tag{3.17}$$

where $\Pi = \alpha_0\tilde{\Pi}$ to display all factors of the coupling explicitly. The key idea is now to *redefine* or renormalise the coupling to include the correction from the loop in the propagator

$$\alpha = \alpha_0[1 - \alpha_0 \tilde{\Pi}(Q^2)]. \tag{3.18}$$

To first order in α, this relation may be inverted and used to define α_0 at a scale $Q^2 = \mu^2$

$$\alpha_0 = \alpha[1 + \alpha \tilde{\Pi}(\mu^2)]. \tag{3.19}$$

This relation for α_0 is now substituted back into equation 3.17 to give

$$A_1(Q^2) = \alpha A_0(Q^2)[1 - \alpha(\tilde{\Pi}(Q^2) - \tilde{\Pi}(\mu^2)) + O(\alpha^2)]. \tag{3.20}$$

It is worth checking these simple manipulations carefully, remembering that one is working to a fixed order in α (or α_0).

What has been achieved? If the cutoff $\Lambda^2 \to \infty$ then Eq. 3.18 implies that the renormalised coupling α will also tend to infinity if α_0 is finite. However as α_0 cannot be measured, but only α, the essence of renormalisation is to assume that α_0 is also infinite as $\Lambda^2 \to \infty$ but in such a way that the infinite terms cancel to give α finite. Returning to Eq. 3.20 the renormalised amplitude, $A_1(Q^2)$, depends on α and has picked up a correction factor which no longer depends on the cutoff Λ^2, though it does depend on the scale, μ^2, at which the renormalised charge is defined

$$\alpha(\tilde{\Pi}(Q^2) - \tilde{\Pi}(\mu^2)) = \frac{\alpha}{3\pi} \ln\left(\frac{\Lambda^2}{Q^2}\right) - \frac{\alpha}{3\pi} \ln\left(\frac{\Lambda^2}{\mu^2}\right) = -\frac{\alpha}{3\pi} \ln\left(\frac{Q^2}{\mu^2}\right).$$

Since the calculation of any physical process involves higher order loops, the bare coupling cannot be measured. Once α has been measured in one process at scale μ^2, it can be calculated at other scales. To see this, eliminate α_0 and Λ^2 between Eqs 3.18 and 3.19 to get

$$\alpha(Q^2) = \alpha(\mu^2)\left[1 + \frac{\alpha(\mu^2)}{3\pi} \ln\left(\frac{Q^2}{\mu^2}\right)\right]. \tag{3.21}$$

In a renormalisable theory all dependence on the cutoff Λ^2 disappears from observable quantities at all orders of perturbation theory. It also appears that the renormalisation of the coupling does not depend on the quantum numbers of the external particles (other than their charges). But this is not obvious. Consider some other higher order corrections shown in Fig. 3.6, all give rise to infinities that must be renormalised and the result may well affect the renormalised charge in a process dependent way. The diagrams shown in the figure do modify the interaction in a manner that depends on the external particles. However the renormalisation of charge is unaffected because the contributions that depend on the external particles cancel exactly between diagrams (a) and (b) plus (c). This is a beautiful result of gauge theories and is guaranteed by what are known as Ward-Takashi identities for QED and extended to non-abelian gauge theories by Slavnov and Taylor. A simple example of gauge invariance and Ward identities in QED is discussed in problem 3 at the end of the chapter.

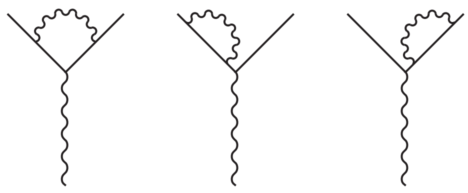

(a) (b) (c)

Fig. 3.6 Other order e^4 corrections to the coupling of the photon to a fermion.

So far only the correction to the photon propagator from the first loop insertion has been considered. What happens if $\alpha_0\Pi$ is not small? For the photon propagator, because of the structure of $\Pi_{\alpha\beta}$ shown in Eq. 3.15, the higher order terms form a geometric series that can be summed. Returning to Eq. 3.17 and Fig. 3.5, the amplitude including all loop insertions may be written schematically as

$$\begin{aligned} A(Q^2) &= \alpha_0 A_0(Q^2)[1-\alpha_0\tilde{\Pi}(Q^2)+\alpha_0^2\tilde{\Pi}^2(Q^2)+\ldots] \\ &= \frac{\alpha_0 A_0(Q^2)}{1+\alpha_0\tilde{\Pi}(Q^2)}. \end{aligned}$$

From the second equation the renormalised charge, summed over leading logs is

$$\alpha(Q^2) = \frac{\alpha_0}{1+\alpha_0\tilde{\Pi}(Q^2)}. \qquad (3.22)$$

As before the dependence on α_0 and Λ^2 is removed by defining α at a scale μ^2

$$\frac{1}{\alpha(Q^2)} - \frac{1}{\alpha(\mu^2)} = \tilde{\Pi}(Q^2) - \tilde{\Pi}(\mu^2) = -\frac{1}{3\pi}\ln\left(\frac{Q^2}{\mu^2}\right)$$

or

$$\alpha(Q^2) = \frac{\alpha(\mu^2)}{1-\frac{\alpha(\mu^2)}{3\pi}\ln\left(\frac{Q^2}{\mu^2}\right)}. \qquad (3.23)$$

Equation 3.21 is just the first term in the expansion of 3.23, valid when $\alpha(\mu^2)\ln(Q^2/\mu^2)$ is small. Both equations demonstrate that the coupling in QED 'runs' with the scale Q^2 of the process. Measured at the scale of the electron mass $\alpha_{qed} = 1/137$ and it increases to a value of $1/125$ at the scale of M_Z.[6]

3.2.2 The QCD running coupling at leading order

Since the space-time structures of QED and QCD are similar, much of what has just been discussed may be taken over essentially unchanged for QCD.

[6] See problem 5 for more details.

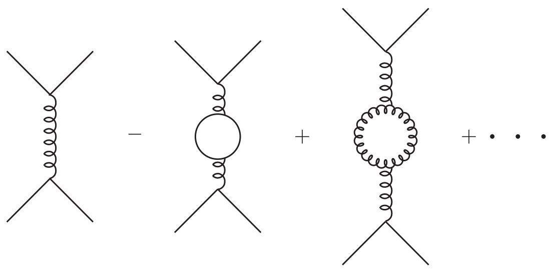

Fig. 3.7 Loop corrections to the gluon propagator.

The QCD analog of the (bare) fine structure constant $(\alpha_S)_0 = g^2/4\pi$ may be defined in terms of the bare coupling constant g appearing in L_{QCD}. The loop insertion Π_{QCD} has a logarithmic divergence but the sign and magnitude of the coefficient (given in Eq. 3.16 for QED) multiplying $\ln(Q^2/\Lambda^2)$ are different in QCD. The differences come from the self coupling of the gluon, which gives rise to a gluon loop insertion in the gluon propagator as well as the fermion loop insertion as shown in Fig. 3.7. In both theories this coefficient may be written as αb_0, where for QED $b_0 = -1/3\pi$ and for QCD with n_f active flavours $b_0 = (33 - 2n_f)/12\pi$.[7] Note that there are two contributions to b_0 for QCD, the fermion loops contribute $-1/6\pi$ for each flavour[8] and the gluon self-coupling loops give a positive contribution of $11/4\pi$.

Using b_0 the generic leading order equation for the running coupling (Eq. 3.23) becomes

$$\alpha(Q^2) = \frac{\alpha(\mu^2)}{1 + \alpha(\mu^2) b_0 \ln\left(\frac{Q^2}{\mu^2}\right)}. \tag{3.24}$$

For QCD one defines the strong running coupling $\alpha_S(Q^2)$, satisfying Eq. 3.24, as $g^2(Q^2)/4\pi$ where $g(Q^2)$ is the renormalised coupling constant at scale Q^2. Because b_0 for QCD is positive $\alpha_S(Q^2)$ decreases as Q^2 increases, formally $\alpha_S(Q^2) \to 0$ as $Q^2 \to \infty$. This remarkable result, known as *asymptotic freedom* is at the core of how QCD can reconcile confined quarks in hadrons on the scale of femtometres (small Q^2) and almost free quarks in DIS (large Q^2). The non-abelian nature of the colour force is responsible for the very different small distance behaviour of QED and QCD. Another major difference between QED and QCD is how to set the reference scale for defining α_S. In QED one can measure α_{qed} in a long range

[7] Here we follow the conventions of [Ell96,Ch.2]. Many authors use $\alpha\beta_0/4\pi$ where $\beta_0 = 4\pi b_0$.

[8] This is the same as in QED when the factor 2 difference between QED and QCD mention in Sec. 3.1.2 is allowed for.

(small Q^2) physical process. In QCD there is no such equivalent because of confinement. By defining a new scale parameter Λ_{QCD},

$$\ln \Lambda^2_{QCD} = \ln \mu^2 - \frac{1}{b_0 \alpha_S(\mu^2)}$$

Eq. 3.24 may be rewritten to show that α_S depends only on Λ_{QCD}

$$\alpha_S(Q^2) = \left[b_0 \ln\left(\frac{Q^2}{\Lambda^2_{QCD}}\right)\right]^{-1} . \tag{3.25}$$

Either $\alpha_S(\mu^2)$ or Λ_{QCD} has to be determined from experimental data. Note that $\alpha_S(Q^2)$ and hence Λ_{QCD} depend on the number of active flavours through the occurrence of n_f in b_0. How to ensure that α_S behaves correctly at a threshold will be considered later. The value of Λ_{QCD} is expected to be of the order of a few 100 MeV, corresponding to the femtometre scale of hadrons. At, or indeed somewhat above, this scale $\alpha_S(Q^2)$ becomes large and perturbative methods are no longer applicable. The strong coupling or long range limit of QCD is the domain of lattice QCD, in which the equations of QCD are discretised on a four dimensional lattice and solved numerically. An introduction to the ideas of lattice QCD is given in [Ynd99,Ch.9].

Physical picture of the running couplings.

3.2.3 Renormalisation group and beyond the leading order

The consequences of the renormalisation of the coupling, mass and wave functions beyond leading order may be evaluated by the study of individual Feynman diagrams, but there is a more abstract and general method, the renormalisation group, that will be outlined in this section. That one needs to go beyond LO is clear from the following simple example. At LO the scale Λ_{QCD} in the QCD running coupling cannot be defined uniquely. Making the replacement $\Lambda_{QCD} \to \Lambda'_{QCD} = \Lambda_{QCD}/\kappa$ in Eq. 3.25 one finds

$$\alpha'_S = \frac{1}{b_0 \ln\left(\frac{Q^2\kappa^2}{\Lambda^2_{QCD}}\right)} = \alpha_S \left[1 + \alpha_S b_0 \ln \kappa^2\right]^{-1}$$

and expanding in powers of α_S

$$\alpha'_S = \alpha_S - \left(b_0 \ln \kappa^2\right) \alpha_S^2 + O(\alpha_S^3)$$

which shows that the change in α_S is absorbed in the $O(\alpha_S^2)$ term. To estimate the scale dependence of a calculation one needs the NLO term.

The renormalisation group method exploits the requirement that in a complete (perturbative) calculation of a physical quantity, Γ, that quantity cannot depend on the particular choice of the scale μ^2 at which the renormalised constants are defined. Γ is invariant with respect to the 'group' of all possible scales. The approach was developed by Stückelberg, Peterman, Gell-Mann and Low in the 1950s for studying the high energy behaviour of perturbation theory and later by Callan and Symanzik in 1970. Here we follow the description by [Wei95,Ch.18] where full references may be found. Consider the physical quantity $\Gamma(s, \alpha_0, m^2)$ where s is the CM energy squared, Q^2 or some similar quantity, α_0 is the bare coupling, m a typical mass and other variables such as angles or ratios of energies have been suppressed. At high energies or scales $s \gg m^2$, Γ might be expected to scale with s according to its mass (or energy) dimension D, for example a cross-section has $D = -2$ and a decay rate $D = -1$

$$\Gamma(s, \alpha_0, m^2) \to s^{D/2}\Gamma(1, \alpha_0, m^2/s).$$

This does not happen because of the large logs, powers of $\ln(s/m^2)$, that occur in perturbative calculations and the scaling factor $s^{D/2}$ gets modified. The logs may be large because s/m^2 is large and $m^2 \neq 0$ or because the mass m has been introduced to avoid the divergence as $m \to 0$ that occur in theories with massless particles such as the photon and gluon. These latter large logs are infrared divergences and will be considered later. Consider first a quantity such as a total cross-section that does not exhibit infrared divergences. Calculate Γ in terms of the running coupling $\alpha(\mu^2)$ defined at a scale $\mu^2 \gg m^2$ so that it does not depend on m. A dependence on μ^2 will be introduced in Γ (see the discussion following Eq. 3.20) and it will scale as

$$\Gamma(s, \alpha(\mu^2), m^2, \mu^2) = s^{D/2}\Gamma(1, \alpha(s), m^2/s, \mu^2/s).$$

Since μ^2 is arbitrary it may be taken to be s, and for $s \gg m^2$

$$\Gamma(s, \alpha(\mu^2), m^2, \mu^2) \to s^{D/2}\Gamma(1, \alpha(s), 0, 1). \tag{3.26}$$

the large logs have been absorbed in $\alpha(s)$ and perturbation theory may be used to calculate Γ. In practice to use perturbation theory, the coupling α must be small enough for higher order corrections to be ignored and this can be achieved by 'sliding' the scale of α in successive steps. Assume that the relationship between α at different scales μ_1^2 and μ_2^2 may be written as[9]

$$\alpha(\mu_2^2) = G(\alpha(\mu_1^2), \mu_2^2/\mu_1^2).$$

To get an equation for continuous changes in scale, differentiate with respect to μ_2^2 and set $\mu_2^2 = \mu_1^2$

$$\mu^2 \frac{d}{d\mu^2}\alpha(\mu^2) = \frac{d}{d\ln\mu^2}\alpha(\mu^2) = \beta(\alpha(\mu^2)), \tag{3.27}$$

where

[9]Any dependence on masses has been ignored since it is assumed that $\mu_i^2 \gg m^2$.

$$\beta(\alpha(\mu^2)) \equiv \left[\frac{\partial}{\partial z} G(\alpha(\mu^2), z)\right]_{z=1} .$$

This is the Callan-Symanzik equation for the running coupling. It may be integrated formally to give an implicit equation for $\alpha(\mu^2)$ in terms of α at a reference scale μ_0^2

$$\ln\left(\frac{\mu^2}{\mu_0^2}\right) = \int_{\alpha(\mu_0^2)}^{\alpha(\mu^2)} \frac{d\alpha}{\beta(\alpha)} \tag{3.28}$$

provided $\beta(\alpha)$ does not vanish in the range of integration. The function β depends only on the coupling and may be calculated perturbatively. In QCD it has been calculated as an expansion in α_S to the third significant term (full references are given in [Ell96,Ch.2])

$$\beta(\alpha_S) = -b_0\alpha_S^2 - b_1\alpha_S^3 - b_2\alpha_S^4 + O(\alpha_S^5) \tag{3.29}$$

and with n_f the number of active flavours,

$$\begin{aligned} b_0 &= \frac{33 - 2n_f}{12\pi}, \\ b_1 &= \frac{153 - 19n_f}{24\pi^2}, \\ b_2 &= \frac{77139 - 15099n_f + 325n_f^2}{3456\pi^3}. \end{aligned} \tag{3.30}$$

If Eq. 3.28 is integrated keeping only the first term in the expansion of $\beta(\alpha_S)$ the result is

$$\frac{1}{\alpha_S(\mu^2)} - \frac{1}{\alpha_S(\mu_0^2)} = b_0 \ln(\mu^2/\mu_0^2)$$

or

$$\alpha_S(\mu^2) = \frac{\alpha_S(\mu_0^2)}{1 + \alpha_S(\mu_0^2) b_0 \ln(\mu^2/\mu_0^2)},$$

which is the leading order result obtained in Eq. 3.24. Keeping the first two terms in the expansion 3.29 the result, now to NLO, may be written

$$\begin{aligned} &\frac{1}{\alpha_S(\mu^2)} - b_0 \ln\mu^2 - \frac{b_1}{b_0}\ln\left(\frac{1}{\alpha_S(\mu^2)} + \frac{b_1}{b_0}\right) = \\ &\frac{1}{\alpha_S(\mu_0^2)} - b_0 \ln\mu_0^2 - \frac{b_1}{b_0}\ln\left(\frac{1}{\alpha_S(\mu_0^2)} + \frac{b_1}{b_0}\right) \end{aligned} \tag{3.31}$$

This an implicit equation for $\alpha_S(\mu^2)$ in terms of $\alpha_S(\mu_0^2)$ and $\ln(\mu^2/\mu_0^2)$ which can be solved numerically. To get the NLO equivalent of Λ_{QCD} replace the 2nd (constant) line of Eq. 3.31 by $-\beta_0 \ln\Lambda^2 - b_1(\ln b_0)/b_0$ and replace μ^2 by Q^2 to give

$$\ln\left(\frac{Q^2}{\Lambda^2}\right) = \frac{1}{b_0\alpha_S(Q^2)} - \frac{b_1}{b_0^2}\ln\left(\frac{1}{b_0\alpha_S(Q^2)} + \frac{b_1}{b_0^2}\right), \tag{3.32}$$

where Λ is Λ_{QCD}(NLO). Note that there are still ambiguities in the definition of Λ which can be absorbed in the higher order terms in α_S. For $\alpha_S(Q^2)$ small Eq. 3.32 can be inverted approximately to give

$$\alpha_S(Q^2) = \frac{1}{b_0\ln(Q^2/\Lambda^2)}\left[1 - \frac{b_1}{b_0^2}\frac{\ln[\ln(Q^2/\Lambda^2)]}{\ln(Q^2/\Lambda^2)} + \ldots\right]. \tag{3.33}$$

Because of the ambiguities in the definition of Λ at both LO and NLO, it has become conventional to quote determinations of the strong coupling in terms of α_S directly at some convenient scale, instead of Λ_{QCD}. Often the scale is chosen to be M_Z^2.

The importance of the running coupling and the renormalisation group method is that they provide a systematic way to sum potentially large logs. Consider for simplicity a case in which Γ is dimensionless, e.g. the quantity $R_{e^+e^-}$. In this case Eq. 3.26 becomes

$$\Gamma(s, \alpha(\mu^2), m^2, \mu^2) = \Gamma(1, \alpha(s), 0, 1), \tag{3.34}$$

which is the solution of the renormalisation group equation for Γ

$$\mu^2\frac{d}{d\mu^2}\Gamma(s, \alpha(\mu^2), m^2, \mu^2) \equiv \left[\mu^2\frac{\partial}{\partial\mu^2} + \beta(\alpha)\frac{\partial}{\partial\alpha}\right]\Gamma = 0,$$

where Eq. 3.27 has been used. What these equations say is that the physical quantity Γ must be independent of the arbitrary choice of scale μ^2 and that the effect of a scale change is compensated for by the change in the running coupling $\alpha(s)$. This means that in the calculation Γ as a perturbation expansion in $\alpha(s)$ certain series of $\ln(s/\mu^2)$ terms get summed. Expand the RHS of Eq. 3.34 in powers of $\alpha(s)$, substituting $\alpha(s) = \alpha_\mu/(1+\alpha_\mu b_0 t)$, where $t = \ln(s/\mu^2)$ and $\alpha_\mu = \alpha(\mu^2)$, to give

$$\begin{aligned}
\Gamma(1, \alpha(s), 0, 1) &= \Gamma_0 + \Gamma_1\alpha_\mu[1 + \alpha_\mu b_0 t]^{-1} + \ldots \\
&= \Gamma_0 + \Gamma_1\alpha_\mu\sum_{n=0}^{\infty}(-\alpha_\mu b_0 t)^n \\
&= \Gamma_0 + \Gamma_1\alpha_\mu[1 - \alpha_\mu b_0 t + \alpha_\mu^2 b_0^2 t^2 + \ldots].
\end{aligned} \tag{3.35}$$

Thus in the renormalisation group result on the first line the logs in the Γ_1 term, known as the 'leading logs', are summed 'automatically'. The last line shows the expansion in terms of α_μ in the form that would be given by perturbation theory without the renormalisation group improvement. If the next term is included, $\Gamma_2\alpha(s)^2$, and expanded in terms of α_μ and t, one gets

$$\Gamma_2\alpha_s^2 \to \Gamma_2\alpha_\mu^2[1 - 2\alpha_\mu b_0 t + \ldots]$$

so at each power of α_μ, the log term is down by one power. These are the next-to-leading logs.

To use renormalisation group methods on more general physical quantities than a dimensionless fully inclusive object like $R_{e^+e^-}$, the behaviour induced by the renormalisation of the fields in the Lagrangian must be included. In detail this is beyond the scope of this book, but since an important concept – the anomalous dimension – depends on it, a brief outline is given here. For simplicity only one type of field, ϕ, with renormalisation factor Z will be considered, then for a quantity depending on n external ϕ fields

$$\Gamma(s, \alpha_\mu, \mu^2) = \left[Z(\alpha_0, \Lambda^2/\mu^2)\right]^n \Gamma_0(s, \alpha_0, \Lambda^2),$$

where the subscript 0 indicates unrenormalised (bare) quantities. The equation shows that there is no dependence on the cutoff Λ in the renormalised function, but it does depend on the scale, μ^2, at which the renormalisation is performed. Since Γ_0 does not depend on μ^2, Γ must satisfy the renormalisation group equation

$$\left[\mu^2 \frac{\partial}{\partial \mu^2} + \beta(\alpha_\mu) \frac{\partial}{\partial \alpha_\mu} + n\gamma(\alpha_\mu)\right] \Gamma(s, \alpha_\mu, \mu^2) = 0, \tag{3.36}$$

where γ is the anomalous dimension function

$$\gamma(\alpha_\mu) = -\mu^2 \frac{\partial}{\partial \mu^2} \left(\ln Z(\alpha_0, \Lambda^2/\mu^2)\right) \tag{3.37}$$

and Eq. 3.27 has been used. Note that γ is not a universal function and depends on the fields involved in a given process. In QCD there will be γ functions for quark and gluon fields.

On dimensional grounds Γ will be a homogeneous function of s and μ^2 (masses are either zero or $s \gg m^2$) and it may be written as $\Gamma(s, \alpha_\mu, \mu^2) = (\mu^2)^{D/2} F(s/\mu^2, \alpha_\mu)$, where D is its mass dimension. Using this, Eq. 3.36 may be solved[10] to show how a change in energy scale $s_0 \to s$ is compensated for by the running coupling and the anomalous dimension

$$\Gamma(s, \alpha, \mu^2) = \Gamma(s_0, \alpha(\mu^2), \mu^2) \exp\left[Dt/2 + n \int_0^t \gamma(t')dt'\right], \tag{3.38}$$

where $t = \ln(s/s_0)$. The name anomalous dimension is now clear, without the complication of the renormalisation factor Z, γ would be zero and the above equation would reduce to a simple scaling by $(s/s_0)^{D/2}$. The $\gamma(\alpha)$ functions can be calculated perturbatively, but not $\Gamma(s_0, \alpha(\mu^2), \mu^2)$.

3.2.4 Infrared safety

Consider the scattering of an electron with a 'heavy muon' so that only radiation from the electron need be considered. The Born diagram which is $O(e^2)$ in the electric charge is shown in Fig. 3.8a. The radiation of real photons from the initial and final state electrons is shown in diagrams (c). The

[10]The details are given for example in [Mut98,Ch.3] or [Ren90,Sec.7.6].

dk/k energy spectrum of the radiated photons has a logarithmic divergence as $k \to 0$. The angular distribution of the photons is also strongly peaked towards $\theta_{e\gamma} \to 0$. These divergences can be regulated by introducing a fictitious photon mass λ^2. On the other hand it is known that the physical process itself is finite. A real detector for the final state electromagnetic particles (e, γ) will have finite resolution in energy and angle and a minimum threshold energy E_0. Thus it will not be able to register a photon with $k < E_0$ or distinguish between an event in which the final state contains a single electron of energy E and one in which E is shared between an electron and a photon emitted at an angle $\theta_{e\gamma}$ less that the angular resolution of the detector. To remove these infrared divergences one must calculate quantities that reflect a real detector. Rather than attempting to calculate

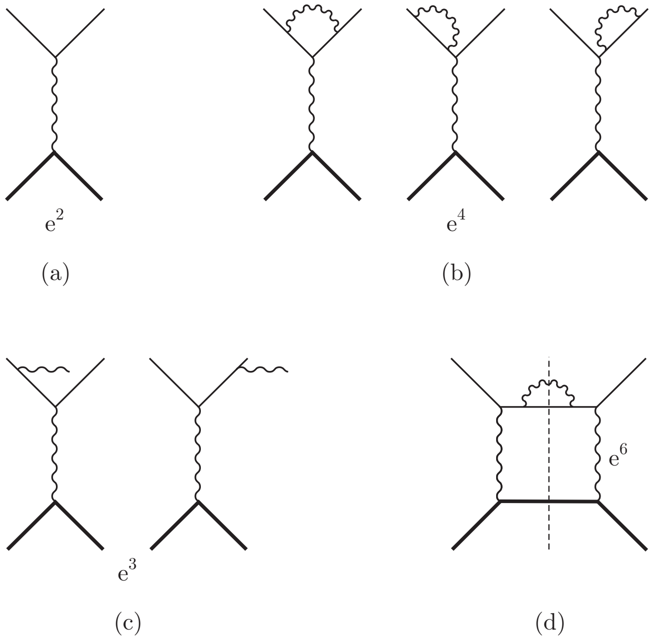

Fig. 3.8 Diagrams for eμ scattering: (a) $O(e^2)$ Born diagram; (b) $O(e^4)$ vertex and external line corrections; (c) $O(e^3)$ initial and final state radiation terms; (d) $O(e^6)$ cut diagram.

a final state with an electron and a specific number of radiated photons, one calculates the cross-section for scattering into a final state with a single electron plus any number of photons with summed energy less than E_{min} or $\theta_{e\gamma} < \theta_{min}$. The result is finite but depends on E_{min} and θ_{min} and it would also appear still to depend on the photon mass λ^2. Consider now the terms shown in Fig. 3.8b, these are $O(e^4)$ but the interference of these terms with the born diagram (a) gives terms of $O(e^6)$ in the cross-section – which is just the same order as the squared bremsstrahlung diagrams (c). The loops in diagrams (b) also give rise to logarithmic infrared divergences which can be regulated by the photon mass λ^2 and unitarity demands that the cutoffs be the same. In turns out that the $\ln \lambda^2$ terms from the interference of (a) and (b) has exactly the same magnitude but opposite sign to those from $|(\mathrm{c})|^2$. One is then left with terms like $\ln(E/E_{min})$ or $\ln(E/m_e)$. In fact one may use unitarity to verify the cancellation. Unitarity gives

$$2\mathrm{Im}A_{ab} = \sum_c (2\pi)^4 \delta^4(p_a - p_c) A_{ac} A^\dagger_{cb}$$

for the imaginary part of the scattering amplitude for initial state a to final state b, $\sum_c$ is a shorthand for the sum over a complete set of real intermediate states c. The $\delta^4()$ guarantees momentum conservation. In a perturbative calculation the equation must be respected order by order. Fig. 3.8d shows the 'cut diagram' for the imaginary part of an $O(e^6)$ box. The particles in the intermediate state cut by the dashed vertical line are taken on the mass shell.[11] Diagram (d) is $AA^\dagger$ from the RH of the $O(e^3)$ radiation diagrams (c). By attaching the photon loop in all possible ways to the electron lines in (d) and cutting the intermediate states in all possible ways one accounts for all the terms at this order in the unitarity sum: $(\mathrm{a})(\mathrm{b})^\dagger$ interference and $|(\mathrm{c})|^2$ terms. The divergent terms in the individual diagrams cancel in the unitarity sum which builds the complete $O(e^6)$ amplitude. Unitarity provides a very useful tool to ensure that the 'book keeping' is done correctly.

Often in QCD one will be calculating with massless quarks as well as massless gluons, thus infrared divergences arising from $\ln(E/m)$ terms as $m \to 0$ will remain even after the cancellation of the infrared gluon divergences. This is a tricky problem but once again it can be shown that if one is guided by what could be measured, infrared finite or 'safe' quantities can be defined and calculated perturbatively. As Weinberg summarises it: 'The transition rate is free of infrared divergences if summed over the subspace of states that would be "dangerous" for given final and initial state configurations'.[12] The art is to identify the dangerous sub-set. Generally the more inclusive a quantity the more likely it is to be infrared safe. Infrared safety is generally guaranteed in both QED and QCD for those quantities, like total cross-sections and structure functions, that can be related to the imaginary parts of amplitudes. It is both more difficult and requires more care for less exclusive quantities like jet rates.

[11] A bit more detail on this point is given in Appendix X on Feynman rules.

[12] See the general discussion of infrared problems in [Wei95,Ch.13], where full references are given.

3.2.5 Renormalisation schemes

In Sec. 3.2.1 the basic idea of renormalisation was sketched with reference to the coupling constant in QED. The important physical outcome was the running coupling. What was not stressed was that in any calculation to a finite order in perturbation theory, the result will depend on the choice of renormalisation scheme. While the actual singularities are well defined, the finite parts 'left over' after the removal of the divergence may differ. The divergences arise from integrals over loops in Feynman diagrams like

$$\int \frac{d^4k}{k^2 - m^2 + i\varepsilon}.$$

This integral diverges quadratically. An early method of regularisation was that of Pauli and Villars in which the denominator is replaced by

$$\frac{1}{k^2 - m^2} \to \frac{1}{k^2 - m^2} - \frac{1}{k^2 - \Lambda^2}$$

where Λ is a large fixed mass – much larger than the mass or energy scales of interest in the problem at hand. The resulting integral is convergent, but depends explicitly on Λ. This method is similar to the simple cutoff used in Sec. 3.2.1. Another method, which matches well the physical result of a running coupling is the momentum subtraction method (MPS or MOM). Here the coupling, for example, is defined by a vertex function at a point where all the external momenta are space-like with $p^2 = -\mu^2$. One advantage of this scheme is that a large class of higher order corrections are absorbed into the renormalised coupling $g(-\mu^2)$, thus improving the convergence of the perturbation series. However the big disadvantage of this scheme is that it does not respect gauge invariance. Since gauge invariance is vital for many of the more tricky higher order calculations, it would be better if the renormalisation scheme allowed this to be manifest. To this end 't Hooft and Veltman [tHo72] introduced the idea of dimensional regularisation.[13] What they proposed was to evaluate the integral in an n-dimensional space ($n \neq 4$) in which it converges

$$\int \frac{d^nk}{k^2 - m^2 + i\varepsilon} \to \mathrm{i}\pi^{\frac{n}{2}}\Gamma(1 - \frac{n}{2})(-m^2)^{\frac{n}{2}-1}.$$

Now

$$\Gamma(1 - \frac{n}{2}) = -\frac{2}{4-n} - 1 + \gamma_E + O(4-n),$$

where γ_E is the Euler constant and the divergence occurs as the pole at $n = 4$. The minimal subtraction scheme (MS) of 't Hooft and Veltman involves the introduction of counter terms to cancel only the singular terms at $n = 4$. However a number of authors have argued that it is more convenient

[13] For a pedagogic introduction see [Vel94].

to remove the terms involving γ_E, which always appear in dimensional regularisation, as well as the singular terms. This scheme is known as the modified minimal subtraction scheme ($\overline{\mathrm{MS}}$). This latter is the one that is now preferred for most perturbative QCD calculations.

3.3 The hadronic tensor $W_{\mu\nu}$

So far in this book the DIS cross-sections and structure functions have been introduced and built up using the framework of the quark-parton model. This gives a good physical intuition, but to apply some of the more powerful mathematical techniques a more general approach is needed. In configuration space the structure of the deep inelastic scattering matrix element for $e(k) + p(p) \to e(k') + X$ is

$$S_{fi} = i \int d^4x\, d^4y\, J_\mu^e(x) D^{\mu\nu}(x-y) J_\nu^h(y),$$

where $J_\mu^e(x)$ is the leptonic EM current acting at x, $D^{\mu\nu}(x-y)$ is the photon propagator and $J_\nu^h(y)$ is the hadronic current acting at point y. Inserting expressions for the space-time structure of the currents and propagator and performing the spatial integrations gives

$$S_{fi} = i(2\pi)^4 \delta^4(p + k - p_X - k')\bar{u}(k')\gamma_\mu u(k) \frac{e^2}{q^2} \langle X | j^\mu(0) | p \rangle,$$

where j^μ is the hadronic EM current operator and normalisation factors have been ignored. Taking the modulus squared of S_{fi}, summed and averaged over spins, gives the familiar expression for the cross-section in terms of a contraction between the leptonic and hadronic tensors. In the lab frame this takes the form

$$\frac{d^2\sigma}{d\Omega dE'} = \frac{\alpha^2}{q^4} \frac{E'}{mE} L_{\mu\nu} W^{\mu\nu},$$

where $q = k - k'$ (more details on cross-section formulae are given in Appendix 13.4). For photon exchange the leptonic tensor is given by QED, ignoring masses

$$L_{\mu\nu} = \frac{1}{2} \mathrm{Tr}[\not{k}' \gamma_\mu \not{k} \gamma_\nu] = 2(k_\mu k'_\nu + k_\nu k'_\mu - k \cdot k' g_{\mu\nu}) \tag{3.39}$$

and the hadronic tensor is written in terms of the hadronic current

$$W_{\mu\nu} = \frac{1}{4\pi} \sum_X (2\pi)^4 \delta^4(q + p - p_X) \langle p | j_\mu^\dagger(0) | X \rangle \langle X | j_\nu(0) | p \rangle, \tag{3.40}$$

where the spin labels have been suppressed and the '$\sum_X |X\rangle\langle X|$' is a shorthand for the full sum and integral over the intermediate state phase space (see Eq. 13.5). For inclusive leptoproduction this expression may be reduced

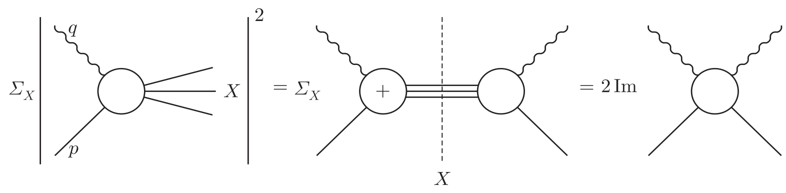

Fig. 3.9 The reduction of the DIS hadronic tensor $W_{\mu\nu}$ to the imaginary part of the forward γ^*p amplitude.

to the form of the imaginary part of the virtual photon proton forward scattering amplitude

$$W_{\mu\nu}(p,q) = \frac{1}{4\pi}\int d^4z\, e^{iq.z}\,\langle p|[j^\dagger_\mu(z), j_\nu(0)]|p\rangle. \tag{3.41}$$

The manipulation, which is essentially an application of unitarity, is shown diagrammatically in Fig. 3.9 and followed algebraically in problem xx at the end of the chapter. The full forward virtual Compton scattering amplitude has a similar form to Eq. 3.41, but is related to the time-ordered product of the currents

$$T_{\mu\nu}(p,q) = i\int d^4z e^{iq.z}\langle p|T(j^\dagger_\mu(z) j_\nu(0))|p\rangle. \tag{3.42}$$

T and W are related by

$$W_{\mu\nu} = \frac{1}{2\pi}\mathrm{Im}\, T_{\mu\nu},$$

and both have the same Lorentz decomposition in terms of momentum tensors. The study of the mathematical structure of models for DIS thus becomes that of virtual Compton scattering.

The manipulations summarised in Fig. 3.9 are also those leading to the optical theorem for the total $\gamma^* p$ total cross-section, which takes the form

$$\sigma^{tot}_{\gamma^* p}(\lambda) = \frac{8\pi^2\alpha}{W^2 - m^2}\varepsilon^\dagger_\mu(\lambda) W^{\mu\nu}\varepsilon_\nu(\lambda),$$

where $\varepsilon_\mu(\lambda)$ is the polarisation 4-vector for the γ^* polarisation states $\lambda = \pm 1, 0$ (more details are give in Appendix 13.4).

3.3.1 Light cone dominance and the covariant parton model

To make contact with the earlier less formal description of the parton model and its QCD improved form, it is useful to look at DIS kinematics and the Compton amplitude in terms of both light cone variables and the Sudakov decomposition. Consider DIS in the rest frame of the target proton, with the z-axis along $\mathbf{q}$, then

$$p = (m, 0, 0, 0), \qquad q = (\nu/m, 0, 0, \sqrt{(\nu/m)^2 + Q^2}),$$

where $\nu \equiv mq_0 = m(E - E')$ and $x = Q^2/(2\nu)$. The *light-cone* variables are defined by

$$a^{\pm} = (a_0 \pm a_3)/\sqrt{2} \quad \text{and} \quad a \cdot b = a^+ b^- + a^- b^+ - \mathbf{a_T} \cdot \mathbf{b_T}.$$

Then in the Bjorken limit ($Q^2 \to \infty$, x fixed), $q_3 \to \nu/m + mx$, so

$$q^+ = (2\nu/m + mx)/\sqrt{2} \to \sqrt{2}\nu/m, \quad q^- = -mx/\sqrt{2},$$

and

$$q \cdot z = q^+ z^- + q^- z^+ \to \sqrt{2}\nu z^-/m - mxz^+/\sqrt{2}.$$

Turning to the expression for $W_{\mu\nu}$ given in Eq. 3.41, the integral will be dominated by contributions for which $q \cdot z \sim 1$. This gives $z_0 - z_3 \sim m/(\sqrt{2}\nu)$, $z_0 + z_3 \sim \sqrt{2}/(mx)$ or $z_0^2 - z_3^2 \sim O(1/Q^2)$. Thus in the Bjorken limit contributions with $z^2 \to 0$ dominate, which means that the current commutator on the light cone is required. Note that causality requires that the commutator vanish for $z^2 < 0$ and that the time scale for DIS is $O(1/\sqrt{Q^2})$, which also vanishes for large Q^2. The amplitude is then dominated by a very short timescale, in which the virtual photon interacts with the target nucleon partons almost 'frozen' in position. The second approach that is useful for formulating the QPM assumptions more precisely is the use of Sudakov variables, in which the decoupling of longitudinal and transverse degrees of freedom is easy to exploit. Two lightlike variables, p and n, are introduced satisfying $n \cdot p = 1$. Any 4-vector k can now be written as

$$k^\mu = ap^\mu + bn^\mu + k_T^\mu, \tag{3.43}$$

where

$$p^2 = 0, \;\; n^2 = 0, \;\; n \cdot k_T = 0, \;\; p \cdot k_T = 0, \quad \text{and} \quad k^2 = 2ab - \mathbf{k_T^2}.$$

Note that k_T^μ is a spacelike vector with $k_T^2 = -\mathbf{k_T^2}$. Ignoring masses, an explicit representation which is close to the infinite momentum frame of the parton model is

$$p^\mu = (p, 0, 0, p), \quad n^\mu = (1/(2p), 0, 0, -1/(2p)),$$

in which $q^\mu = \nu n^\mu + q_T^\mu$ and $q^2 = -\mathbf{q_T^2} = -Q^2$.

Returning to the virtual Compton scattering amplitude, the type of diagram (the 'handbag' diagram) that is relevant for the QPM is shown in Fig. 3.10a in which a parton scatters from the virtual photon and the blob at the bottom represents the non-perturbative part that gives rise to the

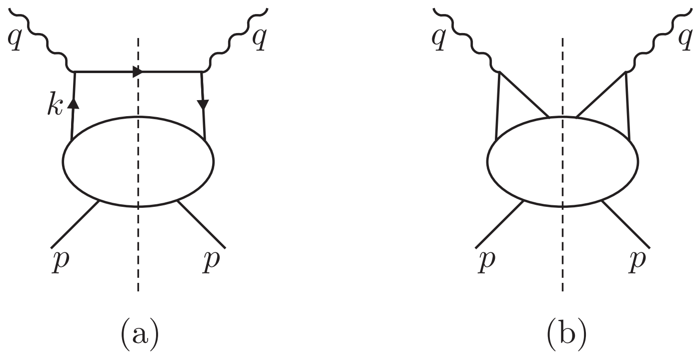

Fig. 3.10 Virtual Compton scattering diagrams for the covariant parton model approach: a) the leading QPM diagram, b) a suppressed higher order contribution (higher 'twist').

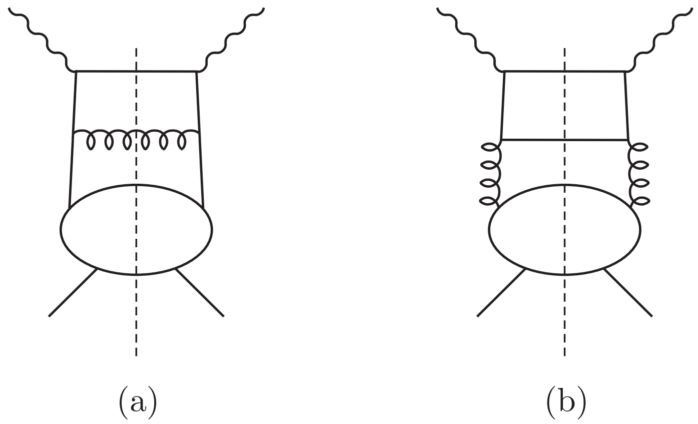

Fig. 3.11 Virtual Compton scattering diagrams for the leading order terms in the QCD enhanced parton model.

parton distribution functions. This approach was pioneered in the covariant parton model of Landshoff and Polkinghorne [Lan72]. The vertical dashed line indicates that the particles are taken on the mass shell. The expression for $W_{\mu\nu}$ then takes the form for massless quarks

$$W_{\mu\nu}(q,p) = \sum_i \int d^4k\, f^i(p,k) w^i_{\mu\nu} \delta((k+q)^2), \tag{3.44}$$

where $w^i_{\mu\nu}$ is the quark-lepton tensor from QED and f^i will be identified with the parton distribution functions. The integral is taken over the parton 'loop' momentum k, which has the Sudakov form

$$k^\mu = ap^\mu + \frac{k^2 + \mathbf{k_T^2}}{2a} n^\mu + k_T^\mu$$

where $a = k \cdot n$. Using this and the expression for q above gives

$$(k+q)^2 = k^2 - Q^2 + 2a\nu + 2\mathbf{q_T} \cdot \mathbf{k_T} \approx 2a\nu - Q^2,$$

where the last step follows from the assumptions of the parton model that amplitudes with large k^2 and large transverse momenta are strongly damped. Changing variables in Eq. 3.44, the integral over the delta function gives

$$\delta((k+q)^2) \approx \delta(2a\nu - Q^2) = \frac{1}{2\nu}\delta(a - Q^2/(2\nu)).$$

Thus $a = Q^2/(2\nu)$, but $a = k \cdot n = k/p$, so a is identified with Bjorken x of the QPM and has its usual form in terms of external variables. The second diagram shown in Fig. 3.10b is another possible contribution, but it is suppressed by the assumptions noted above for the QPM. It is a 'higher twist' contribution as will be explained in the next section. QCD enhancements to the parton model can also be represented in terms of contributions to virtual Compton scattering, two simple examples are shown in Fig.3.11.

3.4 The Operator Product Expansion

The operator product expansion (OPE) is method for studying the structure of field theories in the light-cone limit. It also provides the framework for the all important factorisation theorem which underpins one of the basic assumptions of the QCD improved parton model.

Consider a very simple example of the time-ordered product of two free particle scalar fields $T(\phi(x)\phi^\dagger(y))$. Since a quantum is created by field operator $\phi^\dagger(y)$ at y and annihilated by $\phi(x)$ at x, this is closely related to the propagator $\Delta(x-y)$. Formally

$$T(\phi(x)\phi^\dagger(y)) = \Delta(x-y)\,\mathbf{1} + :\phi(x)\phi^\dagger(y):,$$

where

$$\Delta(x-y) = -\frac{2}{(2\pi)^4}\frac{1}{(x-y)^2 + i\epsilon}$$

and the second term is the normal ordered product of the fields which is non-singular as $x \to y$. The singularity of the operator product as $x \to y$ has been isolated as a product of a known function and an operator (here the unit operator). Knowing that the mass dimension[14] of a scalar field ϕ is 1, the power of the leading singularity in $(x-y)$ must be $0 - 1 - 1 = -2$ on dimensional grounds.

[14] With units $\hbar = c = 1$, mass or energy has dimension [length]$^{-1}$, thus the mass or energy dimension of a field operator may be deduced from the fact that $\int d^4x L$ must be dimensionless. Here $L = m^2\phi\phi^\dagger - \partial^\mu\phi\partial_\mu\phi^\dagger$ and it follows immediately that ϕ has mass dimension 1.

The OPE of Wilson [Wil69] is a powerful generalisation of the above example. The singular part of the product of $A(x)B(y)$ is given by

$$A(x)B(y) \to \sum_j C_j(x-y)N_j(y) \quad \text{as} \quad (x-y)^2 \to 0,$$

where C_j are singular coefficient functions and N_j are non-singular local operators. Dimensional counting suggests that

$$C_i(x-y) \sim (x-y)^{d_{N_i}-d_A-d_B} \quad \text{as} \quad (x-y)^2 \to 0,$$

where d_O is the mass dimension of operator O. This would be the case in a free field theory but it gets modified by renormalisation. There are two important properties of the OPE that make it a powerful method: firstly the dimension of an operator increases as more fields or derivatives are added; secondly because the relation is one between *operators*, although the matrix elements of the operators will depend on the process, the coefficient functions are universal for that product. The first point implies that in a Taylor expansion of an operator product about the light cone successively higher order terms have increasing d_{N_i} and thus *less* singular coefficient functions. The full exposition of the application of the OPE to DIS is rather technical, pedagogical accounts are to be found in [Mut98,Ynd99] among others. Here only the essential steps for the application of the OPE to DIS will be outlined.

The starting point is Eq. 3.42, which shows that the virtual Compton amplitude is related to the product of two EM current operators. To keep things simple the flavour and spin structure will be ignored and only a generic structure function considered (close to the case for non-singlet F_1 or F_2/x). Apply the operator product expansion to $T(j^\dagger_\mu(z)j_\nu(0))$

$$iT(j^\dagger_\mu(z)j_\nu(0)) = \sum_{j,n} C_{j,n}(z^2,\mu^2)z^{\mu_1}\cdots z^{\mu_n}N^{\mu_1\cdots\mu_n}_{j,n}(\mu^2), \tag{3.45}$$

where μ^2 is the factorisation scale and the non-singular operators $N_j(z,\mu^2)$ have been expanded in powers of z

$$N_j(z,\mu^2) = \sum_n z^{\mu_1}\cdots z^{\mu_n}N^{\mu_1\cdots\mu_n}_{j,n}(\mu^2).$$

In a free field theory $C_{j,n}$ would behave like $(z^2)^{\tau/2-d_J}$ for $z^2 \sim 0$, where $\tau = d_{j,n} - n =$ (dimension−spin) is the *twist* of the operator $N_{j,n}$ with mass dimension $d_{j,n}$ and d_J is the dimension of the EM current. In a theory with interactions like QED or QCD, the singular behaviour will be modified by logarithms introduced by renormalisation, which is also why the scale μ^2 appears. For DIS the operators are products of currents and are at least bilinear in the fields, so that the smallest twist is 2. This then gives the leading most singular contribution to the OPE. The dimension, spin and

Table 3.1 Dimension, spin and twist of some operators.

Operator	Mass dimension	Spin	Twist
Scalar field $\phi(x)$	1	0	1
$\phi^\dagger \partial_{\mu_1} \cdots \partial \mu_n \phi$	$n+2$	n	2
Vector field $A_\mu(x)$	1	1	0
$\bar{\psi}\gamma_\mu\psi$	3	1	2

twist for some simple operators are shown in Table 3.1. Redefining $C_{j,n}$ relative to the leading twist by $C_{j,n}(z^2,\mu^2) = C'_{j,n}(z^2,\mu^2)(z^2)^{\tau/2-1}$, the OPE expansion 3.45 is inserted into Eq. 3.42 to give

$$T(q^2,\nu) = \sum_{j,n} \langle p|N_{j,n}^{\mu_1\cdots\mu_n}(\mu^2)|p\rangle \int d^4z\, e^{iq\cdot z}\, z^{\mu_1}\cdots z^{\mu_n} C'_{j,n}(z^2,\mu^2)(z^2)^{\tau/2-1}.$$

The integral is a Fourier transform which will be proportional to $q_{\mu_1}\cdots q_{\mu_n}$ and defines $\tilde{C}_{j,n}(q^2,\mu^2)$

$$\int d^4z\, e^{iq\cdot z}\, z^{\mu_1}\cdots z^{\mu_n} C'_{j,n}(z^2,\mu^2)(z^2)^{\tau/2-1} = q^{\mu_1}\cdots q^{\mu_n}\tilde{C}_{j,n}(q^2,\mu^2)(-q^2)^{1-\tau/2}.$$

The matrix element of the operator $N_{j,n}^{\mu_1\cdots\mu_n}(\mu^2)$ cannot be evaluated completely, but as it can only depend on p, the Lorentz structure (up to contractions) must be proportional to $p_{\mu_1}\cdots p_{\mu_n}$ and this defines a reduced matrix element

$$\langle p|N_{j,n}^{\mu_1\cdots\mu_n}(\mu^2)|p\rangle = p_{\mu_1}\cdots p_{\mu_n}\bar{N}_{j,n}(\mu^2).$$

When these two expressions are taken together to form $T(q^2,\nu)$, the 4-momenta contract to give $(q\cdot p)^n$ and using $q\cdot p = Q^2/(2x)$ gives

$$T(q^2,\nu) = \sum_{j,n} C_{j,n}(Q^2,\mu^2)\bar{N}_{j,n}(\mu^2)\left(\frac{1}{x}\right)^n\left(\frac{1}{Q^2}\right)^{\tau/2-1}, \tag{3.46}$$

where $C_{j,n}(Q^2,\mu^2) = \tilde{C}_{j,n}(q^2,\mu^2)(Q^2/2)^n$.

Having established the OPE expression for $T(q^2,\nu)$, the next step is to relate it to the structure function. This is done by using a dispersion relation for T. Since T is an analytic crossing symmetric function of ν ($T(q^2,\nu) = T(q^2,-\nu)$), it satisfies[15]

$$T(q^2,\nu) = \frac{1}{\pi}\int_{Q^2/2}^{\infty} d\nu' \mathrm{Im}T(q^2,\nu')\left[\frac{1}{\nu'-\nu} + \frac{1}{\nu'+\nu}\right].$$

[15] Masses have been ignored in determining the lower limit of the integral.

Now $\mathrm{Im}T = 2\pi W$, and using $\nu = Q^2/(2x)$ to change variables one finds

$$\begin{aligned} T(q^2, x) &= 4\int_0^1 \frac{dx'}{x'(1 - x'^2/x^2)} W(q^2, x') \\ &= 4\sum_2^\infty \left(\frac{1}{x}\right)^n \int_0^1 dx'\, x'^{n-1} W(q^2, x'), \end{aligned} \tag{3.47}$$

where the sum starts at $n = 2$ and runs over even integers only (from the symmetry of T). By comparing Eq.s 3.46 and 3.47 one can read off the OPE expression for the even-n moments of the structure function

$$\int_0^1 dx'\, x'^{n-1} W(q^2, x') = \frac{1}{4}\sum_j C_{j,n}(Q^2, \mu^2)\bar{N}_{j,n}(\mu^2)\left(\frac{1}{Q^2}\right)^{\tau/2-1}. \tag{3.48}$$

The OPE shows that the moments of structure functions or parton densities can be expanded as a power series in $1/Q^2$. At large Q^2 the moments will be given to a good approximation by the leading twist 2 terms for which the Q^2 dependence is contained in the coefficient functions $C_{j,n}$. These may calculated perturbatively, but the matrix elements $\bar{N}_{j,n}$ are non-perturbative objects. For leading twist the above equation may be simplified to read

$$\int_0^1 dx'\, x'^{n-1} W(q^2, x') = C_n(Q^2, \mu^2)\bar{N}_n(\mu^2)/4 + O(1/Q^2). \tag{3.49}$$

Figure 3.10 (a) and (b) show examples of leading twist 2 and higher twist contributions to the virtual Compton amplitude, respectively. For a crossing anti-symmetric structure function, the OPE method gives the odd-n moments. For both symmetric and anti-symmetric cases the missing moments have to be found by analytic continuation in n.

3.5 Factorisation

The basic idea of factorisation is that the cross-section for DIS may be written as the convolution of two terms: a calculable hard scattering cross-section and a non-perturbative parton density. This is implicit in the discussion of the covariant parton model and is contained in the form of the OPE expression given in Eq. 3.49 for the leading twist terms. It shows that the moments of the structure functions may be written as a product of a calculable term containing the Q^2 dependence and a non-perturbative matrix element. Define functions $q(x, \mu^2)$, $\sigma(z, Q^2, \mu^2)$ such that

$$\int d\xi \xi^{n-1} q(\xi, \mu^2) \quad = \quad \bar{N}_n(\mu^2)/4$$

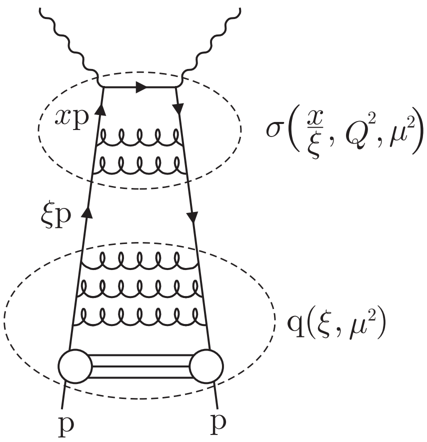

Fig. 3.12 Factorised form of the virtual Compton scattering amplitude from the QCD OPE approach (adapted from [Rob90,Fig.4.5]).

$$\int dz z^{n-1} \sigma(z, Q^2, \mu^2) \quad = \quad C_n(Q^2, \mu^2)$$

then Eq. 3.49 is equivalent to the convolution

$$W(q^2, x) = \int_x^1 \frac{d\xi}{\xi} q(\xi, \mu^2) \sigma\left(\frac{x}{\xi}, Q^2, \mu^2\right),$$

which is shown diagrammatically in Fig. 3.12. The function $q(\xi, \mu^2)$ is the non-perturbative piece that is identified with the parton density function (i.e. the probability to find a quark in the proton with momentum fraction ξ) and $\sigma(z, Q^2, \mu^2)$ is the cross-section for γ^*q scattering. The meaning of the factorisation scale μ^2 is also clear, it is the place in the gluon ladder above which the gluon radiation is considered part of the hard process. It is through gluon radiation that Q^2 dependence and thus scaling violations enter the QCD improved parton model. The proof of factorisation is a technically demanding task. Relevant classes of Feynman diagrams have to be analysed to ensure that all infra-red singularities can be absorbed in the non-perturbative matrix element and that 'interference' diagrams such as Figure 3.10(b) only contribute at higher twist. A good introduction to the subject is to be found in [Col89]. A brief account is also given in [Fur82] which contains a systematic summary of the NLO pQCD formalism for lepton-hadron processes.

3.6 Summary

This chapter has outlined the essential features of QCD that are important for DIS. The basic idea of renormalisation has been illustrated in QED using the example of loop insertions in the photon propagator. In QCD renormalisation leads to a running coupling that decreases at small distances, which is the crucial physical result that underpins the parton model and allows perturbative methods to be applied to certain strong interaction processes. Various formal methods such as the renormalisation group and the operator product expansion have been sketched. Finally applying the OPE method to DIS gives the mathematical framework for verifying the factorisation assumption of the QPM and verifying that it will continue to hold for the QCD improved parton model.

3.7 Questions

1. Check the QED calculation of the Compton scattering cross-section outlined in Sec. 3.1.3. In particular, show that the interference term in the sum over spins is:

$$\sum_{spins} M_a M_b^* = \frac{\mathrm{e}^4}{\mathrm{su}} \mathrm{Tr}[\not{p}' \gamma^\nu (\not{p} + \not{k}) \gamma^\mu \not{p} \gamma_\nu (\not{p} - \not{k}') \gamma_\mu]. \tag{3.50}$$

   Evaluate the trace for the case where the incident photon is virtual with mass $k^2 = -\mathrm{Q}^2$ and other masses are neglected, hence verify the result given in Eq. 3.11.
2. Check the calculation of the BGF cross-section (Eq. 3.14), either directly or by the application of crossing symmetry and suitable adjustments to the colour factors.
3. Gauge invariance and Ward identities. Consider a real photon state with momentum k and polarisation vector ε, $A_\mu = \varepsilon_\mu e^{-ik\cdot x}$, where $k \cdot \varepsilon = 0$ follows from the Lorentz condition $\partial_\mu A^\mu = 0$. EM gauge invariance states that physical results are invariant under the gauge transformation $A_\mu \to A_\mu - \partial_\mu f$, where f is scalar function satisfying $\partial_\mu \partial^\mu f = 0$. Taking $f = \lambda e^{-ik\cdot x}$ show that the gauge transformation is equivalent to the replacement $\varepsilon_\mu \to \varepsilon_\mu + \lambda k_\mu$. The amplitude for $\gamma e \to \gamma e$ (Compton scattering of real photons) has the form $\varepsilon_\mu^\dagger M^{\mu\nu} \varepsilon_\nu$, hence show that gauge invariance requires that $k_\mu M^{\mu\nu} = 0$, $M^{\mu\nu} k_\nu = 0$. Two tree level diagrams contribute to $M^{\mu\nu}$ (refer to Sec. 3.1.3), show that both are required to satisfy gauge invariance, i.e. $k_\mu M_a^{\mu\nu} \neq 0$, $k_\mu M_b^{\mu\nu} \neq 0$ but $k_\mu (M_a^{\mu\nu} \neq 0 + M_b^{\mu\nu}) = 0$. This is an example of a Ward identity.
4. (i) Using Eq. 3.24 for α_{qed} with $\alpha = 1/137$ at $\mu = .51\,\mathrm{MeV}$ but including all relevant fermions (leptons and quarks) in the calculation of b_0 for QED, estimate the value of α_{qed} at the mass of the Z^0 boson (91.2 GeV).
   (ii) Using Eq. 3.25 plot α_S as a function of Q^2 between $1\,\mathrm{GeV}^2$ and $10^5\,\mathrm{GeV}^2$ for $n_f = 3$ and $\Lambda_{QCD} = 200\,\mathrm{MeV}$.
5. Convince yourself that you understand the NLO renormalisation group expressions for α_S, Eqs 3.31 to 3.33. Estimate the size of the NLO

correction in the last equation with Λ of 200 MeV and Q^2 values of 1, 10, 1000 GeV^2.

6. Show that the tensor:

$$L_{\mu\nu} = \frac{1}{2}\mathrm{Tr}\left\{(\not{k}' + m)\gamma_\mu(\not{k} + m)\gamma_\nu\right\}$$

is given by

$$L_{\mu\nu} = 2[k'_\mu k_\nu + k'_\nu k_\mu + \frac{q^2}{2}g_{\mu\nu}]$$

where $k^2 = m^2$, $k'^2 = m^2$ and $q^2 = (k - k')^2$. Show also that $q^\mu L_{\mu\nu} = 0$ and $L_{\mu\nu}q^\nu = 0$. $L_{\mu\nu}$ is known as the leptonic tensor and turns up in the calculation of cross-sections for ep scattering and e^+e^- annihilation.

7. The reduction of Eq. 3.40 to the form 3.41 is most easily demonstrated in the reverse direction. One needs: $j(z) = U(z)j(0)U^{-1}(z)$ and $U(z)|p\rangle = \exp(ip \cdot z)|p\rangle$ for translation by z; the representation

$$(2\pi)^4\delta^4(q) = \int d^4z \exp(iq \cdot z),$$

and the use of momentum conservation to show that the second term in the commutator in Eq. 3.41 gives zero.

4

QCD improved parton model

This chapter uses the results of the previous one to show how QCD extends and improves the quark-parton model. Historically the first calculations of QCD scaling violation were performed using the operator product expansion. That route will not be followed here, rather a more physical approach based on the idea of quark and gluon splitting functions will be used. This leads to the DGLAP equations for the quark and gluon momentum distribution functions (PDF) at LO and NLO. Some basic properties of the solutions of these equations at LO are then discussed. The relationship between the OPE and DGLAP approaches is outlined and some comments made on higher twist terms. The problem of including heavy quarks in the DGLAP framework is considered and a number of approaches summarised. Finally the prospects for going beyond NLO are reviewed briefly.

Too much on heavy quarks, not enough on some other aspects?
Written 2000, not revised.

4.1 Improving the parton model

The basic idea of the QCD improved parton model is summarised in Fig. 4.1 for γ^*p interactions: (a) shows the QPM approach in which the γ^* interacts directly with a quark in the proton; (b) shows the QCD approach in which the γ^* undergoes a more general hard scattering with a quark or gluon from the proton. If Q^2 is the mass or virtuality of the γ^* with 4-momentum q and p is the 4-momentum of the proton, then p in the γ^*p interaction corresponds to $\xi p = p_i$ in the γ^*parton interaction, similarly $x = Q^2/(2p.q) \to z = Q^2/(2p_i.q) = x/\xi$, the partonic scaling variable. The masses of all particles except the γ^* are taken to be zero. The cross-section $\hat{\sigma}$ for the hard γ^*parton interaction is calculable in pQCD and the overall γ^*p cross-section is then given by a convolution of $\hat{s}$ with $f_i(y)$, the probability of finding the parton with momentum fraction y in the proton:

$$\sigma(x, Q^2) = \sum_i \int_0^1 dz \int_0^1 d\xi f_i(\xi)\delta(x - z\xi)\hat{s}(z, Q^2). \qquad (4.1)$$

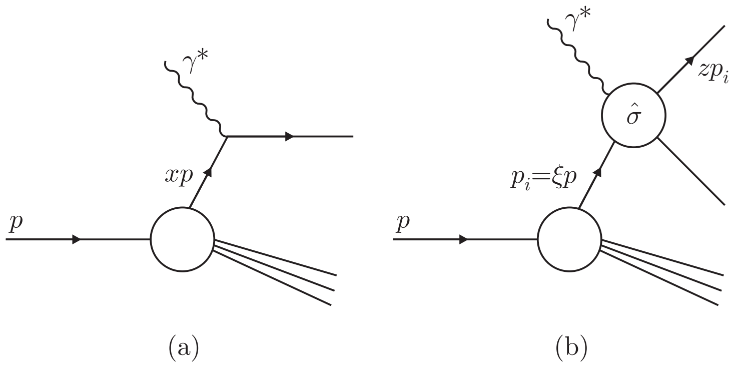

Fig. 4.1 The basic idea of the QCD improved parton model for γ^*p interactions: (a) shows the QPM approach; (b) the QCD improved version.

(Here 'cross-sections' $\sigma, \hat{s}$ could equally well be structure functions.) Note that a key feature of the parton model remains in the QCD approach, namely that the *cross-section* can be factored into a probability density for finding a parton and the probability of a hard scattering. This in turns relies on the time scale of the hard scatter being very much shorter that that of the subsequent hadronisation of the final state. Mathematically this picture is supported by the QCD collinear factorisation.

The physical processes that need to be 'added' to the QPM are the radiation of gluons by quarks and q$\bar{\text{q}}$ pair production by gluons. At high energies the structure functions are related to the cross-sections for transverse and longitudinal virtual photon scattering by[1]

$$\begin{aligned} \sigma_T &= \frac{4\pi^2\alpha}{s} 2F_1 \\ \sigma_L &= \frac{4\pi^2\alpha}{s}\left[\frac{F_2}{x} - 2F_1\right], \end{aligned} \tag{4.2}$$

where the Hand convention has been used for the γ^* flux. It is convenient to define $\sigma_0 = \frac{4\pi^2\alpha}{s}$, where in these expressions s is the γ^*p CM energy squared. To build up the expression for a structure function, the γ^*parton level cross-sections, $\hat{s}_{T,L}$, are needed. To begin with consider the calculation of F_2 in terms of $(\hat{s}_T + \hat{s}_L)/\hat{s}_0$ (with an obvious notation). As outlined in problem 7 at the end of this chapter, it is straightforward to show that for a massless quark of charge e_i the γ^*-quark interaction of Fig. 4.1(a) gives

$$\begin{aligned} \hat{s}_T &= e_i^2 \hat{s}_0 \delta(1-z) \\ \hat{s}_L &= 0. \end{aligned} \tag{4.3}$$

[1]See Eqs 13.16,13.17 of Sec. 13.4.

Substituting this in equation 4.1 gives

$$\begin{aligned} F_2(x,Q^2)/x &= \int_0^1 dz \int_0^1 d\xi\, q_i(\xi)\delta(x - z\xi)e_i^2\delta(1-z) \\ &= \int_x^1 \frac{d\xi}{\xi} q_i(\xi)e_i^2\delta(1 - x/\xi) \\ &= e_i^2 q_i(x) \end{aligned}$$

Which agrees with the QPM result for a single quark flavour.

The first additional hard process beyond the QPM to be considered is gluon radiation from quark lines, there are two diagrams as shown in Fig. 4.2. These are essentially the diagrams of the QCD Compton process

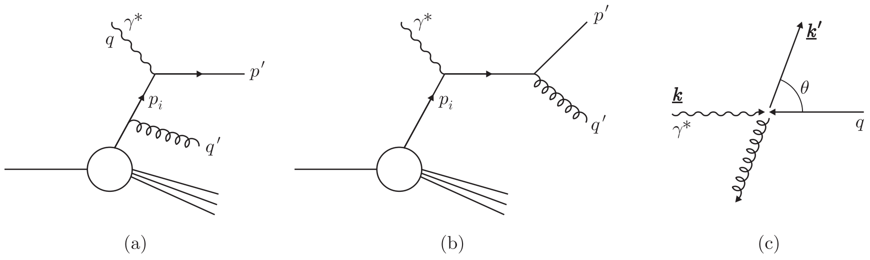

Fig. 4.2 Diagrams for gluon radiation from quarks in DIS via QCDC, together with the parton CM frame.

shown in Fig. 3.3. Using Eq. 3.13 with $t \to u$ and $u \to t$ and in terms of the kinematics of the hard scattering sub-process shown here, the parton level cross-section is

$$\hat{s} = \int d\Omega \frac{2}{3} \frac{e_i^2 \alpha \alpha_S}{\hat{s}} \left[-\frac{\hat{t}}{\hat{s}} - \frac{\hat{s}}{\hat{t}} + \frac{2\hat{u}Q^2}{\hat{s}\hat{t}} \right], \tag{4.4}$$

where $\hat{s} = (p_i + q)^2$, $\hat{t} = (q - p')^2$, $\hat{u} = (q - q')^2$. In the γ^*parton CMS θ is the scattering angle and $k,\ k'$ the magnitudes of the initial and final state 3-momenta. Then

$$\begin{aligned} \hat{s} &= 4k'^2 = 2p_i.q + q^2 = Q^2(1-z)/z \\ \hat{t} &= -2kk'(1 - \cos\theta) \\ \hat{u} &= -2kk'(1 + \cos\theta) \end{aligned}$$

and using these, the terms in the [] brackets in Eq. 4.4 become

$$[\,] \to \left[\frac{1}{1-z} \left(\frac{1-c}{2} \right) + (1-z) \left(\frac{2}{1-c} \right) + \frac{2z}{1-z} \left(\frac{1+c}{1-c} \right) \right], \tag{4.5}$$

where $c \equiv \cos\theta$. As it stands there are singularities for $z \to 1$ and $c \to 1$. The former corresponds to infrared gluon radiation and will be dealt with later as this singularity is cancelled by other terms. The angular integral will be dominated by the contribution from the the last two terms and the $1/(1-c)$ singularity will have to be regulated. The singularities occur as $\theta \to 0$ which corresponds to the gluon being emitted collinear with the initial parton direction. The factor multiplying the pole is $2(1+z^2)/(1-z)$. Rather than proceed with an angular integration, it is instructive to rewrite it in terms of the gluon (or quark) transverse momentum in the parton CMS,

$$p_t^2 = k'^2 \sin^2\theta \simeq \frac{\hat{s}}{4}\theta^2 \text{ for small } \theta.$$

Similarly for small angles $d\Omega \simeq 4\pi dp_t^2/\hat{s}$. Using these expressions and keeping only the dominant $1/(1-c)$ terms

$$\hat{s} \simeq \hat{s}_0 e_i^2 \frac{\alpha_S}{2\pi}\frac{4}{3}\left[\frac{1+z^2}{1-z}\right]\int_0^{p_t^2(max)} \frac{dp_t^2}{p_t^2}, \tag{4.6}$$

where $p_t^2(max) = \hat{s}/4 = Q^2(1-z)/4z$. The p_t^2 integral is regulated at the lower limit by the introduction of a cut-off, κ^2, and it gives

$$\int_{\kappa^2}^{p_t^2(max)} \frac{dp_t^2}{p_t^2} = \ln\left(\frac{Q^2}{\kappa^2}\right) + \ln\left(\frac{1-z}{4z}\right).$$

This result shows explicity where the large logs come from, gluon radiation introduces non-zero p_t and integrating over the characteristic dp_t^2/p_t^2 radiation spectrum will introduce a $\ln(Q^2/\kappa^2)$ scaling violation in the structure function. Define the function

$$P_{qq}(z) = \frac{4}{3}\left[\frac{1+z^2}{1-z}\right], \tag{4.7}$$

which is the probability for q $\to$ gq splitting, then $\hat{s}$ may be written

$$\hat{s}(z) = \hat{s}_0 e_i^2 \frac{\alpha_S}{2\pi}\left[P_{qq}(z)\ln\left(\frac{Q^2}{\kappa^2}\right) + C(z)\right], \tag{4.8}$$

where $C(z)$ includes the terms left over after the identification of the leading $\alpha_S \ln(Q^2/\kappa^2)$ term. $\hat{s}(z)$ can now be added to the zeroth order QPM parton cross-section to give

$$\begin{aligned}\frac{F_2(x,Q^2)}{x} &= \int_0^1 dz \int_0^1 d\xi\, q_i(\xi)\delta(x - z\xi)[e_i^2\delta(1-z) + \hat{s}(z)/\hat{s}_0] \\ &= e_i^2 \int_x^1 \frac{d\xi}{\xi} q_i(\xi)\left[\delta(1-\frac{x}{\xi}) + \frac{\alpha_S}{2\pi}P_{qq}\left(\frac{x}{\xi}\right)\ln\left(\frac{Q^2}{\kappa^2}\right)\right],\end{aligned}$$

(4.9)

keeping only the leading $\alpha_S \ln(Q^2/\kappa^2)$ term. How is this result to be interpreted? The last equation could be interpreted as requiring the replacement of the parton density

$$q_i(x) \to q_i(x) + \Delta q_i(x, Q^2)$$

where

$$\Delta q_i(x, Q^2) = \frac{\alpha_S}{2\pi} \int_x^1 \frac{d\xi}{\xi} q_i(\xi) P_{qq}\left(\frac{x}{\xi}\right) \ln\left(\frac{Q^2}{\kappa^2}\right).$$

However this is not correct as the $\kappa^2 \to 0$ problem is still there. The solution is similar to renormalisation, the $q_i(x)$ used so far must be considered as unmeasurable 'bare' distributions. By introducing a new scale $\mu^2 \gg \kappa^2$, the soft non-perturbative physics is included in the renormalised parton density $q_i(x, \mu^2)$ which is now scale dependent. This is the (collinear) factorisation scale and it is the scale at which the collinear singularity is absorbed into the parton density, $\ln(Q^2/\kappa^2) \to \ln(Q^2/\mu^2) + \ln(\mu^2/\kappa^2)$, and

$$q_i(x, \mu^2) = q_i^0(x) + \frac{\alpha_S}{2\pi} \int_x^1 \frac{d\xi}{\xi} q_i^0(\xi) P_{qq}\left(\frac{x}{\xi}\right) \ln\left(\frac{\mu^2}{\kappa^2}\right), \tag{4.10}$$

with

$$\frac{F_2(x, Q^2)}{x} = e_i^2 \int_x^1 \frac{d\xi}{\xi} q_i(\xi, \mu^2) \left[\delta(1 - \frac{x}{\xi}) + \frac{\alpha_S}{2\pi} P_{qq}\left(\frac{x}{\xi}\right) \ln\left(\frac{Q^2}{\mu^2}\right)\right]. \tag{4.11}$$

The steps from Eq. 4.9 Eqs 4.10 and 4.11 require a bit of care as they are only correct to order α_S. The renormalised parton density $q_i(x, \mu^2)$ cannot be calculated perturbatively, but its variation with $\ln \mu^2$ is given by

$$\frac{\partial q_i(x, \mu^2)}{\partial \ln \mu^2} = \frac{\alpha_S}{2\pi} \int_x^1 \frac{d\xi}{\xi} q_i(\xi, \mu^2) P_{qq}(x/\xi). \tag{4.12}$$

With $\mu^2 = Q^2$, which is the usual choice of factorisation scale in DIS, equation 4.11 reduces to

$$F_2(x, Q^2) = e_i^2 x q_i(x, Q^2) \tag{4.13}$$

which has the form of the QPM result but with $q_i(x) \to q_i(x, Q^2)$.

In addition to gluon bremsstrahlung modifying the QPM results, the process of $g \to q\bar{q}$ will also change the quark momentum densities. The diagrams are those of the BGF process and are shown again together with the parton CM frame variables in Fig. 4.3. In terms of the parton-level

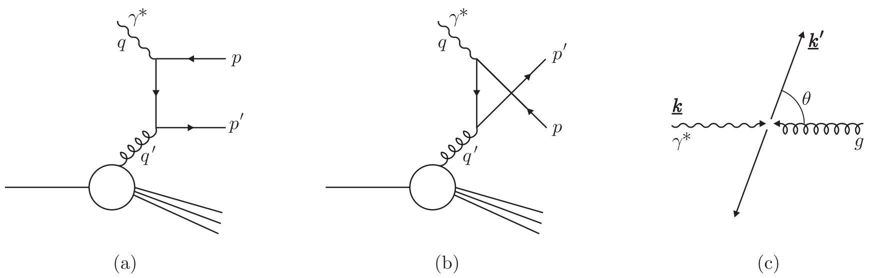

Fig. 4.3 The parton-level diagrams for BGF production of q$\bar{\text{q}}$, together with the parton CM frame.

variables, the cross-section from Eq. 3.14 reads:

$$\frac{d\hat{s}}{d\Omega}|_{BGF} = \frac{1}{4}\frac{e_i^2\alpha\alpha_S}{\hat{s}}\left[\frac{\hat{u}}{\hat{t}} + \frac{\hat{t}}{\hat{u}} - \frac{2\hat{s}Q^2}{\hat{t}\hat{u}}\right], \tag{4.14}$$

where $\hat{s} = (q+q')^2$, $\hat{t} = (q-p)^2$, $\hat{u} = (q-p')^2$ and $z = Q^2/2q.q' = Q^2/(\hat{s}+Q^2)$. Introducing the CM scattering angle θ as shown in the figure, the terms in [] become

$$[\,] \to \left[2\frac{1+c^2}{1-c^2} - 8\frac{z(1-z)}{1-c^2}\right],$$

where $c = \cos\theta$. Both terms are singular as $\theta \to 0, \pi$, which correspond to either the outgoing q or $\bar{\text{q}}$ being collinear with the incoming gluon. Writing the angular integral in terms of the parton p_t and approximating $1+c^2 \approx 2$ in the numerator of the first term

$$\hat{s} \simeq \hat{s}_0 e_i^2 \frac{\alpha_S}{2\pi}\frac{1}{2}[z^2 + (1-z)^2]\int_0^{p_t^2(max)} \frac{dp_t^2}{p_t^2}.$$

Proceeding as above, the p_t integral gives a leading $\ln(Q^2/\kappa^2)$ for large Q^2, where κ^2 regulates the divergence. To relate this result to γ^*p scattering, $\hat{s}$ is convoluted with a gluon density function $g^0(x)$ to give

$$\frac{F_2^g(x,Q^2)}{x} = \int_x^1 \frac{d\xi}{\xi} e_i^2 g^0(\xi)\frac{\alpha_S}{2\pi}P_{qg}\left(\frac{x}{\xi}\right)\ln\left(\frac{Q^2}{\kappa^2}\right), \tag{4.15}$$

where

$$P_{qg}(z) = \frac{1}{2}[z^2 + (1-z)^2] \tag{4.16}$$

is the g $\to$ q$\bar{\text{q}}$ splitting function and only the leading $\alpha_S\ln(Q^2/\kappa^2)$ term has been retained. This additional contribution to F_2 has a number of consequences. The $\kappa^2 \to 0$ singularity is handled as above by renormalisation at the factorisation scale μ^2 leading to an extra contribution to

$q_i(x, \mu^2)$ of a similar form to Eq. 4.10. The variation of $q_i(x, \mu^2)$ with $\ln \mu^2$ picks up a term depending on the gluon density (which is also renormalised $g^0(x) \to g(x, \mu^2)$) so Eq. 4.12 becomes

$$\frac{\partial q_i(x, \mu^2)}{\partial \ln \mu^2} = \frac{\alpha_S}{2\pi} \int_x^1 \frac{d\xi}{\xi} \left[q_i(\xi, \mu^2) P_{qq}(x/\xi) + g(\xi, \mu^2) P_{qg}(x/\xi) \right] . \quad (4.17)$$

At the leading order in α_S, which is being considered here, F_2 continues to be given by Eq. 4.13. Beyond leading order the situation is more complicated and this will be discussed in the next section.

Having seen how gluon processes in QCD give rise to a $\ln Q^2$ breaking of exact QPM scaling in DIS, it is now time to pull the results together into a form that can be confronted with data.

An alternative and instructive approach to the physics of parton splitting can also be built on the QED cross-sections for soft or collinear radiation as outlined in problems 2 to 5 at the end of the chapter.

4.2 The DGLAP equations

Although QCD does not allow a complete calculation of the structure functions in DIS, it does predict how the structure functions should change with Q^2 (at least above some minimum Q_0^2 to ensure validity of the perturbative approach). The first predictions were for structure functions moments derived from the OPE. Although powerful in principle this approach suffers from the practical difficulty of having to integrate the structure functions over the whole range of x from 0 to 1, thus requiring a model for extrapolation beyond the measured region. A more physical approach and one that follows naturally from the calculations of the previous section is due to the work of Gribov and Lipatov [Gri72], Lipatov [Lip75], Altarelli and Parisi [Alt77] and Dokshitzer [Dok77] – collectively referred to as DGLAP. A very accessible account is given in Altarelli [Alt82].

The essence of the approach is contained in Eq. 4.17 which shows how the parton density 'evolves' through the two splitting functions P_{qq} and P_{qg} as the scale μ^2 (Q^2) changes. To form a closed set of equations, two more splitting functions are needed which describe the probabilities for q $\to$ qg and g $\to$ gg splitting. Just as the quark density evolves, so will the gluon density with an equation of similar form to 4.17

$$\frac{\partial g(x, \mu^2)}{\partial \ln \mu^2} = \frac{\alpha_S}{2\pi} \int_x^1 \frac{d\xi}{\xi} \left[\sum_i q_i(\xi, \mu^2) P_{gq}(x/\xi) + g(\xi, \mu^2) P_{gg}(x/\xi) \right] . \quad (4.18)$$

The splitting functions are summarised graphically in Fig. 4.4. The leading order expressions for P_{qq} and P_{qg} are given in Eqs 4.7 and 4.16 respectively. From the figure it is clear that $P_{gq}(z) = P_{qq}(1-z)$, which gives

$$P_{gq}(z) = \frac{4}{3} \left[\frac{1 + (1-z)^2}{z} \right] . \quad (4.19)$$

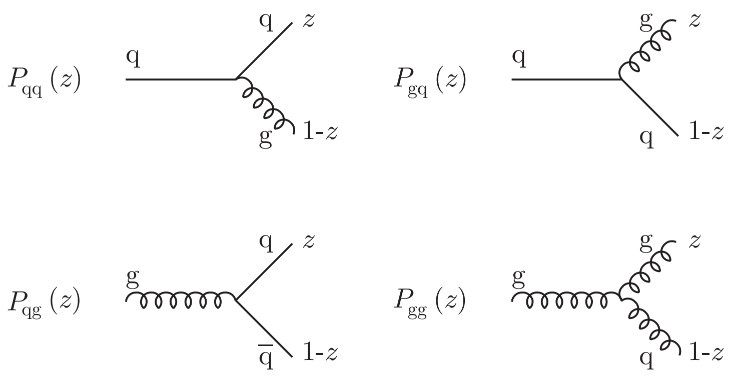

Fig. 4.4 The DGLAP splitting functions.

P_{gg} requires a bit more calculation but follows ultimately from the form of the 3-gluon vertex and is

$$P_{gg}(z) = 6\left[\frac{1-z}{z} + \frac{z}{1-z} + z(1-z)\right]. \tag{4.20}$$

Since the QCD Lagrangian conserves fermion number and flavour, the following sum rules must be obeyed by the renormalised parton densities at least to $O(\alpha_S)$

$$\int_0^1 dx[q_i(x, Q^2) - \bar{q}_i(x, Q^2)] = v_i, \tag{4.21}$$

where $v_i = 2, 1, 0, \ldots$ for the u, d, s,... flavours in the proton. Overall momentum conservation gives

$$\int_0^1 dx\, x[\Sigma(x, Q^2) + g(x, Q^2)] = 1, \tag{4.22}$$

where $\Sigma = \sum_i (q + \bar{q})$ and the sum runs over all flavours. Because these equations are independent of Q^2, the following constraints apply to the splitting functions

$$\int_0^1 dz\, P_{qq}(z) = 0 \tag{4.23}$$

$$\int_0^1 dz\, z[P_{qq}(z) + P_{gq}(z)] = 0 \tag{4.24}$$

$$\int_0^1 dz\, z[2n_f P_{qg}(z) + P_{gg}(z)] = 0 \tag{4.25}$$

where the last two integrals correspond to the conservation of momentum and flavour in quark and gluon splittings respectively.

There is a technical problem with P_{qq} that must be addressed and that is how to cope with the apparent singularity as $z \to 1$. This limit is associated with the emission of soft gluons. As gluon bremsstrahlung is essentially the same as photon bremsstrahlung in QED, the QCDC cross-section is an infrared safe quantity and thus the singularity will be cancelled by $O(\alpha\alpha_S)$ interference terms between the γ^*parton diagram and the virtual loop corrections to it (see Sec. 3.2.4). The required correction terms in P_{qq} are concentrated at $z = 1$ and give a term proporional to $\delta(1-z)$. As P_{qq} is in a mathematical sense a distribution (i.e. it always appears integrated with a function in any physical quantity) the $1/(1-z)$ singularity is regularised by the so-called '+ prescription'

$$\frac{1}{1-z} \to \frac{1}{(1-z)_+} \text{ where } \int_0^1 dz \frac{f(z)}{(1-z)_+} = \int_0^1 dz \frac{f(z)-f(1)}{1-z}$$

and $1/(1-z)_+ = 1/(1-z)$ for $z < 1$. Rather than calculate the additional delta function term directly, it can be found by using Eq. 4.23 and the '+ prescription' to fix the coefficient of the $\delta(1-z)$ term. The resulting regularised splitting function is

$$P_{qq}(z) = \frac{4}{3}\left[\frac{1+z^2}{(1-z)_+} + \frac{3}{2}\delta(1-z)\right]. \tag{4.26}$$

Similarly the $1/(1-z)$ singularity in P_{gg} is regularised by applying equation 4.25 to give

$$P_{gg}(z) = 6\left[\frac{1-z}{z} + \frac{z}{(1-z)_+} + z(1-z)\right] + \frac{33-2n_f}{6}\delta(1-z). \tag{4.27}$$

There is one further vitally important point to be considered before the DGLAP formalism is complete and that is the validity of the $O(\alpha_S)$ results for large Q^2. The leading order QCD corrections to the parton densities are all weighted by $\alpha_S \ln(Q^2/\mu^2)$ and higher order terms will involve powers of this combination. As it stands it looks as though the QCD corrections will diverge for $Q^2 >> \mu^2$. It is at this point that the renormalisation group comes to the rescue. The discussion in Sec. 3.2.3, particularly that preceeding Eq. 3.35, shows that leading logs are summed correctly by the simple replacement of fixed α_S by the running coupling $\alpha_S(Q^2)$. One is then effectively including contributions from multiple gluon emission, as shown in Fig. 4.5, and known as the leading log approximation (LLA). To pick out the leading $\alpha_S \ln(Q^2/\mu^2)$ terms requires that the transverse momenta of the successive steps shown in the diagram must be ordered[2]

$$\mu^2 < p_{1t}^2 < p_{2t}^2 < \ldots < p_{nt}^2 < Q^2. \tag{4.28}$$

[2]See problem 7 at the end of the chapter.

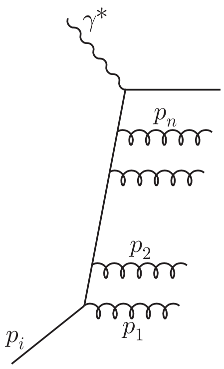

Fig. 4.5 Multiple gluon emissions from a quark line.

The DGLAP equations are coupled equations for the change of the quark, antiquark and gluon densities as $\ln Q^2$ changes

$$\frac{\partial}{\partial \ln Q^2}\begin{pmatrix} q_i(x,Q^2) \\ g(x,Q^2) \end{pmatrix} = \frac{\alpha_S(Q^2)}{2\pi}\sum_j \int_x^1 \frac{d\xi}{\xi} \begin{pmatrix} P_{q_iq_j}(\frac{x}{\xi},\alpha_S(Q^2)) & P_{q_ig}(\frac{x}{\xi},\alpha_S(Q^2)) \\ P_{gq_j}(\frac{x}{\xi},\alpha_S(Q^2)) & P_{gg}(\frac{x}{\xi},\alpha_S(Q^2)) \end{pmatrix} \begin{pmatrix} q_j(\xi,Q^2) \\ g(\xi,Q^2) \end{pmatrix}, \tag{4.29}$$

where the q_i, q_j are taken to include both quarks and antiquark distributions. The splitting functions are expanded as power series in α_S

$$\begin{aligned} P_{q_iq_j}(z,\alpha_S) &= \delta_{ij}P^{(0)}_{qq}(z) + \frac{\alpha_S}{2\pi}P^{(1)}_{qq}(z) + \ldots \\ P_{qg}(z,\alpha_S) &= P^{(0)}_{qg}(z) + \frac{\alpha_S}{2\pi}P^{(1)}_{qg}(z) + \ldots \\ P_{gq}(z,\alpha_S) &= P^{(0)}_{gq}(z) + \frac{\alpha_S}{2\pi}P^{(1)}_{gq}(z) + \ldots \\ P_{gg}(z,\alpha_S) &= P^{(0)}_{gg}(z) + \frac{\alpha_S}{2\pi}P^{(1)}_{gg}(z) + \ldots \end{aligned}$$

The δ_{ij} in front of the leading order term in expansion of P_{qq} follows immediately from the fact that flavour is conserved at a single quark gluon vertex, one must go to higher orders for a change in flavour. Because of charge conjugation and the flavour independence of the QCD Lagrangian, P_{qg} and P_{gq} are independent of quark flavour and the same for q and $\bar{\text{q}}$. $P_{q_iq_j}$ is the same for quarks and antiquarks and the leading order term vanishes unless $\text{q}_i = \text{q}_j$. The leading order splitting functions calculated in this and the previous section correspond to $P^{(0)}$ in the above expansion. Also the integral constraints of Eqs 4.23 to 4.25 apply to the $P^{(0)}$.

It is convenient for future reference to have a shorthand notation for the convolutions that occur in the DGLAP equations, so

$$[q \otimes P](x, Q^2) \equiv \int_x^1 \frac{d\xi}{\xi} q(\xi, Q^2) P\left(\frac{x}{\xi}\right) = \int_x^1 \frac{d\xi'}{\xi'} q\left(\frac{x}{\xi'}, Q^2\right) P(\xi'). \tag{4.30}$$

Often the arguments are dropped as well unless they are not obvious from the context. Because the gluon terms in the DGLAP equations do not carry indices, the structure of the equations can be considerably simplified by separating the quark densities into 'singlet' and 'non-singlet' terms (with respect to their SU(2) and SU(3) or more general flavour structure). The singlet quark density has already been introduced and is

$$\Sigma(x, Q^2) = \sum_i (q_i(x, Q^2) + \bar{q}_i(x, Q^2)) \tag{4.31}$$

where the sum runs over all active flavours. The evolution of Σ is coupled to that of the gluon density

$$\begin{aligned} \frac{\partial}{\partial \ln Q^2} \Sigma(x, Q^2) &= \frac{\alpha_S(Q^2)}{2\pi} ([\Sigma \otimes P_{qq}] + [g \otimes 2n_f P_{qg}]) && (4.32) \\ \frac{\partial}{\partial \ln Q^2} g(x, Q^2) &= \frac{\alpha_S(Q^2)}{2\pi} ([\Sigma \otimes P_{gq}] + [g \otimes P_{gg}]) && (4.33) \end{aligned}$$

A non-singlet combination is the difference of q_i and q_j (where q_j is any quark or antiquark density other than q_i). There are two combinations that are particularly useful

$$\begin{aligned} q_i^-(x, Q^2) &= q_i(x, Q^2) - \bar{q}_i(x, Q^2) \\ q_i^+(x, Q^2) &= q_i(x, Q^2) + \bar{q}_i(x, Q^2) - \frac{1}{n_f}\Sigma(x, Q^2), && (4.34) \end{aligned}$$

where q_i^- is the valence quark distribution for flavour i. The evolution of non-singlet distributions does not involve the gluon density, so

$$\frac{\partial q_i^\pm(x, Q^2)}{\partial \ln Q^2} = \frac{\alpha_S(Q^2)}{2\pi} [q_i^\pm \otimes P_\pm], \tag{4.35}$$

where the splitting functions $P_\pm$ are constructed from those defined in Eqs 4.29.

The DGLAP equations give a formalism for calculating the changes to the parton densities as Q^2 changes, however they do not allow a calculation of the distributions at the starting scale Q_0^2. This information has to come either from non-perturbative methods or by parameterising the x dependence of the parton density at Q_0^2 and determining the parameters by fitting to data. This is now a well established procedure and it will be discussed in detail in Chap. 6. Note that the convolution to determine how a parton density changes with Q^2 at a fixed x_0 requires an integral over the parton densities only at larger values of x.

At LO the expression for F_2 in terms of the parton densities, $q_i(x, Q^2)$, retains its simple QPM form (Eq. 4.13). Beyond leading order, in addition to the extra terms in the splitting functions, terms like the 'C(z)' of Eq. 4.8 and from the higher order diagrams must be allowed for. These extra terms appear in the relationships between the NLO parton densities and the physical observables and they are scheme dependent. Only in the DIS scheme does F_2 remain as given by Eq. 4.13, in more general schemes

$$\frac{F_2(x,Q^2)}{x} = \int \frac{d\xi}{\xi}\left[\sum_i e_i^2 q_i(\xi,Q^2) C_q\left(\frac{x}{\xi},\alpha_S\right) + \bar{e}^2 g(\xi,Q^2) C_g\left(\frac{x}{\xi},\alpha_S\right)\right], \tag{4.36}$$

where $\bar{e}^2 = \sum_i e_i^2$ and the sums run over all active quark and antiquark flavours. C_q an C_g are the coefficient functions, which may be expanded as power series in α_S,

$$\begin{aligned} C_q(z,\alpha_S) &= \delta(1-z) + \frac{\alpha_S}{2\pi} C_q^1(z) + \ldots \\ C_g(z,\alpha_S) &= \frac{\alpha_S}{2\pi} C_g^1(z) + \ldots . \end{aligned}$$

In the $\overline{\mathrm{MS}}$ scheme

$$\begin{aligned} C_q^1(z) &= \frac{4}{3}\left[\frac{4\ln(1-z)-3}{2(1-z)_+} - (1+z)\ln(1-z) - \frac{1+z^2}{1-z}\ln z \right. \\ &\quad \left. +3+2z - \left(\frac{\pi^2}{3}+\frac{9}{2}\right)\delta(1-z)\right], \end{aligned} \tag{4.37}$$

$$C_g^1(z) = \frac{1}{2}\left[\left(z^2+(1-z)^2\right)\ln\left(\frac{1-z}{z}\right) - 8z^2 + 8z - 1\right]. \tag{4.38}$$

Note that the way that parton densities, splitting functions and coefficient functions are defined means that for a complete formalism at NLO the splitting functions must be known up to 'two loops' and the coefficient functions to 'one loop'.[3] At NNLO one then needs splitting functions at three loops and coefficient functions at two loops, etc. It must also be emphasised that the parton densities, the splitting functions and the coefficient functions are all renormalisation and factorisation scheme dependent. Since physical quantities should be scheme independent conversion formulae exist to move between schemes, but care must be exercised to ensure consistency in any given calculation.

[3]The 'loops' referred to here come from the forms that the corresponding Feynman diagrams take, see Fig. 3.11 for a oneloop example.

In the QPM transverse momentum of the partons is assumed to be zero and one of the consequences of this for spin $\frac{1}{2}$ quarks is that the longitudinal structure function ($F_L = F_2 - 2xF_1$) is zero. The QCDC and BGF processes (and higher order diagrams) that give rise to the $\ln Q^2$ scaling violations also give rise to partons with non-negligible p_t. In turn this means that the Callan-Gross relation is no longer satisfied and $F_L \neq 0$. The QCD improved parton model gives an expression for F_L, with $O(\alpha_S)$ leading terms. A similar physical approach to that followed in the previous section but projecting out the longitudinal component of the parton level cross sections $\hat{s}_L$ gives the coefficient functions for F_L [Alt78]. They are factorisation scheme independent at $O(\alpha_S)$ giving

$$\frac{F_L(x,Q^2)}{x} = \frac{\alpha_S}{2\pi}\int_x^1 \frac{d\xi}{\xi}\left[\sum_i e_i^2 \frac{8}{3}\left(\frac{x}{\xi}\right) q_i(\xi,Q^2) + \bar{e}^2 4 \left(\frac{x}{\xi}\right)\left(1-\frac{x}{\xi}\right) g(\xi,Q^2)\right] \tag{4.39}$$

or the first term involving the quark densities may be replaced by $F_2(x,Q^2)$ to give

$$F_L(x,Q^2) = \frac{\alpha_S}{2\pi}\int_x^1 \frac{d\xi}{\xi}\left[\frac{8}{3}\left(\frac{x}{\xi}\right)^2 F_2(\xi,Q^2) + \bar{e}^2 4 \left(\frac{x}{\xi}\right)^2\left(1-\frac{x}{\xi}\right) \xi g(\xi,Q^2)\right]. \tag{4.40}$$

4.3 Parton densities at the starting scale

The pQCD DGLAP approach does not give any information on the shape of the parton momentum density functions at the starting scale Q_0^2. For valence quarks a function of the form

$$xf(x,Q_0^2) = Ax^\alpha(1-x)^\beta$$

where A, α, β are all postive constants might seem a reasonable first guess. The valence quark density is expected to peak at x values around or a bit below 0.3 and to vanish as $x \to 0, 1$. The above expression has the virtue of simplicity and being easy to manipulate analytically. When modified by a low order polynomial in x or $\sqrt{x}$ it is the form used in QCD fits (more on this in Chap. 10). Can one say more about the exponents α and β? For α this is the domain of low x physics and is discussed at length in Chap. 6, it will turn out that for valence PDFs α is expected to be around 0.5 but for the sea and gluon distributions α can be either negative or positive. As $x \to 1$ the PDFs must vanish as the proton's momentum is tending to be carried by a single parton only. How rapidly the distributions tend to zero is the domain of the so-called counting rules. These were originally derived by Matveev *et al.* [Mat73] and Brodsky & Farrar [Bro73,75] in the context of applying the parton model to high energy reactions at large momentum tranfers (see [Clo7,Sec.11.4,14.3] for more details). The form that the counting rule takes for DIS is

$$xf(x, Q_0^2) \sim (1-x)^{2n_s-1} \quad \text{as } x \to 1,$$

where n_s is the number of 'spectators' present apart from the struck parton. Very simple mindedly one has

valence: ignoring the sea and gluon (which is probably reasonable at $x \approx 1$), $n_s = 2$, giving $(1-x)^3$;

sea: if one of a $\mathrm{q\bar{q}}$ pair is struck near $x = 1$, $n_s = 4$ giving $(1-x)^7$, on the other hand if $\mathrm{q\bar{q}} \to \mathrm{g}$ is regarded as the primary process then $n_s = 3$ giving $(1-x)^5$

gluon: the γ^* cannot interact directly with a gluon but if the idea is extended to general partonic interactions then $n_s = 3$ in this case, giving $(1-x)^5$.

For the valence quarks the behaviour as $x \to 1$ can also be related to that of the nucleon elastic form-factor, through the Drell-Yan-West relation, details are given in [Clo79,Sec.10.2].

Non-perturbative models of various sorts have also been applied to predict or limit the form of the parton densities. Some are based on statistical mechanics ideas: for example, making use of the constraint that Fermi-Dirac statistics gives for two identical (valence) quarks in the nucleon. A few attempts have been made to use the large N_c chiral Lagrangian approach to large distance QCD. In principle QCD lattice calculations should be able to say something about at least the low moments of the structure functions. A brief survey of some of thses ideas is given in [Coo98, Sec.6.3] where further references may be found.

In fact in most cases when QCD fits are performed to extract the parton densities all the parameters are varied and only general constraints such as the various sum rules are applied.

4.4 DGLAP evolution at LO

In this section some simple features of the Q^2 evolution predicited by the DGLAP equations are examined. The form of the input distribution is restricted to a non-singular function of the form $x(1-x)^3$.

4.4.1 Valence quark evolution

The DGLAP evolution equation for a valence quark density (or more generally a non-singlet density) is

$$\frac{\partial q^{NS}(x, Q^2)}{\partial \ln Q^2} = \frac{\alpha_S}{2\pi}[q^{NS} \otimes P_{qq}].$$

Substituting the LO expression for $P_{qq}^{(0)}$ gives

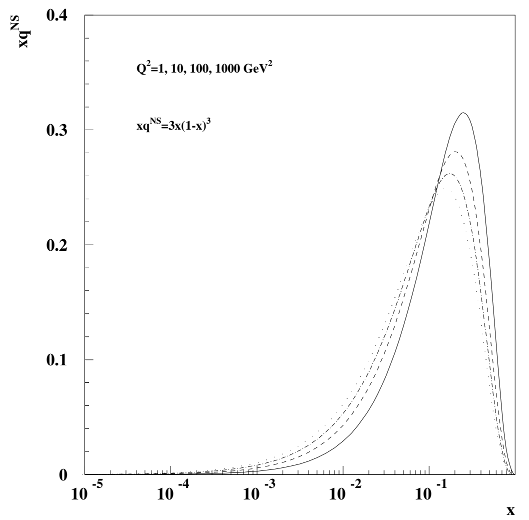

Fig. 4.6 Evolution of non-singlet valence like quark distribution with the LO DGLAP equation. Full line input distribution at $Q^2 = 1\,\mathrm{GeV}^2$, dashed $Q^2 = 10\,\mathrm{GeV}^2$, dot-dashed $Q^2 = 100\,\mathrm{GeV}^2$, dotted $Q^2 = 1000\,\mathrm{GeV}^2$,

$$\frac{\partial q^{NS}(x,Q^2)}{\partial \ln Q^2} = \frac{2\alpha_S}{3\pi}\int_x^1 \frac{dz}{z} q^{NS}(x/z,Q^2)\left[\frac{(1+z^2)}{(1-z)_+} + \frac{3}{2}\delta(1-z)\right] \quad (4.41)$$

where α_S means $\alpha_S(Q^2)$. The first term is integrated using

$$\int_x^1 \frac{f(z)}{(1-z)_+}dz = \int_x^1 \frac{dz}{1-z}[f(z)-f(1)] + f(1)\ln(1-x)$$

with $f(z) = \frac{1+z^2}{z} q^{NS}(x/z,Q^2)$, to give the expression

$$\begin{aligned}\frac{\partial q^{NS}(x,Q^2)}{\partial \ln Q^2} &= \frac{2\alpha_S(Q^2)}{3\pi}\Big\{\big[\frac{3}{2} + 2\ln(1-x)\big] q^{NS}(x,Q^2) + \\ &\int_x^1 \frac{dz}{1-z}\big[\frac{1+z^2}{z} q^{NS}(x/z,Q^2) - 2q^{NS}(x,Q^2)\big]\Big\}.\end{aligned} \quad (4.42)$$

This equation takes an almost identical form for the NS contribution to $F_2^{NS} = xq^{NS}$

$$\frac{\partial F_2^{NS}(x,Q^2)}{\partial \ln Q^2} = \frac{2\alpha_S(Q^2)}{3\pi}\Big\{\big[\frac{3}{2} + 2\ln(1-x)\big] F_2^{NS}(x,Q^2) +$$

$$\int_x^1 \frac{dz}{1-z}\left[(1+z^2)F_2^{NS}(x/z,Q^2) - 2F_2^{NS}(x,Q^2)\right]\Big\}. \tag{4.43}$$

The term outside the integral multiplying F_2^{NS} is positive for $x < 0.53$, whereas the integral always gives a negative contribution. For typical q^{NS} the two contributions cancel at values $x \approx 0.2 - 0.3$ and are positive at smaller x and negative at larger x. The confirmation of Bjorken scaling for $x \approx 0.2 - 0.3$ in the early SLAC experiments was almost fortuitous. This result also shows that the scaling violations for a typical valence quark momentum distribution will be small. Fig. 4.6 shows the LO evolution of $xq^{NS}(x) = 3x(1-x)^3$ from a starting scale of $Q_0^2 = 1\,\mathrm{GeV}^2$ to $Q^2 = 10, 100, 1000\,\mathrm{GeV}^2$.[4] The momentum distribution becomes smeared slightly more towards lower x values as Q^2 increases, but the effect is very small.

4.4.2 Singlet and gluon evolution

The evolution of the singlet and gluon densities are both more complicated and more interesting as they are coupled. The singlet quark density is

$$\Sigma(x,Q^2) = \sum_i (q_i(x,Q^2) + \bar{q}_i(x,Q^2))$$

and coupled evolution equations are

$$\frac{\partial}{\partial \ln Q^2}\Sigma(x,Q^2) = \frac{\alpha_S(Q^2)}{2\pi}\left([\Sigma \otimes P_{qq}] + [g \otimes 2n_f P_{qg}]\right) \tag{4.44}$$

$$\frac{\partial}{\partial \ln Q^2}g(x,Q^2) = \frac{\alpha_S(Q^2)}{2\pi}\left([\Sigma \otimes P_{gq}] + [g \otimes P_{gg}]\right) \tag{4.45}$$

Although the LO splitting functions take rather simple forms, the coupled nature of the singlet equations makes it difficult to solve them analytically. Instead the nature of the solutions are explored with some simple numerical examples. Fig. 4.7 shows the evolution of the singlet and gluon distributions for two cases, both with 'valence like' inputs at $Q_0^2 = 1\,\mathrm{GeV}^2$. The full curves are for singlet input only, so $x\Sigma(x) = 3x(1-x)^3$ and $xg(x) = 0$. The dashed curves correspond to gluon input only, so $x\Sigma(x) = 0$ and $xg(x) = 3x(1-x)^3$. Both input distributions have a maximum value of 0.32 at $x = 0.25$. For the singlet input, already by $Q^2 = 10\,\mathrm{GeV}^2$, the $1/z$ factors in the gluon splitting functions P_{gq} and P_{gg} are having an effect not only on the gluon density but through the coupled evolution on the singlet term as well. By $Q^2 = 1000\,\mathrm{GeV}^2$ the values of $x\Sigma$ and xg at $x = 10^{-5}$ are 1.2 and 7.4 respectively. With gluon only input the effect is even larger at small x. At $Q^2 = 1000\,\mathrm{GeV}^2$ and $x = 10^{-5}$, the values of $x\Sigma$ and xg

[4] The numerical DGLAP evolutions in this chapter have been performed using the QCDNUM code of Botje [Bot97].

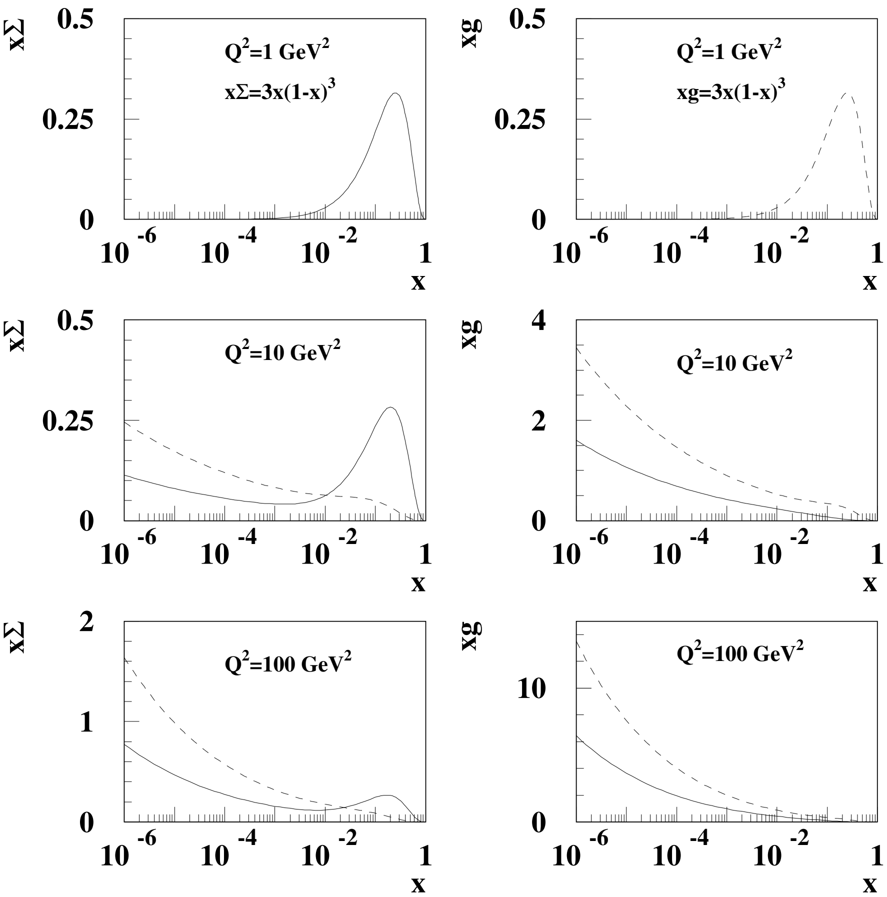

Fig. 4.7 Evolution of the gluon and singlet quark momentum distributions with the LO DGLAP equation. The full curves are for a 'valence like' singlet input distribution at $Q^2 = 1\,\mathrm{GeV}^2$ and the dashed curves for a 'valence like' gluon input distribution at $Q^2 = 1\,\mathrm{GeV}^2$. The input distributions are shown in the top two plots.

are 2.5 and 15.1 respectively. Note that in both cases the gluon density rapidly takes on a form peaked at low x almost independent of shape of input distributions and whether it was a singlet or gluon contribution.

4.5 DGLAP and the OPE

For future reference it will be useful to establish the connection between the DGLAP equations and the OPE approach. For DIS, the key OPE result from Sec. 3.4 is the factorisation at leading twist of the structure function moments, Eq. 3.49 and repeated here

$$\int_0^1 dx'\, x'^{n-1} W(q^2, x') = C_n^{NS}(Q^2/\mu^2, \alpha_S)\bar{N}_n(\mu^2)/4 + O(1/Q^2). \quad (4.46)$$

The label NS has been added as a reminder that this simple form is for a non-singlet structure functions. Writing the arguments of C_n^{NS} as $Q^2, \mu^2 \to Q^2/\mu^2, \alpha_S$, the Q^2 dependence of C_n^{NS} is given by the solution of the appropriate renormalisation group equation with a form similar to Eq. 3.38 (except that the mass dimension $D = 0$)

$$C_n^{NS}(Q^2/\mu^2, \alpha_S) = C_n^{NS}(1, \alpha_S(\mu^2)) \exp\left(\int_0^t dt' \gamma_{NS}(n, t')\right), \quad (4.47)$$

where $t = \ln(Q^2/\mu^2)$. The matrix element $\bar{N}_n(\mu^2)/4$ is now identified with the nth moment of the parton density at scale μ^2, $\tilde{q}_f(n, 0)$, where

$$\tilde{q}_f(n, t) = \int_0^1 dx\, x^{n-1} q_f(x, Q^2).$$

Defining $M_n(Q^2) = \int_0^1 dx'\, x'^{n-1} W(q^2, x')$. Eq. 4.46 becomes

$$M_n(Q^2) = C_n^{NS}(1, \alpha_S(\mu^2))\tilde{q}_f(n, t), \quad (4.48)$$

where

$$\tilde{q}_f(n, t) = \tilde{q}_f(n, 0) \exp\left(\int_0^t dt' \gamma_{NS}(n, t')\right). \quad (4.49)$$

The Q^2 dependence from $C_n^{NS}(Q^2/\mu^2, \alpha_S)$, given by the anomalous dimension $\gamma_{NS}(n, t)$, has been transferred to the the parton density moment. If $\gamma_{NS}(n, t)$ is expanded as a power series in α_S,

$$\gamma_{NS}(n, t) = \gamma_{NS}^{(0)}(n)\frac{\alpha_S(t)}{2\pi} + \ldots$$

the differential form of 4.49 becomes, at LO,

$$\frac{\partial \tilde{q}_f(n, t)}{\partial t} = \frac{\alpha_S(t)}{2\pi}\gamma_{NS}^{(0)}(n)\tilde{q}_f(n, t). \quad (4.50)$$

This equation should have the same physics content as the non-singlet DGLAP evolution given by Eq. 4.35. Taking moments of NS DGLAP equation one finds that the anomalous dimensions [5] are the moments of the DGLAP splitting function

[5]Definitions of the anomalous dimensions differ by factors of π and overall sign. Here we follow the conventions of [Ell96]. The LO anomalous dimensions are collected in the appendix to this chapter.

$$\gamma_{NS}^{(0)}(n) = \int_0^1 dz\, z^{n-1} P_{NS}^{(0)}(z). \qquad (4.51)$$

Finally $C_n^{NS}(1, \alpha_S(Q^2))$ is identified with the nth moment of the DGLAP coefficient function.

The OPE equations for the singlet and gluon contributions are more complicated as they mix. The evolution of the corresponding singlet and gluon moments is given by a set of coupled equations with a 2×2 matrix of anomalous dimensions γ_{qq}, γ_{qg}, γ_{gq}, γ_{gg} which mirrors the form of the coupled DGLAP equations (4.32, 4.33)

$$\begin{aligned} \frac{\partial \Sigma(n,t)}{\partial t} &= \gamma_{qq}(n,t)\Sigma(n,t) + 2n_f \gamma_{qg}(n,t) g(n,t) \\ \frac{\partial g(n,t)}{\partial t} &= \gamma_{gq}(n,t)\Sigma(n,t) + \gamma_{gg}(n,t) g(n,t), \end{aligned}$$

where γ_{qq} etc are expanded in powers of α_S and the coefficients related to the moments of the corresponding splitting functions as in Eq. 4.51. Note that the evolution equations for the moments of parton densities are first order differential equations without convolutions. This provides a very efficient numerical method for solving the DGLAP equations.

Mathematically the various moments (of structure functions, parton densities, etc.) are *Mellin* transforms. The OPE equations are for even-n moments of crossing symmetric structure functions and odd-n moments for crossing anti-symmetric ones. The other moments have to found by analytic continuation in n space. Once all the moments have been determined, the parton densities or structure functions are calculated by inverting the Mellin transformation. This is done formally by a contour integral

$$V(x,t) = \frac{1}{2\pi i} \int_C dn\, x^{-n} V(n,t)$$

where $V(x,t)$ is a parton density or structure function and the contour C runs parallel to the imaginary axis and is to the right of the right-most singularity of $V(n,t)$ in complex n-space. Usually the integral can only be performed numerically. Through the evolution equations the position of the right-most singularity will depend on the n-space singularity structure of both the anomalous dimension and $\tilde{q}_f(n,0)$ the moment of the parton density at the starting scale μ^2.

4.6 Higher Twist

The OPE analysis of DIS structure functions shows that they can be written as power series in $(1/Q^2)^{\tau/2-1}$ (Eq. 3.48) where τ is the twist of the corresponding operator and the coefficients have logarithmic Q^2 dependence. At leading twist $\tau = 2$ and the only Q^2 dependence is from the coefficients. This agrees with the DGLAP approach as outlined in the previous section.

The outline for a systematic approach to higher twist terms was given by Ellis *et al.* [Ell83], but to date there are only incomplete calculations. At large x 4-quark operator terms will probably be the most important and some details of early estimates are given in [Rob90,Ch. 6]. Recently there have been some estimates using renormalon techniques.[6]

Higher twist contributions are likely to be non-negligible at large x and lowish Q^2, which corresponds to a low $\gamma^* p$ CM energy W. In the absence of calculations, groups fitting the data have taken a pragmatic approach with a modification to the structure function of the form

$$F_i^{HT}(x, Q^2) = F_i^{QCD}(x, Q^2)[1 + H(x)/Q^2],$$

where F_i^{QCD} is the twist 2 QCD prediction and $H(x)$ is either a constant for each x bin in the data sample or paramterised as a low order polynomial in x with the coefficients determined from the fit. At the rather low ep energies, with low Q^2 and large x, of the early fixed target experiments some higher twist contributions have a known origin. They come from the neglect of $O(m^2/Q^2)$ terms in the expressions for the kinematic variables - so called 'target mass' corrections. Sometimes these are taken into account by modifying the scaling variable x

$$x \to \xi = \frac{2x}{1+r} \quad \text{where} \quad r = \sqrt{1 + \frac{4m^2x^2}{Q^2}},$$

with the remaining 'dynamic higher twist' contribution parameterised as above. Figure 4.8 shows some results on higher twist terms at fixed target energies. The data points are the fitted constants in x bins from the analysis of SLAC and BCDMS data by Virchaux and Milsztajn [Vir92]. The curves are from the renormalon calculation of Dasgupta and Webber [Das96] which shows that the higher twist terms for the EM structure function F_2 (full line) are positive at all x whereas those for the parity violating structure function in neutrino scattering xF_3 (dashed line) are positive only at the largest x values. In all cases the contributions are small except at the very largest x values.

Apart from parameterising the higher twist effects at large x, one may reduce their significance by applying cuts on Q^2 and W^2, for example $Q^2 > 4\,\mathrm{GeV}^2$ and $W^2 > 10\,\mathrm{GeV}^2$. More will be said about this in Chap. 10 where the use the leading twist NLO QCD formalism to extract parton densities is discussed in detail.

In addition to the possible effects of higher twist at large x, there may also be non-negligible effects at very low x. This will be touched on briefly in Chap. 6.

[6]The renormalon method allows one to sum certain classes of multiloop insertions in Feynman diagrams and it has been used to estimate $1/Q$ corrections to event shape variables in both e^+e^- annihilation and ep scattering. More details are given in Chap. 8.

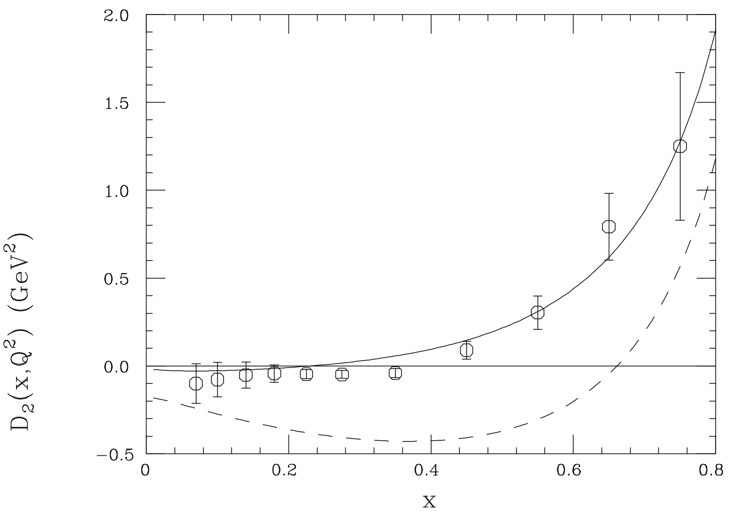

Fig. 4.8 The data points show the higher twist contribution to F_2 from an analysis of SLAC and BCDMS data by Virchaux and Milsztajn and the curves ar renormalon predictions for F_2 (full line) and xF_3 (dashed line) - from [Das96].

4.7 Heavy quarks

At the x and Q^2 values probed at HERA heavy quarks may contribute up to 30% of the structure function F_2. The most important mechanism for heavy quark production in DIS is through the BGF process, although it is still an open question whether or not there is a small intrinsic heavy $q\bar{q}$ component in the nucleon's wave function. Apart from the physics interest, the introduction of massive quarks requires an extension of the DGLAP formalism discussed so far. First the impact on the running of α_S is considered, then a brief summary of the approaches for heavy flavours is given together with an outline of the BGF process for massive quarks and a discussion of why the extension of the formalism is not straightforward.

4.7.1 Matching prescriptions for α_S

There are no mass terms in the expansion of the β function given in Eq. 3.29 but n_f will change by one unit when a quark threshold is crossed. In the renormalisation schemes that are commonly used in DIS, it is conventional to use the massless expressions for the b_i and put all the terms depending on m_Q^2/μ^2 into the coefficient functions. In addition one needs a prescription for taking α_S across a threshold – or equivalently changing Λ_{QCD}. There is no unique solution and it is important to check which method is being used in a particular calculation. Some of the more frequent choices are:

- Define $\alpha_S^{(5)}(\mu^2)$ to be the numerical solution of the RG equation to a given order (eg Eq. 3.31) with $n_f = 5$ in terms of the reference value

$\alpha_S(M_Z^2)$. Then $\alpha_S^{(5)}(m_b^2)$ is also known. For $m_c^2 < \mu^2 < m_b^2$, $\alpha_S^{(5)}(m_b^2)$ is used as the new reference value for the numerical solution of the RG equation with $n_f = 4$ to give $\alpha_S^{(4)}(\mu^2)$ and in particular $\alpha_S^{(4)}(m_c^2)$. For $\mu^2 < m_c^2$, $\alpha_S^{(4)}(m_c^2)$ is used, in turn, as the new reference value for the RG equation with $n_f = 3$ to give $\alpha_S^{(3)}(\mu^2)$. Thus the value of α_S for any $\mu^2 < M_Z^2$ is known. This procedure is not difficult to implement numerically.

- The parameterisations of α_S in terms of Λ_{QCD} are convenient but less well defined. At a threshold Λ will change to reflect the change in n_f, but this is clumsy. A better method is to exploit the freedom in the definition of Λ to introduce an extra constant that is used to fix the matching of α_S at a threshold. For simplicity the procedure will be outlined using the LO expressions. Using the freedom in the choice of Λ, rewrite Eq. 3.25 as

$$[\alpha_S(\mu^2, n_f)]^{-1} = b_0(n_f)\ln(\mu^2/\Lambda^2) + C(n_f)$$

where $C(n_f)$ is a constant to be determined and Λ is independent of n_f. At a threshold the values of α_S must match, $\alpha_S(m_Q^2, n_f) = \alpha_S(m_Q^2, n_f + 1)$. Define Λ to be that for $n_f = 4$ so that $C(4) = 0$, then $\alpha_S(m_c^2, 3) = \alpha_S(m_c^2, 4)$ fixes

$$C(3) = b_0(4)\ln(m_c^2/\Lambda^2) - b_0(3)\ln(m_c^2/\Lambda^2) = -\frac{1}{6\pi}\ln(m_c^2/\Lambda^2) \quad (4.52)$$

similarly $\alpha_S(m_b^2, 4) = \alpha_S(m_b^2, 5)$ fixes $C(5)$. With more complicated expressions the same procedure may be applied to the NLO expressions. In both LO and NLO, this choice of matching gives convenient expressions for numerical evaluation.

- Although in both the previous examples the matching condition is applied at $\mu^2 = m_Q^2$, this is also arbitrary and sometimes $4m_Q^2$ is preferred. Beyond NLO the matching becomes yet more complicated and α_S itself may not necessarily be continuous at a threshold. The subject has been studied in detail by Bernreuther (Bernreuther [Ber83]) and a prescription based on his work is recommended by the particle data group. At the centre of the analysis by Bernreuther is the process independent relation between $\alpha_S^{(-)}$, the coupling for $n_f - 1$ light quark flavours, and α_S, the coupling for the full theory with an additional heavy quark,

$$\alpha_S^{(-)}(\mu^2) = \alpha_S(\mu^2)\left(1 + \sum_{k=1}^{\infty} C_k(x)\left(\frac{\alpha_S(\mu^2)}{\pi}\right)^k\right)$$

where $x = \ln(m_Q^2(\mu^2)/\mu^2)$ and $m_Q^2(\mu^2)$ is the running heavy quark mass. The above relation is considerably simplified by choosing the scale $\mu^2 = m_Q^2(\mu^2)$, so that $x = 0$. For $\overline{\text{MS}}$ it is

$$\alpha_S^-(m_Q^2) = \alpha_S(m_Q^2) + 7\alpha_S^3(m_Q^2)/72\pi^2.$$

Full details on how to match the Λ parameters are given by Bernreuter. The numerical differences between α_S calculated by the different prescriptions at NLO and beyond are small, although the differences between Λ parameters can be quite large.

4.7.2 Heavy quark production in DIS

For simplicity the possibility of intrinsic charm in the proton is ignored and $\bar{c}(x, Q^2) = c(x, Q^2)$ is assumed throughout this section. The most frequent approaches to the inclusion of heavy quarks (eg charm of mass m_c) within the DGLAP framework are:

- ZM-VFNS (zero-mass variable flavour number scheme) in which the charm parton density $c(x, Q^2)$ satisfies $c(x, Q^2) = 0$ for $Q^2 \leq \mu_c^2$ and $n_f = 3 + \theta(Q^2 - \mu_c^2)$ in the splitting functions and β function. The threshold μ_c^2, which is in the range $m_c^2 < \mu_c^2 < 4m_c^2$, is chosen so that $F_2^c(x, Q^2) = 2e_c^2 x c(x, Q^2)$ gives a satisfactory description of the data and α_S is matched by one of the prescriptions described in the previous section. The advantage of this approach is that the simplicity of the massless DGLAP equations is retained. The disadvantage is that the physical threshold $\hat{W}^2 = Q^2(\frac{1}{z} - 1) \geq 4m_c^2$ is not treated correctly ($\hat{W}$ is the $\gamma^* g$ CM energy).
- FFNS (fixed flavour number scheme) in which there is no charm parton density and all charmed quarks are generated by the BGF process. The advantage of the FFNS scheme is that the threshold region is correctly handled, but the disadvantge is that large $\ln(Q^2/m_c^2)$ terms appear and charm has to be treated ab initio in each hard process.
- VFNS (variable flavour number scheme) in which F_2^c is calculated by interpolating between the FFNS approach at low Q^2 and the ZM-VFNS scheme for large Q^2. The goal here is to combine the correct features of the FFNS scheme near threshold with the appearance of a charm parton density at large Q^2.

The essence of the problem may be understood by looking at the full expression for F_2^c in the FFNS at order α_S

$$F_2^c(x, Q^2) = 2\int_x^1 \frac{dz}{z} x g_3(x/z, \mu^2) C_g^{FF}(z, m_c^2/Q^2, \mu^2) \tag{4.53}$$

where g_3 is the gluon density for 3 light quark flavours (u,d,s). At LO the scale μ^2 is not fixed, the obvious choice is $\mu^2 = Q^2$. However Glück *et al.* [Glu94] have argued that $\mu^2 = 4m_c^2$, the threshold for charm pair production, is more appropriate. Expanding the massive FF coefficient function gives

$$C_g^{FF}(z, m_c^2/Q^2, \mu^2) = \frac{\alpha_S(\mu^2)}{2\pi} e_c^2 C_g^{1,FF}(z, m_c^2/Q^2) + \ldots,$$

with

$$C_g^{1,FF}(z, m_c^2/Q^2) =$$
$$\frac{1}{2}\left\{ \left[z^2 + (1-z)^2 + \frac{4m_c^2}{Q^2}z(1-3z) - 8z^2(\frac{m_c^2}{Q^2})^2\right] \ln\left(\frac{1+\beta}{1-\beta}\right) \right.$$
$$\left. + \left[8z(1-z) - 1 - \frac{4m_c^2}{Q^2}z(1-z)\right]\beta \right\} \theta(\hat{W}^2 - 4m_c^2), \tag{4.54}$$

where β is the velocity of the charm quark and $\beta^2 = 1 - 4m_c^2/\hat{W}^2$. Note that the θ function guarantees correct threshold behaviour. For $Q^2 \gg m_c^2$, $\beta \to 1$ and

$$\frac{1+\beta}{1-\beta} \to \frac{Q^2}{m_c^2}\frac{1-z}{z}$$

so

$$C_g^{1,FF}(z, m_c^2/Q^2) \quad \to \quad \frac{1}{2}\left\{ [z^2 + (1-z)^2] \ln\left(\frac{1-z}{z}\right) + 8z(1-z) - 1 \right.$$
$$\left. + [z^2 + (1-z)^2] \ln\left(\frac{Q^2}{m_c^2}\right) \right\}. \tag{4.55}$$

The first two terms in the above expression are the same as the gluon coefficient function C_g^1 (Eq. 4.38) of the massless DGLAP formalism. It is the last term with the $\ln(Q^2/m_c^2)$ that is the problem. Comparing the above expressions with Eq. 4.15 and the discussion preceeding it for the massless BGF case, one sees that m_c^2 is replacing the infrared cutoff κ^2 in the integration over p_t^2. Since m_c^2 is non-zero the heavy quark contribution is finite. For massless partons in the DGLAP framework the large infrared logs are absorbed by the renormalisation of the parton density at the factorisation scale and the large Q^2 logs are resummed by the renormalisation group procedure. Although the massive BGF coefficient functions have been calculated to NLO, they are not available for an all orders resummation. It is of course precisely this problem that the ZM-VFNS scheme solves, but at the price of incorrect thresold behaviour.

Generically in VFNS schemes one has

$$F_2^c(x, Q^2) =$$
$$2e_c^2 \int_x^1 dz \frac{x}{z} \left[c(x/z, \mu^2) C_q^{VF}(z, Q^2/\mu^2) + g_4(x/z, \mu^2) C_g^{VF}(z, Q^2/\mu^2)\right],$$

where c and g_4 are charm parton and gluon densities for 4 flavours (u,d,s,c) and the coefficent functions have the expansions

$$C_q^{VF} \quad = \quad C_q^{0,VF} + \frac{\alpha_S}{2\pi} C_q^{1,VF} + \ldots$$

$$C_g^{VF} \quad = \quad \frac{\alpha_S}{2\pi} C_g^{1,VF} + \ldots.$$

For $Q^2 < m_c^2$ the coefficient functions and parton densities are those of the FF scheme given by Eq. 4.53 and for $Q^2 \gg m_c^2$ they should tend to the massless DGLAP forms given in Eqs 4.36 to 4.38. At a scale in the vicinity of m_c^2 the FF and VFNS expressions are matched with expressions of the form [Buz96]

$$\begin{aligned} c(x, \mu^2) &= A^{cg}(\mu^2/m_c^2) \otimes g_3(\mu^2) \\ g_4(x, \mu^2) &= A^{gg}(\mu^2/m_c^2) \otimes g_3(\mu^2) \\ C_b^{VF}(z, Q^2/\mu^2) &= C_a^{FF}(Q^2/\mu^2) \otimes \left[A^{ba}(\mu^2/m_c^2\right]^{-1}, \end{aligned} \tag{4.56}$$

where A^{cg} etc are elements of a complete 5×4 coefficient matrix matching the 3 and 4 massless flavour (plus gluon) parton densities. At order α_S the first two of these equations take the form (with $\mu^2 = Q^2$)

$$\begin{aligned} c(x, Q^2) &= \frac{\alpha_S}{2\pi} \ln\left(\frac{Q^2}{m_c^2}\right) P_{qg}^{(0)} \otimes g_3 \\ g_4(x, Q^2) &= \left(1 - \frac{\alpha_S}{6\pi} \ln\left(\frac{Q^2}{m_c^2}\right)\right) g_3(x, Q^2) \end{aligned} \tag{4.57}$$

and matching the coefficient functions gives

$$\begin{aligned} &C_g^{1,FF}(z, Q^2/m_c^2) = \\ &\qquad C_g^{1,VF}(z, Q^2/m_c^2) + C_q^{0,VF}(z, Q^2/m_c^2) \otimes P_{qg}^{(0)} \ln\left(\frac{Q^2}{m_c^2}\right). \end{aligned} \tag{4.58}$$

In addition α_S for 3 and 4 massless flavours has to be matched. If $C_q^{0,VF}$ is known then Eq. 4.58 serves as a definition of $C_g^{1,VF}$. In two versions of VFNS schemes (ACOT [Aiv94] and MRRS [Mar98a]), $C_q^{0,VF}$ takes the form

$$C_q^{0,VF}(z, Q^2/m_c^2) = z\delta\big(z - 1/(1 + m_c^2/Q^2)\big)\big(1 + 4m_c^2/Q^2\big).$$

The two schemes differ in how the parton densities are evolved, ACOT assumes standard massless DGLAP evolution and MRRS modifies the $P_{qg}^{(0)}$ splitting function to include some mass terms. Neither approach is regarded as completely satisfactory, as the choice of $C_q^{0,VF}$ gives rather too sudden a 'switching on' of the charm parton contribution [Rob98a]. Roberts and Thorne [Rob98b] argue that a more physically acceptable scheme is possible by the addition of an extra matching condition which fixes $C_q^{0,VF}$. The additional condition is to require that $dF_2^c/d\ln Q^2$ also matches smoothly. Matching at m_c^2 simplifies the resulting condition which is

$$C_q^{0,VF}(Q^2/m_c^2) \otimes P_{qg}^{(0)} = \frac{\partial C_g^{1,FF}(z, Q^2/m_c^2)}{\partial \ln Q^2}. \tag{4.59}$$

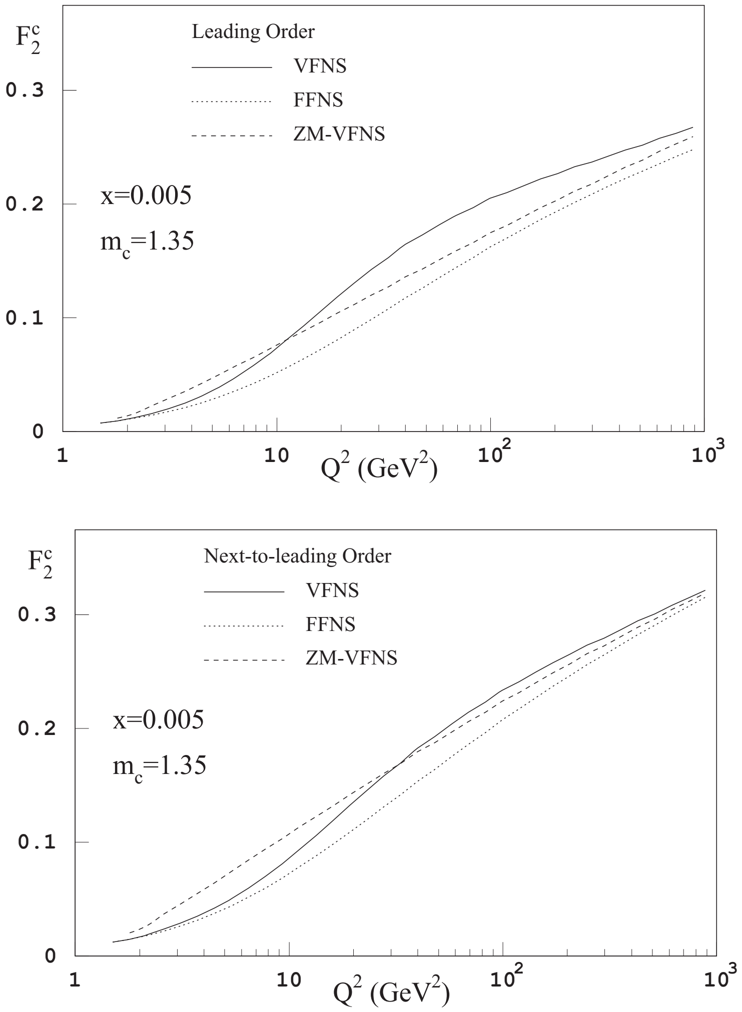

Fig. 4.9 F_2^c at LO and NLO from the VFNS scheme of Roberts and Thorne [Rob98b].

The RHS of this equation may be found by direct differentiation of Eq. 4.54 and in the limit of large Q^2 it tends to $P_{qg}^{(0)}(z)$. Using the extra condition Eq. 4.58 becomes

$$C_g^{1,VF}(z,Q^2/m_c^2) = C_g^{1,FF}(z,Q^2/m_c^2) - \frac{\partial C_g^{1,FF}(z,Q^2/m_c^2)}{\partial \ln Q^2} \ln\left(\frac{Q^2}{m_c^2}\right). \tag{4.60}$$

This equation has a number of virtues, it gives $C_g^{1,VF}$ the same threshold behaviour as $C_g^{1,FF}$ (by construction) and the second term removes the $P_{qg}^{(0)}\ln(Q^2/m_c^2)$ term from $C_g^{1,FF}$ at large Q^2 to leave the correct massless coefficient function. The disadvantage is that the general solution of equation 4.59 is not easily found. However what is actually required is the convolution $C^{0,VF}\otimes c$ and this has been calculated. The procedure has been extended to NLO and also for F_L. In all cases it produces a very satisfactory and smooth interpolation between the FFNS near threshold and the zero mass evolution at large Q^2. This is shown in Figure 4.9 for F_2^c at $x = 0.005$ as a function of Q^2. Although the VFNS scheme of Roberts and Thorne is satisfactory, it is not the only possibility. Some of the other possibilities are summarised by Krämer *et al.* [Kra00] and Smith [Smi00]. What is clear is that there has been a significant improvement in the handling of heavy flavours in DIS and both the ACOT and Roberts-Thorne VFNS schemes have been used successfully in global fits to extract parton densities. It will be some time before the data on F_2^c is precise enough to discriminate between the different schemes.

4.8 Beyond NLO

As data on hard scattering processes get more precise the theoretical uncertainties from having to work at NLO may become comparable to the experimental systematic uncertainties. The usefulness of parton densities extracted from such processes, for example for calculating standard model cross-sections at the LHC, may be comprised by the resulting level of combined uncertainty. It is thus important to extend the hard-scattering formalism beyond NLO. This is most advanced for DIS, but still incomplete. As summarised by van Neerven and Vogt [vNe00a,b], the QCD β function is known to NNNLO, the two-loop coefficient functions for DIS are known at NNLO, but the three-loop splitting functions ($P_{ij}^{(2)}$) are incomplete. For $P_{NS}^{(2)}$ one has: the first six even-integer moments for the '+' combination (see Eq. 4.34); the first six odd-integer moments for the '$-$' combination; the complete contribution to both combinations from the term proportional to n_f^2 and the leading $\ln^4 x$ terms. For the singlet splitting functions on has: the first six even-integer moments; the $C_A n_f^2$ contribution to $P_{gg}^{(2)}$; the leading $\ln x/x$ terms for all except $P_{gq}^{(2)}$. The NNLO moment calculations are from the systematic studies of Vermaseren and colleagues [Moc00]. van Neerven and Vogt have taken the available information and derived approximations for the complete NNLO splitting functions. First the n_f dependence is made explicit by writing

$$P^{(2)} = P_0^{(2)} + n_f P_1^{(2)} + n_f^2 P_2^{(2)}$$

then each term is expanded in terms of a set of basis functions $\{f_n(x)\}$

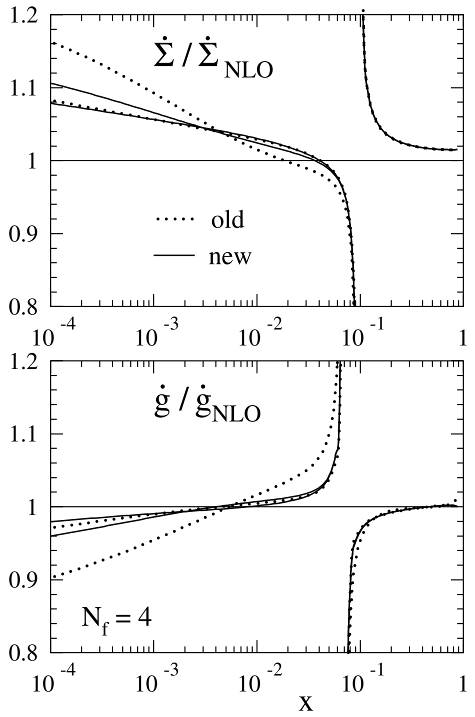

Fig. 4.10 NNLO singlet (Σ) and gluon (g) contributions relative to NLO terms (from [vNe00b]). The solid curves show the extreme variations (A and B) of the most recent parameterisations. The dotted curves refer to an earlier version valid only to $x = 10^{-3}$.

$$P_m^{(2)}(x) = \sum_{n=1}^{n_m} A_n f_n(x) + f_e(x)$$

where $n_m = 5$, (4) for non-singlet (singlet) and the A_n are determined from the known moments. The function f_e takes care of the other constraints given above. The uncertainties in the full $P_{ij}^{(2)}$ are then estimated by 'reasonable' variation in the choice of basis functions. Using the ensemble of approximate functions, two (labelled A and B) are chosen to the give the extremes in variation. The differences can be quite large at small x and show oscillations at larger x, however when the splitting functions are convoluted with a typical parton density function the latter are smoothed out. To estimate the effect of the NNLO terms on parton evolution the authors calculate the derivatives $\dot{q} \equiv d \ln q / d \ln \mu_f^2$, $q = q_{\rm NS}^+, \Sigma, g$, at a reference scale $\mu_{f,0}^2 = 30$ GeV^2 corresponding to $\alpha_s(\mu_r^2 = \mu_{f,0}^2) = 0.2$. Typical input parton densities at $\mu_{f,0}^2$ are taken to be $xq_{\rm NS}^+ = x^{0.5}(1-x)^3$,

$$x\Sigma = 0.6\,x^{-0.3}\,(1-x)^{3.5}(1+5\,x^{0.8}) \quad \text{and} \quad xg = 1.0\,x^{-0.37}(1-x)^5.$$

Results for the singlet and gluon are shown in Fig. 4.10. The NNLO parameterisations are shown as solid lines from the two extreme cases (A and B). The uncertainties in the calculation (difference between the A and B curves) are negligible for $x > 0.1$ and less than 2% for x larger than a value of about 10^{-4}. Scale uncertainties are also significantly reduced. The dotted curves show an earlier version of the approximations, valid to $x = 10^{-3}$, calculated before the highest moments were known. The uncertainty at the lowest x values does increase as the μ_f^2 scale decreases below $10\,\mathrm{GeV}^2$ to roughly 4% by $3\,\mathrm{GeV}^2$. In the same papers referred to above the authors provide compact approximations to the coefficient functions. They also note that the quark coefficient functions contain large soft gluon emission contributions giving a larger change in the structure function than the NNLO term in the splitting function for $x > 0.01$. For very large $x > 0.8$, it will probably be necessary to use the results of soft-gluon resummation, see [Rob90,Sec.6.2] for details and [Vog99] for more recent calculations. The impact of the NNLO contributions on the determination of parton densities will be taken up in Chapter 10.

4.9 Summary

This chapter has given an account of the QCD improved parton model, which is the paradigm for how perturbative QCD may be used to calculate hard scattering processes. The crucial insight, which is underpinned by the factorisation theorems based on the operator product expansion, is that a hard scattering cross-section can be separated into a calculable process dependent part and universal non-perturbative parton densities. The exposition has concentrated on the physical processes of gluon radiation and $\mathrm{g} \to \mathrm{q\bar{q}}$ leading to the DGLAP equations at LO and NLO for the Q^2 evolution of parton densities. The relation of the DGLAP equations to the more formal approach of the OPE has been outlined and a brief account of higher twist terms given. The problem and some practical approaches to including heavy flavours with the DGLAP formalism have been summarised. Finally the prospects for going beyond NLO have been outlined.

4.10 questions

1. Using the Feynman rules for QED, calculate the $\gamma^*\mathrm{q}$ cross-sections given in Eqs 4.3. Start from the matrix element

$$iee_q\varepsilon_\mu\bar{u}(p')\gamma^\mu u(p) \qquad \text{for}\gamma^*(q)\mathrm{q}(p) \to \mathrm{q}(p'),$$

   where $p' = q + p$.
2. Soft or collinear photon emission kinematics. Consider the process shown in Fig. 4.11(a) an electron of energy p emits a photon with energy zp and transverse momentum q_t ($q_t << p$), leaving an electron

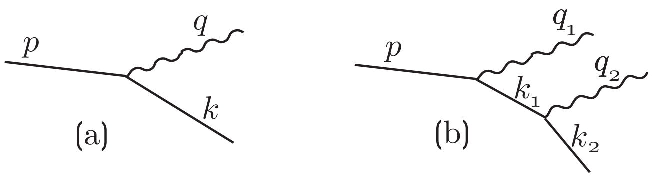

Fig. 4.11 (a) Single soft photon emission. (b) Emission of two soft photons.

with energy $(1-z)p$. At high energies all particles may be taken as massless. One may write

$$p=(p,0,0,p), \quad q=(zp,q_t,0,zp), \quad k=((1-z)p,-q_t,0,(1-zp)$$

with $p^2 = q^2 = k^2 = 0$ to order q_t^2. For cross-section and other calculations that will involve either k or q as a propagator one needs to refine the calculation slightly.

- Real photon emission, electron propagator. Show that writing $q = (zp, q_t, 0, zp - q_t^2/(2zp))$, gives $q^2 = 0$ and $k^2 = -q_t^2/z$ to order q_t^4.
- Real electron emission, photon propagator. Show that writing $q = (zp, q_t, 0, zp + q_t^2/(2(1-z)p))$, gives $k^2 = 0$ and $q^2 = -q_t^2/(1-z)$ to order q_t^4.

Consider next successive emissions of two photons from an electron with the momenta as shown in Fig. 4.11(b). Use arguments similar to the above to show that if $q_1^2 = q_2^2 = 0$, $k_2^2 = -(q_{1t}+q_{2t})^2-(1-z_2)q_{2t}^2/z_2$, where q_{1t}, q_{2t} are the photon transverse momenta (w.r.t. p) and z_2 is the fraction of the energy of electron k_1 carried off by q_2. Hence k_2^2 will only be $O(q_{2t}^2)$ if $q_{1t}^2 << q_{2t}^2$.

3. Matrix element for nearly collinear photon emission. Use the momenta and kinematics of Fig. 4.11(a) and assume the result that at high energies the EM coupling preserves helicity. Consider first the matrix element for $e_L^- \to e_L^- \gamma$ which may be written

$$iM = \overline{u}_L(k)(-ie\gamma_\mu)u_L(p)\varepsilon_T^{*\mu}(q),$$

where $u_L(p) = (1-\gamma_5)u(p)/2$ and $\varepsilon_T^\mu(q)$ are the (transverse) polarisation 4-vectors of the photon. Define the energy fraction z and transverse momentum q_T of the photon as in the previous question. First show that (ignoring masses)

$$u_L(p) \to \sqrt{p}\begin{pmatrix} \xi_- \\ -\xi_- \end{pmatrix}, \quad u_L(k) \to \sqrt{(1-z)p}\begin{pmatrix} \eta_- \\ -\eta_- \end{pmatrix}$$

$$\text{where} \quad \xi_- = \begin{pmatrix} 0 \\ 1 \end{pmatrix}, \quad \eta_- = \begin{pmatrix} \frac{q_t}{2(1-z)p} \\ 1 \end{pmatrix},$$

$$\text{and}\quad \varepsilon_R^\mu = \frac{1}{\sqrt{2}}(0,1,i,-\frac{q_t}{zp}),\quad \varepsilon_L^\mu = \frac{1}{\sqrt{2}}(0,1,-i,-\frac{q_t}{zp}).$$

Show next that the contributions to the matrix element are:

$$\begin{aligned} iM(e_L^- \to e_L^- \gamma_R) &= (-ie)\frac{\sqrt{2(1-z)p}}{z} q_t \\ iM(e_L^- \to e_L^- \gamma_L) &= (-ie)\frac{\sqrt{2(1-z)p}}{z(1-z)} q_t \end{aligned}$$

Parity invariance says that the matrix elements must be the same if all helicities are flipped so one does not need to calculate $e_R^- \to e_R^- \gamma$ separately and the the spin summed and averaged matrix element is

$$\frac{1}{2}\sum_{spins} |M(e^- \to e^- \gamma)|^2 = \frac{2e^2 q_t^2}{z(1-z)}\left[\frac{1+(1-z)^2}{z}\right].$$

4. Nearly collinear pair production $\gamma(q) \to e^+(k_+)e^-(k_-)$. The spin averaged cross-section for this process may be calculated in a similar way to the previous question. For an electron with LH helicity the positron must have RH helicity, because of helicity conservation at the vertex. Then using parity conservation one only needs to calculate the matrix element

$$iM(\gamma \to e_R^+ e_L^-) = \overline{(u)}_L(k_-)(-ie\gamma_\mu)v_R(k_+)\varepsilon_T^\mu(q).$$

Taking the 4-momenta to be

$$q = (q,0,0,q),\quad k_+ = (zq, k_t, 0, zq),\quad k_- = ((1-z)q, -k_t, 0, (1-z)q).$$

show that

$$\begin{aligned} iM(\gamma_L \to e_L^- e_R^+) &= (-ie)\frac{\sqrt{2z(1-z)p}}{z} k_t \\ iM(\gamma_R \to e_L^- e_R^+) &= (+ie)\frac{\sqrt{2z(1-z)p}}{z(1-z)} k_t \end{aligned}$$

and thus

$$\frac{1}{2}\sum_{spins} |M(\gamma \to e^- e^+)|^2 = \frac{2e^2 k_t^2}{z(1-z)}[z^2 + (1-z)^2].$$

5. Processes with soft or collinear radiation. The results of questions 2 to 4 may be used to calculate the factorised forms of the cross-sections for the processes shown in Fig. 4.12. First for (a) in a which a real (soft or collinear) photon is emitted by the electron before it iteracts. The

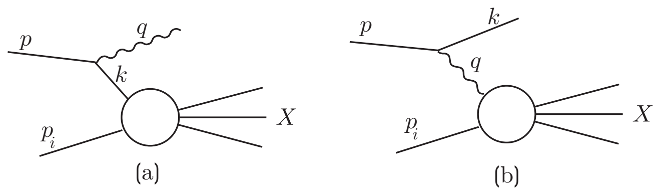

Fig. 4.12 (a) Soft or collinear radiation before scattering. (b) Equivalent photon approximation.

kinematics is as in Q2 for $q^2 = 0,\ k^2 = -q_t^2/z$ and using the formulae given in App. 13.3 one may write

$$\sigma(ep \to \gamma X) = \frac{1}{4pE_i(1+v_i)} \int \frac{d^3q}{(2\pi)^3 2q^0} \times \int d\Pi_X \frac{1}{2} \sum |M(e \to e\gamma)|^2 \left(\frac{1}{k^2}\right)^2 \sum_X |M(ep \to X)|^2,$$

where $\int \Pi_X$ is the final state phase-space for X. Next rewrite the photon phase-space integrand as $d^3q = pdz\pi dq_t^2$, substitute for k^2 and insert the result of Q3 for the $e \to e\gamma$ matrix element squared to get

$$\sigma(ep \to \gamma X) = \int_0^1 dz \int \frac{dq_t^2}{q_t^2} \frac{\alpha}{2\pi} \left[\frac{1+(1-z)^2}{z}\right] \sigma(ep \to X),$$

where

$$\sigma(ep \to X) = \frac{1}{4(1-z)pE_i(1+v_i)} \int d\Pi_X \sum_X |M(ep \to X)|^2.$$

Note that one factor of q_t^2 in the propagator has been cancelled by the q_t^2 from the $e \to e\gamma$ matrix element squared. Finally the integral over the transverse momentum may be performed to give

$$\sigma(ep \to \gamma X) = \int_0^1 dz \frac{\alpha}{2\pi} \ln \frac{\tilde{s}}{\mu^2} \left[\frac{1+(1-z)^2}{z}\right] \sigma(ep \to X),$$

where $\tilde{s}$ is of the order of the ep CM energy squared and μ here would be the electron mass. For a comparison with the parton model, note that the intermediate electron is carrying a fraction $(1-z)$ of the incident electron's energy. Thus a substitution $x = (1-z)$ gives something very similar to the calculation leading to Eq. 4.8 for the probabilty of finding an electron with momentum fraction x in the original electron of

$$p_{ee}(x) = \frac{\alpha}{2\pi} \ln \frac{\tilde{s}}{\mu^2} \left[\frac{1+x^2}{1-x}\right].$$

One must also take into account the case in which no radiation occurs giving $\delta(1-x)$ and regularise the singularity at $x = 1$.

Similarly the cross-section for the process shown in Fig. 4.12(b) may be written

$$\sigma(ep \to eX) = \int_0^1 dz \frac{\alpha}{2\pi} \ln \frac{\tilde{s}}{\mu^2} \left[\frac{1 + (1-z)^2}{z} \right] \sigma(\gamma p \to X),$$

where

$$\sigma(\gamma p \to X) = \frac{1}{4zpE_i(1+v_i)} \int d\Pi_X \sum_X |M(\gamma p \to X)|^2$$

and the intermaediate photon carries a fraction z of the energy of the incident electron. This is the *equivalent photon approximation* of Weizsacker and Williams. One can identify a a probability function $p_{\gamma e}$ similar to P_{gq} of the parton model. Using a similar factorisation of the cross-sections and the matrix elements from Q4 one can also calculate $p_{e\gamma}$ the analog of P_{qg}. The one parton splitting function that cannot be derived using QED results and colour factors is P_{gg}. The reader interested in this approach to the DGLAP equations should consult, for example, [Pes95,Ch.17] for more details.

6. Verify the regularisation of P_{gg}, Eq. 4.27.
7. Strong ordering of p_T^2 in DGLAP, Eq. 4.28 and Fig. 4.5. Consider just the first two gluon emissions as shown in Fig. 4.11. For the DGLAP (leading log approximation) one needs the double collinear limit to give
$$\left(\frac{\alpha}{2\pi}\right)^2 \int_{\mu^2}^{Q^2} \frac{dp_{2t}^2}{p_{2t}^2} \int_{\mu^2}^{p_{1t}^2} \frac{dp_{1t}^2}{p_{1t}^2} = \frac{1}{2} \left(\frac{\alpha}{2\pi}\right)^2 \ln^2 \left(\frac{Q^2}{\mu^2}\right).$$
Using the results of Q2 and Q5 show that the approximations used in calculation of the matrix elements and the propagator will not cancel for the second photon emission unless $q_{1t}^2 << q_{2t}^2$.
8. Using the definition given in Eq. 3.32 for Λ_{QCD} at NLO, find the equivalant condition to that given in Eq. 4.52 for matching α_S at the charm threshold.

4.11 Appendix: LO splitting functions and anomalous dimensions

The LO DGLAP splitting functions are:

$$
\begin{aligned}
P_{qq}(z) &= \frac{4}{3}\left[\frac{1+z^2}{(1-z)_+} + \frac{3}{2}\delta(1-z)\right] \\
P_{qg}(z) &= \frac{1}{2}[z^2 + (1-z)^2] \\
P_{gq}(z) &= \frac{4}{3}\left[\frac{1+(1-z)^2}{z}\right] \\
P_{gg}(z) &= 6\left[\frac{1-z}{z} + \frac{z}{(1-z)_+} + z(1-z)\right] + \frac{33-2n_f}{6}\delta(1-z).
\end{aligned}
$$

The '+ prescription' is

$$
\begin{aligned}
\frac{1}{(1-z)_+} &= \frac{1}{(1-z)} \quad \text{for } z<1, \quad \text{and} \\
\int_0^1 dz \frac{f(z)}{(1-z)_+} &= \int_0^1 dz \frac{f(z)-f(1)}{1-z}.
\end{aligned}
$$

The LO expressions for the anomalous dimensions are:

$$
\begin{aligned}
\gamma_{qq}^{(0)}(n) &= \frac{4}{3}\left[\frac{1}{n(n+1)} - \frac{1}{2} - 2\sum_2^n \frac{1}{k}\right] \\
\gamma_{qg}^{(0)}(n) &= \frac{1}{2}\left[\frac{2+n+n^2}{n(n+1)(n+2)}\right] \\
\gamma_{gq}^{(0)}(n) &= \frac{4}{3}\left[\frac{2+n+n^2}{n(n^2-1)}\right] \\
\gamma_{gg}^{(0)}(n) &= 6\left[\frac{1}{n(n-1)} + \frac{1}{(n+1)(n+2)} - \frac{1}{12} - 2\sum_2^n \frac{1}{k}\right] - \frac{n_f}{3}
\end{aligned}
$$

Note that the term $2\sum_2^n \frac{1}{k}$ comes from the $1/(1-z)_+$ term in the splitting functions and behaves like $\sim \ln n$ for large n. The signs and conventions agree with those of [Ell96,Ch.4], where expressions for the NLO splitting functions may also be found. Summaries of the full structure of the DGLAP formalism at NLO are given by Furmanski and Petronzio [Fur82] and Adel *et al.* [de97].

5

DIS experiments and data

Since the first experiments on deep inelastic scattering the use of leptonic probes ($e^{\pm}$, $\mu^{\pm}$, ν, $\bar{\nu}$) has been the dominant experimental technique. The DIS double differential cross-section is related to the measured number of events, binned in x and Q^2 by

$$\frac{d^2\sigma}{dxdQ^2} = \frac{N(x,Q^2)}{L \cdot A(x,Q^2)} \tag{5.1}$$

where $N(x,Q^2)$ is the number of events measured in the bin at (x,Q^2), L is the integrated luminosity or beam flux and $A(x,Q^2)$ is the correction function that accounts for finite resolution, efficiencies and acceptance. For an accurate measurement one must identify the DIS events cleanly, reconstruct x and Q^2, account for any background, measure L accurately and have sufficient information to construct A. For this last point the response of the detector must be understood very well and this is achieved by direct measurement and simulation using the Monte Carlo method.

This chapter covers in turn: kinematics for fixed target and HERA experiments; essential features of the detectors; an outline of how DIS events are selected and the raw data corrected to give the cross-section; a summary of nucleon structure function data from the classic DIS experiments, including HERA data for $Q^2 < M_Z^2$ (data for high Q^2 NC and CC processes at HERA is considered in Chapter 8). The chapter ends with a brief account of structure function data in the 'transition region' between photoproduction at $Q^2 = 0$ and deep inelastic scattering with $Q^2 > 1\,\mathrm{GeV}^2$.

Written 2000, revised Xmas 2001.

5.1 Kinematics

In Sec. 2.1 the various Lorentz invariant variables for DIS were introduced and defined in terms of 4-momenta. Here the determination of x, Q^2 and other variables from quantities measured in DIS experiments is discussed. Expressions for both fixed target and HERA experiments are given and limitations on the accessible regions of the (x,Q^2) kinematic plane are outlined. The physical region in x and Q^2 is a triangle bounded by $0 < Q^2 < s$, $0 < x < 1$ and the line $y = 1$, $Q^2 = sx$. This follows from

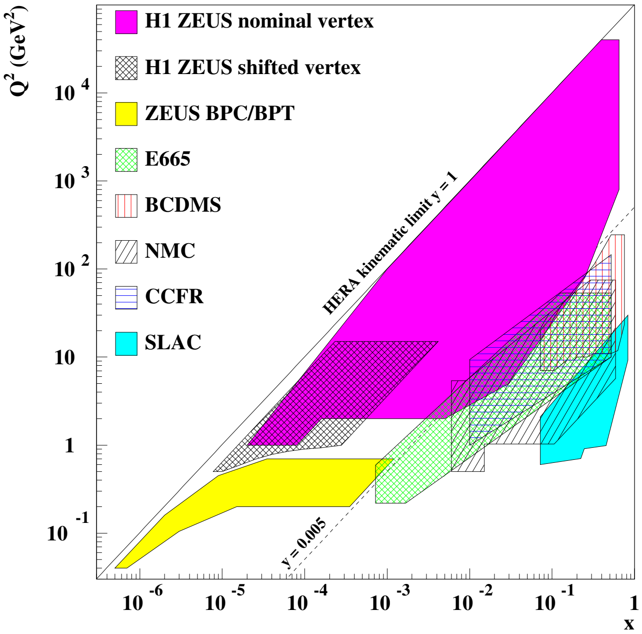

Fig. 5.1 Regions in the (x, Q^2) plane covered by DIS experiments. *HERA region needs updating to 96/97*

the relation $Q^2 = sxy$ and the ranges $0 < x, y < 1$, which also give the maximum value of Q^2 to be s (the ℓp CM energy squared). The physical region for the HERA collider is that below the diagonal $y = 1$ on the x, Q^2 plot shown in Fig. 5.1.

5.1.1 Fixed target

The classic fixed target experiments were performed at SLAC using electron beams and at CERN and Fermilab using muon and neutrino beams. For a fixed target experiment with an incident charged lepton beam of energy E, the detector for an inclusive measurement needs only to measure the energy and angle of the scattered beam electron or muon. The incident beam direction defines the axis from which the scattered lepton angle, θ, is measured, E' is the energy of the scattered lepton and m_N is the nucleon mass. Then, ignoring the lepton mass,

$$s = 2m_N E \qquad \text{and} \qquad y = (E - E')/E, \tag{5.2}$$

$$Q^2 = 4EE' \sin^2 \frac{\theta}{2}, \tag{5.3}$$

$$x = \frac{2EE' \sin^2 \frac{\theta}{2}}{m_N(E - E')}. \tag{5.4}$$

It is also useful to define the energy loss of the lepton in the lab frame $\tilde{\nu} \equiv \nu/m_N = E - E'$.[1] For fixed target experiments the relation $x = Q^2/(2m_N\tilde{\nu})$ is often used. In the (x, Q^2) plane lines of constant scattering angle θ are given by $Q^2 = sxD/(x+D)$ where $D = 2E\sin^2\frac{\theta}{2}/m_N$ and lines of constant E' are given by straight lines $Q^2 = 2m_N(E - E')x$. A real detector cannot measure θ to zero degrees or E' below some minimum value. Both these constraints will limit the accessible (x, Q^2) region. Further restrictions may follow from the finite resolution with which a given detector can measure θ and E'. This can be seen from the expressions for the relative errors

$$\begin{aligned} \frac{\delta Q^2}{Q^2} &= \frac{\delta E'}{E'} \oplus \cot\left(\frac{\theta}{2}\right)\delta\theta \\ \frac{\delta x}{x} &= \frac{1}{y}\frac{\delta E'}{E'} \oplus \cot\left(\frac{\theta}{2}\right)\delta\theta \end{aligned} \tag{5.5}$$

where $\oplus$ indicates addition in quadrature. Apart from the obvious dependence of the resolutions on $\delta E'$ and $\delta\theta$, both δQ^2 and δx get magnified at small scattering angles by the $\cot\left(\frac{\theta}{2}\right)$ factor. This is not such a severe constraint as very small angles cannot usually be measured. However, for x the error in the energy gets magnified at small values of y and this does give an additional limitation on the region in which accurate measurements can be made. Apart from control of $\delta\theta$ and $\delta E'$, a good understanding of the relative calibration of E and E' is important. In a fixed target experiment E' cannot be larger than the incident beam energy E.

In charged current DIS with an incident neutrino, the neutrino energy is not known but has to be inferred from the final state measurements. The detector has to be more complicated and able to measure the final state hadronic system in addition to the high energy muon from the leptonic vertex. The variables x and Q^2 are first estimated from the measured ('visible') quantities by:

$$Q^2_{vis} = 4E_{vis}E_\mu \sin^2\frac{\theta_\mu}{2}, \qquad x_{vis} = \frac{Q^2_{vis}}{2m_N E_{had}}, \tag{5.6}$$

since the lepton energy loss $\tilde{\nu}_{vis} = E_{had}$. The visible quantities are then corrected for detector effects using Monte Carlo simulation.

5.1.2 HERA collider

HERA is the first *ep* collider and consists of two separate rings of circumference 6.3 km, one a warm magnet electron (or positron) ring with energy 27.5 GeV and the other a superconducting magnet proton ring of energy 920 GeV. The two general purpose detectors, H1 and ZEUS, are

[1] Note that $\tilde{\nu}$ is often written as ν in earlier works on DIS.

multi-purpose devices designed to investigate all aspects of high energy ep collisions. In DIS both the scattered electron and the hadronic system are measured, the latter allowing one to estimate the energy and angle of the struck quark. Together with the information from the scattered electron one has an overdetermined system and there are many ways to reconstruct x and Q^2. Three methods will be covered here: the electron (E), double angle (DA) and sigma (Σ) methods. More details are covered in the exercises and a nice summary is given by Bassler and Bernardi [Bas99].

First the electron (E) method. The proton axis is conventionally taken to define the positive z direction from which all angles are measured. At low Q^2 this means that the electron scattering angle approaches 180°. If E_e, E_p are the electron and proton beam energies, E' and θ_e the energy and angle of the scattered electron, then:

$$s = 4E_eE_p \qquad \text{and} \qquad y_e = \left(1 - \frac{E'}{E_e}\sin^2\frac{\theta_e}{2}\right), \tag{5.7}$$

$$Q_e^2 = 4E_eE'\cos^2\frac{\theta_e}{2} = \frac{E'^2\sin^2\theta_e}{1-y_e}, \tag{5.8}$$

$$x_e = \frac{E_eE'(1-\sin^2\frac{\theta_e}{2})}{E_p(E_e - E'\sin^2\frac{\theta_e}{2})}. \tag{5.9}$$

Note that if $E' = E_e$ then $x = x_0 \equiv E_e/E_p$, the position of the so-called kinematic peak. In the (x, Q^2) plane lines of constant scattering angle θ are given by $Q^2 = sxC/(sx + C)$ where $C = 4E_2^2\cot^2\dfrac{\theta_e}{2}$ and lines of constant E' are given by $Q^2 = (4xE_e(E_e - E'))/(x_0 - x)$. Fig. 5.2 shows contours of constant E' and θ_e. The contours of large θ_e show clearly how the minimum electron scattering angle of a detector restricts the accessible phase space. The large region around the kinematic peak, in which E' is roughly constant is evident. Kinematic peak events, which can be selected to be almost independent of the structure function samples, are used for calibration purposes by both H1 and ZEUS. The figure also shows that on the high x high Q^2 side of the kinematic peak the scattered $e^\pm$ has energies $E' > E_e$.

As in a fixed target experiment, E' is required to be greater than a minimum value and θ_e less than a maximum angle for the scattered electron to be properly measured. Although there are differences of detail, the formulae for the resolutions of x and Q^2 in terms of $\delta E'$ and $\delta\theta_e$ are similar to those of Eqs 5.5.[2] The conclusion is the same, that at small y (large x) the resolution in x deteriorates.

[2]See [Bas99] for details.

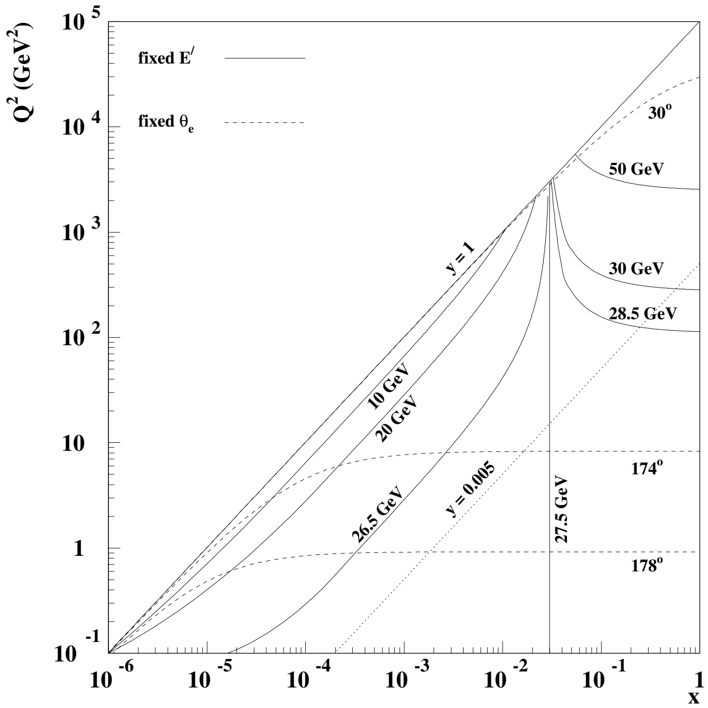

Fig. 5.2 Contours of constant E' and θ_e for the HERA with $E_e = 27.5\,\mathrm{GeV}$ and $E_p = 920\,\mathrm{GeV}$. The vertical line at $x_0 = E_e/E_p$ divides the kinematic peak region.

In the double angle (DA) method [Ben91][3], only angles are used to reconstruct x and Q^2. In addition to θ_e one constructs the angle γ from the hadronic energy flow using:

$$\cos\gamma = \frac{(\sum_h p_x)^2 + (\sum_h p_y)^2 - (\sum_h (E - p_z))^2}{(\sum_h p_x)^2 + (\sum_h p_y)^2 + (\sum_h (E - p_z))^2} \tag{5.10}$$

where $\sum_h$ runs over all calorimeter energy deposits (with momentum vectors (p_x, p_y, p_z)) not assigned to the scattered electron. In the QPM γ is the polar angle of the struck quark. The variables x and Q^2 are then determined by:

$$Q^2_{DA} = 4E_e^2 \frac{\sin\gamma(1+\cos\theta_e)}{\sin\gamma + \sin\theta_e - \sin(\gamma+\theta_e)} \tag{5.11}$$

[3] The derivation of the DA formulae is followed in Q2-4 at the end of the chapter.

$$x_{DA} = x_0 \frac{\sin\gamma + \sin\theta_e + \sin(\gamma + \theta_e)}{\sin\gamma + \sin\theta_e - \sin(\gamma + \theta_e)} \tag{5.12}$$

The method is insensitive to hadronization and, to first order, is independent of the detector energy scales. At small values of θ_e or γ the resolution in x_{DA} and Q^2_{DA} worsens. For the hadronic system to be well measured, it is necessary to require a minimum of hadronic activity away from the beampipe. A suitable quantity for this purpose is the hadronic estimator of y [Jac79] :

$$y_{JB} = \frac{\sum_h (E - p_z)}{2E_e} \tag{5.13}$$

At low y (< 0.04) and low Q^2, there is low hadronic activity in the detector and the DA method becomes sensitive to noise in the calorimeter.

A variation on the DA method, introduced by ZEUS [ZEU96], is the PT method. In this the expression for γ given in Eq. 5.10, is modified in two ways:

- first, the hadronic transverse momentum $(\sum_h p_x)^2 + (\sum_h p_y)^2$ is replaced by that of the electron $(\mathbf{p}_T^e)^2$ as it more accurately measured;
- second, the hadronic longitudinal momentum – energy difference $\sum_h (E - p_z)$ is corrected using the Monte Carlo simulation of the detector for energy loss through the forward beamhole.

To improve the resolution of x at small y and to reduce radiative corrections H1 use the Σ method of reconstruction [Bas95]. Returning to Eq. 5.13, $\sum_h (E - p_z)$ is referred to as Σ, and the essence of the idea is to remove explicit dependence on E_e from the kinematic reconstruction of the electron method. This is done by noting that energy and momentum conservation gives $2E_e = \Sigma + E'(1 - \cos\theta_e)$. Using this to replace $2E_e$ in the denominator of y_{JB} gives

$$y_\Sigma = \frac{\Sigma}{\Sigma + E'(1 - \cos\theta_e)} \qquad Q^2_\Sigma = \frac{E'^2 \sin^2\theta_e}{1 - y_\Sigma}. \tag{5.14}$$

The variable x is then calculated from $Q^2 = sxy$. Apart from allowing an extension of the measurements to lower y values than the E method, the Σ method has a reduced sensitivity to initial state radiative corrections because E_e no longer appears explicitly.

In practice to get the best possible resolution over the complete (x, Q^2) space available at HERA both H1 and ZEUS use combinations of the above methods.

For the charged current process at HERA in which the outgoing scattered lepton is a neutrino, only final state hadronic information is available for the reconstruction of the kinematic variables. It is for this type of measurement that hemiticity of the HERA detectors is essential. For a CC interaction in a completely hermetic detector, the neutrino is the only undetected particle and its 4-momentum can be deduced by using 4-momentum conservation since the initial 4-momenta are known. However, in reality, although the HERA detectors cover more than 99% of 4π, energy escapes through the hole for the beam pipe – particularly in the forward (proton) direction. The Jacquet-Blondel method of estimating y (Eq. 5.13) is insensitive to loss of energetic particles at very forward angles for which $E \approx p_z$. Once y is known Q^2 is given from Eq. 5.8 using conservation of transverse momentum by

$$Q^2 = \frac{(\sum_h p_x)^2 + (\sum_h p_y)^2}{1 - y_{JB}}. \tag{5.15}$$

Finally x is determined from $x = Q^2/sy$. The regions in the x, Q^2 plane in which structure functions have been measured at HERA are shown in Fig. 5.1.

5.2 Detectors

How well can the requirements for measuring DIS kinematic variables in fixed target and collider frames be realised in experiments? In this section the essential experimental techniques will be outlined by reference to the E665 and CCFR spectrometers and the ZEUS and H1 experiments at HERA.

5.2.1 The E665 muon scattering experiment

The Experiment E665 [Ada90] was located at the end of the NM beamline at Fermilab. The NM beam provided muons of average energy 470 GeV with a spread of 50 GeV. The design of the muon beam is itself an interesting problem in particle physics and charged particle beam optics. Muons occur as the decay products of π and K mesons produced in the interaction of a a primary 800 GeV proton beam with a Be target. The 1.5 km length of the beamline is needed to allow enough mesons to decay, to remove unwanted hadrons and to focus the final muon beam. The experiment took data in 1987-88, 1990 and 1991-92. The detector, shown in Fig. 5.3, was designed to measure beam and scattered muons with high precision and to provide measurement of charged and neutral particles in the final state. The technique used to analyse the charged particles, particularly the scattered muon, is bending in a powerful magnetic field. Note the linear scale of the apparatus, roughly 30 m between the target and the final muon detection system (PTM/SPM). Another point to remember in the design of a high energy fixed target experiment is the forward collimation of the reaction products because of the large Lorentz boost – for the NM nominal beam energy of 470 GeV on a stationary proton target the CM system has a γ factor of 15.84. Aspects of the detector important for measuring DIS are:

Beam spectrometer. This was positioned between the end of the NM beamline and the main detector. It consisted of 4 measuring stations each

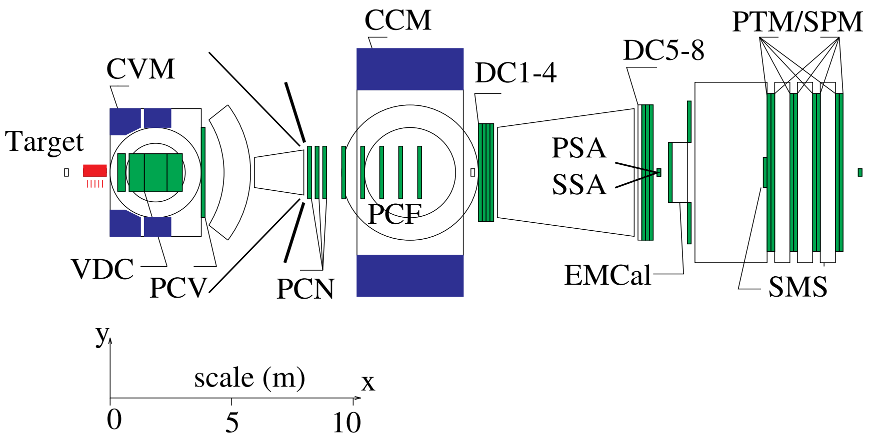

Fig. 5.3 The E665 detector.

equipped with beam hodoscopes and multiwire proportional chambers, two before a dipole magnet and two after, each lever arm of approximately 27 m resulting in a resolution on the beam momentum of $\delta(p^{-1}) \sim 8\times 10^{-6}\,\mathrm{GeV}^{-1}$.

Target. The target assembly was placed in the field free region in front of the first spectrometer magnet (CVM). It consisted of three identical target cells on a precision table that moved the targets laterally into the beam following a regular cycle. The three target cells were identical and of active length 1 m, two were filled with liquid hydrogen and liquid deuterium respectively. The third was empty and was used to provide data for subtraction of off-target scatters.

Main spectrometer. The charged particle spectrometer was constructed around two large magnets with reversed polarities (CVM 4.315 Tm and CCM −6.734 Tm) arranged so that the position of the scattered muon at a focussing plane in the muon detector was independent of momentum and depended only on the scattering angle. Tracking was performed using planar drift chambers placed inside both magnets and before and after the CCM. For tracks that traversed the full length of the spectrometer a momentum resolution of $\delta(p^{-1}) \sim 2\times 10^{-5}\,\mathrm{GeV}^{-1}$ was achieved, which gave resolutions of about 5% on x at low x and about 4% on Q^2. Muons were identified by four sets of wire planes (PTM) placed behind a 3 m iron absorber, with the sets separated by 1 m thick concrete absorbers.

EMcal. The electromagnetic calorimeter was placed just in front of the muon absorber and was a 20 radiation length lead-plate gas sampling device. In addition to measuring photons from neutral hadron decays it also provided information on elastic muon-electron scatters.

Trigger. The large angle trigger required a beam muon and a scattered muon with hits in at least 3 of the 4 scintillator planes (SPM) of the muon detector after the absorber. The muon beam passes through a 20 cm × 20 cm hole in the SPM array, giving an angular cut of 3.3 − 4.7 mrad, which corresponds to $Q^2 = 2.7 - 5.5\,\mathrm{GeV}^2$ for 500 GeV muons. A goal of the E665 experiment was to study DIS at smaller values of x than in earlier fixed target experiments. To achieve this it had to be triggered on events in which the scattered muon was within the envelope of the beam. This was achieved by a veto trigger based on a finely segmented scintillator array (SMS) placed in the beam immediately after the absorber. The small angle trigger was a combination of a beam muon and the absence of a signal in the SMS at the position predicted for that muon (without interaction). It was efficient down to angles as small as 1 mrad ($Q^2 = 0.5\,\mathrm{GeV}^2$ for 500 GeV muons).

Flux. The integrated incident muon flux was measured by assuming that the beam spectrometer response was the same for random and physics triggers. The number of usable beam muons was determined by counting the number of random beam triggers with a good muon and multiplying by the pre-scale factor. The latter was determined by comparing the number of random beam triggers with the actual number counted by scalers.

Calibration. The calibration and resolution of the E665 spectrometers was checked using the following techniques. Primary protons at $800.6 \pm 2\,\mathrm{GeV}$ (determined from the Tevatron magnet currents) were directed through the apparatus. The relative calibration of the beam and main spectrometers was checked using non-interacting muons and comparing the difference of the momenta measured in the two spectrometers in data and simulation. This lead to an estimate of 0.13% relative error at the nominal muon beam energy of 470 GeV. Elastic muon-electron scattering events also provided information on the calibration and resolution of the spectrometer. Using signals from the EMcal, the events have a distinctive signature and are constrained by kinematics to have $x = m_e/m_N$.

5.2.2 The CCFR neutrino scattering experiment

The CCFR neutrino scattering experiment is shown schematically in Fig. 5.4. It was exposed to the Tevatron Quad-Triplet wide-band neutrino beam, which was composed of neutrinos with average energy 185 GeV and antineutrinos of average energy 143 GeV. The maximum beam energy was about 600 GeV and the ratio of $\nu : \bar{\nu}$ was about 2.5 : 1. The CCFR detector [Sak90,Kin91] consists of a 17.7 m long 690 ton unmagnetized steel-scintillator target calorimeter, which is instrumented with drift chambers for muon tracking. The hadronic energy resolution of the calorimeter is $\sigma/E = 0.85/\sqrt{E(\mathrm{GeV})}$. The calorimeter energy scale was calibrated to 1% using momentum analysed hadron beams with energies between 15 and 450 GeV. The target is followed by a 17.8 m long solid iron toroidal magnetic spectrometer for muon identification and momentum measurement. The

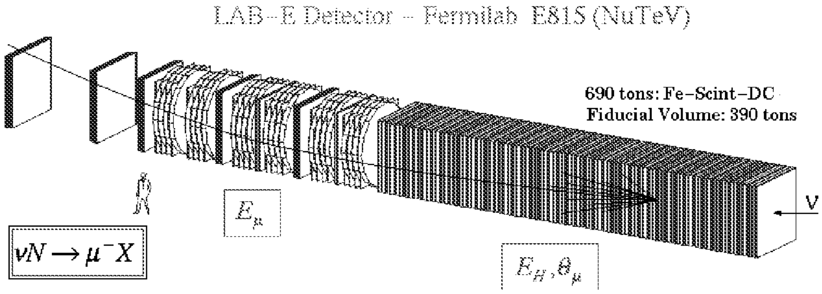

Fig. 5.4 The CCFR-NuTeV detector.

spectrometer was calibrated to about 0.5% using a momentum analysed muon beam with energies of 50, 75, 120 and 200 GeV. The muon momentum resolution is $\Delta p/p = 0.11$ and it is limited by multiple Coulomb scattering in the iron. The detector provides measurements of the visible hadronic energy E_{had}, the momentum, p_μ, and angle with respect to the neutrino beam line, θ_μ, of the scattered muon. The relative neutrino flux at different energies and the relative $\bar{\nu}/\nu$ flux are obtained from events with low hadron energy, $E_{had} < 20\,\text{GeV}$. The absolute normalization is determined so that the total νN cross-section equals the average value for Fe from the CHDSW and CCFR experiments of $\sigma^{\nu N}/E = (0.677 \pm 0.014) \times 10^{-42}\,\text{m}^2\text{GeV}^{-1}$ per nucleon and $\sigma^{\bar{\nu}N}/\sigma^{\nu N} = 0.499 \pm 0.005$.

5.2.3 Detectors for the ep collider HERA

A cross-section of the ZEUS detector is shown in Fig. 5.5. The first thing to note is the very different layout compared to a fixed target detector. The ZEUS and H1 detectors are designed to measure as much as possible of all final states in ep collisions at HERA, which means NC and CC DIS processes and almost-real photon interactions. Although there is a large disparity in the proton (920 GeV) and $e^\pm$ (27.5 GeV) beam energies, the γ factor of the ep CM system in the HERA frame is only 2.98. The proton remnant is thrown forward, but the scattered beam $e^\pm$ and other products of the hard interaction (the quark or 'current' jet system) will emerge at larger angles. If the detectors are to have good efficiency for reconstructing the final state and to be able to measure CC DIS with a missing neutrino then the sensitive components must be nearly hermetic, particularly the calorimeters. The HERA detectors differ from e^+e^- or $p\bar{p}$ detectors in being asymmetric, both H1 and ZEUS have deeper calorimeters in the proton direction and both have sophisticated forward muon detectors. The main differences between the ZEUS and H1 detectors are in the size of the solenoidal coils for the central tracking systems and the calorimeter technology. ZEUS has a 2 m diameter coil providing a 1.43T field with the

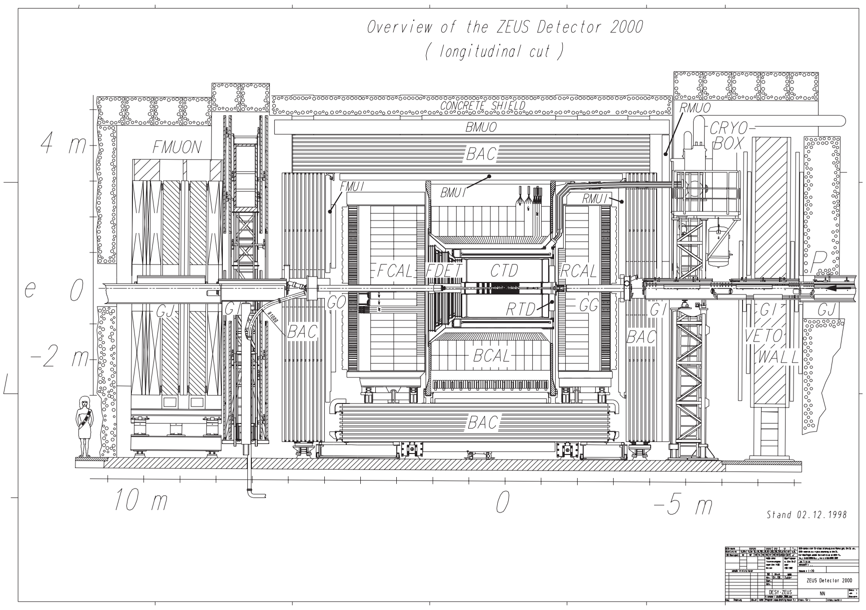

Fig. 5.5 The ZEUS detector.

calorimeter outside the coil, H1 has a 6 m diameter coil giving a 1.15T field with the lead liquid-argon calorimeter inside the coil. The main components of the H1 detector are shown in the event display of Fig. 5.6.

The ZEUS calorimeter is a compensating uranium-scintillator sandwich design (UCAL) which gives an equal response to electromagnetic and hadronic particles of the same energy and is thus optimised for measuring hadronic jets at large Q^2. The polar angle coverage is $2.6°$ to $176.2°$. Under test beam conditions the energy resolution is $\sigma_E = 0.35\sqrt{E(\mathrm{GeV})}$ for hadrons and $\sigma_E = 0.18\sqrt{E(\mathrm{GeV})}$ for electrons. The UCAL also provides a time resolution of better than 1 ns for energy deposits greater than 4.5 GeV, which is used for background rejection. The H1 liquid argon calorimeter (LAR) is used to measure the hadronic final state and scattered electrons for $Q^2 > 120\,\mathrm{GeV}^2$. The LAR covers the angular range $3° - 155°$ and has an EM section with lead absorber plates of $20 - 30$ radiation lengths and a hadronic section with steel absorber plates giving a total depth of $4.5 - 8$ interaction lengths. For EM particles the energy resolution is $12\%/\sqrt{E(\mathrm{GeV})}$, and for hadrons $50\%/\sqrt{E(\mathrm{GeV})}$. In the rear direction, which is important for low Q^2 ($< 120\,\mathrm{GeV}^2$), H1 have a lead-scintillating fibre calorimeter (SPACAL) covering the angular range $153° - 178.5°$ with high granularity giving an angular resolution of $1 - 2\,\mathrm{mrad}$. Energy resolution, measured during experimental operations, is $7.5\%/\sqrt{E(\mathrm{GeV})} \oplus 2.5\%$.

Outside the main calorimeters, both experiments have instrumented iron to catch energy leaking from the calorimeters and to provide absorbers before the barrel muon chambers.

H1 and ZEUS have extensive tracking systems inside the main calorimeters and within the magnetic volume. Around a thin beam pipe are silicon microstrip vertex detectors, then cylindrical drift chambers (CTD). For a full length track in the ZEUS CTD, the resolution in transverse momentum is $\sigma_{p_T}/p_T = 0.005p_T \oplus 0.016$ (for p_T in GeV). In the forward direction there are further drift chambers and straw tube chambers for charged particle tracking. One of the important functions of the central tracking systems is to measure the position of the primary event vertex. The vertex detectors will be particularly important for physics after the HERA upgrade (see Chap. 8). The detectors consist of two or three layers of microstrip modules around the beampipe and three or four 'wheels' in the forward direction. Typical individual hit resolutions are better than $20\,\mu$m. Apart from providing a large improvement in momentum resolution and primary vertex position, the vertex detectors will be used to improve efficiency for detection of charm and beauty states.

Because of the interest in measuring the behaviour of F_2 or the total $\gamma^* p$ cross-section as $Q^2 \to 0$, both ZEUS and H1 have extended their detectors to be able to measure θ_e very close to 180°. For example the ZEUS beam pipe calorimeter (BPC) is located at 2.9 m from the interaction point adjacent to the beam pipe on the (rear) electron side and covers $e^\pm$ scattering angles in the range 15 to 43 mrad. It is a small tungsten-scintillator sampling calorimeter with energy resolution $\Delta E/E = 17\%/\sqrt{E(\mathrm{GeV})}$ and was installed in ZEUS in 1995. A couple of years later, the BPC was augmented by two planes of silicon microstrip tracking detectors – the beam pipe tracker (BPT). This improved the acceptance for very low angle scattered positrons and the BPC/BPT combination gave an angular resolution of $\Delta\theta_e = 0.2$ mrad. In addition data have been taken with special runs of the HERA collider in which the primary interaction vertex is shifted by 70 cm in the proton beam direction. The interaction is thus further from the rear calorimeters which are used to identify the scattered electron and hence smaller angles can be reconstructed. The regions in the x, Q^2 plane at the very small values of Q^2 reached by these techniques are shown in Fig. 5.1. These detectors were removed in 2000 as they are incompatible with the extra final focus magnets inserted for the HERA upgrade.

The interval between bunch crossings in HERA is 96 ns which necessitates sophisticated multi-level trigger systems. For ZEUS and H1, at the first level data is stored temporarily ('pipelined') while hardware specific trigger processors, operating synchronously with HERA beam crossings, arrive at a decision in about $2 - 5\,\mu$s. The higher trigger levels operate asynchronously and involve more sophisticated calculations, culminating in an 'event filter' which uses a fast version of the offline reconstruction code running on a farm of RISC processors. The overall reduction achieved is from a raw interaction rate of many 100 KHz (which is very sensitive to beam conditions in HERA) to about $5-10$ Hz written to tape.

At HERA, ep luminosity is measured using the very small Q^2 Bethe-Heitler process $ep \to ep\gamma$, for which the cross-section is large and known accurately. Photons emerging from the electron-proton interaction point (IP) at angles $\theta_\gamma \leq 0.5$ mrad with respect to the electron beam axis hit the photon calorimeter at 107 m (103 m) from the IP for ZEUS (H1). Electrons emitted from the IP at scattering angles less than or equal to 6 mrad and with energies $0.2E_e < E_e' < 0.9E_e$ are deflected by beam magnets and hit the electron calorimeter placed 35 m (33 m) from the IP. The systematic error on the luminosity measurement is typically less than 2%.

Something on lumi detector upgrade?

5.3 Measurement of the cross-section

The first step in the measurement of $\dfrac{d^2\sigma}{dxdQ^2}$ is to identify the DIS events. The problems faced by fixed target and HERA experiments are somewhat different. In the case of a fixed target muon scattering experiment, the event selection criteria fall into two categories. First, those based on information from the beam spectrometer to select events with a single well measured muon on the target. Second, those based on information from the main detector which define a well measured scattered muon originating from the fiducial volume of the target. Typical cuts require a minimum momentum (p_μ) and a minimum energy energy loss ($\tilde{\nu}$). Further cuts are then applied to ensure that the events lie in the 'well-measured' region of kinematic plane as discussed in Sec. 5.1 above.

At HERA the signature of a DIS NC event is one in which the scattered beam electron is recorded in the EM section of the calorimeter and the total transverse momentum of the final state is approximately zero. An example of a high Q^2 NC event in the H1 detector is shown in Fig. 5.6. For this type of event the electron and hadron energy deposits are well separated and there is little chance of confusion in electron identification. At low x and Q^2 both the scattered electron and the hadronic system emerge at small angles to the rear beam pipe and may well overlap in the calorimeter. In such events track reconstruction may also be difficult. At HERA there are two large backgrounds to be overcome. The first is from beam-gas interactions, mainly beam protons striking rest gas molecules in the long straight section leading up to the interaction region. This background is reduced very effectively by precise timing – a genuine ep scattering event will give signals at roughly the same time in all parts of the detector whereas an up-stream p-gas interaction will produce debris which hits the rear detectors before the forward sections. Good reconstruction of the the primary vertex position along the beam line by the tracking system is also important for reducing the level of beam-gas background. The second large background is from fake electron signals in photoproduced events. This happens because

Candidate from NC sample

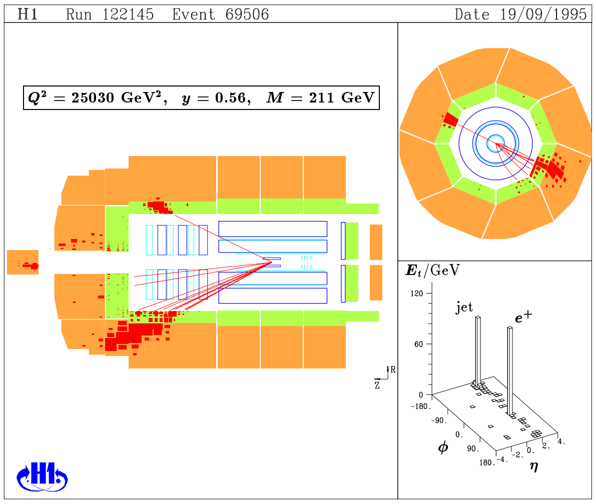

Fig. 5.6 A DIS NC event in the H1 detector at HERA. The figure also shows the main active components, central and forward tracking detectors as open rectangles surrounded by the liquid argon calorimeter. At the rear is the SPACAL and in the forward beam hole is the plug calorimeter.

the photoproduction cross-section is large and in some events an overlap of a π^0 and a charged particle in the final state may produce an EM cluster with a track pointing at it. In principle the size of this effect can be reduced by good granularity in the EM calorimeter. A variable that is effective in reducing the photoproduction background is

$$\delta = \sum_i (E_i - E_i \cos\theta_i) = \sum_i (E - p_z)_i, \tag{5.16}$$

where the sum runs over all calorimeter deposits E_i with polar angle θ_i. From conservation of longitudinal momentum, in an ideal detector, δ sums to twice the electron beam energy $2E_e$. For photoproduction background events, δ peaks well below $2E_e$ because the genuine scattered electron remains in the beam pipe. In a real detector the DIS peak at $2E_e$ is smeared out by finite resolution and becomes asymmetric because of initial state radiation. For $E_e = 27.5\,\text{GeV}$, typical cuts on δ are $38 < \delta < 65\,\text{GeV}$.

Once the DIS sample has been selected and the corresponding luminosity measured, a number of corrections have to be applied to give the Born level cross-section.

5.3.1 radiative corrections

We will not consider the full electroweak corrections, but only the important features of QED corrections for NC reactions. The corrections are of two sorts, virtual corrections and the infra-red part of real photon emission which give an overall modification to the Born cross-section and non-infra-red real photon emission in which the photon is not identified. The radiative process $e(k)p(p) \to e(k')\gamma(\ell)X$ (symbols in brackets indicate the corresponding 4-momenta) is dominated by photon emission from the initial and final lepton. In principle there is also interference between the two. Consider first the situation when the kinematics is reconstructed using the scattered lepton only and the radiation is from the initial lepton (ISR). The standard definitions of the kinematic variables are (where ℓ indicates that they have been calculated from the lepton side),

$$Q_\ell^2 = -(k-k')^2 \qquad x_\ell = \frac{Q_\ell^2}{2p.(k-k')} \qquad y_\ell = \frac{p.(k-k')}{p.k}. \tag{5.17}$$

The effect of the radiation of a photon of 4-momentum l, is to lower the actual centre of mass energy in the ep interaction from $s = (k+p)^2$ to $s' = (k-l+p)^2$. The true kinematic variables are correctly reconstructed from the hadron side

$$Q_h^2 = -(k-k'-l)^2 \qquad x_h = \frac{Q_h^2}{2p.(k-k'-l)} \qquad y_h = \frac{p.(k-k'-l)}{p.(k-l)}. \tag{5.18}$$

For collinear ISR the lepton side and true variables are related by

$$Q_h^2 = z_i Q_\ell^2 \qquad\qquad x_h = \frac{x_\ell y_\ell z_i}{y_\ell + z_i - 1} \tag{5.19}$$

where z_i is the fractional energy loss from the initial state lepton $z_i = (E - E_\gamma)/E$. Similar expressions may be deduced for the case of collinear radiation from the final state lepton (FSR). The size of the radiative contributions is characterised by $\ln(m_\ell^2/Q^2)$ where m_ℓ is the electron or muon mass, and are thus generally more severe for ep than μp scattering. For a measurement at (x_ℓ, y_ℓ), the radiative correction is calculated by integrating over the region $x_\ell \leq x \leq 1,\ 0 \leq y \leq y_\ell$ which implies a priori knowledge of the cross-section being measured.

The procedure adopted for fixed target experiments is to use a phenomenological parameterisation of $F_2(x, Q^2)$ chosen to give a good representation of the data over a wide range of Q^2 and particularly at very small values. The radiative corrections are then estimated using the parameterised F_2. As the data from the experiment in question may be used in the parameterisation, the fit parameters may be improved during unfolding so the whole procedure is iterated. One of the biggest uncertainties comes from lack of knowledge of R. The radiative corrections are sizeable for large

y and small x, for example in the lowest x bins of the E665 experiment the corrections reach 40% at the largest Q^2 values [Kot95].

At HERA, even though the lepton beam is composed of electrons or positrons, the radiative corrections turn out to be less severe. There are two reasons for this. The first is that since the scattered electron is measured by calorimetric methods the energy lost through FSR will usually be deposited in the same calorimeter cell as the electron itself. The second is that kinematic information is measured from both the electron and hadron sides. The variable δ introduced in the previous section plays an important role. In the case of ISR, the energy of the electron in the ep interaction is less than E_e by the amount E_γ and thus δ will sum to $2E_e - 2E_\gamma$. The requirement of a minimum value for δ, used to reduce photoproduction background, will also remove ISR events and limit the size of the radiative correction. Over the region of the (x, Q^2) plane used for F_2 measurements at HERA, radiative corrections do not exceed 10% and are typically a factor 2 smaller.

5.3.2 Monte Carlo corrections

The final step to get from binned numbers of events, $N(x, Q^2)$, to the cross-section is the calculation of the correction function $A(x, Q^2)$ defined in Eq. 5.1. $A(x, Q^2)$ is calculated by Monte Carlo simulation in two stages: firstly DIS ep interactions are generated and secondly the simulated events are passed through a simulation of the detector. Here the procedure for HERA experiments will be outlined.

NC DIS events including radiative effects are simulated, at the level of lepton-parton interactions, using the HERACLES program.[4] In HERACLES, corrections for initial- and final-state radiation, vertex and propagator corrections, and two-boson exchange are included. The QCD cascade and the hadronic final state are simulated using the color-dipole model of ARIADNE, with the MEPS (order α_S QCD matrix elements plus parton showers) option of LEPTO as an alternative for checking systematic effects. Both programs are from the Lund family and both use the Lund string model [And98] of JETSET for the hadronisation. Photoproduction background is estimated using events simulated with the HERWIG or PYTHIA event generators. The output of the event generator is a set of 4-vectors describing the 'stable' final state particles (that is particles with lifetimes of order 10^{-8} s and longer), together with a complete history of the event. The event is then input to the detector simulation. Many simulations of high energy physics detectors are based on the GEANT package. This is a suite of programs that allow detector elements with different geometrical shapes (planes, cylinders etc) to be put together in a consistent way. The program also takes care of transporting the particles through the geometry

[4] More details and references to the latest versions of the Monte Carlo packages are given in Appendix E.

and material of the detectors, allowing for the different interactions of electromagnetic particles, hadrons, muons, etc. The response of each type of detector (calorimeter, drift chamber, etc) is simulated to a sufficient level of detail to model the actual signals. At each stage of the detector simulation, the history of the interactions is recorded so that it is possible to relate the 'signals' to the input particles from the event generator. The final output of the complete DIS event simulation consists of three parts: the 4-vectors of the physics event, the simulated detector signals in the same format as a real event and a history record linking the two.

Although both the event generators and the detector simulations are based on physics, there are still many parameters to be tuned. For the event generators this is particularly true of the hadronisation process. One of the advances in understanding that has followed from the quark-parton model and QCD, and which is built in to the event generators, is the extent to which the hadronisation of quarks and gluons should be independent of production process. Since a consistent framework is used for many different types of interaction (e^+e^- annihilation, ep DIS and hard $\mathrm{p\bar{p}}$ processes), common hadronisation parameters have often been fixed by the detailed studies of jet physics at LEP. However there are still parameters specific to ep processes to be fixed by tuning to HERA data. On the detector side, information on the response of detector elements is input from test-beam data and by tuning the simulation to describe the real signals. A crucial control of the whole process of simulation is to demonstrate that the Monte Carlo data does describe the key variables used in the analysis.

An example from the ZEUS measurement of the medium Q^2 $\mathrm{e^+p}$ NC cross-section and structure function F_2 using the HERA 1994 data sample is shown in Fig. 5.7. The number of events generated is matched to the luminosity of the data sample. The overall level of agreement between simulation and data is good. Plots (a) and (b) show the energy and angle of the scattered positron and (c) Z_{vertex} the position of the primary event vertex along the beamline. An accurate description of this last distribution is particularly important for a correct calculation of the geometrical acceptance, as the NC cross-section is a very rapidly varying function of angle. The shape of the vertex distribution is typically measured from an unbiased sample of general ep interactions and it is dependent on the optics and general setup of the HERA collider. Plots (d)-(f) are control plots for the PT kinematic reconstruction procedure (see the discussion following Eq. 5.13 above). The vertical lines on plots (c)-(f) indicate the positions of event selection cuts.

The alert reader will have noticed a serious flaw in the procedure described in the last few paragraphs – at the centre of the event simulation is the cross-section that is being measured! Most techniques for solving this problem involve iteration in some form. A conceptually simple and frequently used approach is known as bin-by-bin unfolding. Starting from a recent set of parton density functions, the input structure function, $F^0(x, Q^2)$

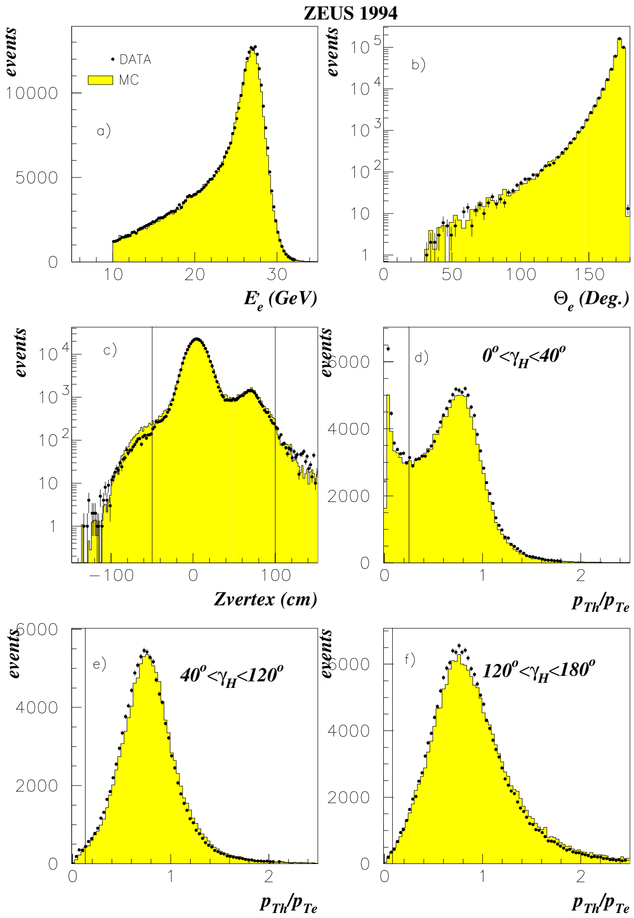

Fig. 5.7 ZEUS medium Q^2 e^+p NC analysis control plots: (a) E'; (b) θ_e; (c) Z_{vertex}; (d-f) p_T^h/p_T^e for different ranges of the hadronic angle γ_h. The vertical lines in plots (c)-(f) show the positions of selection cuts. The Monte Carlo distributions are normalised to $2.5\,\mathrm{pb}^{-1}$, the integrated luminosity of the data. From [ZEU96].

is calculated. This is then used to generate a distribution of simulated events $N^{MC}(x_m, Q_m^2)$ with respect to the measured variables x_m and Q_m^2 and normalised to the measured luminosity. N^{MC} together with the distribution of real observed events $N^{obs}(x_m, Q_m^2)$ give a corrected structure function

$$F^{i+1}(x, Q^2) = \frac{N^{obs}(x_m, Q_m^2)}{N^{MC}(x_m, Q_m^2)} F^i(x, Q^2), \tag{5.20}$$

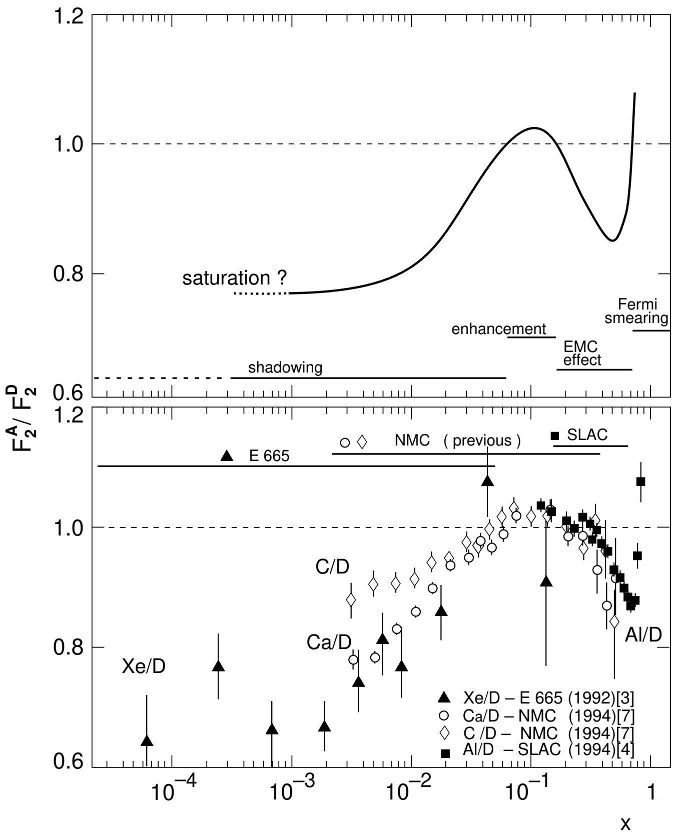

Fig. 5.8 The structure function ratio $R^A(x) = F_2^A(x)/F_2^D(x)$ as a function of x. Upper plot: the trend of the data; lower plot ratio data for a variety of nuclei. From [Esk99]??

where $F^i = F^0$ initially. The F^{i+1} values are 'smoothed', either by fitting a suitable function of (x, Q^2) or by a NLO QCD fit. The smoothed structure function, F^{i+1}, is then used to re-weight the Monte Carlo events for a second iteration of the procedure. The procedure is repeated, usually only 2-3 times, until a convergence criterion is satisfied (typically that the change in F is less than $0.2 - 0.5\%$). Bin-by-bin unfolding works well only if the initial Monte Carlo data gives a good description of the real data, hence the need to check this carefully.

5.3.3 Nuclear effects

The study of DIS from nuclear targets is an interesting subject in its own right and it has provided some surprises, for example the 'EMC effect'. In recent years, there has been a revival of interest because of high energy heavy-ion collision experiments and related new semi-classical approaches to QCD for regimes with very high gluon densities. Also, it is becoming possible to study the propagation of quarks and gluons in extended hadronic matter with sophisticated modern detectors (reference???). However, these topics are beyond the scope of this book; here we are concerned with how structure function data from nuclear targets, particularly from neutrino scattering experiments, is corrected to that for a single nucleon. Nuclear effects in DIS are encapsulated by studying the ratio of structure functions from nucleus A to that of deuterium, $R^A(x) = F_2^A(x)/F_2^D(x)$, as a function of x. To a good approximation the effects show little dependence on Q^2. The data for $R^A(x)$ is summarised in Fig. 5.8. The lower plot shows the data, averaged over Q^2, from experiments on a variety of nuclear targets as a function of x. The curve in the upper plot shows the trend of the data and indicates the various regions described below.

Before the EMC experiment of 1982, it was assumed that nuclear effects would only be seen at low x where nuclear shadowing occurs and as $x \to 1$ where additional smearing from nuclear Fermi motion is expected. The EMC experiment showed that for x roughly in the range $0.3 - 0.8$, R^A was significantly less than 1. Both the NMC and E665 experiments were designed in part to study R^A in detail. Special attention was paid to target design to reduce systematic errors in the measurement of cross-section ratios. There are many models for the EMC effect but most fall into one of two categories: nuclear models in which the partons are unchanged but nuclear binding effects give rise to a rescaling in x; models in which the quark confinement size in nuclear matter is larger than for a free nucleon giving a decrease in the Fermi momentum and leading to a rescaling in Q^2. The subject of the EMC effect is well covered in Chapter 8 of [Rob90] and in the review article by Arneodo [Arn94]. Two parameterisations of $R^A(x)$ by Smirnov [Smi99] and by Eskola et al [Esk99] give very good representations of the data and have been used in global fits to determine parton distribution functions.

For most purposes the nuclear binding effects in deuterium are ignored, but Bodek and Yang [Bod98] have used recent calculations to argue that this is not correct. Using data from SLAC to fix the nuclear binding correction to F_2^D/F_2^{p+n} they are able to get a better description of the NMC data on the ratio F_2^D/F_2^p for $x > 0.4$. This in turn leads to a modification of the d/u ratio of parton distributions at large x. The errors on the current parton distributions at large x [Bot00] are such that the modification of Bodek and Yang is not required, however it does give qualitative improvement to the description of the W leptonic decay asymmetry from CDF and to the high Q^2 e^+p CC cross-section at HERA. This will certainly be an important topic for high luminosity measurements at HERA which will probe the large x region at high Q^2.

5.4 Structure function data

As shown in Appendix D and Chapter 8, the double differential differential neutral current cross-section at high energy is expressed in terms of the structure functions by

$$\frac{d^2\sigma(\ell^\pm N)}{dxdQ^2} = \frac{2\pi\alpha^2}{Q^4 x}\left[Y_+\, F_2^{lN}(x,Q^2) - y^2\, F_L^{lN}(x,Q^2) \mp Y_-\, xF_3^{lN}(x,Q^2)\right], \tag{5.21}$$

where $Y_\pm = 1 \pm (1-y)^2$ and mass terms have been ignored. For Q^2 values well below that of the Z^0 mass squared, the parity violating structure function xF_3 is negligible and the structure functions F_2, F_L are given purely by γ^* exchange. This is true of all fixed target data and for HERA data with $Q^2 < 1000\,\mathrm{GeV}^2$. For $Q^2 > 1000\,\mathrm{GeV}^2$, the contributions from Z^0 exchange, including xF_3 cannot be ignored. In the extraction of F_2^{EM} from the cross-section data, the contributions from Z^0 exchange are calculated using the standard model expressions and a recent set of parton densities. The values of the terms subtracted are tabulated along with the data, so that corrections could be made at a latter date.

For data at large x and small Q^2 (eg the SLAC data) some terms involving the nucleon mass become non-negligible and equation 5.21 becomes

$$\frac{d^2\sigma(\ell^\pm N)}{dxdQ^2} = \frac{4\pi\alpha^2}{Q^4 x}\left[1 - y - \frac{M_N^2 x^2 y^2}{Q^2} + \frac{y^2}{2}\frac{1+4M_N^2 x^2/Q^2}{1+R}\right] F_2^{EM}(x,Q^2), \tag{5.22}$$

written now in terms of F_2 and R. $R = \sigma_L/\sigma_T$, the ratio of the longitudinally to transversely polarized virtual photon absorption cross-sections and, ignoring mass terms, $R = F_L/(F_2 - F_L)$. To disentangle F_2 and F_L or R at fixed (x, Q^2) requires data collected at different centre of mass energies. This has been done by most of the fixed target experiments and more details are given in Sec. 5.4.3. At HERA, which has run at essentially a fixed CM energy, F_L is usually a calculated correction. In fact for most of the experiments considered here, the effect of F_L on the cross-section is small because it appears multiplied by y^2, which is a small quantity. However, given the intrinsic accuracy of the structure function data, a consistent treatment of R is important and the lack of such has caused apparent inconsistencies between data sets in the past.

The key parameters of the data sets considered here are summarised in Table 5.1. For most of the experiments listed the measurement of the NC cross-section, $\dfrac{d^2\sigma(\ell N)}{dxdQ^2}$, has been essentially that of F_2^{EM} up to small corrections and unless otherwise stated, F_2 will be taken to mean F_2^{EM} for the proton. Although a number of other DIS experiments are of great historical importance, the experiments considered here are the ones that provide the bulk of the data for the determination of parton densities. References to the original measurements and other information on how to get access to structure function data are given in Appendix F.

Table 5.1 Key parameters of DIS experiments.

Beam(s)	Targets	Experiment	Q^2 (GeV^2)	x	R	Process
e^-	p,d,A	SLAC	$0.6 - 30$	$0.06 - 0.9$	$\surd$	NC
μ	p,d,A	BCDMS	$7 - 260$	$0.06 - 0.8$	$\surd$	NC
μ	p,d,A	NMC	$0.5 - 75$	$0.0045 - 0.6$	$\surd$	NC
μ	p,d,A	E665	$0.2 - 75$	$8 \cdot 10^{-4} - 0.6$	-	NC
$\nu, \bar{\nu}$	Fe	CCFR	$1. - 500.$	$0.015 - 0.65$	$\surd$	CC
$e^{\pm}$, p	-	H1	$0.35 - 3 \cdot 10^5$	$6 \cdot 10^{-6} - 0.65$	$\surd$	NC,CC
$e^{\pm}$, p	-	ZEUS	$0.045 - 3 \cdot 10^5$	$6 \cdot 10^{-7} - 0.65$	-	NC,CC

The regions in (x, Q^2) covered by the experiments are shown in Fig. 5.1, the Q^2 scale is that of the HERA collider. The fixed target experiments occupy the lower right hand corner. For all experiments there is broad correlation between x and Q^2 – large x is reached only at large Q^2. The constraints outlined in 5.1 are also evident in the figure. For a given experiment, the region at low Q^2 is limited by the angular acceptance of scattered beam lepton detector and each region is limited at small y by worsening x resolution. For large y, the limit is set by the minimum value of the scattered $e^{\pm}$ that can be efficiently identified in the rear calorimeters. For standard triggers, the values are 6.9 and 8 GeV for H1 and ZEUS respectively. Worsening resolution at large x accounts for the limited overlap of the regions covered by the fixed target and HERA experiments. However a direct comparison of normalisations is important and in the analysis of the very large 1996/7 HERA data samples improved methods of kinematic reconstruction using combinations of electron and hadron information have allowed a significant extension to small y, giving a region of overlap. In addition, because of the very large CM energy available at HERA, new regions of phase have been opened up at both large Q^2 and small x.

5.4.1 F_2

An overview of the data for F_2 is shown in Fig. 5.9. The data is plotted at fixed x over 5 orders of magnitude as a function of Q^2, which ranges over 4 orders of magnitude. For x bins larger than 0.01, the data shows only a gradual or even zero dependence on Q^2. This is Bjorken scaling, as expected from the simple quark-parton model (Chapter 2). For smaller values of x, F_2 is rising quite strongly with Q^2. Another important feature is the consistency of the data from the different experiments, both fixed target and HERA collider. The good agreement in shape and normalisation between the F_2 data sets is shown in more detail as a function of Q^2 in Fig. 5.10 for six bins of x.

Although on the scale of Fig. 5.9 there is apparent Bjorken scaling over quite a range of x values, the precision of the F_2 data sets allows this to be studied in detail. Exact scaling in Q^2 is rather the exception than the rule. Of the x bins shown in Fig. 5.10, scaling is only evident for $x = 0.18$.

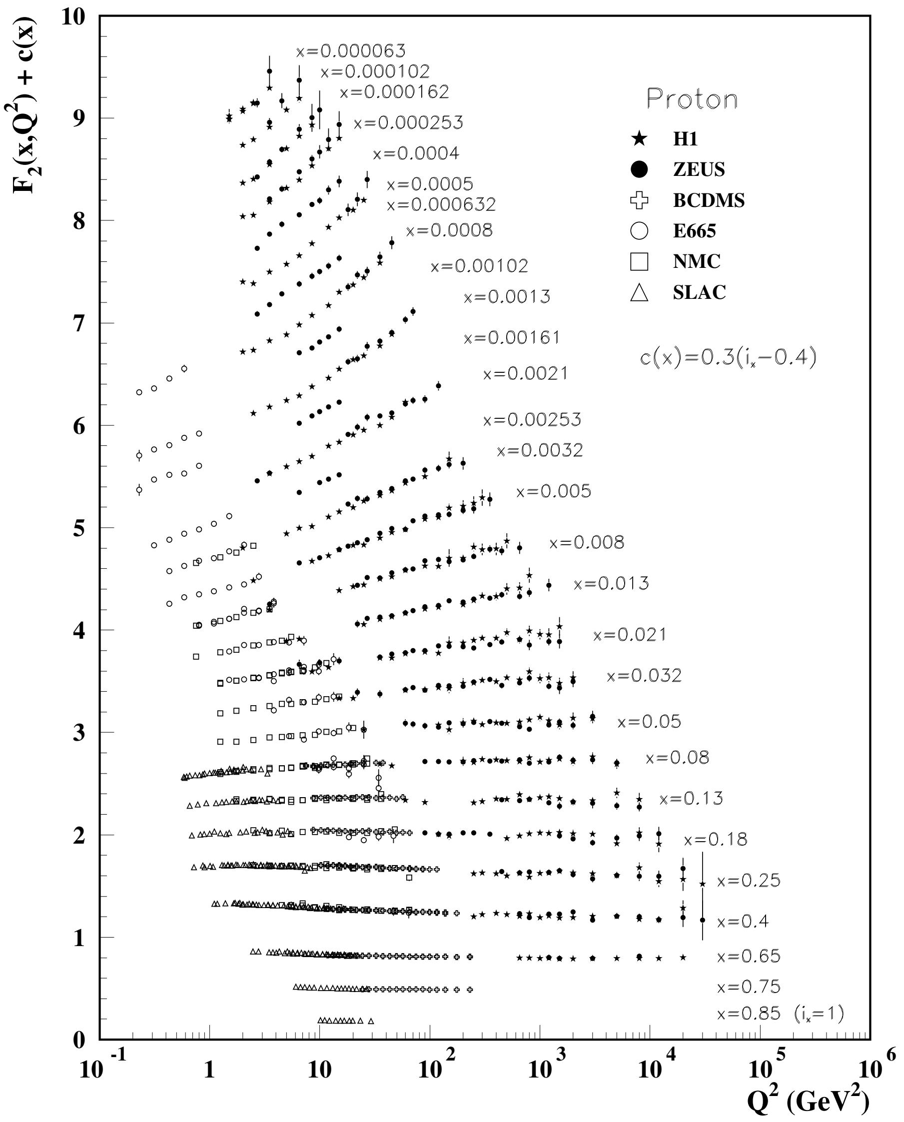

Fig. 5.9 F_2^p data from HERA and fixed target experiments at fixed x as a function of Q^2. Note that for clarity a constant $c(x) = 0.3(i_x - 0.4)$ has been added to F_2 where i_x labels the 28 bins x bins in decreasing order. The plot is from the PDG tables [PDG02] and full references to the data are given in Appendix F.

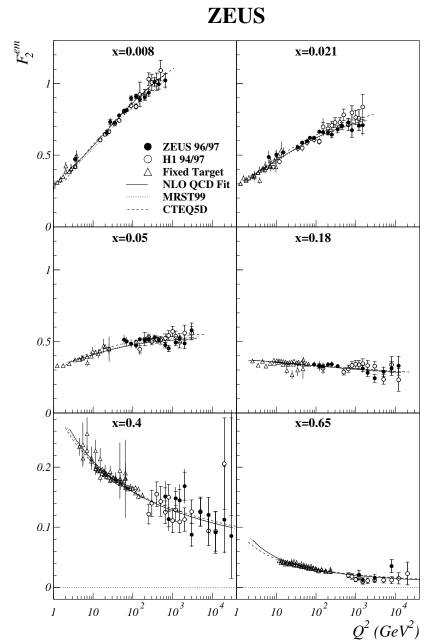

Fig. 5.10 F_2^p in six x bins showing the good agreement in shape and normalisation between fixed target and HERA data.

Similar features are shown for some of the fixed target experiments in Fig. 5.11, it is clear that there is a systematic breaking of exact scaling. At large values of x, F_2 decreases as Q^2 increases and at small values of x the structure function increases with Q^2. In both cases the variation with Q^2 is approximately logarithmic, as expected from the QCD enhanced parton model (Chapter 4).

For most of the fixed target data and the HERA data for Q^2 up to almost $1000\,\mathrm{GeV}^2$, systematic errors are larger than statistical. Systematic errors are typically at the level of 2% or less and are dominated by uncertainties in absolute energy calibrations and beam flux or luminosity measurements. For the HERA data, F_L was calculated using the QCD expression (Eq. 4.39) with a consistent set of parton densities. Most of the fixed target experiments made use of a parametrisation of R, produced by Whitlow et al [Whi90] in the course of reanalysis of the original DIS data from SLAC. However as R was usually measured in the same experiment, the direct measurement provided an alternative approach and certainly a check on the parametrisation.

So far the data has been plotted in a way that illustrates immediately the essential prediction of pQCD, namely logarithmic breaking of scaling with Q^2. Perturbative QCD and particularly the standard DGLAP

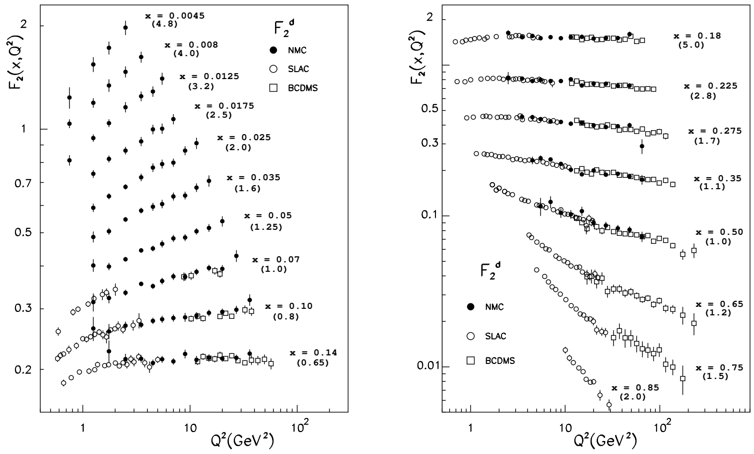

Fig. 5.11 A comparison of F_2^d from the NMC(97), SLAC and BCDMS datasets. The SLAC and BCDMS data were rebinned to the NMC x bins. The data in each x bin are scaled by the factors indicated in brackets. The error bars represent the total error, apart from the overall normalization.

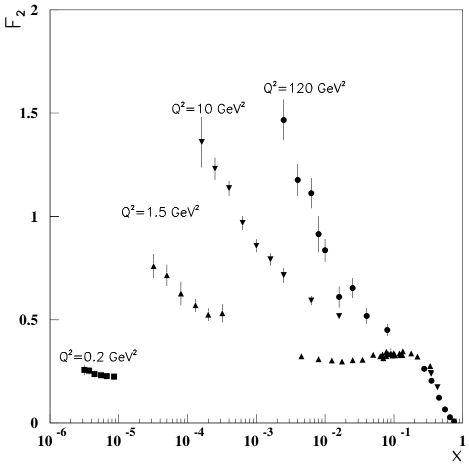

Fig. 5.12 F_2^p data showing the strong rise at small x. The HERA data are from the 1994 runs and the data for $Q^2 = 1.5\,\mathrm{GeV}^2$ and $x > 10^{-3}$ (triangles) are from fixed target experiments. Figure from [Abr99].

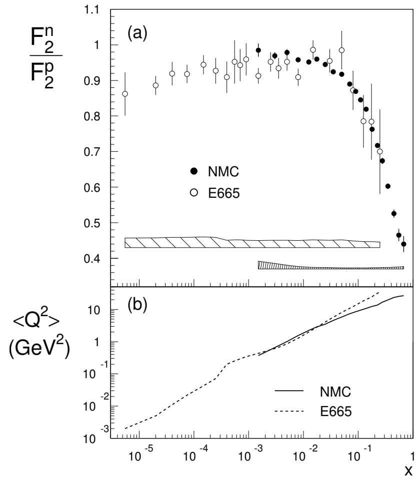

Fig. 5.13 (a) F_2^n/F_2^p averaged over Q^2 as a function of x from the NMC and E665 experiments. (b) $\langle Q^2 \rangle$ for the above data as a function of x. From [NMC97b].

approach has much less to say about the x dependence of the structure functions. To illustrate one of the most striking features of the F_2 results from HERA, it is necessary to plot the data versus x at fixed Q^2. This is done for three representative values of Q^2 in Fig. 5.12 and it shows that F_2 rises steeply as x decreases and that the strength of the rise increases as Q^2 increases. The rise in x is strong, at $Q^2 = 120\,\text{GeV}^2$ F_2 increases by almost a factor of 3 as x decreases from 0.08 to 0.003. Possible explanations for this behaviour are discussed in Chapter 7. It is worth remarking that while a range of possible behaviours had been predicted for F_2 at small x, including a strong rise, when the first preliminary HERA data showing a rising F_2 was presented at the Durham Workshop in 1993 [DeR93] it caused great excitement. The data for $Q^2 = 1.5\,\text{GeV}^2$ and $x > 10^{-3}$ (triangles) in Fig. 5.12 shows why – before HERA the data showed a fairly flat behaviour as x decreased with only the merest hint of a possible rise.

At very low Q^2, F_2 no longer rises steeply. Although it perhaps cannot be described as deep inelastic scattering, the behaviour of F_2 for very small Q^2 is very interesting and has been investigated in some detail at HERA. The measurements are summarised in Sec. 5.5.

A measurement that is of importance for the extraction of nucleon parton densities is the ratio F_2^n/F_2^p. Both the E665 and NMC experiments have deduced the ratio from primary measurements on the ratio of deuterium to proton cross-sections. A summary of the data, averaged over Q^2,

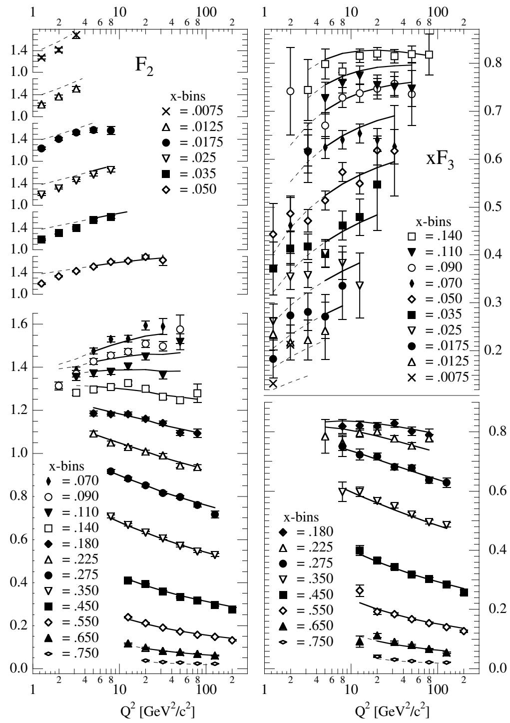

Fig. 5.14 CCFR(97) F_2 and xF_3 data as functions of Q^2 at fixed x. The results of a NLO QCD are also shown (full line), the dashed line is the extrapolation of the fit to lower Q^2. From [Sel97].

is shown in Fig. 5.13(a), the lower part of the figure (b) shows how the average value of Q^2 varies with x. The size of the systematic errors are also indicated. The F_2^n/F_2^p ratio approaches 1, within errors, as x decreases and appears to be approaching 0.4 as x tends to 1.

5.4.2 $F_2^{\nu N}$ and $xF_3^{\nu N}$

Most DIS experiments with incident neutrino beams have been performed on heavy targets to increase the interaction rate. The CCFR/NuTeV experiment is the most recent and probably definitive such experiment to date. Because of the handedness of the $\nu, \bar{\nu}$ couplings, the parity violating structure function xF_3 can be determined as well as F_2. This is important because the scaling violations of xF_3 in QCD do not involve the gluon density and hence offer, in principle, a direct way of measuring α_S (see Secs **??** and 4.2). CCFR data for F_2 and xF_3 have been measured for x between 0.0075 and 0.75 and Q^2 between 1.3 and 126 GeV^2 and are shown in Fig. 5.14. The major difference between this data and the other data considered in this chapter, is that significant nuclear corrections must be

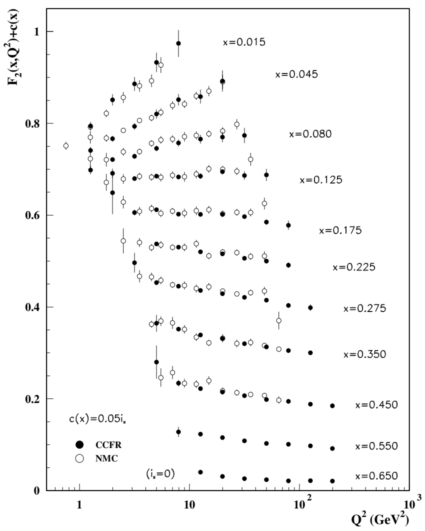

Fig. 5.15 Comparison of $F_2^{\mu d}$ from NMC [NMC97a] and $F_2^{\nu d}$ derived from CCFR data [Yan01] using Eq. 5.23. For clarity a constant $c(x) = 0.05(i_x - 1)$ has been added to F_2 where i_x labels the 11 bins x bins in decreasing order. From PDG data tables [PDG02].

applied to the CCFR before it can be compared with DIS data from proton or deuterium targets or vice-versa. The $F_2^{\nu N}$ data (per nucleon) show a similar pattern of scaling violations to that already discussed. The curves shown in Fig. 5.14 are from an NLO QCD fit to determine α_S.

From the QPM one expects $F_2^{\ell N} \approx \frac{5}{18} F_2^{\nu N}$ and this was an important early test of the model (see Sec. 2.4). CCFR have used the more exact form of the relation (Eq. **??**)

$$F_2^{\mu d} = \frac{5}{18} F_2^{\nu d} - \frac{1}{6}\left(s + \bar{s} - c - \bar{c}\right) \tag{5.23}$$

to compare their data with that from NMC and other fixed target e and μ iduced DIS experiments [Yan01]. Nuclear corrections are applied to the Fe target neutrino data to produce $F_2^{\nu d}$ equivalent data. Fig. 5.15 shows the relationship between the neutrino and muon data are in good agreement over a wide range of x and Q^2. To achieve this level of agreement, which at the same time removes an earlier discrepancy in the lowest x bin, the CCFR group had to modify some details of how F_2 was extracted from the differential cross-sections [Yan01]. Most of the discrepancy arose from model dependent assumptions on the form of $\Delta x F_3$[5] and heavy quark

[5]The difference between the values for ν and $\bar{\nu}$ beams.

threshold behaviour in the extraction of F_2^ν. Heavy quark effects are different in μ and ν induced DIS, a single charm quark may be produced from the strange sea $\nu s \to \mu^- c$ for example, whereas in μN $c\bar{c}$ pairs have to be produced through the boson-gluon fusion mechanism. These differences will be particularly important in the charm threshold region spanned by the data. The latest analysis is much less model dependent using $\Delta x F_3$ derived from the CCFR data itself and NLO massive quark behaviour for the charm threshold, the Thorne-Roberts formulation giving the best fit (see Sec. 4.7.2 for more details). This brief outline shows both that the QCD enhanced parton model is in good shape and that the level of precision of structure function data demands careful attention to many details.

5.4.3 F_L

Although F_L or R is usually treated as a small correction in the extraction of F_2 from $\dfrac{d^2\sigma}{dxdQ^2}$, it is an important quantity because of its rather direct relation to xg – the momentum density of the proton. Starting from Eqs 5.21, 5.22 at the start of Sec. 5.4 and ignoring xF_3 and mass terms one may express the cross-section as

$$\frac{d^2\sigma}{dxdQ^2} = \frac{2\pi\alpha^2}{Q^4 x} Y_+ \left(1 - \frac{y^2}{Y_+}\frac{F_L}{F_2}\right) F_2(x,Q^2) \tag{5.24}$$

$$= \frac{2\pi\alpha^2}{Q^4 x} Y_+ \left(\frac{1+\varepsilon R}{1+R}\right) F_2(x,Q^2), \tag{5.25}$$

where in the second expression the polarisation parameter of the virtual photon has been introduced, $\varepsilon = \dfrac{2(1-y)}{1+(1-y)^2}$ and $R = F_L/(F_2 - F_L)$. To measure R or F_L directly at a fixed value of (x, Q^2) requires data at two different values of y and hence at two different centre of mass energies (because of the constraint $Q^2 = sxy$). Since R is determined by the ratio of subtracted quantities, one needs very small statistical errors and very good control of the systematic errors at the two different energies. Another way of looking at the problem is to examine the 'leverage' from varying ε as a function of y, the largest variation in ε, for a given change in $\sqrt{s}$, is at large y. This in turn means being able to measure small scattered lepton energies (small E'), which is usually difficult. The fixed target experiments SLAC, BCDMS and NMC have used data taken at different values of s to extract R.

Although no direct measurements of R have been made at HERA, the H1 collaboration [H1 97] have estimated F_L from their large low Q^2 DIS neutral current data sample [H1 01a]. The idea of the method follows from Eq. 5.24, which shows the suppression of the F_L at small y, and the fact that NLO QCD evolution describes the HERA F_2 data very well. F_2 is first determined by applying a NLO QCD fit to H1 data satisfying $y < 0.35$, i.e. in a region where the effect of F_L in the cross-section is small. The fit

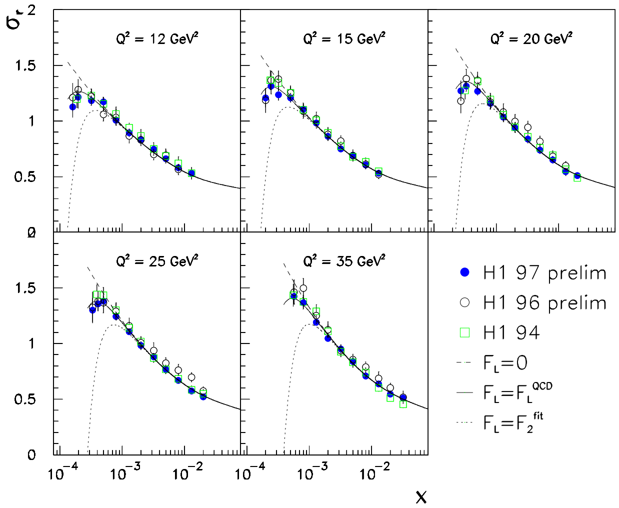

Fig. 5.16 The QCD subtraction method used by H1 to extract F_L.

is then extrapolated to the high y region and used to subtract the contribution of F_2 from the cross-section at high y (≈ 0.7). The principle of the method is shown in Fig. 5.16. For this analysis the minimum cut on E' was lowered from 6.9 to 3 GeV, thus extending the y range to $y \leq 0.89$. The identification of very low energy scattered positrons in the H1 SPACAL was made possible by associating charged particle tracks from the central tracker with SPACAL energy clusters. A summary of the resulting data on F_L from H1 and from fixed target experiments is shown in Fig. 5.17. Although the errors are large, the data are well consistent with the behaviour expected from QCD as shown by the fit curve in the figure.

5.4.4 $F_2^{c\bar{c}}$

The structure functions studied so far are inclusive objects and thus contain contributions from both valence and sea quarks. The ability of a detector to provide identification of a particular quark flavour opens up the possibility of studying the contribution of that flavour to F_2. This is particularly interesting in the case of heavy flavours, as they are likely to be produced in the hard scattering and not in the subsequent hadronisation of the struck parton. It is estimated that charm could account for as much as 30% of F_2 for $x < 0.001$ and $Q^2 > 10\,\mathrm{GeV}^2$. At order α_S heavy quark production in DIS occurs through the boson-gluon fusion process (BGF). This process involves the gluon density xg directly so it gives another experimental handle on this quantity. As heavy flavour production by BGF occurs at relatively small x, a signal at large x might indicate other production mechanisms or even be evidence for intrinsic heavy flavour in the proton.

The first measurements of $F_2^{c\bar{c}}$ were made by fixed target experiments at FermiLab and CERN. For example the EMC collaboration [Aub83] mea-

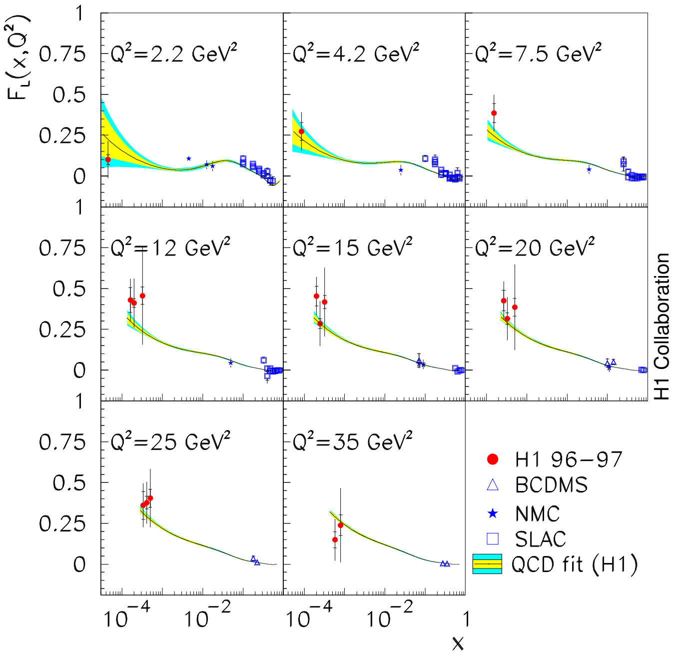

Fig. 5.17 F_L as a function of x in bins of Q^2 as obtained by H1 using the QCD fit and extrapolation method explained in the text, together with measurements from fixed target experiments at larger x. The curve and error band shows the result of a QCD by H1. From [H1 01a].

sured $F_2^{c\bar{c}}$, in the range $0.0042 < x < 0.422$, $1 < Q^2 < 70\,\text{GeV}^2$, from di- and trimuon events produced from 250 GeV muon scattering on an iron target. The advent of HERA, with a reach to much smaller x values, together with detectors capable of measuring details of the DIS final state gives the prospect of accurate data on $F_2^{c\bar{c}}$ over a much wider range of x and Q^2. The second major step forward since the early measurements is the improved theoretical treatment of heavy quark production to order α_S^2, as described in Sec. 4.7. Expressions for the rapidity and transverse momentum distributions of the charm quark have been worked out to the same order and incorporated into a Monte Carlo code describing the production and fragmentation of heavy quarks in ep scattering (HVQDIS, [Har98]). Heavy quark production has also been incorporated into the CASCADE Monte Carlo code [Jun01], which is based on the CCFM equation (which effectively resums certain higher order terms at low x – see Sec. 7.6). Heavy quark events may be identified by a variety of techniques: D^* and D decays for charm; high p_T electrons and muons; secondary vertices and broading of charged track impact parameter distributions. Most of the data on charm production in DIS from HERA-I has come from the first technique. Heavy quark physics is one of the major goals of the HERA-II programme and

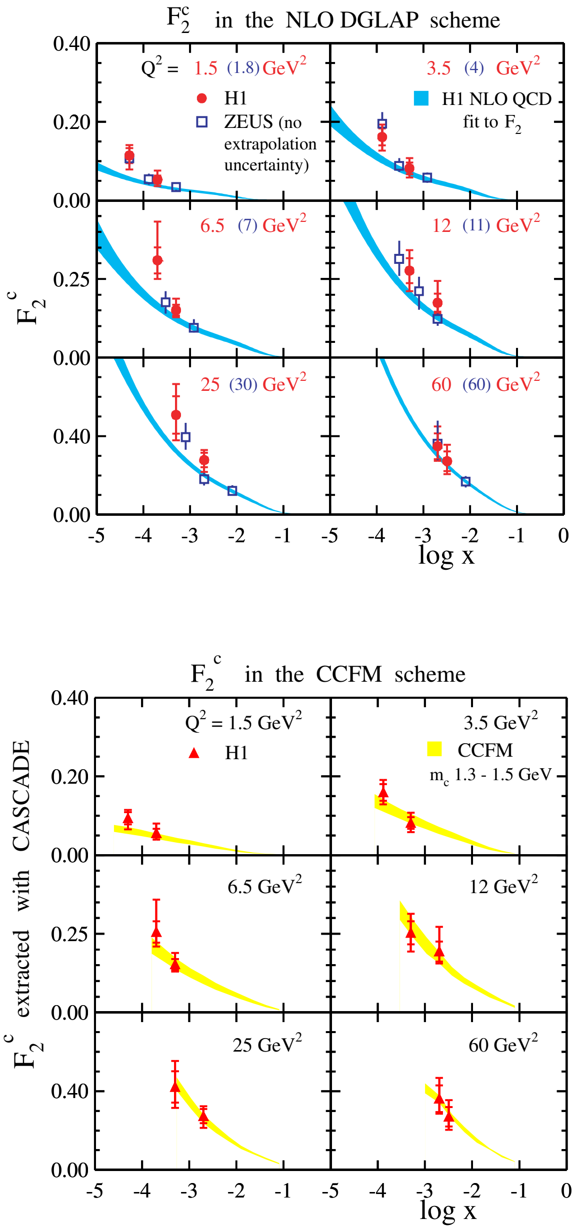

Fig. 5.18 $F_2^{c\bar{c}}$. The upper plots show data from the ZEUS and H1 corrected with HVQDIS and compared to NLO QCD calculation using the H1 gluon density. The lower plots show the H1 data corrected using the CASCADE Monte Carlo. From [H1 01b].

event selection efficiencies will be improved significantly by the use of new or improved microvertex detectors.

Both the H1 and ZEUS experiments have searched for D^* production in DIS using the well-established technique which exploits the accurately known mass difference $\Delta M = M(K\pi\pi_s) - M(K\pi)$ (from the decay chain $D^{*+} \to D^0\pi_s^+ \to K^-\pi^+\pi_s^+$) as the primary signal. The D^* is only just above threshold and its decay produces a 'slow' pion, π_s. H1 have also identified $D^0 \to K^+\pi^-$ decays directly and ZEUS have added the $D^0 \to K^+3\pi$ decay channel. Although the signal is a very clean one, the combined branching ratios are small (for the $D^* \to K\pi\pi$ it is $2.62 \pm 0.10\%$) which means that high luminosity is required.

For example in the analysis of the $37\,\mathrm{pb}^{-1}$ of data collected by ZEUS in 1996/7, the data sample of D^* events amounted to 2064 ± 72 $(K2\pi)$ and 1277 ± 124 $(K4\pi)$ [ZEU00a]. From these events the $ep \to eD^*X$ cross-section is measured in a restricted region of D^* phase space, defined by cuts on $p_T(D^*)$ and $\eta(D^*)$. The measured cross-section for each D^* decay channel is then extrapolated to the full phase space using the HVQDIS code – clearly an important prerequisite is that the simulation describes the $p_T(D^*)$ and $\eta(D^*)$ distributions in the measured regions. In a similar analysis H1 [H1 01b], has also measured D^* production, paying particular attention to the model uncertainties in the extraction of the cross-section. For the H1 data, from $18.6\,\mathrm{pb}^{-1}$, the integrated cross-section for D^* meson production in the kinematic region $1 < Q^2 < 100\,\mathrm{GeV}^2$ and $0.05 < y < 0.7$, and in the visible D^* range $|\eta^{D^*}| < 1.5$ and $p_T^{D^*} > 1.5\,\mathrm{GeV}$ is

$$\sigma_{vis}(e^+p \to e^+D^{*\pm}X) = 8.50 \pm 0.42(\mathrm{stat.})^{+1.02}_{-0.76}\,(\mathrm{syst.}) \pm 0.65(\mathrm{model})\,\mathrm{nb}.$$

The errors are those from statistics, experimental systematics and additional systematics related to the changes in efficiency obtained by using different Monte Carlo generators and varying the model parameters. The value of the predicted cross-section shows a large variation with the mass of the charm quark, fragmentation function parameters and the overall theoretical approach. For example, using the NLO DGLAP scheme with the HVQDIS the predictions range from 5.17 nb to 7.02 nb for $m_c = 1.5 \to 1.3\,\mathrm{GeV}$[6] For the same variation of m_c, calculations based on the CCFM approach, as implemented in the CASCADE program, yield significantly higher cross-sections of 8.04 nb and 10.77 nb, respectively.

To get from the measured $ep \to eD^*X$ cross-section to the inclusive charm production cross-section one needs to extrapolate to the full D^* phase space, to know the probability that the charm quark will fragment into a D^* meson $(P(c \to D^*))$ and to correct for the small fraction (ξ) of indirect D mesons produced through B meson decay or fragmentation,

[6] The fragmentation function has also been varied, but the largest effect is from the charm mass uncertainty.

$$\sigma(ep \to ec\bar{c}X) = \frac{1}{2}\frac{\sigma(ep \to eDX)}{P(c \to D)(1+\xi)}. \tag{5.26}$$

From measurements at e^+e^- colliders,$P(c \to D^{*\pm}) \sim 25\%$ and ξ is about 2%. Finally $F_2^{c\bar{c}}$ is related to the $ep \to ec\bar{c}X$ cross-section by

$$\frac{d^2\sigma(c\bar{c})}{dxdQ^2} = \frac{2\pi\alpha^2}{Q^4 x}\left(F_2^{c\bar{c}} - y^2 F_L^{c\bar{c}}\right), \tag{5.27}$$

where the small contribution from $F_L^{c\bar{c}}$ is either ignored or calculated from QCD.

The upper plots in Fig. 5.18 show the ZEUS and H1 $F_2^{c\bar{c}}$ data derived from D^* decays using the HVQDIS approach for extrapolation to the full phase space. The size of the error bars reflects the limited statistics and the model uncertainties. The data from the two experiments are in good agreement with each other. The curves shown are NLO massive quark DGLAP predictions using a gluon density derived from fitting H1 F_2 scaling violations. The uncertainty comes largely from the uncertainty in m_c. Although the overall agreement with data is quite good, there is a tendency for the theory to undershoot the data at low x. H1 have investigated this further by using the CCFM CASCADE code for the extrapolation – the results are shown in the lower plots of Fig. 5.18. In the same plots the data are compared with a CCFM calculation using an unintegrated gluon density derived from fitting H1 F_2 and forward jet data, the uncertainty in the calculation is again from the spread in m_c. A comparison of the upper and lower plots shows a steeper rise in the predicted $F_2^{c\bar{c}}$ at small x using CCFM evolution than that obtained from NLO DGLAP. Using the acceptances and efficiencies calculated from the CASCADE program the measured values of the H1 $F_2^{c\bar{c}}$ are found to be systematically smaller than those determined with the HVQDIS program. The largest differences (up to $\approx 20\%$) are observed at small x values. Clearly high statistics measurements of $F_2^{c\bar{c}}$ at HERA-II are going to be an important tool for furthering the understanding of low x parton dynamics.

5.5 F_2^p at very low Q^2

A remarkable feature of the proton structure function F_2 is its rapid rise at low x – shown in Fig. 5.12. First observed for Q^2 values above $10\,\mathrm{GeV}^2$, the persistence of this rise down to Q^2 values as small as $0.65\,\mathrm{GeV}^2$ challenges our understanding of QCD. For smaller values of Q^2, the rise of the structure function at small x diminishes, as shown in Fig. 5.19. It is not surprising that the behaviour of F_2 changes as $Q^2 \to 0$ for x small. At small x F_2 is related to the $\gamma^* p$ total cross-section

$$\sigma_{tot}^{\gamma^* p}(W^2, Q^2) \equiv \sigma_T + \sigma_L = \frac{4\pi^2\alpha}{Q^2}F_2(x, Q^2),$$

where $W^2 \approx Q^2/x$ (the derivation of this relation is given in Appendix D). The above equation shows that $F_2(x, Q^2) \to \mathrm{const.}Q^2$ as $Q^2 \to 0$, as it

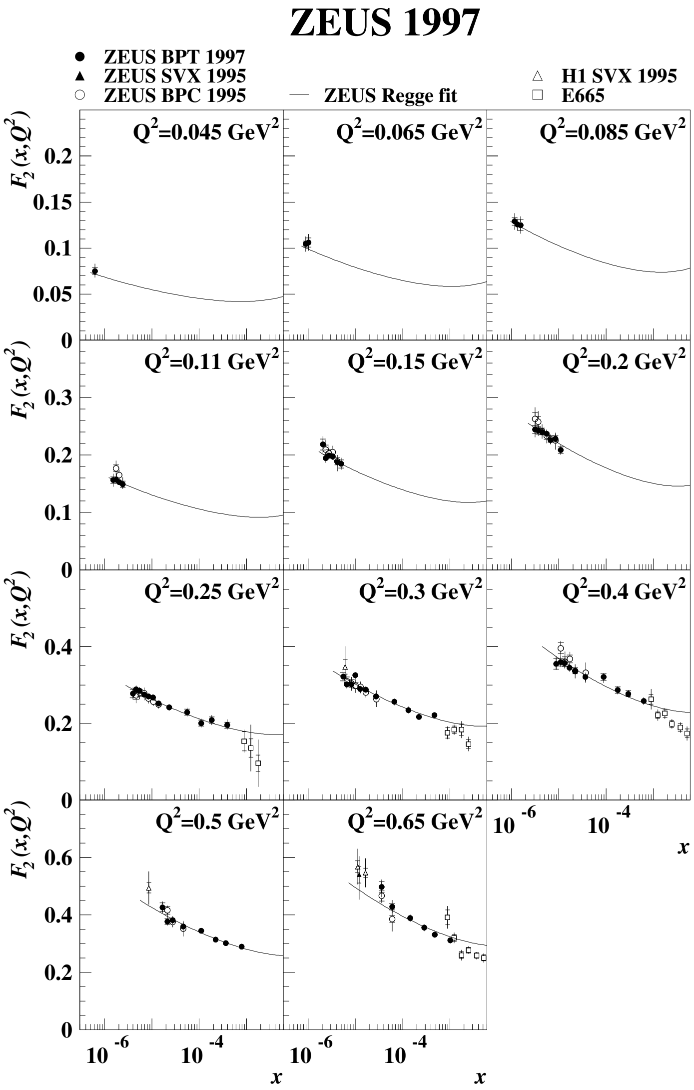

Fig. 5.19 F_2 as a function of x in bins of Q^2 at low Q^2. Data from ZEUS and H1 measurements as indicated. The solid line is a Regge parameterisation discussed in the text. From [ZEU00c].

must to satisfy conservation of the electromagnetic current. The surprising features of the HERA data are that NLO QCD appears to describe the data to really quite low values of Q^2 and that the strong rise of F_2 at small persists to even smaller Q^2 values. HERA has opened a new arena in which to investigate the limits of pQCD.

The ZEUS collaboration has investigated the transition from deep inelastic scattering to photoproduction [ZEU99s]. This first study used data from the ZEUS BPC and 'shifted vertex' data from ZEUS and H1, as well as data at low x and Q^2 from the fixed target E665 experiment. It was found that the hadronic Regge parameterisation (see Sec. 7.4) which gives a good description photoproduction data, fails to describe the F_2 data in the region above $Q^2 = 0.9\,\mathrm{GeV}^2$. Next-to-leading-order QCD fits are successful when taken down to these low Q^2 values. As Q^2 approaches $1\,\mathrm{GeV}^2$, however, the fits yield vanishing gluon densities at low x, while the sea-quark density remains finite. This behaviour and the problem of interpreting it are discussed in detail in Chapter 6, particularly 6.5.

To provide more precise data to assist in answering some of these questions, the ZEUS collaboration made further measurements at low Q^2 using the more precise BPC/BPT combination [ZEU00c]. The BPC/BPT data, from an integrated luminosity of $3.9\,\mathrm{pb}^{-1}$, spans the kinematic ranges $0.045 < Q^2 < 0.65\,\mathrm{GeV}^2$ and $6 \cdot 10^{-7} < x < 1 \cdot 10^{-3}$. Fig. 5.20 shows the BPC/BPT data for F_2 as a function of Q^2 in bins of y. Data from other ZEUS and H1 measurements at low Q^2 are also shown. The dashed curves show a ZEUS NLO QCD fit, which describes the data well down to $Q^2 \sim 1\,\mathrm{GeV}^2$. The solid curve labelled 'ZEUS Regge fit' is the function

$$F_2(x, Q^2) = \left(\frac{Q^2}{4\pi^2\alpha}\right)\left(\frac{M_0^2}{M_0^2 + Q^2}\right)\left(A_{\mathbb{R}}\left(\frac{Q^2}{x}\right)^{\alpha_{\mathbb{R}}-1} + A_{\mathbb{P}}\left(\frac{Q^2}{x}\right)^{\alpha_{\mathbb{P}}-1}\right), \tag{5.28}$$

with $\alpha_{\mathbb{R}} = 0.5$ fixed and $A_{\mathbb{R}} = 147.8 \pm 4.6\,\mu\mathrm{b}$, $A_{\mathbb{P}} = 62.0 \pm 2.3\,\mu\mathrm{b}$, $\alpha_{\mathbb{P}} = 1.102 \pm 0.007$, $M_0^2 = 0.52 \pm 0.04\,\mathrm{GeV}^2$ (statistical and systematic errors added in quadrature) determined from the final iteration of the bin-by-bin unfolding of F_2 from the raw data. The form of Eq. 5.28 is based on a minimal combination of vector dominance and Regge theory (see [ZEU99s] for details). What is important here is that it incorporates the required behaviour of F_2 as $Q^2 \to 0$ and shows that the data is compatible with a smooth transition in the Q^2 range $0.1 - 1\,\mathrm{GeV}^2$ from an approximately constant behaviour to $F_2 \approx \mathrm{const} \cdot Q^2$. Much more detail on the physics of the low x region is given in Chapter 7, particularly Secs 7.3, 7.4 and 7.8.

5.6 summary

This chapter has given an account of the detectors used for fixed target and HERA collider deep inelastic scattering, together with the principal methods for reconstruction of the kinematic variables, x, y and Q^2, and the extraction and correction of the cross-sections and structure functions from the measured event rates. The main features of structure function data for $Q^2 < M_Z^2$ from the 'classic' fixed target and HERA experiments have been outlined, particularly the rise of F_2^p at low x. The importance of neutrino induced DIS has been touched upon and the promise of learning more about parton dynamics at low x from accurate measurements of $F_2^{c\bar{c}}$

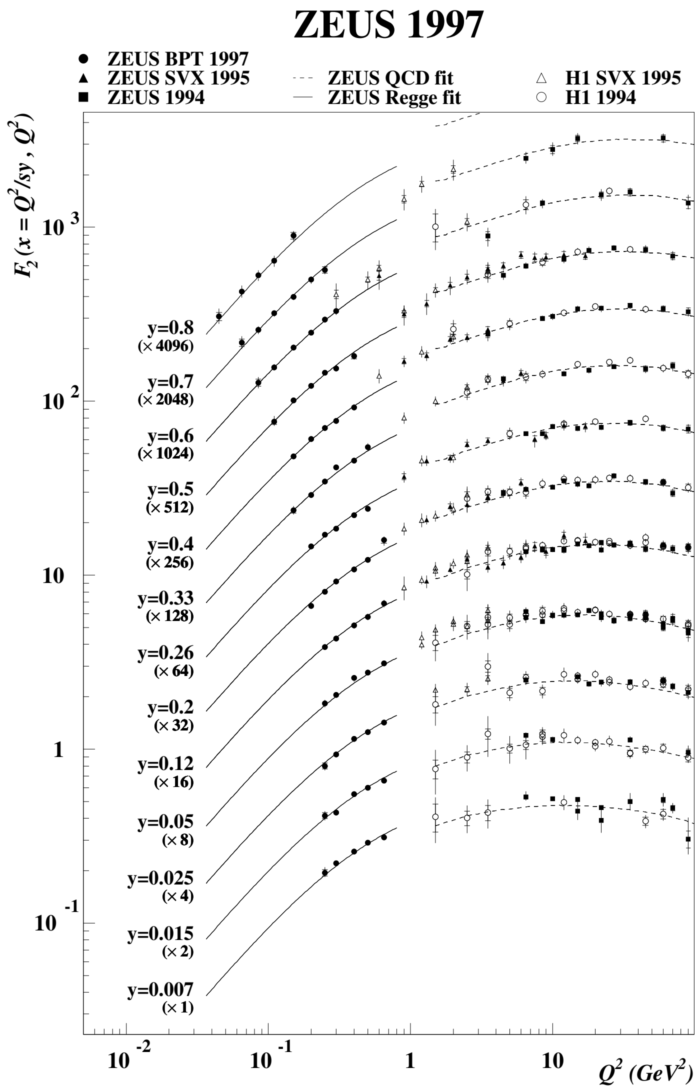

Fig. 5.20 F_2 as a function of Q^2 in bins of y at low Q^2. The solid circles show the data from the ZEUS BPC/BPT and data from other ZEUS and H1 measurements as indicated. The solid line is a Regge parameterisation and the dashed line a ZEUS NLO QCD fit. From [ZEU00c].

elaborated. The chapter ends with an outline of the precise measurements of F_2 in the 'transition region' as $Q^2 \to 0$.

For the immediate future, there is a wealth of new data expected from HERA-II and more neutrino induced DIS data from the NuTeV experiment (which evolved from CCFR) at the Tevatron.

5.7 questions

1. Use the equations of Sec. 5.1.1 to work out the region in the x, Q^2 plane in which a fixed target detector with the given characteristics could measure x to within 10% and Q^2 to within 5%. [$E_\mu = 280\,GeV$; $E'_{min} = 40\,\text{GeV}$; $\theta_{min} = 15\,\text{mrad}$; $\delta E'/E' \sim 10^{-4}$; $\delta\theta \sim 1\,\text{mrad}$.]
2. The hadronic angle γ for DIS at HERA. Assume that in the hard ep interaction, the electron strikes a quark with momentum xP to produce the scattered electron (E',θ) and a massless object of energy F at an angle γ. Assume further that the proton remnant has zero transverse momentum. Show that: $F = \sum_h E - (1-x)P$; $F\cos\gamma = \sum_h p_z - (1-x)P$; $F\sin\gamma = \sqrt{\sum_h p_t^2}$; where $\sum_h$ is the sum over *all* final state hadrons. From these results find an expression for F and verify that $\cos\gamma$ is given by equation 5.10.
3. Derive the Jaquet-Blondel formula for y at HERA (equation 5.13).
4. Using the results of the previous two questions, complete the derivation of the double angle formulae for HERA kinematics (Eqs 5.11, 5.12). [You may find it helpful to derive an expression for y first, starting from y_Σ.]
5. Design a beam line to provide high energy ν and $\bar{\nu}$ for DIS experiments. Assume that high intensity 400 GeV charge selected $\pi^\pm$ and $K^\pm$ beams are available. What will the range of neutrino energies be?
6. Taking the dimensions of the ZEUS detector (shown in Fig. 5.5) as typical, estimate the timing resolution needed to reject cosmic ray muons and beam-gas interactions. [Assume that all particles travel at the speed of light.] *Could extend this to include some rate estimates if cross-section details given...*
7. Show that $F_2^{\ell N} = \dfrac{5}{18}\left(1 - \dfrac{3}{5}\dfrac{s+\bar{s}-c-\bar{c}}{\sum(q+\bar{q})}\right) F_2^{\nu N}$ is valid for isoscalar nucleon structure functions ($F_2^N = 0.5*(F_2^p + F_2^n)$). What assumptions have to be made and why is the expression only valid beyond the leading order in QCD in the DIS renormalisation scheme?
8. Verify Eq. 5.25 for R and the expression $\varepsilon = \dfrac{2(1-y)}{1+(1-y)^2}$. Sketch ε as a function of y.

6

Extraction of parton densities

The chapter discusses how parton momentum densities are extracted from data. First the general framework based on NLO pQCD is outlined. Next various sources of input data and possible corrections, complications and uncertainties are considered. An important practical consideration is the choice of functional form and the number of parameters needed to describe the x-dependence of the momentum density at the starting scale, Q_0^2. The concept of the *global fit* is introduced and the choice of reactions and data sets discussed. A detailed account of the results of some global fits is then given. Particular attention is paid to the behaviour of the gluon and sea densities at low x and low Q^2. The problem of defining a reasonable measure of the error on a parton density and how to estimate it are also addressed.

Section 6.5 may contain a bit too much detail

Written Summer 2001, revised Xmas 2001, not yet complete.

6.1 Determining parton distribution functions

This section outlines how the framework developed in the last few chapters has been used to determine parton distributions. Particular attention is paid to the extraction of the gluon distribution since most cross-sections at hadron colliders, present and future, are dominated by gluon induced processes. However, the gluon distribution is the least accurately determined of the parton distributions.

Perturbative QCD predicts the Q^2 evolution of the parton distributions, but not the x dependence. Ideally one would like to find analytic parametrizations of parton distributions, which are consistent with the Q^2 dependence predicted by pQCD. The problem is to perform a Mellin inversion of the exact predictions of pQCD for the moments of structure functions in order to find suitable analytic expressions for the structure functions themselves. However, if one requires consistency with pQCD beyond leading order, one cannot find exact analytic expressions which are valid for more than a limited x, Q^2 range. (Although forms valid in the limits $x \to 0$ and $x \to 1$ can be derived, see [Ynd99]). For this reason, the most commonly used method of extracting parton distributions is to perform a direct numerical integration of the DGLAP equations at NLO. The technique is broadly as follows. An analytic shape for the parton distributions (valence, sea and gluon) is assumed to be valid at some starting value of $Q^2 = Q_0^2$. This starting value is arbitrary, but should be large enough to ensure that $\alpha_s(Q_0^2)$ is small enough for perturbative calculations to be applicable. Then the DGLAP equations (see Secs. 4.2, 4.4) are used to evolve the parton distributions up to a different Q^2 value, where they are convoluted with coefficient functions, appropriate to the chosen renormalization scheme, in order to make predictions for the structure functions. These predictions are then fitted to the data, for whatever x, Q^2 points have been measured. The fit parameters are those necessary to specify the input analytic shape, and Λ_{QCD}, or $\alpha_s(M_Z^2)$. The input analytic form assumed for the parton distributions is only valid at the starting scale Q_0^2. For other Q^2 values the distributions must be interpolated from values at grid points, such as those provided on the Durham data base for the PDFs extracted by the MRS, CTEQ and GRV groups, see Appendix G.

Many groups now produce PDF sets using the method outlined above. The philosophy of the GRV PDFs is somewhat different and Sec 6.5.3 is devoted to explaining it. The experimental groups ZEUS, H1 have concentrated on estimating the uncertainties on such sets from experimental sources and the theoretical groups MRS and CTEQ have concentrated on estimating uncertainties from the input assumptions and theoretical framework. Independent authors such as Botje, Alekhin, Zomer have also made global fits which address the problems of estimating exerimental and model unceratinties.

6.2 Treatment of data sets in global analyses

The most reliable parton distributions are obtained by making global analyses of a wide range of data from DIS and other hard processes. There are various pitfalls to be avoided when combining data from different sources.

6.2.1 Nuclear binding corrections

Firstly, data must be taken on comparable targets. As discussed in Sec. 5.3.3 a heavy nuclear target cannot simply be treated as an additive combination of nucleons, and data taken on such a target have to undergo corrections for nuclear shadowing, binding and Fermi motion effects, before they can be used to extract information on parton distributions within the free nucleon. Modern data are taken on hydrogen or deuterium targets to avoid the need for such corrections. However, in current global fits ν, $\bar{\nu}$ data is still very important in determining the valence distributions and for such beams the event rate on proton/deuterium targets is very low. Accordingly the CCFR ν,$\bar{\nu}$ scattering experiment uses a heavy target and the data are corrected for nuclear effects before they are compared to the electroproduction data.

Thus high luminosity HERA data will be very valuable, since the information which is currently obtained from CCFR data can also be obtained in the charged current processes $e^+p \to \nu X$, $e^-p \to \bar{\nu}X$. For $e^-p \to \nu X$ and left handed polarization

$$\begin{aligned} F_2 &= 2x(u(x,Q^2) + c(x,Q^2) + \bar{d}(x,Q^2) + \bar{s}(x,Q^2)), \\ xF_3 &= 2x(u(x,Q^2) + c(x,Q^2) - \bar{d}(x,Q^2) - \bar{s}(x,Q^2)) \end{aligned} \tag{6.1}$$

(and $F_2 = xF_3 = 0$, for right handed polarization). Whereas for $e^+p \to \bar{\nu}X$ and right handed polarization

$$\begin{aligned} F_2 &= 2x(d(x,Q^2) + s(x,Q^2) + \bar{u}(x,Q^2) + \bar{c}(x,Q^2)), \\ xF_3 &= 2x(d(x,Q^2) + s(x,Q^2) - \bar{u}(x,Q^2) - \bar{c}(x,Q^2)), \end{aligned} \tag{6.2}$$

(and $F_2 = xF_3 = 0$, for left handed polarization). Thus, at large x, these structure functions will give information on the u_v and d_v distributions.

Furthermore, for precision measurements, the need for correction even extends to deuterium targets. Current disagreement on the size of these corrections leads to uncertainty in the d_v/u_v ratio at high x (as discussed in Sec. 5.3.3). The high luminosity HERA charged current data will constrain this ratio without need of such corrections.

6.2.2 Data Consistency

The data sets must be consistent with each other. In the late 1980's there were significant disagreements between various data sets. The muo-production experiments EMC [Aub87] and BCDMS [Ben89,Ben90] disagreed in both normalization and shape and the neutrino production data of the CDHSW and CCFR collaborations differed in shape at low x. A complete re-analysis of the old SLAC experiment was undertaken incorporating modern understanding of relevant corrections, in order to help to resolve these discrepancies. The EMC data have now been superseded by the increased precision of the NMC data, and the CDHSW data have been superseded by the increased precision of the CCFR data. A long standing disagreement in the shape of F_2 as measured in muon (NMC) and ν scattering experiments (CCFR) has recently been resolved by an improved heavy quark treatment (see Sec. 5.4.2)

The DIS data sets which are used in current global analyses are: NMC F_2 data on muon scattering from p and D targets, including the special extraction of the ratio $F_2^{\mu D}/F_2^{\mu p}$ with minimal systematic error; E665 and BCDMS F_2 data on muon scattering from p and D targets; CCFR F_2 and xF_3 data on ν, $\bar{\nu}$ scattering on an Fe target; the reanalysed SLAC data on electron scattering on a proton target; and HERA data from ZEUS and H1 on electron/positron scattering on a proton target. These data sets are presented in Chap 5 and their kinematic ranges on the x, Q^2 plane are shown in Fig. 5.1.

These data sets have been used since they represent the highest precision data sets available, and because detailed information is available on systematic errors and their correlations. The importance of this is explored below.

6.2.3 Treatment of correlated systematic uncertainties

A further problem in the combination of data from different experiments concerns the treatment of systematic errors. Conventionally point to point systematic errors are accounted for by adding them in quadrature to the statistical errors. To date, most global fits do not take full account of correlations between experimental systematic errors since this information was not available for all data sets. The correct procedure when combining different data sets is still a subject of active discussion. This section summarizes the current state of the art.

Update after Durham workshop?

When comparing these χ^2 values one should bear in mind that it is not really possible to define a one standard deviation covariance matrix of uncertainties on these parton distribution functions. Firstly, because the correlations between experimental systematic errors are not easily taken into account *as explored here*. Secondly because there are theoretical uncertainties, which are not easy to quantify in terms of a correlated systematic uncertainty. Sources of such theoretical or 'model' uncertainty are discussed in the next section). Uncertainty is also introduced in the form of parametrization.

A related issue arises when using PDFs as input for calculations of high energy scattering processes in order to constrain the parameters of the Standard Model, or even to investigate physics beyond the Standard Model. The systematic uncertainty on a result coming from the choice of PDF is not easily quantified since the best global fits are derived from similar assumptions. It is necessary to consider variants on the standard PDFs in which the parameters most sensitive to the derived result are varied as widely as possible, while maintaining a reasonable global fit quality taking into account the systematic errors on the input data. An example of such a study id dicussed in Sec. 10.7.2. For an interesting discussion of these issues see *all CTEQ latest - details to be added.*

For example one may vary the gluon parameters in the global analysis in order to delineate the range of admissible distributions bounded by fits which show clear disagreements with one or more data sets. Disagreement seems to consist of an increase in total chisq of ~ 100, i.e. tolerance ~ 10. One should avoid too restrictive a parametrization of the gluon.

Alekhin used only the DIS process for experiments which provided correlated errors and chose $Q^2 > 10\,\mathrm{GeV}^2$ to minimize theoretical uncertainty. One of the most complete works on PDF errors to date comes from Botje [Bot01].

Differences in normalization between data sets may be accounted for by allowing the relative normalizations of data sets to float within the overall absolute normalization uncertainties given by the experiments.

normalisation errors are the ultimate correlated systematics and are non Guassian - to be expanded.

6.3 Theoretical and 'model' uncertainties

6.3.1 Higher Twist Contributions

The DGLAP equations embody the predictions of pQCD in the NLLA at leading twist only. Thus one must be sure that the data which are fitted are not likely to be subject to strong higher twist corrections.

As explained in Sec. 4.6, kinematic higher twist terms, or target mass corrections, arise from the neglect of $O(m^2/Q^2)$ terms in the formalism. These may be accounted for by modifying the scaling variable x. Dynamical higher twist terms have been parametrized by multiplying QCD prediction for the leading twist structure function by a factor $(1 + \frac{h}{Q^2})$, where h is fitted separately in each x bin for which one has data. Fits to the early data (see also Fig. 4.8) indicated that such contributions are large only for high x and low Q^2.

Thus the traditional consensus is that one may cut out the need for higher twist contributions by cutting out the kinematic region in which they are important. A standard choice is to include only data for which $Q^2 \gtrsim 4\,\mathrm{GeV}^2$, $W^2 \gtrsim 10\,\mathrm{GeV}^2$.

However note that: i) F_L may be subject to higher twist corrections for all x, at low Q^2; ii) the renormalon predictions indicate that xF_3 may have small higher twist corrections for all x; iii) if the Q^2 cut is lowered to $1\,\mathrm{GeV}^2$, as in the most recent global fits, one should be more cautious. However since the data at such low Q^2 are also at low x, conventional higher twist terms of the kind discussed in Sec. 4.6 are not expected to be very significant.

In HERA very low x data one might expect to see the effects of unconventional higher twist effects which contribute to parton shadowing (these are discussed in Sec. 7.9). However, modern global fits including higher twist parameters, such as the h defined above, have indicated a need for small negative higher twist terms at medium x values $(0.01 < x < 0.3)$, but no need for higher twist terms at very low x (see Sec 6.5.2). This is in agreement with the low x higher twist calculations which suggest cancellations in the contributions to F_2.

6.3.2 Diffractive Events

When considering the applicability of QCD analyses of DIS data it is also necessary to consider the presence of diffractive-like events in the deep inelastic scattering event sample. It has been established that there is a contribution to this sample of approximately 10% from events with a large rapidity gap towards the proton remnant, with characteristics as measured in hadronic diffractive exchange [Gal97,Eic97]. These events may originate from a different production mechanism as compared to the bulk of the deep inelastic scattering data, for example, they include processes such as exclusive vector meson production. So far no special account has been taken of this in the extraction of partons from inclusive F_2 measurements.

6.3.3 Heavy Quark Production Schemes

The treatment of heavy quark thresholds, needs careful consideration. The theoretical background to this has been given in Sec. 4.7. Historically the global fits used a zero-mass variable flavour number (ZM-VFNS) scheme, assuming $c(x, Q^2) = 0$ for $Q^2 \leq m_c^2$. The charm content of the nucleon at higher Q^2 is then generated by the boson-gluon fusion process, as embodied in the DGLAP equations for massless partons. Clearly such a treatment of heavy quarks can only be valid far above the relevant thresholds, $W^2 \gg 4m_q^2$. Near threshold a proper treatment of quark mass effects is required. The fixed flavour number schemes (FFNS) treat the threshold correctly, generating charm by BGF for $W^2 > 4m_c^2$, but $\ln(Q^2/m_c^2)$ terms are not resummed for higher Q^2. One requires a consistent treatment of charm from threshold to high Q^2. The formalism of such general mass variable flavour number schemes (GM-VFNS), has been described in Sec. 4.7.2 and is used in many of the modern global fits.

(*Illustrative figure with F_2^{charm} done all 3 ways?*)

The contributions of bottom and top quarks are treated similarly to charm, and but they turn out to be negligible for present data. A further small uncertainty come from the value used for the heavy quark mass.

One should also be careful when comparing data from neutrino and muon/electron scattering, since the effect of mass thresholds will be different. In neutrino scattering charmed quarks can be produced directly from scattering off the strange sea, as well as in the boson-gluon fusion process (flavour excitation, $W^* s \to c$, as well as flavour creation, $W^* g \to s\bar{c}$) and the former process is dominant at the energies at which present day neutrino data have been taken. Historically neutrino data were corrected with a 'slow rescaling' prescription to allow for the charm mass threshold in the flavour excitation process [Bro80]. However this is not really adequate when doing a NLO analysis. This was the source of a long standing disagreement between F_2 measurements in muon (NMC) and neutrino (CCFR) scattering. A full GM-VFN treatment of the flavour creation process has resolved the discrepancy, see Sec. 5.4.2.

6.3.4 Which evolution equation?

It is implicitly assumed that the DGLAP evolution equations can be applied in the kinematic range studied. However, at low x, it may be necessary to consider the BFKL equation, or at least to include $\alpha_s \ln(1/x)$ resummation terms, as discussed in Chap. 7, particularly 7.3, 7.5. The use of the DGLAP equations down to low $Q^2 \sim 1\,\mathrm{GeV}^2$ is also questionable. Not just because non-perturbative physics may be important, but also beacuse at low Q^2 and low x high parton densities may require non-linear evolution equations (see Sec. 7.7).

6.3.5 The need to go beyond NLO and scale uncertainty

NLO DGLAP QCD fits give good descriptions of F_2 data down to Q^2 values in the range $1-2\,\mathrm{GeV}^2$. Such fits assume the validity of the NLO DGLAP QCD formalism even for low Q^2, where α_S is becoming larger such that NNLO corrections are increasingly important. Calculations to NNLO are now available and although the calculations of the 3-loop splitting functions are as yet incomplete, the results are considered reliable to within 2% for $x > 10^{-4}$. The impact of such contributions has been considered by van Neerven and Vogt who have examined the effects of LO, NLO and NNLO evolution on a fixed set of partons, as discussed in Sec. 4.8. The impact on PDF fits is discussed in Sec. 6.5.2.

In addition to NNLO corrections soft gluon resummations of $\alpha_S \ln(1-x)$ terms may be necessary at high $x > 0.8$. Current data do not access such large x, with the exception of the very low Q^2 SLAC data which are generally not fitted since they fail the cuts imposed to minimize higher twist effects.

6.3.6 Assumptions

There are various common assumptions made in PDF extractions, in order to limit the number of parameters. All of these are very reasonable within the framework of the parton model, but all may be challenged since the starting shapes of the parton distributions at Q_0^2 involve unknown non-perturbative input.

- It is usually assumed that strong isospin swapping relates the parton distributions in the proton and the neutron such that $d_{proton} = u_{neutron}$ and vice versa. However, some authors have considered charge symmetry violation (CSV). There is as yet no evidence for this.
- It is also assumed that $q_{sea} = \bar{q}$, for all flavours. However, at low energies, meson cloud models suggest that the proton may fluctuate into a meson and a baryon such as $K\Lambda$. Thus the s and the $\bar{s}$ quarks may have different momentum distributions, although their numbers must cancel when integrated over all x. The evidence for this asymmetry from current $\nu, \bar{\nu}$ scattering data is not compelling (see Zomer *Ref ??*).
- Historically, it was assumed that $\bar{d} = \bar{u}$. This is violated, and some violation should be expected from Pauli suppresion. However, it seems that this is not enough, and meson cloud models involving proton fluctuations into $N\pi$ have been invoked to explain the size of this effect. This inequality is now built into PDF extractions.
- Historically, it was assumed that $d_v/u_v = 1/2$ for all x, but this relationship need only be true for the overall number integrals. The u_v valence shape is not the same as the d_v valence shape as established by the measurements of the ratios $F_2^{\nu p}/F_2^{\bar{\nu} p}$ and $F_2^{\mu D}/F_2^{\mu p}$, which indicate that $d_v/u_v \ll 1/2$ as $x \to 1$ (see Fig. 5.13). This is now built into the PDF extractions such that most parametrizations have

$d_v/u_v = (1-x)^p$ $(p > 0)$ as $x \to 1$. Recently, it has been suggested that the nuclear corrections applied to the deuterium target data are inadequate, and that a re-evaluation of these corrections would yield $d_v(x)/u_v(x) \to 0.2$ as $x \to 1$ (see Sec. 5.3.3). Since the current $\nu, \bar{\nu}$ scattering data on proton targets are insufficently accurate to confirm this, HERA data on $e^+p \to \nu X$, $e^-p \to \bar{\nu} X$, will be particularly valuable to clarify this situation.
- All PDF extractions have to make choices such as: the value of Q_0^2; the minimum values of Q^2, W^2, x; the values of quark masses in heavy quark treatment; etc. All of these can have small systematic effects on the PDF shapes extracted

6.3.7 Comparability of evolution programmes

Since various groups make PDF extractions the compatibility of the codes must be ensured. A lot of work was done on this for the HERA 96 workshop *needs Ref.* One particular issue to consider is whether evolution is done in moment-space or x space. *Then theres Yndurains Bernstein polynomials, plus Russian groups approach, plus Pascaud/Zomer, Santorelli/Scrimieri etc ... would be useful to have a brief summary! RD.*

6.4 Global fits: the general formalism

This section gives a general description of the forms of the parametrizations and the considerations which motivate the choice of these forms.

There is some flexibility as to which parton distributions one choses to parametrize. A typical choice is u_v, d_v, S, g, $\bar{d} - \bar{u}$ but u, $\bar{u}$, d, $\bar{d}$, g is also used. The quark distributions must be combined to form singlets and non-singlets which are then evolved appropriately.

The parton distributions must be parametrized by a suitably flexible analytic form at the starting $Q^2 = Q_0^2$. Before HERA the choice was $Q_0^2 \sim 4\,\mathrm{GeV}^2$, but the inclusion of the HERA data in fits stimulated the MRS group to drop their starting scale to $Q_0^2 = 1\,\mathrm{GeV}^2$, in response to the fact that the data extend down to low Q^2, and to the work of various authors which made it apparent that DGLAP evolution could be successfully extended down to such low Q^2 values. Data to support this somewhat surprising observation are shown in Sec. 5.5 and it is discussed further in Sec.6.5.

Note that it is possible to evolve down in Q^2, so that the value of Q_0^2 can be chosen above the minimum value of Q^2 of data input to a fit. The quality of the fit and the resulting parton parametrizations should not be sensitive to the choice of Q_0^2.

The form of the input parametrization is usually

$$xu_v = A_u x^{\eta_1}(1-x)^{\eta_2} P(x,u) \tag{6.3}$$

$$xd_v = A_d x^{\eta_3}(1-x)^{\eta_4} P(x,d) \tag{6.4}$$

$$xS = A_S x^{-\lambda_S}(1-x)^{\eta_S} P(x,S) \tag{6.5}$$

$$xg = A_g x^{-\lambda_g}(1-x)^{\eta_g} P(x,g) \tag{6.6}$$

where $P(x,i)$ is a polynomial in x, for example $(1 + \epsilon_i\sqrt{x} + \gamma_i x)$, or $P(x,i) = (1 + \gamma_i x^{\epsilon_i})$, or sums of Chebyshev Polynomials. Not all of the normalizations A_i are free parameters: A_u, A_d are determined by the need to satisfy flavour sum rules and A_g is determined in terms of the other three by the momentum sum rule.

The distributions are usually defined within the $\overline{\text{MS}}$ renormalization and factorization scheme and this will be assumed unless otherwise stated. Conventionally, analyses are done assuming that the factorization scale, μ_f^2, and the renormalization scale, μ_r^2, are both equal to Q^2. This is the obvious choice of scale for the DIS process. However, varying these scales gives an estimate of the importance of NNLO corrections which are not included in the analyses.

The QCD scale parameter Λ_{QCD} is usually a parameter of the fit. The treatment of Λ_{QCD} across flavour thresholds is described in Sec.4.7. Historically some authors have expressed their results in terms of Λ_{QCD} for four flavours, and others have expressed their results in terms of Λ_{QCD} for five flavours. It is modern practice to consider $\alpha_s(M_Z^2)$ for all analyses.

6.4.1 The form of the parametrization

Some comments on the choice of parametrization are in order. The simple form $x^a(1-x)^b$ respects the limits at $x \to 0, 1$ as suggested by Regge theory (see Sec. 7.4)and the counting rules, respectively (see Sec.4.3). The values of a and b for each distribution can also be predicted from these considerations. However one cannot be sure at what value of Q^2 such predictions may be valid and, since the parametrizations describe the data only at the value Q_0^2, such predictions should be taken only as a rough guide to the sorts of value to be expected. Furthermore, whereas the valence parameters are not very sensitive to the chosen value of Q_0^2, the sea and especially the gluon parameters are sensitive, because the shapes of these distributions evolve fast with Q^2, as dicussed in Sec.4.4.

The valence parameters η_2, η_4 are expected to have the value ~ 3 from the counting rules. Measurements indicate values of roughly this magnitude with $\eta_4 > \eta_2$, such that $d_v/u_v \to 0$, as $x \to 1$ as discussed previously. The counting rules also lead to the expectations $\eta_g \sim 5$, $\eta_S \sim 7$ for the high x behaviour of the gluon and sea distributions. These values are only very approximately in agreement with the fitted values. Note that there is a a correlation between the high x η values and the corresponding values of γ, thus to understand results in detail one should consider the whole shape of the high x distributions, not just a single parameter.

The parameters η_1, η_3 for the valence (non-singlet) distributions are expected to have values ~ 0.5, close to the value $1 - \alpha_R(0)$ deduced from the non-singlet Regge trajectory intercept (see Sec.7.4) and this is roughly true for $Q_0^2 \sim 1 - 4\,\mathrm{GeV}^2$.

The value of λ_g which describes the gluon shape at small x is also suggested by Regge behaviour. Since the gluon and singlet quark distributions mix, a value related to the singlet Pomeron trajectory $1 - \alpha_P(0)$ is expected. The conventional Regge exchange is that of the soft Pomeron, giving $\lambda_g \sim 0.08$. However, for $Q_0^2 \gtrsim 4\,\mathrm{GeV}^2$ data indicate the need for a larger value. This may reflect the need for a contribution from a hard Pomeron, with $\lambda_g \sim 0.5$, or it may simply be a feature of the fast evolution of the gluon distribution such that the smaller value $\lambda_g \sim 0.08$ would be appropriate at a lower starting scale. The variation of the value of λ_g with the value of Q_0^2 for a typical fit is illustrated in Fig. 6.14. The theoretical interpretation of the low x behaviour of the gluon distribution is an active research topic which is discussed in detail in Chap. 7.

The value of λ_S which describes the sea shape at small x should be similar to λ_g since, at small x, the singlet distribution is dominated by the sea and the process $g \to q\bar{q}$ dominates the evolution of the sea quarks. Hence one expects $\lambda_S = \lambda_g - \epsilon$, but only if Q_0^2 is large enough for the effect of DGLAP evolution to be seen. This expectation is not fulfilled until $Q_0^2 \sim 10\,\mathrm{GeV}^2$ as will be discussed in Sec. 6.5.

Finally the extracted values of $\lambda_{S,g}$ should not be interpreted without also considering the values of the parameters $\epsilon_{S,g}$ which are correlated with them. The steepness of the low x shape of the data cannot be judged from the values of $\lambda_{S,g}$ alone.

6.4.2 The flavour composition of the sea

The flavour composition of the sea also needs some discussion. The sea distribution refers to all flavours $S = 2(\bar{u} + \bar{d} + \bar{s} + \bar{c})$, where one has assumed $q_{sea} = \bar{q}$ as usual. The treatment of the charmed sea has already been discussed. The strange sea is not treated with such sophistication. It is suppressed relative to the u and d seas because of its larger mass and this is accounted for by introducing a simple suppression factor: for example, $\bar{s} = (\bar{u} + \bar{d})/4$, such that the strange sea is suppressed by 50% compared to the u and d sea distributions at Q_0^2. The justification for this comes from CCFR opposite sign dimuon data [Baz95]. Briefly, opposite sign dimuon events dominantly arise in $(\bar{\nu})$ ν scattering when the struck quark is an $(\bar{s})s$ quark which becomes a $(\bar{c})c$ quark through the flavour changing weak current. This $(\bar{c})c$ quark then decays through the muon channel to $(\bar{s}\mu^-\nu_\mu)$ $s\mu^+\nu_\mu$ yielding a muon of opposite sign to that at the original lepton scattering vertex. The rate for the process thus gives a measure of the size of the strange sea, which is consistent with $\sim 40\%$ suppression. Recent dimuon data indicate that the average value of Q^2 at which this result is applicable is around $Q^2 \sim 20\,\mathrm{GeV}^2$, but results are not very sensitive to this value.

Early parametrizations assumed that the u, d content of the sea is flavour symmetric, but there is no necessity for this and in 1992 NMC gave the first evidence that this is not the case [NMC92]. The Gottfried sum rule (see Sec. 2.7) is violated. If the assumption $\bar{u} = \bar{d}$, which was used in its derivation, is abandoned the integral becomes

$$\int_0^1 \frac{dx}{x}(F_2^p - F_2^n) = \frac{1}{3}\int_0^1 dx(u_v - d_v) + \frac{2}{3}\int_0^1 dx(\bar{u} - \bar{d}) \tag{6.7}$$

Thus the observation of the value ~ 0.23 for this integral indicates that $\bar{d} > \bar{u}$. Hence the structure of the sea at Q_0^2 may be expressed as

$$2\bar{u} = 0.4(1-\delta)S-\Delta,\ 2\bar{d} = 0.4(1-\delta)S+\Delta,\ \ 2\bar{s} = 0.2(1-\delta)S,\ 2\bar{c} = \delta S \tag{6.8}$$

where δ gives the small contribution of the charmed sea at Q_0^2 and $x\Delta$ is given by

$$x\Delta = x(\bar{d} - \bar{u}) = A_\Delta x^{\lambda_\Delta}(1-x)^{\eta_S} P(x, \Delta) \tag{6.9}$$

with the normalisation A_Δ fixed to agree with data on the Gottfried sum-rule.

6.4.3 Global fits: the relationship of the measurements to the parton distributions

The relationship between the measured structure functions and the parton distributions is not straightforward at NLO since the evolved parton distributions must be convoluted with coefficient functions and all types of parton may contribute to a particular structure function through the evolution. However, the simple QPM formulae of Sec. 2.4 give a good guide to the major contributions.

- (Anti-)neutrino CCFR data on xF_3 gives information on the valence shapes for all x, with u_v and d_v on an equal footing (Eq. 2.41). This information is most reliable at large x, since the nuclear corrections are less well determined for $x < 0.1$.
- NMC data on the ratio $F_2^{\mu D}/F_2^{\mu p}$ gives information on the ratio d_v/u_v at large x (Eq. 2.44) and is thus the only data set currently used which strongly constrains the difference in the shapes of d_v and u_v.
- The F_2^{lD}, F_2^{lp} data from NMC, BCDMS, E665, SLAC and the F_2 data from CCFR, give information on singlet combinations of quarks (see Eqs. 2.31, 2.33), which thus gives accurate information on the sea distributions throughout the x, Q^2 ranges covered by each of these experiments. These data have also been used to constrain the gluon distribution. Since the gluon does not couple to the photon it does not enter the expressions for the structure functions at all in the QPM. It is constrained by the momentum sum rule, and by the way the DGLAP equations feed its evolution into the sea distribution, see Eqs 4.32,4.33. The shape of the gluon distribution extracted from a DGLAP QCD fit will be correlated with the value of α_s, since an increase in α_s

increases the negative contribution from the P_{qq} term but this may be compensated by a positive contribution from the P_{qg} term if the gluon is made harder. Hence, a fixed value of α_s, as determined from independent data, is often assumed.

- Information on the difference $\bar{d} - \bar{u}$ comes from the different combinations of $\bar{u}$ and $\bar{d}$ entering into the isoscalar and proton target structure function data (see Eqs 2.31, 2.33).
- CCFR dimuon data gives information on $\bar{s}$ as explained in Sec 6.4.2.
- Current HERA reduced cross-section data give information on the shape of the sea distribution way down into the low x region. Post upgrade it will also give precision imformation on valence distributions, particularly the less well known d_v distribution.
- HERA data are invaluable in constraining the gluon distribution. As discussed above, the gluon is the parton which has the largest uncertainty because of the indirect way in which it relates to the measurements. However because QCD evolution at small x is gluon dominated, the P_{qg} term in Eq. 4.32 becomes dominant and uncertainties are considerably reduced. For x values below the valence region F_2 is essentially given by the singlet sea quark distribution, which in turn is driven by the gluon. In this region the gluon distribution may be obtained almost directly from the F_2 scaling violation data using Eq. 7.2. Although this approximation is only expected to hold to within 20% at $x = 10^{-3}$, its application to the data gives a correct impression of the strikingly strong rise of the gluon distribution at low x. More accurate detrminations are discussed in Sec. 6.5.

6.4.4 Information on Quark Distributions from non DIS data

Valuable information on PDFs may also be gained from a variety of non-DIS processes. The data which constrain quark distributions will be considered first.

As discussed in Sec. 10.3 Drell-Yan dilepton production in the process $pN \to \mu^+\mu^- X$ can be a sensitive probe of the sea quark distribution since the dominant subprocess is $q\bar{q} \to \gamma^*$, and thus the cross-sections are directly proportional to the antiquark distributions. The E605 data have been used to constrain the sea distribution at medium to large x values, $0.15 < x < 0.4$, and the more recent data from E772 have extended the range down to $x \simeq 0.025$. Data on the asymmetry, A_{DY}, between the differential cross-sections $\dfrac{d^2\sigma}{dMdy}$ at $y = 0$ for the processes $pp \to \mu^+\mu^- X$ and $pn \to \mu^+\mu^- X$ (where M and y are the invariant mass and rapidity of the lepton pair) can give information on the difference $\bar{d} - \bar{u}$. The dominant subprocesses are $u\bar{u}, d\bar{d} \to \gamma^*$, and the partons are to be evaluated at $x = M/\sqrt{s}$. Eqs. 10.12, 10.13 give the relationships of the measurements to the parton distributions. NA51 data constrains $(\bar{d} - \bar{u})$ at the x value, $x \sim 0.18$ and more recent data from the E866 experiment have given data which measure the shape of the $\bar{d} - \bar{u}$ in the x range $0.03 < x < 0.35$, see Fig. 10.5.

As discussed in Sec. 10.4 data on W production may also be used to investigate quark distributions. The processes $p\bar{p} \to W^+(W^-)X$ proceed via the subprocesses $u\bar{d} \to W^+(d\bar{u} \to W^-)$ and the cross-sections are thus sensitive to the u and the d distributions at $x \sim M_W/\sqrt{s}$, i.e. $x \sim 0.13$ at CERN, where UA2 data are taken, and $x \sim 0.05$ at FNAL, where CDF and D0 data are taken. The $W^\pm$ charge asymmetry, $A_W(y)$, (discussed in Sec.10.4.3) probes the slope of the d/u ratio, since the u quarks carry more momentum on average than the d quarks and so the W^+ tend to follow the direction of the incoming proton and the W^- that of the antiproton. These measurements give a more direct probe of the d/u distribution than the F_2^D/F_2^p ratio at intermediate x values, since W production, at Tevatron energies, is less sensitive to the contribution of the antiquarks.

6.4.5 Information on the gluon from non-DIS data

An overview of the data that can contribute to the gluon extraction is given in Fig. 6.1 as function of x.

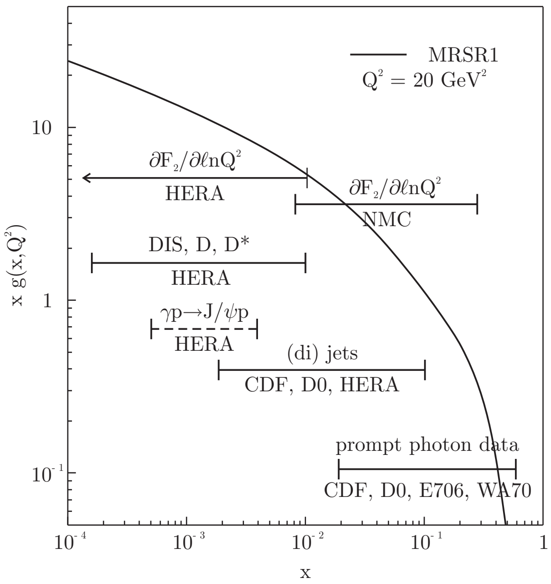

Fig. 6.1 The x intervals in which the gluon may be constrained by various sets of data. The MRSR1 gluon distribution is superimposed.

The contribution of the gluon in the DGLAP equations as a means of extracting the gluon distribution from NLO QCD fits to DIS scaling violation data has already been outlined in Sec. 6.4.3. A common problem in extracting the gluon using only DIS structure function, or reduced cross-section, data is the limited sensitivity to the gluon at large x, as illustrated clearly by error bands on the ZEUS gluon (see Fig 6.4). The global analyses of MRS, CTEQ and GRV have always included additional data from non-DIS processes in their fits in order to constrain the gluon. Data on prompt photon production and single inclusive jet data from hadronic collisions have been used to date.

The prompt photon process is discussed in Sec. 10.6. Prompt photon data have been used for the x range: $0.02 < x < 0.5$ (see Fig.6.1). The process $pN \to \gamma X$ should provide information on the gluon distribution since the dominant subprocess is $gq \to \gamma q$, at leading order. However, one must also account for non-direct γ production in fragmentation processes from other partons. There is also some uncertainty from factorization and renormalization scale dependence. Low energy data from WA70, UA6 and E706 on $pp \to \gamma X$ should constrain the gluon in the x range, $0.3 \leq x \leq 0.5$. ISR data, extend to lower x, $(0.15 \leq x \leq 0.3)$, and data from UA2 and CDF extend into the medium-small x region ($0.05 \leq x \leq 0.15$ and $0.02 \leq x \leq 0.1$, respectively). These higher energy data also indicate that the shape of the E_T distribution of the photons with respect to the beam axis is steeper than that predicted by pQCD calculations (even after correction for fragmentation effects). More recent precision data from E706 establishes that this is also the case for lower energy data ($\sqrt{s} = 31.5, 38.8$ GeV).

These data can be described by including the effects of 'intrinsic' k_T, i.e. k_T broadening of initial state partons due to soft gluon radiation with $\langle k_T \rangle \approx 1\,\text{GeV}$. Such broadening would have to vary with $\sqrt{s}$ (as $\sim \ln(\sqrt{s})$ in order to describe all the data and there is some evidence for this, see Fig. 10.20. E706 data are particularly sensitive to such effects because at higher energy the photon p_T is large and k_T enhancement affects only the lowest end of the spectrum, whereas at lower energies (UA6, WA70) the k_T enhancement has less p_T dependence, so that it can be masked by scale or normalization uncertainties. For E706 data both the shape and the normalization of the p_T spectra are affected. The MRST group addressed this problem by providing several versions of their PDFs with more or less k_T broadening as far as can be consistent with the WA70 data. Unfortunately not all implementations of the effects of k_T broadening agree with each other so that, more recently, both the CTEQ and the MRST groups consider that until resummation of multi-gluon radiation is rigorously included in QCD calculations it is unreliable to use prompt photon data to pin down the gluon.

Further information on the gluon may come from high E_T jet production. There are high statistics jet measurements from the CDF and D0 collaborations at $\sqrt{s} = 1.8$ TeV as discussed in Sec. **??**. The single jet inclusive cross-sections in hadro-production, for jets with transverse energies $E_T \sim 100\,\text{GeV}$, are dependent on the gluon via gg, gq and $g\overline{q}$ initiated subprocesses. . For jets with transverse energy $50 \lesssim E_T \lesssim 200\,\text{GeV}$ pQCD calculations are considered reliable. Soft gluon effects are not important because of the high energy scale. The slope of the E_T distribution constrains the combination $\alpha_s(\mu^2)g(x,\mu^2)$ at the scale $\mu^2 = E_T^2$ and $x = 2E_T/\sqrt{s} \sim 0.1$. The CTEQ group and more recently the MRST group have included this information in global fits to constrain the high x gluon. A correct treatment of correlated systematic errors is essential because CDF and D0 data are inconsistent if statistical errors alone are considered.

6.4.6 Future prospects for information on the gluon

With HERAII data, accurate information on the gluon may come from the following measurements.

- The longitudinal structure function depends directly on the gluon distribution at low x. At $x \lesssim 10^{-3}$ the dominant contribution to F_L comes from the gluon regardless of the exact shape of the gluon distribution, see Sec. 7.1.2. Although F_L has been estimated by the H1 experiment at HERA using an extrapolation method at a single CM energy, a direct measurement requires data at two, or more, different beam energies as discussed in Sec. 5.4.3. With a very large integrated luminosity, it may also be possible to use ISR events.

- Dijet production initiated by the DIS processes $\gamma^* g \to q\overline{q}$ and $\gamma^* q \to qg$ can also been used to extract the gluon distribution. The NLO corrections are known and the effects of scheme dependence and jet algorithms have been quantified. At present the results are not competitive with those from scaling violation data and there are still some unresolved theoretical questions on the absolute normalization of the jet rates, but the outlook is promising.

- Open charm production, which tags the boson-gluon fusion process and hence the gluon density directly. The charm data in DIS have been discussed in Sec. 5.4.4, and Fig.5.18 shows the comparison of the HERAI measurements of $F_2^{c\overline{c}}$ with the predictions using the gluon distribution from the H1 NLO QCD fit. The agreement is good but the data errors are still too large to make a competitive extraction. High luminosity at HERAII and improved detectors (e.g. use of Si vertex detectors) will facilitate accurate measurements of the gluon density in the x range $0.0001 < x < 0.01$.

- Elastic (diffractive) J/ψ production in DIS and in photoproduction may yield information on the gluon distribution, since the cross-section depends on $[xg(x, Q_V^2)]^2$. Similarly, diffractive production of ρ and ϕ in DIS at higher Q^2, depends on the square of the gluon density. These data could give information on the gluon distribution in the region $0.0001 < x < 0.01$.

6.5 Results on PDF extraction

6.5.1 Fits by experimental groups

The fits made by experimentalists to their own data are considered first. The experimental collaborations have the advantage of knowing the correlations between their systematic errors in detail and can thus produce the most reliable error bands on the extracted distributions.

In 1993 the NMC collaboration used their F_2 data on proton and deuteron targets in the kinematic range $0.008 \leq x \leq 0.5$, $1 \leq Q^2 \leq 48\,\mathrm{GeV}^2$ to make an NLO QCD analysis [NMC93]. The gluon distribution extracted is shown in Fig. 6.9 for the fixed value of $\alpha_s = 0.113$. The uncertainty on the distribution is calculated taking into account the statistical errors, the systematic errors including correlations, the contribution of the unmeasured region, and the uncertainties on α_s and higher twist contributions. The total uncertainty at $x = 10^{-2}$ amounts to $\sim 20\%$. These data cover the region $x > 0.01$ and the gluon distribution shows a moderate rise at low x compatible with $\lambda_g = 0.08$ from the soft Pomeron.

The gluon distribution may be extended into the low x region by NLO QCD fits to HERA data. Both the H1 and the ZEUS collaborations have made such fits.

The goal of the H1 fit was to extract the gluon distribution and the value of α_s, using just the H1 reduced cross-section data plus the BCDMS proton target F_2 data to give information at high x. Thus uncertainties due to nuclear effects and the combination of different data sets are minimized. The extracted gluon distribution is shown in Fig. 6.2 for three Q^2 values. The gluon density rises dramatically towards low x and this rise increases with increasing Q^2. The inner error band results from the statistical and systematic errors taking into account correlations (see Sec. 6.2.3) from a fit with $\alpha_s(M_Z^2) = 0.115$ fixed. The central error band shows the additional error induced by letting α_s be a parameter of the fit. The outer error band represents various model errors, such as varying the cuts on the data entering the fit, the value of Q_0^2, and the form of the parametrizations at Q_0^2.

The goal of the ZEUS fit was an extraction of the valence, sea and gluon PDFs as well as the value of α_s, so that a global fit to ZEUS reduced cross-section data together with all the modern precision fixed target DIS structure function data was made, including correlated systematic errors, as described in Sec 6.2.3. A comparison of all the PDFs from the ZEUS fit at $Q^2 = 10\,\mathrm{GeV}^2$ is shown in Fig 6.3

The ZEUS gluon distribution for several different Q^2 values is shown in Fig. 6.4. The error bands shown represent the statistical (inner), statistical plus correlated systematic (middle), additional error due to the variation of α_s (outer). The significance of the error bands is better appreciated by considering the ratio plots of Fig. 6.5.

Comparing the experimental error bands for the gluon extractions from

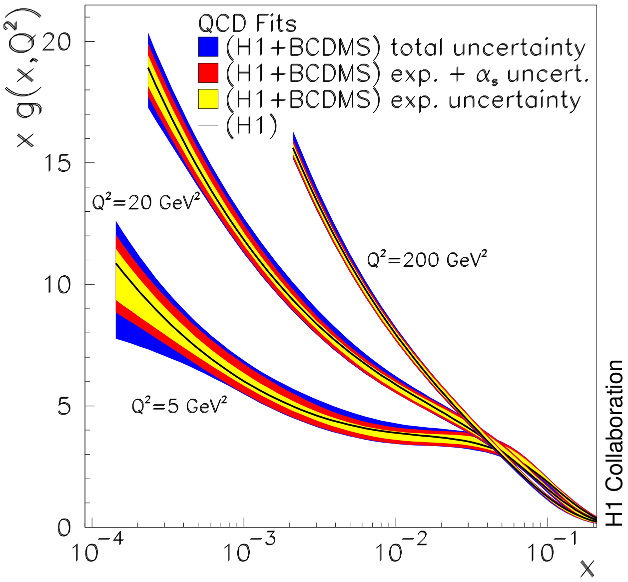

Fig. 6.2 Gluon distribution from an NLOQCD fit to H1 plus BCDMS data, for various Q^2

ZEUS and H1 at a common value of $Q^2 = 20\,\mathrm{GeV}^2$, shows that the error estimates from the H1 fit are somewhat more resitrictive than those of the ZEUS fit and that shape of the high x gluon is different. This is because the treatment of χ^2 in the two approaches is very different (as discussed in Sec 6.2.3) and the high x parametrizations of the gluon are different. It has already been noted that the high x gluon is uncertain when constrained only by fits to DIS data. Nevertheless the gluon is now determined to within $\sim 10\%$ for $Q^2 > 20\,\mathrm{GeV}^2$, $10^{-4} < x < 10^{-1}$, and its uncertainty decreases as Q^2 evolves upwards.

At low Q^2 the gluon shape flattens at low x, and if the fit is extrapolated back to $Q^2 = 1\,\mathrm{GeV}^2$ the gluon shape becomes valence like, with low x values that are negative within errors. This unexpected prediction of the fit is discussed further in Sec. 6.5.2.

To illustrate the contribution of HERA data to the knowledge of the gluon distribution Fig. 6.6 shows a fit to fixed target data without the inclusion of HERA data, compared to the fit including ZEUS data. The ZEUS fit indicates the need for a much steeper gluon distribution.

In Fig 6.7 the extracted sea distribution from the ZEUS fit is shown in several Q^2 bins and the uncertainty in this extraction is further illustrated in Fig 6.8. The uncertainty in these distributions is considerably less that that of the gluon distributions. It is less than $\sim 5\%$ for $Q^2 \gtrsim 2.5\,\mathrm{GeV}^2$ and $10^{-4} < x < 10^{-1}$. It can be seen that, even at the smallest $Q^2 \sim 1\,\mathrm{GeV}^2$,

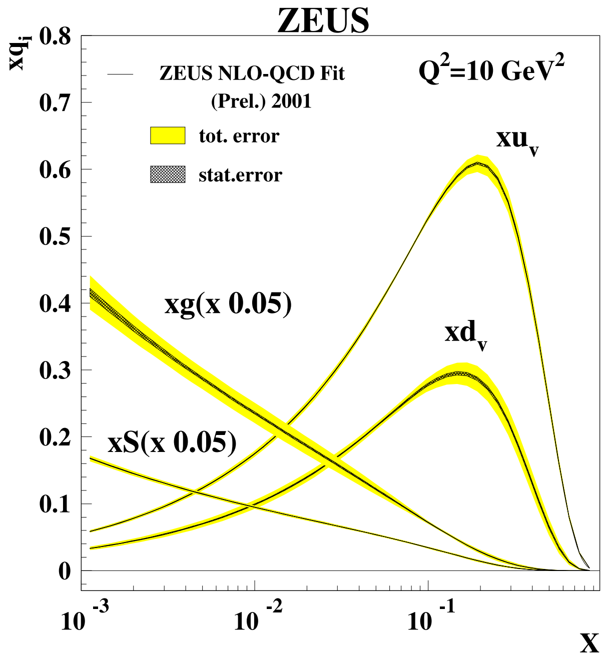

Fig. 6.3 The PDF distributions at $Q^2 = 10\text{GeV}^2$, from an NLO QCD fit to ZEUS plus fixed target data. Note that the gluon and sea distributions are scaled down by a factor of 20.

the sea distribution is still rising slightly at small x. In the same Q^2, x region the gluon distribution is falling and is consistent with zero. This feature of the fits is discussed further in Sec. 6.5.2.

Fig. 6.9 shows $xg(x)$ at $Q^2 = 20$ GeV^2 for a fit including both H1 and ZEUS data using the ZEUS procedure. The error bands account for statistical and systematic errors including correlations, with $\alpha_s(M_Z^2) = 0.118$ fixed. At the lowest x values $\sim 10^{-4}$ the gluon distribution is now determined with a precision of about $xx\%$, an impressive improvement in reach and precision compared with previous fits. At around $x = 0.01$ the HERA fits make contact with the fit performed by the NMC collaboration on their own data. The agreement with the NMC result is very good.

In Figs 6.10, 6.11 the valence distributions xu_v and xd_v extracted from the ZEUS fit are shown. Note that the abscissa is linear and the ordinate is logarithmic, to illustrate these valence distributions at high x, where the fixed target data constrain them. The u valence distribution is much better determined than the d valence distribution since fixed target structure function data are dominated by the u quark even for the isoscalar deuterium and iron targets.

This figures also illustrate the results of a fit using only ZEUS data,

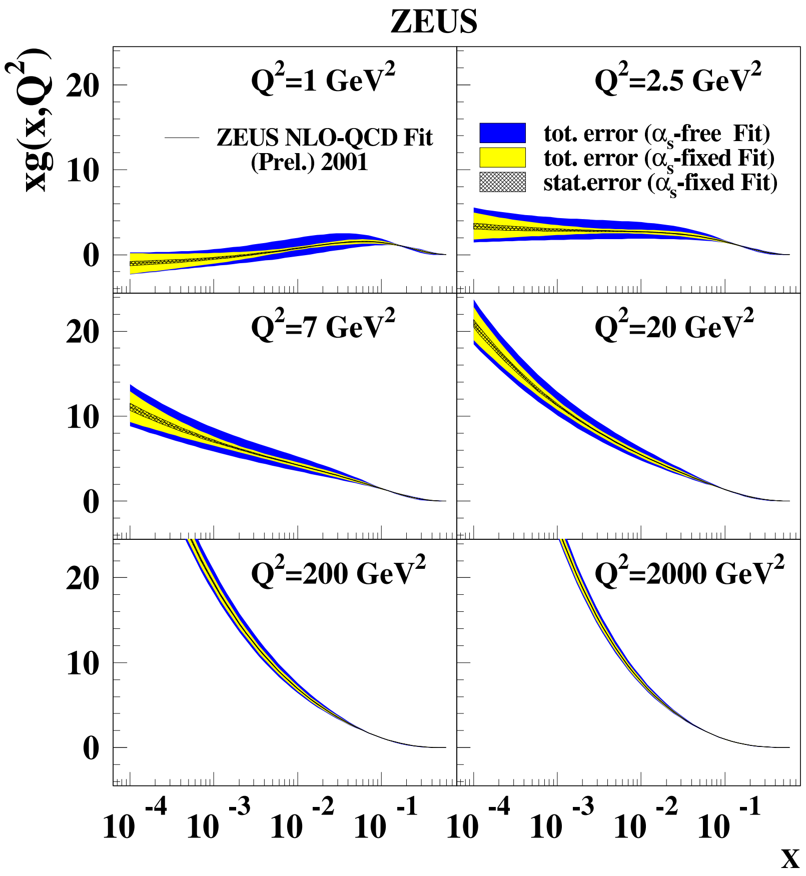

Fig. 6.4 Gluon distribution from an NLOQCD fit to ZEUS plus fixed target data, for various Q^2

including the high Q^2 charged current e^+p reduced cross-section data and the neutral and charged current e^-p data from 1998/1999. These data have been presented in Chapter 8. Clearly the standard fit gives a more precise determination but this is subject to corrections for the nuclear target of CCFR and the deuterium target of NMC. The high Q^2 ZEUS reduced cross-section data is able to provide some constraint on the valence distributions which indicates that ZEUS data prefer a larger d valence distribution at high x than the standard fit. These PDF extractions will be considerably improved with HERAII data.

maybe show the uncertainty on the d/u ratio at high x

ZEUS have also compared their NLO QCD fit to very low Q^2 data from the ZEUS BPT (see Sec. 5.5) In Fig 6.12 the ZEUS 96/7 data and the ZEUS BPT data are shown in very low Q^2 bins compared to the

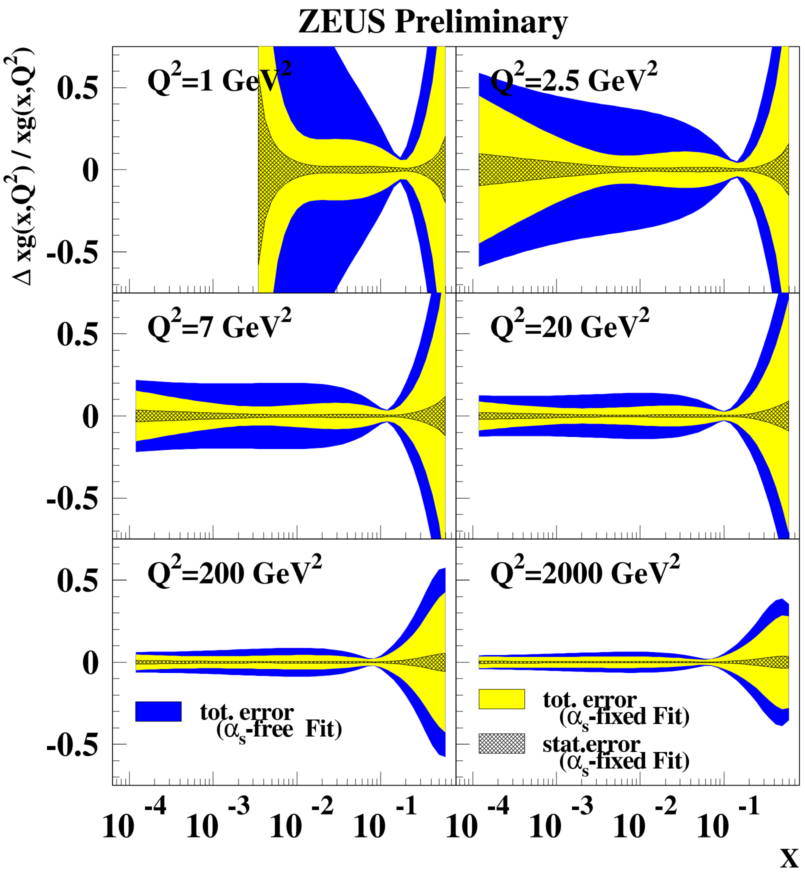

Fig. 6.5 The ratio of the gluon error bands to the central value, from an NLO-QCD fit to ZEUS plus fixed target data, for various Q^2

ZEUS fit predictions. The fit is unable to describe the very precise BPT data for $Q^2 < 0.65\,\mathrm{GeV}^2$, even when the full error bands due to the correlated systematic errors are included. Referring to Fig. 6.6 it is clear that it is the extreme steepness of the ZEUS data at intermediate Q^2 ($2.7 < Q^2 \lesssim 200\,\mathrm{GeV}^2$) which prevents a fit to the very low Q^2 BPT data. In Fig 6.13 the predictions for F_L from the ZEUS fit are also shown for these low Q^2 values. F_L is significantly negative for $Q^2 \lesssim 0.8\,\mathrm{GeV}^2$ indicating that the fit is unable to describe the data in this region. This breakdown of the applicability of the DGLAP equations at low Q^2 is discussed further in Sec. 7.7.

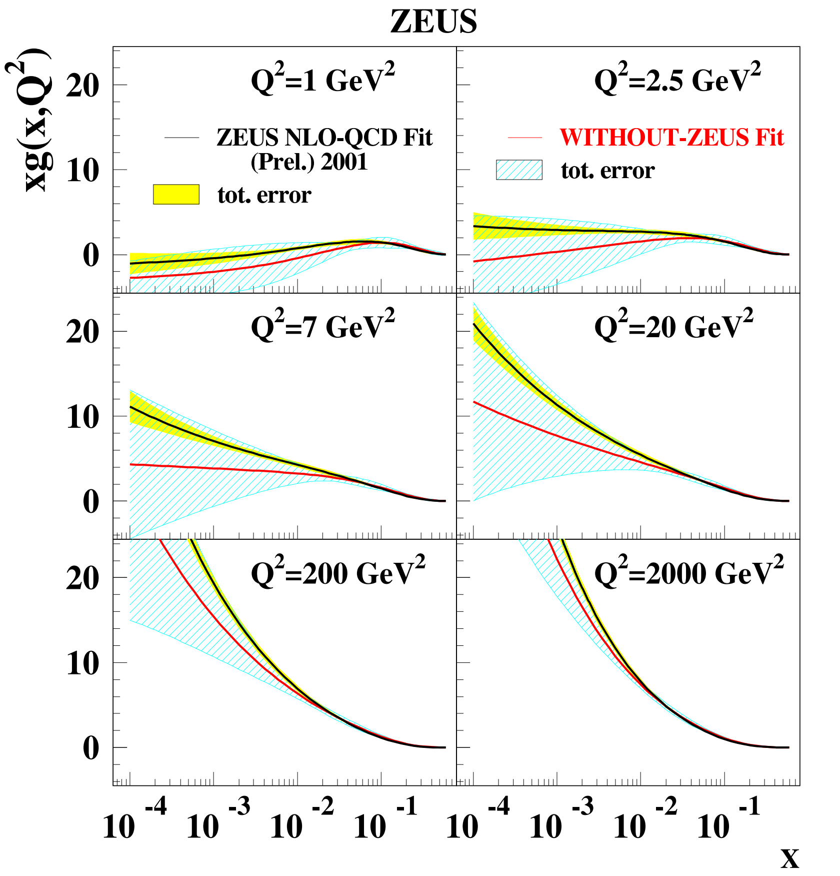

Fig. 6.6 The gluon distribution from the NLOQCD fit excluding ZEUS data

6.5.2 Fits by the theoretical teams MRS & CTEQ

The theoretical teams have included more extensive non-DIS data sets in their analyses and they have evaluated the effect of the various theoretical assumptions which go into PDF extraction, and produced variants of their fits which account for many of these.

They have also used their PDFs as input for calculations of various cross-sections at future colliders, in order to evaluate the uncertainty on predictions of conventional processes which constitute the background to physics beyond the standard model (see Sec. 10.7.2 for an example). Such work has also been extended to encompass a systematic study of methods to evaluate the uncertainties on PDFs as discussed in Sec 6.2.3.

Fig. 6.9 shows a collection of recent determinations from the global analyses of CTEQ, GRV and MRS. Although these analyses include additional data to constrain quark and gluon distributions, the resulting gluon distributions are broadly similar to the HERA fits and to each other in the

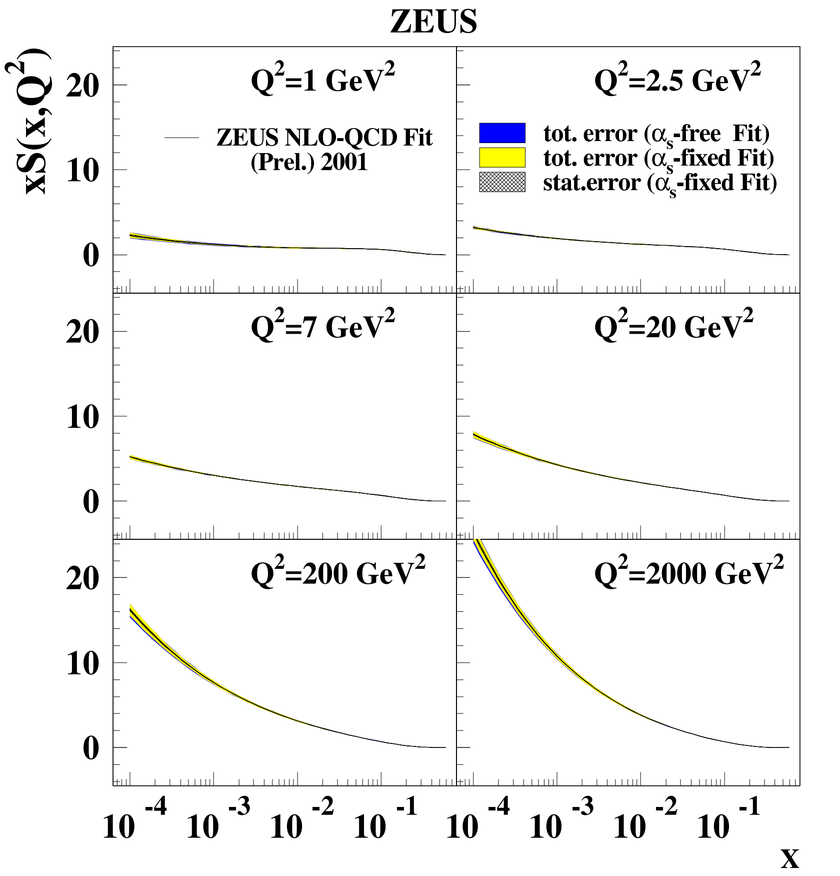

Fig. 6.7 Sea distribution from an NLOQCD fit to ZEUS plus fixed target data, for various Q^2

fitted region.

(*It remains to update/make such a plot*)

The theoretical teams were the first to observe that when the starting scale of the fits is dropped to $Q_0^2 \sim 1\,\mathrm{GeV}^2$, or lower, the gluon becomes 'valence-like' in shape, or even negative. In fact GRV team predicted such behaviour. The GRV approach is rather different than that of MRS,CTEQ or the experimental teams. A full discussion of it is given in Sec 6.5.3

At $Q^2 \sim 1\,\mathrm{GeV}^2$ the gluon low x slope has become valence-like, however this quickly changes as Q^2 increases. The MRS group studied this by fitting the analytic forms of Eqns. 6.5, 6.6 to their evolved distributions for Q^2 values from $1 \to 10^3\,\mathrm{GeV}^2$ and plotting the extracted values of λ_S, λ_g for the MRST98 parametrization, see Fig. 6.14. For low Q^2, $\lambda_g < \lambda_S$, these values become equal at $Q^2 \sim 10\,\mathrm{GeV}^2$ and for larger Q^2, $\lambda_g > \lambda_S$,

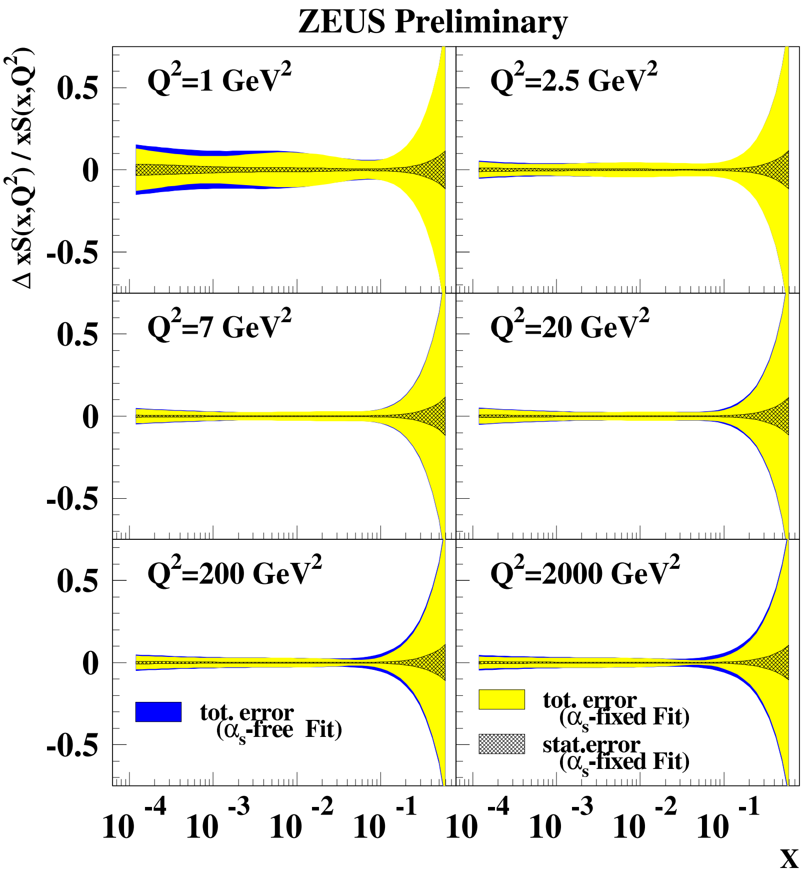

Fig. 6.8 The ratio of the sea error bands to the central value, from an NLOQCD fit to ZEUS plus fixed target data, for various Q^2

as expected in pQCD from $g \to q\bar{q}$ splitting. This behaviour is typical of NLO pQCD fits performed within the DGLAP formalism. It is interesting to compare the slope of the sea distribution, λ_S, shown in Fig. 6.14 to the effective slope of F_2, λ_{eff}, obtained directly from the data as shown in Fig. 7.7. Whereas the variation of the measured slope λ_{eff} with Q^2 is compatible with the predictions of pQCD for $Q^2 \gtrsim 1\,\mathrm{GeV}^2$, it is nevertheless disturbing that the fits predict that $\lambda_g < \lambda_S$ for $1 < Q^2 \lesssim 10\,\mathrm{GeV}^2$, since it indicates that the rise in the sea distribution cannot be driven by the gluon $g \to q\bar{q}$ splitting in this region.

The fact that at low Q^2 the low x gluon is tending to become negative is even more disturbing but, since parton distributions have to be convoluted with coefficient functions to produce observable quantities such as structure functions, a negative gluon distribution is not necessarily an indication that

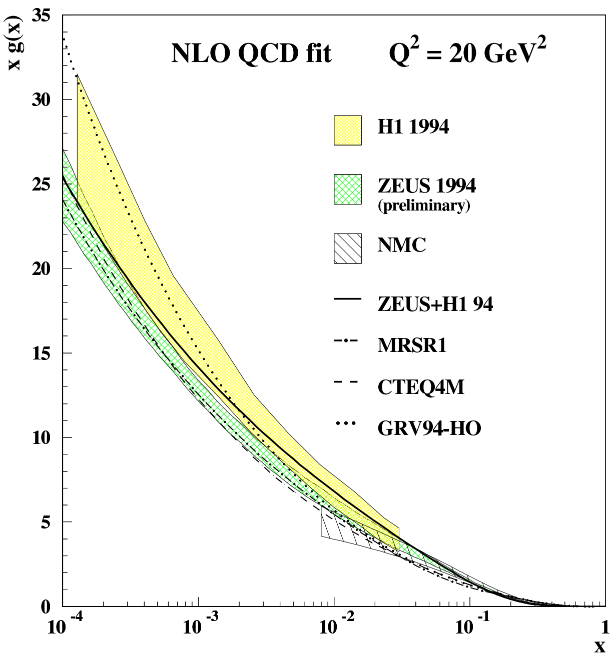

Fig. 6.9 update this to show a fit with H1 and ZEUS using ZEUS procedure, NMC old plus some MRS/CTEQ/GRV

the perturbative approach has broken down. For this reason the behaviour of F_L, the structure function most closely related to the gluon is often investigated. An example from the ZEUS fit has already been shown in Fig. 6.13.

Sensitivity to the standard theoretical assumptions has been extensively investigated by both MRS and CTEQ (see Appendix G). A few important examples are discussed below.

It is interesting to investigate whether there is any evidence for higher twists in the low x HERA data. MRST have included lower W^2 data in their fit in order to investigate this. Higher twist terms of the form $h(x)/Q^2$ are included in the fit and the value of $h(x)$ is fitted in different x bins. It is found that the higher twist contribution is negligible for $x < 10^{-2}$, but that small negative higher twist terms improve the χ^2 for $10^{-2} < x < 0.5$ (where it is the χ^2 for NMC data which improves the most). Then large positive higher twist terms are needed at large x because target mass effects are not included in the formalism. The MRS group have also tried forcing the gluon at $Q_0^2 = 1\,\mathrm{GeV}^2$ to be flat or singular to see whether a contribution from higher twist at low x could mimic the effect of the 'valence-like' gluon found in the standard fits. This possibility is strongly excluded.

There have always been variants of the standard fits done at LO rather

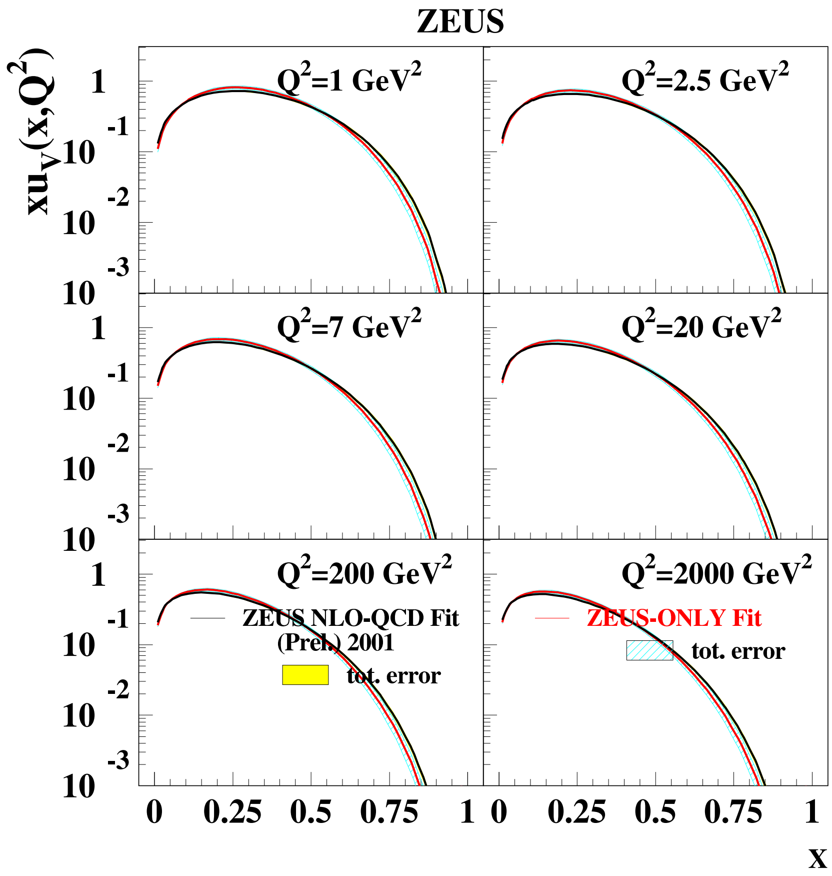

Fig. 6.10 The xu_v distribution from the NLOQCD fit to ZEUS data alone

than NLO. Recently NNLO variants have become available. Rather than considering the differences between LO, NLO and NNLO on a fixed set of partons as discussed in Sec. 4.8, MRST have considered a complete re-fit of the data at each order. Fig 6.15 displays the gluon distributions for fits done to LO, NLO and two versions of NNLO which represent extremes of fast and slow evolution compatible with the current level of our knowledge. It is evident that the gluon PDF is very sensitive to the difference between LO/NLO and NNLO for low Q^2, and this sensitivity persists at low x even for relatively high Q^2. The NNLO predictions are negative at low x even for Q^2 as high as $Q^2 = 2\,\mathrm{GeV}^2$. Hence the prediction for F_L is also shown in Fig 6.16. Whereas F_L is not negative for low Q^2 its shape is odd for both NLO and NNLO predictions until $Q^2 > 5\,\mathrm{GeV}^2$.

MRST have also investigated higher twist terms within an NNLO analysis. Strong positive higher twist contributions are still necessary at large x and low W^2 to account for target mass effects. However, the small negative

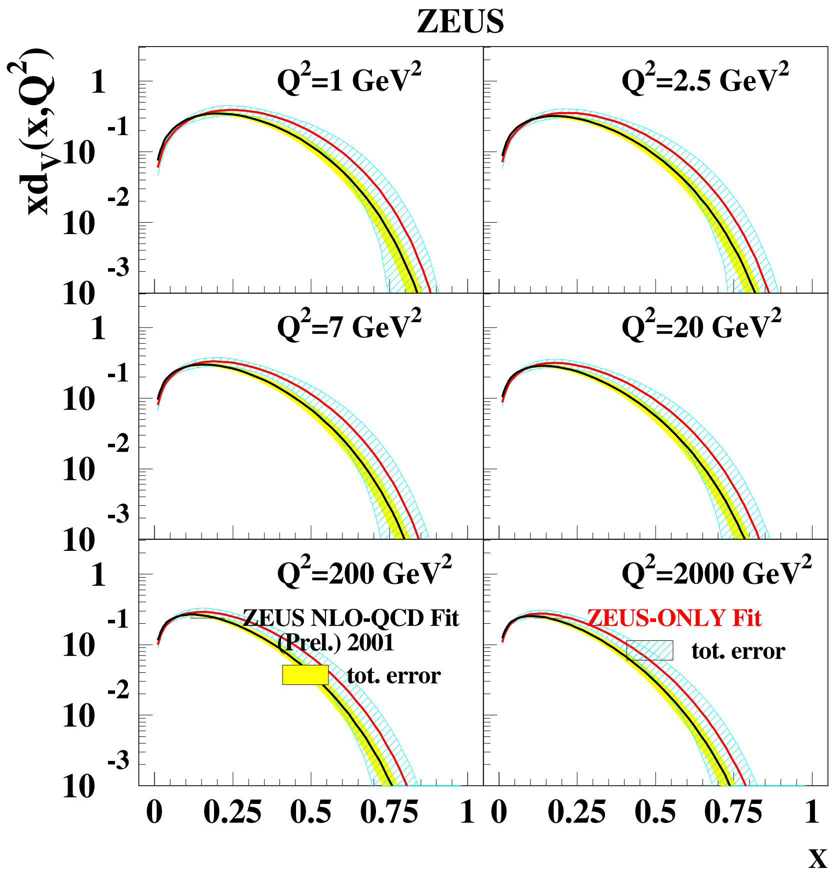

Fig. 6.11 The xd_v distribution from the NLOQCD fit to ZEUS data alone

higher twist contributions at intermediate x are much reduced, confirming the idea from renormalon theory that the higher twist terms are related to the truncation of the perturbative series.

The gluon extraction is particularly vulnerable to the assumption that the DGLAP evolution equations can be applied in the kinematic range studied. The difference between the standard DGLAP gluon extractions and an extraction including $\ln(1/x)$ resummation terms (discussed in Sec. 7.3.2, 7.5.4) is illustrated in Fig. 6.17 [Tho01]. Note that the standard DGLAP fits shown in this figure are not identical to those of Fig 6.16 because they represent the results of a more recent set of fits including the most up to date HERA data. These data require the gluon to be negative at small x and Q^2 even at NLO. This persists in the prediction for F_L, however at NNLO the coefficient functions have compensated for this, resulting in the peculiar shape of F_L at NNLO. The shape of the prediction including $\ln(1/x)$ resummation is much more reasonable.

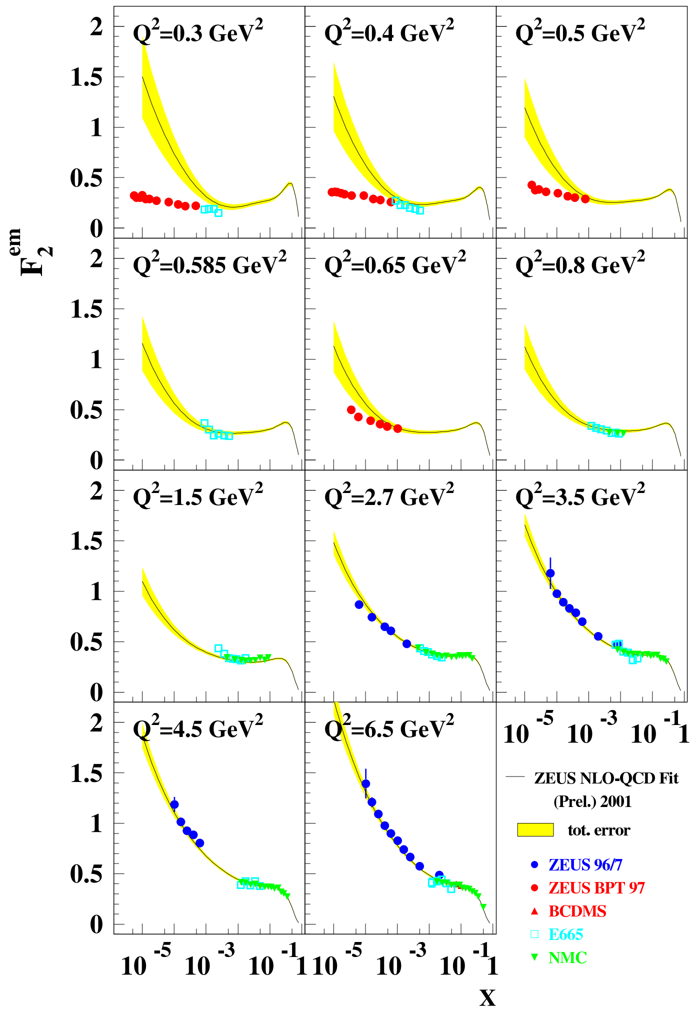

Fig. 6.12 F_2 data down to the very low Q^2 (including BPT data) compared to the standard NLOQCD fit backward extrapolated

There are variants of the MRST99 fits to account for a larger or smaller amount of high x gluon. These derive from varying the amount of k_T broadening of initial state partons in the prompt photon process from $\langle k_T \rangle = 0$ to $\langle k_T \rangle = 0.64\,\text{GeV}$, in the fit to low energy WA70 data. CTEQ have also provided a variant (CTEQ4HJ) with the high x gluon enhanced to describe early measurements of an excess of very high $E_T > 200\,\text{GeV}$ jets at CDF.

There are variants of the MRST fits to account for larger or smaller amounts of u and d quarks at low x. These derive from varying the nor-

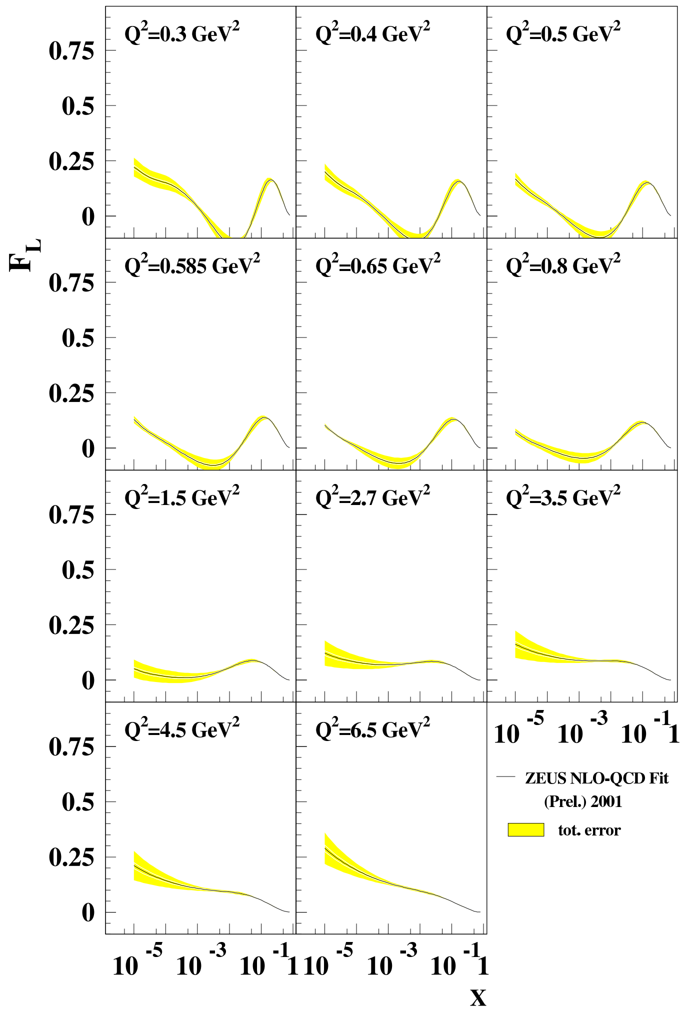

Fig. 6.13 The prediction of the standard NLOQCD fit for F_L backward extrapolated to very low Q^2

malisations of the HERA data sets up and down within their quoted normalisation errors. There are variants with more or less s quarks which derive from changing the strangeness suppression applied at Q_0^2 by $\pm 10\%$ and there are variants with more or less c quarks which derive from varying the mass of the charmed quark. A special variant with a finite d/u ratio at large x is also available, because the usual parametrizations of d_v and u_v predict either $d_v/u_v \to 0$, or $d_v/u_v \to \infty$ as $x \to 1$, and are not optimal for estimating the error on a prediction such as $d_v/u_v = 0.2$.

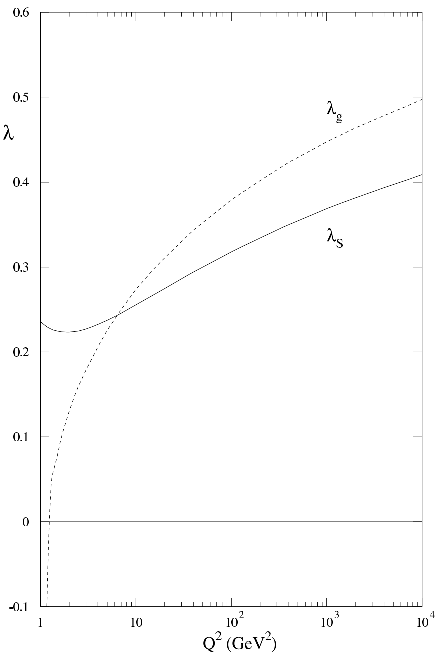

Fig. 6.14 The evolution of the parameters λ_S, λ_g with Q^2 for the MRST98 central fit.

CTEQ provide variants using different heavy quark production schemes: zero mass variable flavour number, general mass variable flavour number and fixed flavour number with either 3 or 4 flavours. The GM-VFN schemes have not been fully worked out for all of the non-DIS processes of interest so that a consistent set of PDFs worked out in the same scheme may be needed when comparing predictions to data.

Finally, there are variants of both CTEQ and MRST fits which allow for different fixed values of $\alpha_s(M_Z^2)$.

6.5.3 Dynamically generated partons, the GRV approach

Whereas the parametrizations provided by the MRS and CTEQ groups depend crucially on the non-perturbative input parametrization at Q_0^2, the parametrizations of the GRV group (see Appendix G) are far less dependent on their inputs.

The original idea behind these parametrizations is that at some VERY LOW scale $Q^2 = \mu^2$ the nucleon consists only of constituent valence quarks. As Q^2 increases, one generates the gluons and sea quarks in the nucleon dynamically from these valence quarks, through the conventional DGLAP equations for the processes $q \to qg$, $g \to q\bar{q}$. It did not prove possible to describe all relevant data using such a picture, and it was accordingly

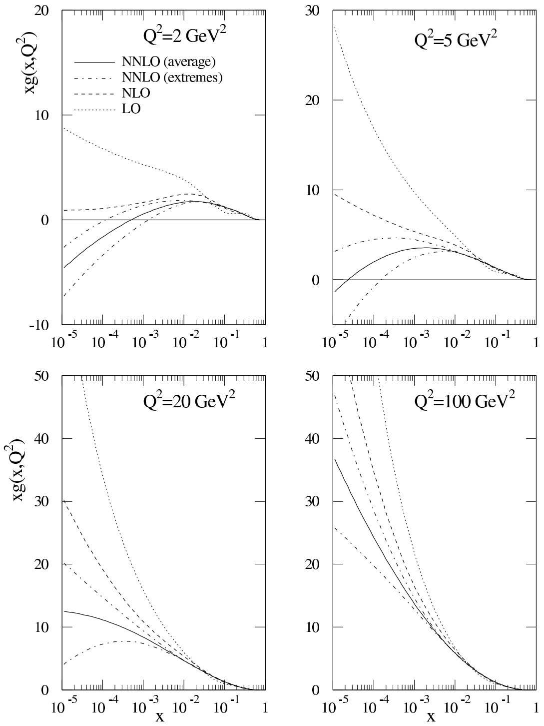

Fig. 6.15 Comparison of gluon PDFs at various Q^2 from MRST00 DGLAP fits performed to LO, NLO and two extreme versions of NNLO.

modified to include gluons and sea quarks at the starting scale μ^2, BUT these distributions have a valence-like shape (i.e. small at small x). One may even interpret this picture by saying that the gluons and sea quarks are frozen upon the valence current quarks for $Q^2 < \mu^2$, and these composite objects form the constituent quarks.

The scale μ^2 is set as the scale at which the gluon distribution is as hard as the valence quark distribution u_v. The splitting $q \to qg$ naturally generates a softer distribution in the split products than that of the original quark, hence a gluon distribution which is harder than the valence quark distribution which generates it is considered physically unreasonable. Thus the scale μ at which $g \sim u_v$ is assumed to be the lowest scale at which the DGLAP equations may be used.

It turns out that $\mu^2 \sim 0.4\,\mathrm{GeV}^2$ at NLO, which seems a very low scale at which to use perturbative QCD. However, GRV argue that it is the value of $\alpha_s(\mu^2)/\pi \sim 0.2$, which determines the relative size of higher order corrections, not the value of $\alpha_s(\mu^2)$, and that their predictions are perturbatively stable between LO and NLO if one considers measurable quantities

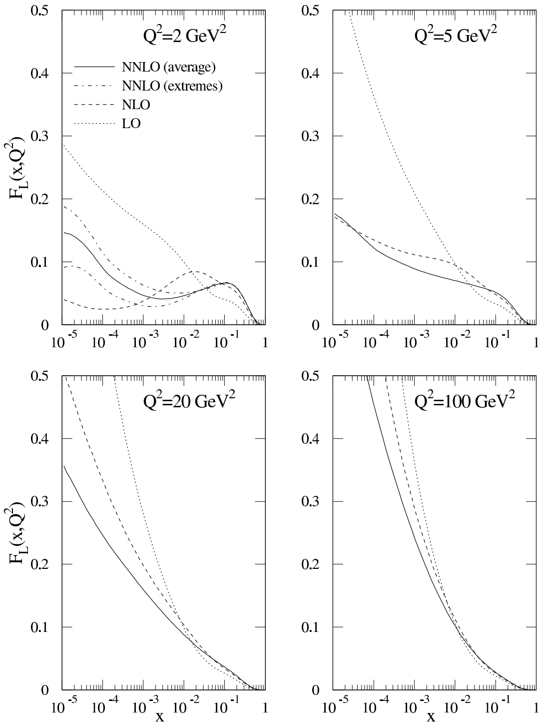

Fig. 6.16 Comparison of F_L at various Q^2 from MRST00 DGLAP fits performed to LO, NLO and two extreme versions of NNLO.

like structure functions, rather than parton distributions. They emphasize that their calculation is only applicable to the leading twist operators of QCD, and clearly at very low Q^2 higher twist operators can be important. Hence GRV state that the calculation can be made consistently at low Q^2, but they only expect the resulting parametrization to describe reality for somewhat higher Q^2 ($\gtrsim 0.6\,\mathrm{GeV}^2$).

Whereas at larger x, $x > 0.01$, the approach is similar to that of MRS and CTEQ, at small x, $x < 0.01$, it loses sensitivity to the form of the initial distributions at $Q^2 = \mu^2$. This is because of the long evolution length between μ^2 and the Q^2 values at which the comparison with data is made, taken together with the fact that the initial distributions are valence-like and thus vanishing at small x. Thus the resulting steepness of the gluon and sea quark distributions at small x and larger Q^2 is dynamically generated by pQCD. HERA data were not input to the original GRV parametrization so that it represented a successful prediction for the steep behaviour of F_2 in the HERA region. The flattening of F_2 as Q^2 decreases is also predicted, but pQCD fits indicate that whereas the gluon PDF becomes valence-like

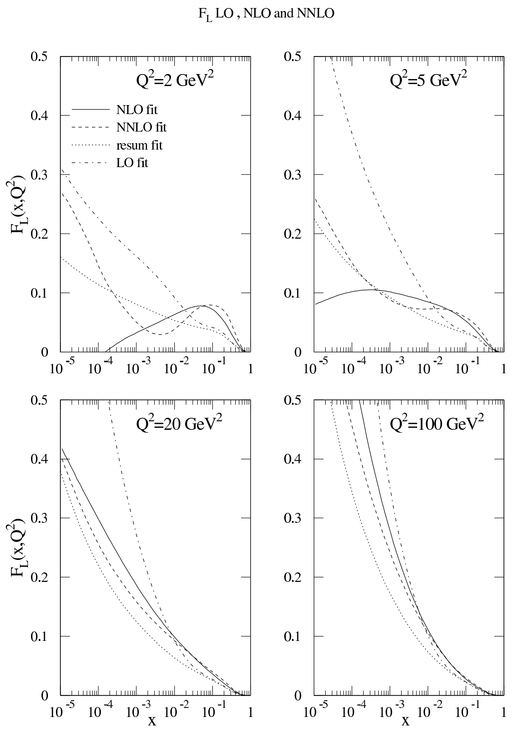

Fig. 6.17 Comparison of F_L at various Q^2 from MRST01 DGLAP fits performed to LO, NLO and NNLO, with the result of a fit including $ln(1/x)$ resummation terms

at low Q^2 the sea quark PDF does not. This presents a potential difficulty for the GRV approach, however currently a small amount of fine tuning of the original choice of the scale μ and the input valence-like shapes can produce a good fit to HERA data, provided $\alpha_s(M_Z^2) \lesssim 0.114$.

6.6 Summary

This chapter has covered the practical aspects of how parton momentum densities are extracted using the technique of NLO QCD based global fits. The sources of data and uncertainties have been addressed. A summary of the resulting parton densities from the 'theory teams' and experimental groups has been given. Overall the results are in good agreement with each other, but there is still a range of opinion on how to define and measure the error on a parton density, particularly that arising from experimental systematic errors.

6.7 Questions

1. Using the information in Secs 2.4 & 4.2 discuss possible choices of parton densities for for global fits. Consideration should be given to sources of data, primary purpose of the fit (e.g. extraction of valence quark distributions or the gluon, determination of α_S from scaling violations) and computational efficiency.

7
DIS at low x

This chapter is concerned with physics at low values of Bjorken x, below 10^{-3}. In this region the $q\bar{q}$ sea and gluon dynamics are dominant and their study has been made possible by the advent of data from the HERA collider (see Fig. 5.1). The principle new feature of the data is the dramatic rise of F_2 at low x, the rise becoming more rapid as Q^2 increases (see Fig 5.12). Can the data be explained within the framework of standard DGLAP NLO QCD or does it require new aspects of QCD? If not what are the new features? The HERA DIS experiments have also collected very accurate data at low x as $Q^2 \to 0$ which allow the study of the transition region from pQCD to non-perturbative physics. The chapter is organised as follows. First a few remarks are made about the dominance of the gluon density in the DGLAP equations at low x and how this could be used to measure it. Then a discussion of the low x limits of the DGLAP equations and their dependence on the nature of the input gluon density at the starting scale. Beyond DGLAP one may consider more general pQCD approaches but also general theories of scattering at high energies, since low x implies a large $\gamma^* p$ CM energy. Both 'classical' Regge theory and its pQCD equivalent (the BFKL equation and variants) are discussed. Finally the chapter ends with a discussion of unitarity constraints and saturation and their realisation in dipole models. Many of the topics discussed in this chapter are the subject of active research, some of the formalism is not yet stable and conclusions are inevitably somewhat tentative.

Balance? Too much on BFKL? Dipoles?

Written 2000, not revised.

7.1 The gluon from $\partial F_2/\partial \ln Q^2$ and F_L

The numerical study of the DGLAP equations at LO, particularly for the singlet and gluon components (Sec. 4.4.2), shows that the gluon density very rapidly becomes dominant at low x as Q^2 increases. This observation is the basis of two approximate methods to extract the gluon density from structure function data.

7.1.1 $\partial F_2/\partial \ln Q^2$

Using the DGLAP equations, the LO evolution equation for F_2 is

$$\frac{\partial F_2(x,Q^2)}{\partial \ln Q^2} = \frac{\alpha_S(Q^2)}{2\pi}\{P_{qq}\otimes F_2 + 2\bar{e}^2 P_{qg}\otimes xg\},$$

where $\bar{e}^2 = \sum_i^{n_f} e_i^2$. Prytz [Pry93] realised that for $x < 0.01$ the contribution of the P_{qq} term from quark splitting was negligible in comparison to the gluon term. Dropping the first term in the above equation and with an obvious change of integration variable,

$$\frac{\partial F_2(x,Q^2)}{\partial \ln Q^2} \approx \bar{e}^2\frac{\alpha_S(Q^2)}{\pi}\int_0^{1-x} G(\frac{x}{1-z})P_{qg}(z)dz,$$

where $G(x) = xg(x)$. The splitting function $P_{qg}(z) = \frac{1}{2}(z^2+(1-z)^2)$ is symmetrical and slowly varying over the range $(0,1)$ so the above convolution may be approximated by expanding $G(x/(1-z))$ about $z = 1/2$,

$$G(x/(1-z)) = G(2x) + (z-1/2)G'(2x) + \ldots$$

Because $P_{qg}(z)$ is symmetric about $z = 1/2$ the 2nd term in the expansion will integrate to zero and a good approximation is obtained by keeping only the first term (with $1-x \to 1$ as the upper limit of integration)

$$\begin{aligned}\frac{\partial F_2(x,Q^2)}{\partial \ln Q^2} &\approx \bar{e}^2\frac{\alpha_S}{\pi}G(2x)\int_0^1 P_{qg}(z)dz \\ &\approx \frac{\bar{e}^2\alpha_S}{3\pi}G(2x). \end{aligned} \tag{7.1}$$

The last equation may be inverted to give

$$xg(x) \approx \frac{3\pi}{\bar{e}^2\alpha_S}\frac{dF_2(x/2,Q^2)}{d\ln Q^2}. \tag{7.2}$$

The Prytz method gives a simple way of estimating $xg(x)$ at low x, but note that the derivative of F_2 is required at $x/2$ for the extraction of xg at x. The method has been extended to NLO but it loses some of its simplicity. Given the existence of efficient numerical codes for full DGLAP NLO evolution and fitting, the approximate inversions of the DGLAP equations are no longer a preferred method for accurate extraction of the gluon density.

7.1.2 F_L

The lowest order DGLAP expression for F_L is

$$F_L(x,Q^2) = \frac{\alpha_S}{2\pi}\int_x^1 \frac{d\xi}{\xi}\left[\frac{8}{3}\left(\frac{x}{\xi}\right)^2 F_2(\xi,Q^2) + \bar{e}^2 4\left(\frac{x}{\xi}\right)^2\left(1-\frac{x}{\xi}\right)\xi g(\xi,Q^2)\right]$$

For $x \lesssim 5\times 10^{-2}$, the gluon density dominates the integral. Cooper-Sarkar *et al.* [Coo88] approximated the integrals as follows. First define the two integrals

$$I_F = \int_x^1 \frac{d\xi}{\xi}\left(\frac{x}{\xi}\right)^2 F_2(\xi,Q^2), \quad I_G = \int_x^1 \frac{d\xi}{\xi}\left(\frac{x}{\xi}\right)^2 \left(1-\frac{x}{\xi}\right) G(\xi,Q^2),$$

then change variables $\xi = x/(1-z)$ to give

$$I_F = \int_0^1 dz\,(1-z)F_2(x/(1-z)), \quad I_G = \int_0^1 dz\,z(1-z)G(x/(1-z)),$$

where the approximation $1-x \to 1$ has been made for the upper limit of integration. For I_F expand $F_2(x/(1-z))$ about $z=1/2$ to give $I_F \approx F_2(2x)/2$. I_G requires a little more attention as $G(x) = xg(x)$ may behave like $x^{-\delta}$, $\delta > 0$ at small x. By considering $\tilde{G} = x^\delta G(x)$ and allowing a variation $0 \le \delta < 1$, $I_G \approx G(x/0.4)/5.9$ was found to be a good approximation at small x. Using these two expressions for the integrals, the convolution for F_L is reduced to an algebraic relation which may be inverted to give

$$xg(x,Q^2) \approx \frac{9}{5}\left\{\frac{3\pi}{2\alpha_S(Q^2)}F_L(0.4x,Q^2) - F_2(0.8x,Q^2)\right\}, \tag{7.3}$$

which shows that a measurement of F_L at low x would give a very direct determination of xg. Unfortunately F_L is a very difficult quantity to measure experimentally.

7.2 Double asymptotic scaling

The dominance of the gluon contribution to the DGLAP equations at small x and large Q^2 allows one to make an interesting prediction for the proton structure function in the so called double asymptotic limit. Of course this also assumes that the DGLAP formalism remains valid in the region of small x DIS, a question that will be taken up later. The result was an early prediction of QCD (De Rujula *et al.* [DeR74]), which was revived by the work of Ball and Forte [Bal94]. A simplified account, at LO, following the approach of the latter authors is given here.

The behaviour of the parton densities at small x is, in large part, controlled by the behaviour of the splitting functions $P_{ij}(z)$ as $z \to 0$, since in the convolution integrals $z < x$. At LO one has

$$P_{qq}(z) \to \frac{4}{3}, \quad P_{qg}(z) \to \frac{1}{2}, \quad P_{gq}(z) \to \frac{8}{3z}, \quad P_{gg}(z) \to \frac{6}{z},$$

thus the gluon splitting functions are the most singular and P_{gg} has the larger coefficient. The numerical studies of Sec. 4.4.2 also show that the gluon contribution is by far the most important at low x, already at rather modest values of Q^2 much larger than the singlet term. Using these results, the gluon evolution Eq. 4.45 is simplified by dropping the singlet term

$$\frac{\partial g(x,t)}{\partial t} \approx \frac{\alpha_S(t)}{2\pi}\int_0^{\ln(1/x)} d(\ln(1/\xi))g(\xi,t)P_{gg}(x/\xi)$$

where a change of integration variable has been made and $t = \ln(Q^2/\Lambda^2)$ introduced (the appearance of the constant Λ makes no difference to the derivative with respect to $\ln Q^2$). Next approximate P_{gg} by its most singular term and substitute the LO expression $\alpha_S(Q^2) = 1/(b_0 t)$ to give

$$t\frac{\partial xg(x,t)}{\partial t} \approx \frac{3}{\pi b_0}\int_0^{\ln(1/x)} d(\ln(1/\xi))\xi g(y\xi, t).$$

This equation is now differentiated with respect to $\ln(1/x)$. First introduce the two variables

$$u = \ln\left(\frac{t}{t_o}\right), \qquad v = \ln\left(\frac{x_0}{x}\right), \tag{7.4}$$

then differentiating with respect to v and using u in place of $\ln t$ gives

$$\frac{\partial^2 G(u,v)}{\partial u \partial v} = \gamma^2 G(u,v) \quad (\gamma^2 = \frac{3}{\pi b_0}), \tag{7.5}$$

where $G(u,v) = xg(x,Q^2)$. (Again the extra constants introduced, t_0 and x_0, make no difference to the derivative.) Equation 7.5 is of the form of a wave equation. Ball and Forte make use of this analogy to discuss the general behaviour of $G(u,v)$ – including some sub-leading terms ignored here. To find the solution for the double asymptotic limit, $\ln Q^2 \to \infty$, $\ln(1/x) \to \infty$, it is convenient to make another change of variables

$$\rho = \left(\frac{v}{u}\right)^{1/2}, \qquad \sigma = (uv)^{1/2}. \tag{7.6}$$

The limit required corresponds to $\sigma \to \infty$ with ρ fixed (at a value $O(1)$). Changing the variables in the derivative gives

$$4\frac{\partial^2}{\partial u \partial v} = \frac{\partial^2}{\partial \sigma^2} - \frac{\rho}{\sigma^2}\frac{\partial}{\partial \rho} + \frac{1}{\sigma}\frac{\partial}{\partial \sigma} - \frac{\rho^2}{\sigma^2}\frac{\partial^2}{\partial \rho^2},$$

but for the asymptotic solution at large σ only the first term on the RHS is retained and Eq. 7.5 becomes

$$\frac{\partial^2 G(\sigma,\rho)}{\partial \sigma^2} = 4\gamma^2 G(\sigma,\rho). \tag{7.7}$$

This equation may now be solved immediately

$$G(\sigma,\rho) = A\exp\bigl(2\gamma\sigma\bigr), \tag{7.8}$$

where A is a constant, or

$$G(u,v) = A\exp\bigl(2\gamma\sqrt{uv}\bigr), \tag{7.9}$$

or

$$xg(x,Q^2) = A\exp\left\{\sqrt{\frac{12}{\pi b_0}\ln\bigl(\frac{t}{t_0}\bigr)\ln\bigl(\frac{x_0}{x}\bigr)}\right\} \tag{7.10}$$

which are different forms of the double asymptotic scaling (DAS) limit for the gluon density. Note that, in addition to the asymptotic dependence on

σ, the gluon density, xg, is predicted to be independent of ρ. As will be discussed in more detail in Sec. 7.3.1, this limit of the DGLAP equations is valid provided that $xg(x, Q_0^2)$ is non-singular, i.e. $xg(x, Q_0^2) \sim x^{-\lambda}$, $\lambda \leq 0$, [For95,Lop96].

Having got an expression for xg at small x one may now use a modified form of the Prytz approximation to estimate F_2. Returning to Eq. 7.1, expand $G(x/(1-z))$ about $z = 0$ and keep only the leading term.[1] Substituting the LO expression for α_S then gives

$$t\frac{\partial F_2}{\partial t} \approx \frac{\bar{e}^2}{3\pi b_0} G(x, Q^2)$$

or

$$\frac{\partial F_2(u,v)}{\partial u} = \frac{A\bar{e}^2}{9}\gamma^2 \exp\left(2\gamma\sqrt{uv}\right), \tag{7.11}$$

where $\pi b_0 = 3/\gamma^2$ has been used. By using $w^2 = u$ this equation can be integrated to give (reverting to variables ρ, σ)

$$F_2(\rho,\sigma) = \frac{A\bar{e}^2}{9}\frac{\gamma}{\rho}\exp(2\gamma\sigma)[1 + O(1/\sigma)] \tag{7.12}$$

for $\sigma \to \infty$ and ρ fixed. Ball and Forte found that with appropriate boundary conditions the asymptotic region could be reached for values of σ and ρ well within the range of the HERA experiments. The constant A has to be determined from the data and the choice of x_0 and Q_0^2 will define the range of data points included. Fig. 7.1 shows the results of a study by H1 [H1 95a] of the LO DAS prediction, using their 1993 F_2 data[2] with $x_0 = 0.1$, $Q_0^2 = 1\,\mathrm{GeV}^2$ and $\Lambda = 185\,\mathrm{MeV}$. The upper plot of the figure shows $\ln(R'_F F_2)$ as a function of σ, where $R'_F \sim (\rho/\gamma)$ removes that factor and some smaller sub-leading terms that have been ignored here, resulting in a quantity that should rise linearly with σ with slope 2γ. The lower plot shows $\ln(R_F F_2)$ as a function of ρ, where $R_F = \exp(-2\gamma\sigma)R'_F$. This tests the second prediction of DAS that this quantity should be independent of ρ. It can be seen that 'ρ-scaling' is reasonable for $\rho > 1.2$ or so. Applying this cut to the data and fitting the slope of the first plot gives $2.22 \pm 0.04(\mathrm{stat.}) \pm 0.10(\mathrm{sys.})$, to be compared to $2\gamma = 2.4$ the LO prediction for 4 flavours. The expressions for DAS have also been worked out for NLO [Bal95] and applied to data [H1 96a].

7.3 General behaviour at low x

Double asymptotic scaling is one possible solution of the DGLAP equations at low x. To discuss more general possibilities for DGLAP and beyond it

[1] This can be justified by a more careful treatment of the small z approximation for P_{qg}, see Ball and Forte 1994 for details.

[2] The data covered the range $4.5 < Q^2 < 1600\,\mathrm{GeV}^2$ and $1.8 \times 10^{-4} < x < 0.13$.

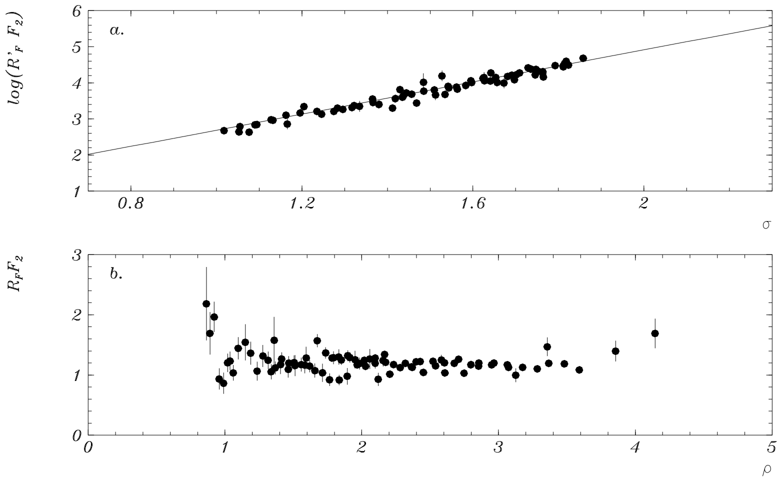

Fig. 7.1 Evidence for double asymptotic scaling, data from the H1 experiment compared with the LO DAS prediction: (a) $\ln(R'_F F_2)$ as a function of σ; (b) $R_F F_2$ as a function of ρ. R_F, R'_F and the variables σ and ρ are defined in the text.

is convenient to use the language and formalism of the operator product expansion. In particular the use of moments (Mellin transforms) will provide powerful insights and simplifications. The n-th moment of a parton density or structure function is defined by

$$\tilde{q}(n, Q^2) = \int_0^1 dx\, x^{n-1} q(x, Q^2).$$

For splitting functions the moments are the anomalous dimension functions $\gamma(n)$ (see Sec. 4.5). The inverse Mellin transform is a contour integral

$$q(x, Q^2) = \frac{1}{2\pi i} \int_C dn\, x^{-n} \tilde{q}(n, Q^2)$$

where the contour C runs parallel to the imaginary axis and is to the right of the right-most singularity of $\tilde{q}(n, Q^2)$ in complex n-space. The behaviour at low x of a PDF or structure function is controlled by the position of the rightmost singularity. In the case (such as DGLAP) where a convolution is involved (which becomes a product of moments in n-space) this could from either the PDF at the starting scale or the anomalous dimension. First the DGLAP case is used as an example, then some general remarks are made about resummations before the specific case of BFKL summation at low x is considered.

7.3.1 DGLAP at low x

The LO expressions for the anomalous dimensions are given in the App. 4.11 and they have poles in n at the negative integers and $n = 0, 1$. The poles at $n = 1$ occur in $\gamma_{gq}^{(0)}$ and $\gamma_{gg}^{(0)}$ for the gluon and they correspond to the $1/z$ terms in the gluon splitting functions since

$$\int_0^1 dz\, z^{n-1}(1/z) = 1(n-1).$$

Suppose that the gluon density at the starting scale μ^2 and for small x has the behaviour

$$xg(x, \mu^2) = Ax^{-\lambda_g}$$

then

$$\tilde{g}(n, \mu^2) = A \int_0^1 dx\, x^{n-1} x^{-\lambda_g - 1} = A/(n - \lambda_g - 1),$$

showing that $\tilde{g}(n, \mu^2)$ has a pole at $n = 1 + \lambda_g$. Considering the grossly simplified case of LO gluon evolution in which the singlet quark terms are ignored, it can be seen that the rightmost pole in n-space is at $n = 1$ from the anomalous dimension unless $\lambda_g > 0$. For $\lambda_g < 0$ ('valence like' gluon density) the asymptotic behaviour as $x \to 0$ is given by the evolution kernel and is the double asymptotic scaling solution discussed in Sec. 7.2. For $\lambda_g > 0$ the singular power behaviour of the input distribution is the dominant behaviour for all Q^2.

The calculation is more complicated if both quarks and gluons are included at LO or NLO as the singlet-gluon anomalous dimension matrix has to be diagonalised. The critical value of λ_g (or the equivalent power for the structure function) maybe somewhat larger than 0, the value also depending on the starting scale μ^2 (the details are explored in Ellis *et al.* [Ell94]). However the essential feature of two possible behaviours at low x for DGLAP evolution remains. If μ^2 is not large and $xg(x, \mu^2)$ not too singular then one finds double asymptotic scaling (xg or F_2 growing faster than a log but slower than a power in x). If $xg(x, \mu^2)$ is more singular at low x then $xg(x, Q^2) \sim x^{-\lambda_g}$ with the behaviour in x now independent of Q^2. The latter case has been explored in detail by Yndurain and co-workers [Lop80,Lop96]. F_2 is split into its singlet (F_S) and non-singlet (F_{NS}) components respectively. The Q^2 behaviours of both pieces are calculated at LO and NLO in terms of α_S and anomalous dimensions. The x dependence is constructed from powers of x and $(1 - x)$ with a small number of parameters. At small x, F_2 is dominated by the singular term in F_S, which at LO takes the form

$$F_S(x, Q^2) \approx B_S[\alpha_S(Q^2)]^{-d_+(1+\lambda_S)} x^{-\lambda_S},$$

where d_+ is the largest eigenvalue of the singlet anomalous dimension matrix and λ_S is a parameter to be determined from the data. Three other

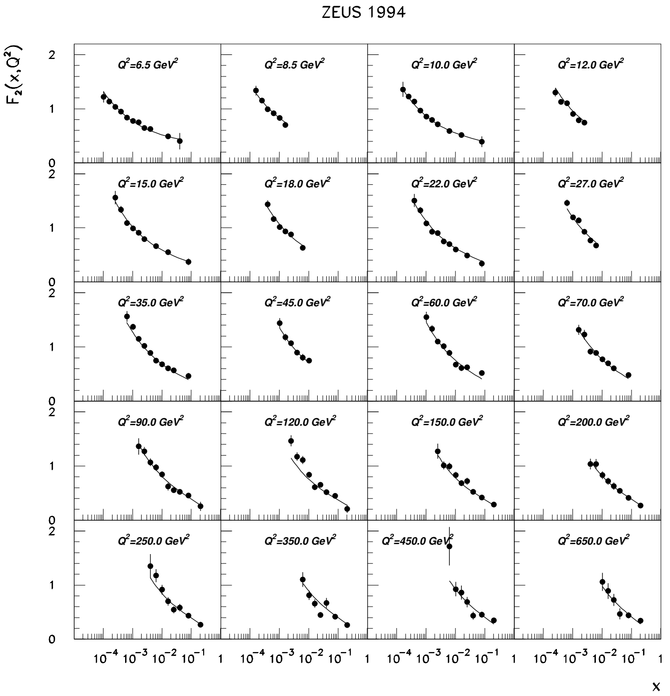

Fig. 7.2 The fit to the ZEUS 1994 F_2 data by Lopez *et al.* [Lop96] using the singular solution to the DGLAP equations at low x .

parameters are needed in the complete expression for F_2. Fitting to HERA 1994 data (H1 and ZEUS separately), good descriptions of the data are obtained with vales of λ_S in the range $0.33 - 0.36$. An example of the fit to the ZEUS data is shown in Fig 7.2.

7.3.2 Resummations

For simplicity, continuing to restrict the discussion to the behaviour of the gluon distribution function only, the form of the DGLAP evolution equation at low x is

$$\frac{\partial g(x,Q^2)}{\partial \ln Q^2} = \int_x^1 \frac{d\xi}{\xi} P(x/\xi, \alpha_S) g(\xi, Q^2),$$

where the overall factor of $\alpha_S/(2\pi)$ has been absorbed into the splitting function and the label gg has been dropped. For small x the leading term in $P(x, \alpha_S)$ is then $\bar{\alpha}_S/x$ where $\bar{\alpha}_S = 3\alpha_S/\pi$. In general the DGLAP splitting functions are expanded in powers of $\alpha_S/(2\pi)$

$$P(x, \alpha_S) = \sum_{j=1}^{\infty} \left(\frac{\alpha_S}{2\pi}\right)^j P^{(j)}(x)$$

at low x the functions $xP^{(j)}(x)$ have a leading behaviour of $\ln^{j-1}(1/x)$ and may be written as

$$xP^{(j)}(x) = \sum_{k=1}^{j} A_k^{(j)} \ln^{k-1}(1/x) + x\overline{P}^{(j)}(x),$$

where $\overline{P}^{(j)}$ is finite as $x \to 0$. So the full expansion for the splitting function is

$$xP(x, \alpha_S) = \sum_{j=1}^{\infty} \left(\frac{\alpha_S}{2\pi}\right)^j \left[\sum_{k=1}^{j} A_k^{(j)} \ln^{k-1}(1/x) + x\overline{P}^{(j)}(x)\right]$$

Such an expression holds for all splitting functions. Considering only the singular terms as $x \to 0$ and absorbing the factors of 2π in the coefficients, the expansion becomes a double sum over terms of the form $\alpha_S^p \ln^q(1/x)$

$$xP(x, \alpha_S) = \sum_{j=1}^{\infty} \sum_{k=1}^{j} \tilde{A}_k^{(j)} \alpha_S^j ln^{k-1}(1/x). \tag{7.13}$$

Or in terms of the anomalous moments

$$\gamma(n, \alpha_S) = \sum_{j=1}^{\infty} \sum_{k=1}^{j} a_{jk} \alpha_S^j (n-1)^{-k},$$

where the Mellin transform $x^{-1} \ln^{k-1}(1/x) \to (k-1)!(n-1)^{-k}$ has been used. The leading coefficient for γ_{gg} is $a_{11} = \bar{\alpha}_S$.

The DGLAP splitting functions correspond to a particular restricted form of the double sum. Referring to Fig. 7.3 various approximations to the splitting functions may be defined:

DLLA leading double asymptotic scaling limit with $j = 1, k = 1$;

LL(Q^2) LO DGLAP, $j = 1$ and the sum over k runs from negative powers to $k = 1$ to include the expansion of the non-singular part;

NLL(Q^2) NLO DGLAP, $j = 1, 2$ sums over k as in the previous case;

LL($1/x$) LO BFKL, $j \geq 1, k = j$;

NLL($1/x$) NLO BFKL, $j \geq 1, k = j, j-1$.

Note the the DLLA limit is common to both the BFKL and DGLAP summations at LO. The challenge is to find techniques for performing the summations. Apart from DGLAP and DAS already discussed, the BFKL formalism will be outlined in some detail and a brief account given of angular ordering. First a historical interlude in which the ideas of Regge theory are introduced as it is the framework in which the BFKL equation was developed and it also gives an alternative perspective on low x behaviour.

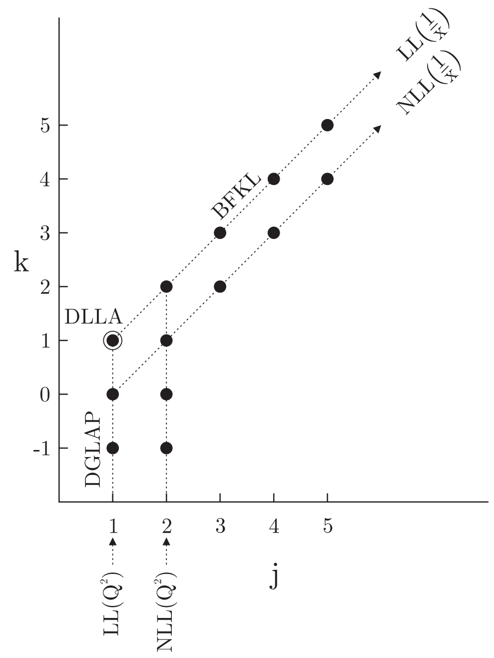

Fig. 7.3 Various resummation schemes.

7.4 Regge Theory

Regge theory, which predates QCD, is concerned with the high energy behaviour of hadron-hadron and photon-hadron cross-sections. This is relevant for DIS at low x because W, the $\gamma^* p$ CM energy, is given by $W^2 = Q^2(1/x - 1) \approx Q^2/x$. At large W^2 the structure function F_2 is simply related to the $\gamma^* p$ total cross-section (Eq. 13.19 of App. 13.4)

$$\sigma_{\gamma^* p}^{tot}(W^2, Q^2) \equiv \sigma_T + \sigma_L \approx \frac{4\pi^2\alpha}{Q^2} F_2(x, Q^2). \tag{7.14}$$

Regge theory grew out of the study of the analytic properties of the scattering amplitudes for strong interaction processes.[3] It provides a systematic framework for describing the high energy behaviour of hadronic total cross-sections and forward differential cross-sections. Consider a two-body scattering process $a + b \to c + d$ with the usual Mandelstam variables s, t, u ($s = (p_a + p_b)^2$, $t = (p_a - p_c)^2$, $u = (p_a - p_d)^2$) and ignore spin and masses for simplicity. The key physical idea is to relate the high energy behaviour of the s-channel amplitude to the quantum numbers that are exchanged in the t-channel. But why is Regge theory necessary for

[3] A comprehensive account is given in Collins [Col77a] and a brief introduction in Forshaw & Ross [For97,Ch. 1].

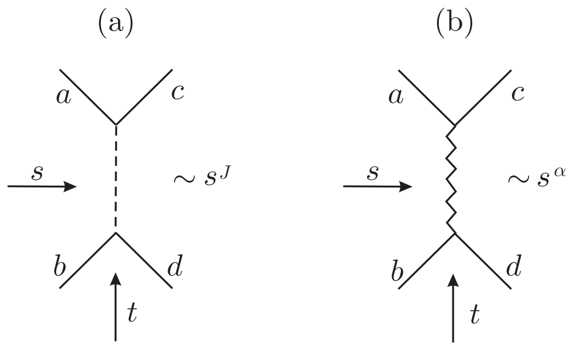

Fig. 7.4 Contributions in the t-channel for $ab \to cd$: (a) a resonance with spin J; (b) a Reggeon R with trajectory α.

this? Expand the s-channel amplitude in terms of t-channel partial wave amplitudes $a_l(t)$

$$A_{ab:cd}(s,t) = \sum_{l=o}^{\infty}(2l+1)a_l(t)P_l(\cos\theta_t),$$

where θ_t is the t-channel scattering angle and $\cos\theta_t = 1+2s/t$. Suppose now that a single resonance with mass M_J and spin J dominates the t-channel (Fig. 7.4(a)), then at high energy the amplitude has the form

$$A_{ab:cd}(s,t) \sim \frac{C}{t - M_J^2}\left(\frac{2s}{t}\right)^J$$

where C is a constant and $P_l(z) \sim z^l$ for z large has been used. There is evidence to support this idea for states with low values of J and small masses that are then 'near' s-channel physical region. For example single pion exchange dominates $ep \to e\pi^+n$ at low energy and small $|t|$ and it provides a way of measuring the EM form factor of the pion [Dev72]). However this fails in general for large J as the amplitude grows too large at large s and a single t-channel exchange is unlikely to be dominant anyway. Regge theory comes to the rescue by exploiting the properties of analytic functions. First the t-channel partial wave expansion is written as a contour integral

$$A_{ab:cd}(s,t) = \frac{1}{2i}\oint_{C_1} dl(2l+1)\frac{a(l,t)}{\sin\pi l}P(l,\cos\theta_t),$$

where the contour C_1 surrounds the positive real axis as shown in Fig. 7.5. The integrand has poles at the positive integers from the $\sin\pi l$ and thus reproduces the original sum. The contour C_1 is now opened out so that it

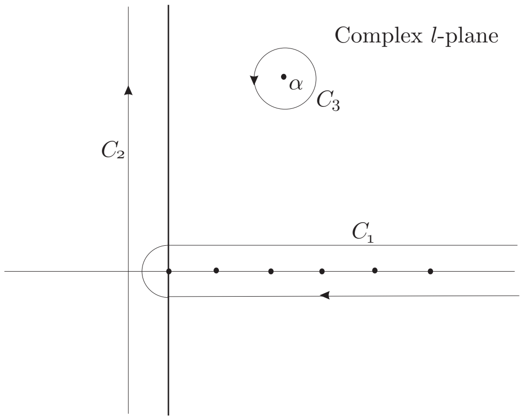

Fig. 7.5 The complex l-plane showing the contours for manipulating the partial wave sum.

forms a semi-circle with diameter, C_2, vertical at $\mathrm{Re}\, l = -1/2$ and closed to the right at infinity. Suppose the partial wave amplitude has a pole

$$a(l,t) = \frac{\tilde{\beta}(t)}{l - \alpha(t)}$$

then the contribution of that pole to A is picked up by the closed contour C_3 to give

$$A(s,t) = \frac{(2\alpha(t)+1)\pi\tilde{\beta}(t)}{\sin \pi\alpha(t)} P(\alpha(t), \cos\theta_t).$$

If the contribution of the contour C_2 is small then the complete t-channel partial wave sum has been replaced by that of a single Regge pole or possibly a finite sum of such terms. Many technical details have been ignored in this outline but one must be mentioned: to ensure that the analytic continuation can be performed uniquely the odd and even partial waves must be continued separately. A factor $(\eta + e^{-i\pi l})/2$ where $\eta = \pm 1$ is introduced into the partial wave sum to pick out the odd or even partial waves. Finally, using again the large argument approximation for $P(\alpha, z)$, one has the expression for the contribution of a single Regge pole (for $s >> |t|$)

$$A_{ab:cd}(s,t) = \frac{\eta + e^{-i\pi\alpha(t)}}{2} \beta(t) \left(\frac{s}{s_0}\right)^{\alpha(t)} \tag{7.15}$$

where s_0 is a scale factor, usually taken to be $1\,\mathrm{GeV}^2$ (and often omitted), η is known as the *signature* of the Regge pole. The function $\beta(t)$ is related to $\tilde{\beta}$ but has absorbed various other factors, some t dependent. The function $\alpha(t)$ is known as the *trajectory* of the Regge pole and the one with the largest real part will control the high energy behaviour of the amplitude.

The crucial advance is that for t-channel ($a\bar{c} \to \bar{b}d$) scattering $\alpha(t)$ passes through integer spin values J at physical states with mass m_J such that $\alpha(m_J^2) = J$, but when the trajectory is continued to the s-channel, $t < 0$, $\alpha(t)$ is usually less than 1 (see below). In a sense the Regge pole is equivalent to exchanging a 'tower' of angular momentum states and if the trajectory can be determined the energy dependence of the amplitude is given.. For a simple Regge pole, R, the residue function factorises $\beta(t) = \gamma_{acR}(t)\gamma_{bdR}(t)$ (see Fig. 7.4(b)) but the forms of these functions are not specified by the theory. A Regge pole has definite quantum numbers, such as isospin, charge conjugation and 'natural or unnatural parity'. Natural parity means that the parity of the states on the trajectory satisfy $P = (-1)^J$, unnatural parity corresponds to $P = -(-1)^J$. The contribution of a single Regge pole to the differential cross-section takes the form

$$\frac{d\sigma}{dt} \sim f(t)s^{2\alpha(t)-2},$$

and if there is more than one pole there will be interference effects from the signature factors. Of more interest here is the contribution of a Regge pole to the total cross-section for $ab \to all$. Using the optical theorem this is related to the contribution of the pole to the forward elastic amplitude for $ab \to ab$

$$\sigma_{ab}^{tot} \sim constant\, s^{\alpha(0)-1},$$

with an obvious generalisation if more than one pole contributes.

Figure 7.6 shows some of the low-lying meson states plotted on a Chew-Frautschi diagram (spin versus mass^2) with associated Regge trajectories, which are approximately linear ($\alpha(t) = \alpha(0) + \alpha' t$). The trajectories are built from valence q$\bar{\text{q}}$ states and follow the pattern of their quantum numbers. The $\rho - a_2$ trajectory ($I = 1$, C odd, natural parity) and $\omega - f_2$ ($I = 0$, C odd, natural parity) are essentially degenerate with $\alpha(0) = 0.55$ and $\alpha' = 0.86\,\text{GeV}^{-2}$.[4] The $\phi - f_2'$ ($I = 0$, C odd, natural parity) is from states predominantly s$\bar{\text{s}}$ and has a lower intercept. The $\pi - b_1$ ($I = 1$, C even, unnatural parity) has a still lower intercept. Assuming that the linear form of the trajectory may be extrapolated to negative t values (at least for small $|t|$) one can predict the energy dependence in the s-channel. All these trajectories correspond to the exchange of quantum numbers in the t-channel and give contributions to total cross-sections decreasing as $s^{-0.45}$ or faster. This is in line with general results proved by Pomeranchuk and Okun [Oku56]. However total cross-sections are mostly constant or slowly increasing with increasing energy. Foldy and Peierls [Fol63] showed that such behaviour must be associated with the exchange of states with vacuum quantum numbers. A new Regge trajectory, with $I = 0$, C even and natural parity is required. It is called the Pomeron (after Pomeranchuk)

[4] For a simple account of why the meson trajectory slopes all be the same see Bowler [Bow90, Ch. 5].

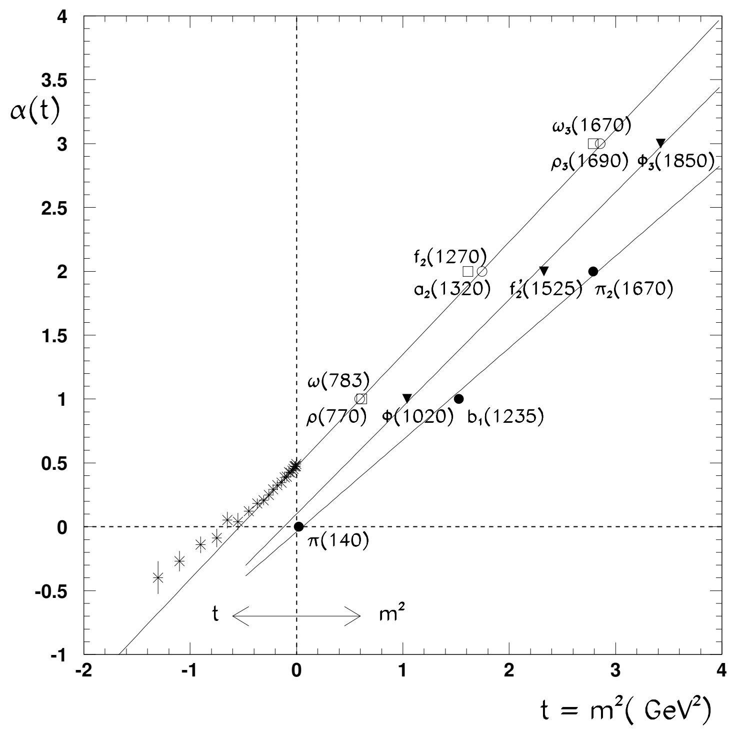

Fig. 7.6 Chew-Frautschi plot of spin versus mass^2 for low-lying meson states and associated Regge trajectories.

and must have an intercept $\alpha_P(0) \approx 1$, its slope (from diffractive scattering which also involves vacuum exchanges) is around $0.25\,\mathrm{GeV}^{-2}$. To meet the requirement of another high energy theorem of Pomeranchuk, namely that $\sigma_{ab}^{tot} \to \sigma_{a\bar{b}}^{tot}$ as $s \to \infty$, the Pomeron must couple equally to ab and $a\bar{b}$. To date it has not been possible to relate the Pomeron trajectory unambiguously to meson states, but it may be related to a glueball candidate. In QCD, the Pomeron would be a colourless object with vacuum quantum numbers composed of at least two gluons.

In recent years Donnachie and Landshoff [Don92], Cuddell *et al.* [Cud97] have shown that high energy total cross-section data (particularly that for pp and p$\bar{\text{p}}$) may be fit by the form

$$\sigma_i^{tot}(s) = A_i^P s^{\alpha_P(0)-1} + A_i^R s^{\alpha_R(0)-1} \tag{7.16}$$

where P, R refer to the Pomeron and other Regge exchanges respectively and the A_i are process dependent constants. The intercepts of the Pomeron and Regge trajectories are universal. By fitting to cross-section data they find that $\alpha_R(0) \approx 0.5$ in line with the expectation from the fit to meson state data of the $\rho - a_2$ and $\omega - f_2$ trajectories. For the Pomeron intercept, $\alpha_P(0)$, values in the range $1.081 - 1.094$ are found. It has also been shown that Eq. 7.16 (with the intercepts fixed) describes other hadronic total cross-section data including that of real photoproduction on protons. Donnachie and Landshoff [Don93] showed that this approach could be extended successfully to the then existing data on $\sigma^{tot}_{\gamma^* p}$ (or F_2) up to Q^2 values of about $10\,\mathrm{GeV}^2$. Their fundamental assumption is that the intercepts controlling the energy dependence should remain universal and Q^2 independent and all Q^2 dependence be contained in the Regge pole residue functions. To study the behaviour of F_2 at small x the approximation $s_{\gamma^* p} = W^2 \approx Q^2/x$ is used and to meet the requirement of Eq. 7.14, the coefficients must be proportional to Q^2 as $Q^2 \to 0$. Finally to reproduce the approximate scaling of the F_2 data, the coefficients should tend towards 1 for large Q^2. A minimal form that meets these requirements is

$$F_2(x, Q^2) = Ax^{1-\alpha_P(0)} \left(\frac{Q^2}{Q^2 + a}\right)^{\alpha_P(0)} + Bx^{1-\alpha_R(0)} \left(\frac{Q^2}{Q^2 + b}\right)^{\alpha_R(0)}, \tag{7.17}$$

with

$$4\pi^2 \alpha A a^{-\alpha_P(0)} = A^P_{\gamma p} \quad \text{and} \quad 4\pi^2 \alpha B b^{-\alpha_R(0)} = A^R_{\gamma p}.$$

The latter constraints ensure that the fit to real photoproduction data is recovered as $Q^2 \to 0$. Although the authors used more elaborate forms to fit data over a wider range of x, the above expression provided a good description of the lowest x data then available, principally from the NMC experiment [NMC92]. The important result from this approach is that the structure function F_2 is expected to rise only very slowly as $x \to 0$, roughly as $F_2 \sim x^{1-\alpha_P(0)}$ or $\sim x^{-0.08}$.

Remembering the relationship of the Reggeon and Pomeron trajectories to the quark and gluon states one can see that the Pomeron term is associated with the singlet (gluon and sea) and the Reggeon with the non-singlet (valence) contributions to F_2. Given the success of Regge theory in correlating the high energy behaviour of hadronic cross-sections, it might seem safe to extend it to the small x behaviour of structure functions. However as Donnachie and Landshoff remark at the end of their 1993 paper: *If the HERA experiments find results for F_2 significantly larger at small x than our extrapolation, we claim that this will be a clear signal that they have discovered new physics.* What they had in mind, if this happened, was evidence for the 'Lipatov' (BFKL) or perturbative Pomeron.

The striking result from HERA is that F_2 does rise very much more steeply that the 'standard' Regge approach predicts. A nice way of summarising the behaviour of the data at low x is to plot the effective power of F_2 as function of Q^2, $F_2 \sim x^{-\lambda_{eff}}$ or $\lambda_{eff} = d\ln F_2/d\ln(1/x)$. An example from ZEUS [ZEU99s] is shown in Fig. 7.7, λ_{eff} is calculated by fitting data in bins of Q^2 to $F_2 = Ax^{-\lambda_{eff}}$ (note that this gives a correlation between the value of Q^2 and the mean value of x from which λ_{eff} was

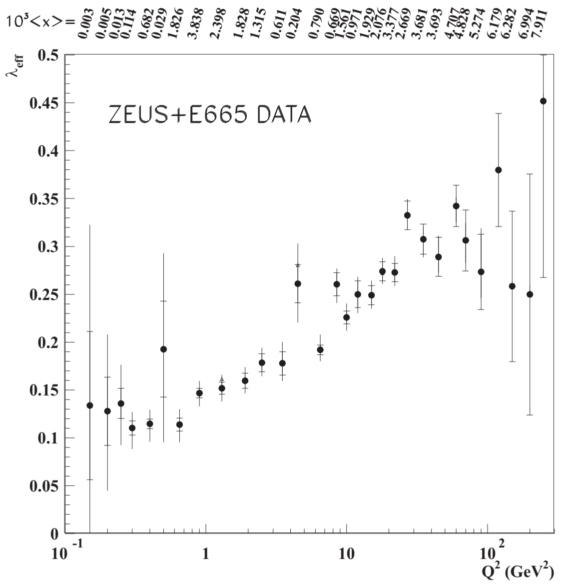

Fig. 7.7 The effective exponent of F_2 ($\lambda_{eff} = d \ln F_2 / d \ln(1/x)$)at low x as a function of Q^2 (from [ZEU99s]). Note the values of Q^2 and x are correlated.

determined). In Regge language $\lambda_{eff} = \alpha_P(0) - 1$. The plot shows that below $Q^2 \sim 1\,\mathrm{GeV}^2$ the data are compatible with a conventional hadronic Pomeron exponent but that for large Q^2 values λ_{eff} increases steadily to a value between $0.3 - 0.4$ for $Q^2 \sim 100\,\mathrm{GeV}^2$ and above.

Before moving on to the calculation of the perturbative Pomeron it is worth noting that Donnachie and Landshoff [Don98] have added a 'hard' Pomeron to their Regge ansatz for F_2 and with the three component model are able to give a good description of F_2 proton data with $x < 0.7$, the charm structure function F_2^c and $\sigma(\gamma p \to J/\psi p)$. In more detail, the structure function is written as

$$F_2(x, Q^2) = \sum_i f_i(Q^2) x^{-\epsilon_i},$$

where $\epsilon_0 + 1$ is the intercept of the hard Pomeron to be determined from the data. The parameters $\epsilon_1 = \alpha_P(0) - 1 = 0.0808$ and $\epsilon_2 = \alpha_R(0) - 1 = -0.4525$ are fixed by the intercepts of the conventional 'soft' Pomeron and $f - a$ Regge poles as determined from hadron-hadron data. The functions $f_i(Q^2)$ take the forms

$$f_0(Q^2) = A_0 \left(\frac{Q^2}{Q^2 + a_0} \right)^{1+\epsilon_0} \left(1 + X \log(1 + Q^2/Q_0^2)\right)$$

$$f_1(Q^2) = A_0 \left(\frac{Q^2}{Q^2 + a_1}\right)^{1+\epsilon_1} \frac{1}{1+\sqrt{Q^2/Q_0^2}}, \quad f_2(Q^2) = A_0 \left(\frac{Q^2}{Q^2 + a_2}\right)^{1+\epsilon_2}.$$

There are now a total of 10 parameters to be varied in the fit and the resulting value of ϵ_0 is 0.418.

7.5 The BFKL equation

Returning now to the central theme of this chapter, the prospect that QCD opened up was the *calculation* of the Pomeron trajectory and thus an understanding of the high energy behaviour of cross-sections. Or in the language of Eq. 7.13 the prospect of being able to sum the large $\ln(1/x)$ terms and thus determine the behaviour of the gluon density at low x. Using the methods of the 'Reggeised gluon' the LO BFKL equation with fixed α_S is considered first, then how the BFKL amplitude is related to hadronic scattering through so-called impact factors. A brief mention is made of an alternative formulation in terms of dipole scattering. The limitations of the LO fixed α_S result are then considered together with a summary of work on BFKL beyond the LO fixed α_S calculation..

7.5.1 The reggeised gluon and the LO BFKL equation

In the 1960s it was established that sums of ladder diagrams in scalar field theories could give Regge behaviour (i.e. the scattering amplitude behaving like $s^{\alpha(t)}$ for $s >> |t|$). Referring to Fig. 7.8, if the momentum, k_i, of the ith vertical leg in the ladder is written in Sudakov form in terms of the external momenta p_1, p_2, $k_i^\mu = \rho_i p_1^\mu + \lambda_i p_2^\mu + k_{iT}^\mu$, then the Regge limit is obtained by requiring a strong ordering in the Sudakov ρ and λ parameters. Specifically $\rho_i >> \rho_{i+1}$ and $|\lambda_{i+1}| >> |\lambda_i|$ with the transverse momentum $k_{iT}^2 \approx -\mathbf{k^2}$ of the order of the external transverse momenta.[5]

Balitsky, Fadin, Kuraev and Lipatov (BFKL) applied these ideas to gluon ladders in QCD (Kuraev *et al.* [Cur77], Balitsky & Lipatov [Bal78], Lipatov [Lip80]). The strong ordering in the Sudakov parameters is equivalent to a strong ordering of the longitudinal components (w.r.t. the external momenta) of the ladder momenta and in DGLAP language this is a strong ordering in the x_i of the internal momenta. In addition in the DGLAP case the internal loop transverse momenta are strongly ordered. These two restrictions mean that only simple quark or gluon ladder diagrams (as shown in the figure) have to be considered in the DGLAP case. For the BFKL Pomeron there are two complications, the first is that the internal transverse momenta are no longer ordered and the second is that one must project out the colour singlet states. The former means that many more diagrams have to be considered. The first step is to study the Regge limit for the scattering of two quarks by a colour octet exchange. It is found that in this limit the relevant diagrams have a ladder like structure in which

[5] A recent account of such calculations is given in [For97,Ch.2].

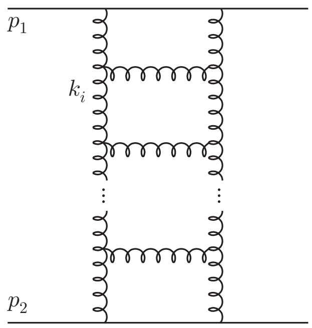

Fig. 7.8 A ladder diagram for studying the Regge limit of field theories.

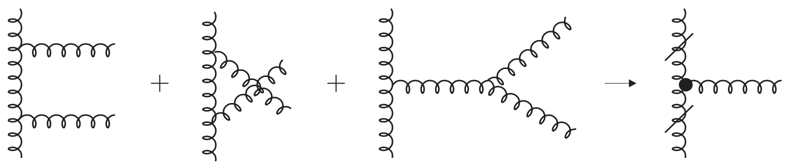

Fig. 7.9 The basic idea of the 'reggeised' gluon and effective vertex.

the vertical links are themselves constructed from ladders (the 'reggeised' gluons) coupled to simple gluon 'rungs' using effective vertices as shown in Fig. 7.9. Other diagrams involving crossed rungs or quark line insertions give sub-leading behaviour.

Using these ideas the Regge limit of colour singlet gluon exchange between two quarks is given by diagrams of the form shown in Fig. 7.10(a), with (b) representing the summed contribution of all such diagrams. BFKL found and solved an integral equation for the reggeised gluon four-point function, essentially the diagram (b) above with the external quark lines removed. A brief account is given here following Forshaw and Ross [For97,Chs 4,5,6].

The BFKL amplitude $\hat{f}(\omega, \mathbf{k}_1, \mathbf{k}_2, \mathbf{q})$ is related to the colour singlet quark scattering amplitude, $A^S(s,t)$, by a Mellin transform[6]

$$\begin{aligned} \tilde{A}^S(\omega, t) &= \int_1^\infty dz z^{-\omega-1} \frac{A^S(s,t)}{s} \\ &= 4i\alpha_S^2 G^S \int \frac{d^2\mathbf{k}_1 d^2\mathbf{k}_2}{\mathbf{k}_2^2(\mathbf{k}_1 - \mathbf{q})^2} \hat{f}(\omega, \mathbf{k}_1, \mathbf{k}_2, \mathbf{q}), \end{aligned} \tag{7.18}$$

where $z = s/\mathbf{k}^2$ ($\mathbf{k}^2$ is a scale factor typical of the external transverse momenta) and G^S projects out the colour singlet term. It will also be

[6]Note that the Mellin transform variable ω here corresponds to $n-1$ used earlier in the chapter – low x corresponds to large s.

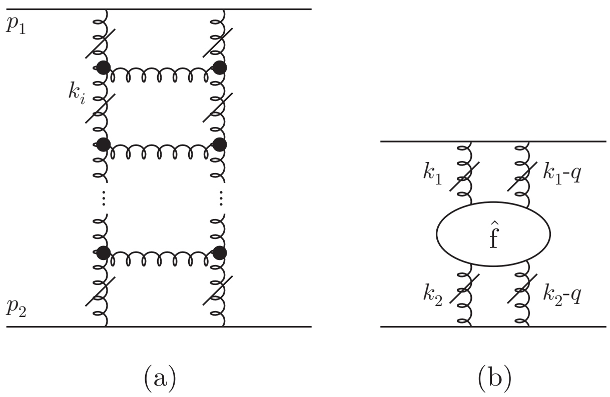

Fig. 7.10 Diagram showing reggeised two-gluon exchange between two quarks: (a) the lowest order contribution to the singlet state, (b) the general term.

convenient to define $F(s, \mathbf{k}_1, \mathbf{k}_2, \mathbf{q})$, the Mellin inverse of $\hat{f}(\omega, \mathbf{k}_1, \mathbf{k}_2, \mathbf{q})$. The simplest term in $A^S(s,t)$ is given by the exchange of two reggeised gluons and further terms have the form of ladder diagrams as in Fig. 7.8 but with the vertical gluon links replaced by reggeised gluons. The BFKL amplitude satisfies a linear integral equation of the form

$$\omega \hat{f}(\omega, \mathbf{k}_1, \mathbf{k}_2 . \mathbf{q}) = \delta^2(\mathbf{k}_1 - \mathbf{k}_2) + K_0 \otimes \hat{f}(\omega, \mathbf{k}_1, \mathbf{k}_2, \mathbf{q}) \tag{7.19}$$

which is shown diagrammatically in Fig. 7.11. Since the forward amplitude $A^S(s,0)$ is required for the total cross-section, only the forward BFKL amplitude with $\mathbf{q} = 0$ will be considered here. The convolution on the RHS with the LO BFKL kernel K_0 is

$$\begin{aligned} K_0 \otimes \hat{f}(\omega, \mathbf{k}_1, \mathbf{k}_2, 0) &= \frac{\bar{\alpha}_S}{\pi} \int \frac{d^2\mathbf{k}'}{(\mathbf{k}_1 - \mathbf{k}')^2} \\ \big[\hat{f}(\omega, \mathbf{k}', \mathbf{k}_2, 0) &- \frac{\mathbf{k}_1^2}{\mathbf{k}'^2 + (\mathbf{k}_1 - \mathbf{k}')^2} \hat{f}(\omega, \mathbf{k}_1, \mathbf{k}_2, 0)\big], \end{aligned} \tag{7.20}$$

where $\bar{\alpha}_S = 3\alpha_S/\pi$. Note that in the LO BFKL equation α_S does not run but is fixed at a scale typical of the external transverse momentum. The BFKL amplitude is infra-red finite as the terms in the [] brackets in the above expression vanish as $\mathbf{k}' \to \mathbf{k}_1$. The solution to the BFKL equation may be written schematically in terms of the eigenfunctions $\phi_i(\mathbf{k})$ of the kernel

$$\hat{f}(\omega, \mathbf{k}_1, \mathbf{k}_2, 0) = \sum_i \frac{\phi_i(\mathbf{k}_1)\phi_i^*(\mathbf{k}_2)}{\omega - \lambda_i} \tag{7.21}$$

where

$$K_0 \otimes \phi_i(\mathbf{k}) = \lambda_i \phi_i(\mathbf{k}).$$

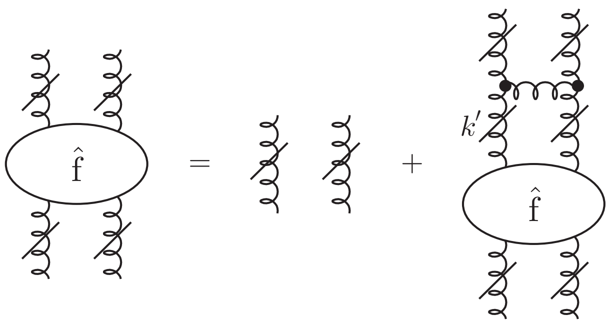

Fig. 7.11 Diagrammatic form of the BFKL equation.

In the 2-dimensional $\mathbf{k}'$ space write $\mathbf{k}' = (k', \theta')$ then the eigenvalue, $\lambda_i \equiv \omega_n(\nu) = \bar{\alpha}_S \chi_n(\nu)$, depends on two variables, ν and n, corresponding to k' and θ' respectively. The function $\chi_n(\nu)$ is the *characteristic* function of the BFKL kernel. The eigenfunctions have the form

$$\phi_\nu^n(\mathbf{k}) = \frac{1}{\pi\sqrt{2}} (k^2)^{-1/2+i\nu} e^{in\theta} \tag{7.22}$$

and in 7.21 $\sum_i \to \sum_{n=0}^{\infty} \int_{-\infty}^{\infty} d\nu$. $A^S(s,0)$ is given by the Mellin inversion of 7.21 and thus the leading behaviour in s is given by rightmost singularity in ω which means the eigenvalue with the largest real part. The function $\chi_n(\nu)$ decreases as n increases from 0 and decreases as $|\nu|$ increases. Keeping only the leading $n = 0$ term

$$\hat{f}(\omega, \mathbf{k}_1, \mathbf{k}_2, 0) = \frac{1}{\pi k_1 k_2} \int_{-\infty}^{\infty} \frac{d\nu}{2\pi} \left(\frac{k_1^2}{k_2^2}\right)^{i\nu} \frac{1}{\omega - \bar{\alpha}_S \chi_0(\nu)}. \tag{7.23}$$

It is convenient to rewrite this result in terms of the variable $\gamma = \frac{1}{2} + i\nu$, as it takes the form of a Mellin integral in γ-space (conjugate to transverse momentum)

$$\hat{f}(\omega, \mathbf{k}_1, \mathbf{k}_2, 0) = \frac{1}{\pi k_1^2} \int_{\frac{1}{2}-\infty}^{\frac{1}{2}+\infty} \frac{d\gamma}{2\pi i} \left(\frac{k_1^2}{k_2^2}\right)^{\gamma} \frac{1}{\omega - \bar{\alpha}_S \chi(\gamma)}, \tag{7.24}$$

where the subscript 0 has been dropped from χ and

$$\chi(\gamma) = 2\psi(1) - \psi(\gamma) - \psi(1-\gamma),$$

where $\psi(x)$ is the digamma function $\frac{d}{dx} \ln \Gamma(x)$. Using 7.24 the amplitude $F(s, \mathbf{k}_1, \mathbf{k}_2)$ may be expressed as a double Mellin integral

$$F(s, \mathbf{k}_1, \mathbf{k}_2) = \int \frac{d\omega}{2\pi i} \left(\frac{s}{\mathbf{k}^2}\right)^{\omega} \frac{1}{\pi k_1^2} \int \frac{d\gamma}{2\pi i} \left(\frac{k_1^2}{k_2^2}\right)^{\gamma} \frac{1}{\omega - \bar{\alpha}_S \chi(\gamma)}, \tag{7.25}$$

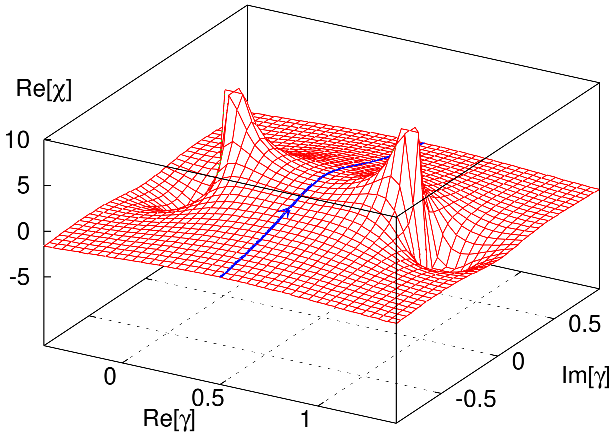

Fig. 7.12 Real part of the LO BFKL characteristic function χ in the complex γ plane and the contour for the Mellin inversion using the saddle point method at $Re(\gamma) = 1/2$ (from [Sal99]).

where the contour in ω runs parallel to the imaginary axis and to the right of all singularities in the ω-plane. The integrand has a simple pole at $\omega = \bar{\alpha}_S \chi(\gamma)$ and thus the ω integration gives

$$F(s, \mathbf{k}_1, \mathbf{k}_2) = \int \frac{d\gamma}{2\pi i} \left(\frac{s}{\mathbf{k}^2}\right)^{\bar{\alpha}_S \chi} \frac{1}{\pi k_1^2} \left(\frac{k_1^2}{k_2^2}\right)^{\gamma}, \tag{7.26}$$

where the contour runs parallel to the imaginary γ axis. For large $s/\mathbf{k}^2$ the integral is controlled by χ, Fig.7.12 shows $\mathrm{Re}(\chi)$ in the complex γ plane and the integration contour for the final Mellin inversion. The integral may be evaluated by a saddle point approximation[7] about $\mathrm{Re}(\gamma) = 1/2$ giving,

$$F(s, \mathbf{k}_1, \mathbf{k}_2) = \frac{1}{\pi k_1 k_2} \frac{(s/\mathbf{k}^2)^{\bar{\alpha}_S \chi(1/2)}}{\sqrt{2\pi \bar{\alpha}_S |\chi''(1/2)| \ln(s/\mathbf{k}^2)}}. \tag{7.27}$$

Finally $A(s, 0)$ is obtained by integrating over $\mathbf{k}_1^2$ and $\mathbf{k}_2^2$

$$\frac{A(s,0)}{s} = 4i\alpha_S^2 G^S \int \frac{d^2\mathbf{k}_1}{\mathbf{k}_1^2} \frac{d^2\mathbf{k}_1}{\mathbf{k}_1^2} F(s, \mathbf{k}_1, \mathbf{k}_2),$$

giving a high energy behaviour

$$A(s, 0) \sim \frac{(s/\mathbf{k}^2)^{1+\omega_0}}{\sqrt{\ln(s/\mathbf{k}^2)}},$$

where $\omega_0 = \bar{\alpha}_S \chi(1/2) = 4\bar{\alpha}_S \ln 2$. If α_S is taken to be 0.2, $\omega_0 = 0.53$ giving a very strongly rising cross-section for quark-quark scattering.

[7] The details can be followed in problem 2 at the end of the chapter.

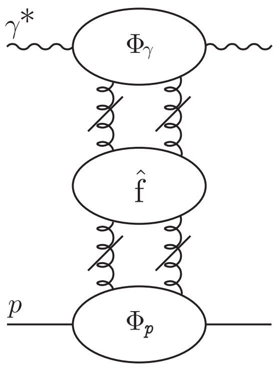

Fig. 7.13 The BFKL contribution to the γ^*p total cross-section.

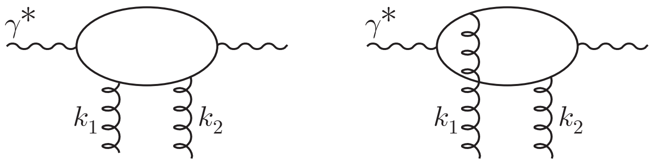

Fig. 7.14 The BFKL impact factor Φ_λ for the virtual photon.

7.5.2 BFKL for hadronic processes

To connect the BFKL result to hadron-hadron scattering or DIS requires replacing the quark lines by *impact factors* which are, in general, non-perturbative objects relating the hadrons to their quark content. For the case of DIS, or more precisely, the γ^*p total cross-section this is shown in Fig. 7.13 and is

$$\sigma_\lambda(W^2, Q^2) = \frac{1}{(2\pi)^4} \int \frac{d^2\mathbf{k}_1}{\mathbf{k}_1^2} \frac{d^2\mathbf{k}_2}{\mathbf{k}_2^2} \Phi_{\gamma,\lambda}(\mathbf{k}_1)\Phi_p(\mathbf{k}_2)F(W^2, \mathbf{k}_1, \mathbf{k}_2), \quad (7.28)$$

where $\lambda = T, L$ designates the polarisation state of the γ^* and $\Phi_{\gamma,\lambda}$, Φ_p are the virtual photon and proton impact factors respectively. The colour factor G^S has been absorbed into Φ_p. Φ_γ can be calculated in terms of $\gamma^* \to q\bar{q}$ as shown in Fig. 7.14.[8] Equation 7.28 is an example of $\mathbf{k}_T$ factorisation, which is analogous to the collinear factorisation of the DGLAP approach.

Φ_p is a non-perturbative quantity, which when convoluted with $F(x, \mathbf{k}_1, \mathbf{k}_2)$ gives the *unintegrated gluon density function* $F_g(x, \mathbf{k})$, where the relation $x \approx Q^2/W^2$ has been used to replace the energy variable W^2 by x. More precisely

$$F_g(x, \mathbf{k}) \equiv \frac{1}{(2\pi)^3} \int \frac{d^2\mathbf{k}'}{\mathbf{k}'^2} \Phi_p(\mathbf{k}')\mathbf{k}^2 F(x, \mathbf{k}, \mathbf{k}'), \quad (7.29)$$

[8] Details are given in [For97,pp 169–173].

and $F_g(x, \mathbf{k})$ is related to the gluon density that appears in the DGLAP equations by

$$xg(x, Q^2) = \frac{1}{\pi} \int_0^{Q^2} \frac{d^2\mathbf{k}}{\mathbf{k}^2} \Theta(Q^2 - \mathbf{k}^2) F_g(x, \mathbf{k}). \tag{7.30}$$

Although a complete calculation of xg requires a model for Φ_p, it can be seen that the leading behaviour at low x is given by $xg(x, Q^2) \sim x^{-\omega_0}/\sqrt{\ln(1/x)}$. Similarly $\sigma_\lambda(W^2, Q^2) \sim (W^2)^{\omega_0}/\sqrt{\ln(W^2)}$. If the BFKL exponent is re-expressed as the Pomeron intercept, then $\alpha_P^{BFKL}(0) = 1 + \omega_0 \approx 1.53$ which is much larger than the values of about $1.08 - 1.09$ that are found from hadron-hadron data.

7.5.3 The BFKL/QCD dipole model

This approach to low x dynamics considers the behaviour of the wavefunction of a heavy (colourless) $\mathrm{Q\overline{Q}}$ 'onium' state. It enables both the BFKL kernel to be derived and the scattering of two colourless objects to be studied without the complication of non-perturbative impact factors. The method has been developed by Mueller [Mue94a,b] and Nikolaev and Zakharov [Nik94]. An introduction is also given in [Ell96, Sec.4.6.5].

The essence of the idea is that after a soft gluon is radiated the original $\mathrm{Q\overline{Q}}$ dipole becomes two colour dipoles ($\mathrm{Q\bar{q}}$, $\mathrm{\overline{Q}q}$) where the gluon colour charge has been treated as if it were a $\mathrm{q\bar{q}}$ pair. In the limit of large N_c one arrives at a picture in which the gluon ladder is replaced by a cascade of dipoles. The equivalent of the LO BFKL equation may be formulated either in impact parameter space ($\mathbf{b}$) or in transverse momentum ($\mathbf{k}$). The onium wavefunctions in the two representations are related by

$$\psi(\mathbf{b}, z) = \int \frac{d^2\mathbf{k}}{(2\pi)^2} e^{i\mathbf{k}\cdot\mathbf{b}} \psi(\mathbf{k}, z)$$

where z is the longitudinal momentum fraction. For ease of comparison with the results of the previous section, the $\mathbf{k}$-space representation will be used here. The cross-section for the scattering of two onia with wavefunctions ψ_A, ψ_B takes the form

$$\sigma_{AB}(Y) = \frac{1}{(2\pi)^4} \int \frac{d^2\mathbf{k}_1}{\mathbf{k}_1^2} \frac{d^2\mathbf{k}_2}{\mathbf{k}_2^2} \Phi_A(\mathbf{k}_1) \Phi_B(\mathbf{k}_2) G_(Y, \mathbf{k}_1, \mathbf{k}_2),$$

where $\Phi(\mathbf{k}) = |\psi(\mathbf{k}, z)|^2$ and Y ($\simeq \ln(1/x)$) is the rapidity. Comparing this equation to Eq. 7.28, one sees that the $\Phi_{A,B}$ are the equivalent of the impact factors and $G_0(Y, \mathbf{k}_1, \mathbf{k}_2)$ the equivalent of the BFKL amplitude. The LO expression for G is

$$G_0(Y, \mathbf{k}_1, \mathbf{k}_2) = \frac{e^{E_0(Y, k_1, k_2)}}{2\pi k_1 k_2 \sqrt{4\pi D Y}} \tag{7.31}$$

where

$$E_0(Y, k_1, k_2) = \omega_0 Y - \ln^2(k_1/k_2)/4DY$$

and

$$\omega_0 = \frac{4\alpha_S(\mu^2)}{\pi} N_c \ln 2, \quad D = \frac{7\alpha_S(\mu^2)}{2\pi} N_c \zeta(3).$$

Comparing Eq. 7.31 with Eq. 7.27, using $\chi(1/2) = 4\ln 2$, $\chi''(1/2) = -28\zeta(3)$, $N_c = 3$ and $Y = \ln(s/\mathbf{k}^2)$, one sees that the high energy behaviours are the same. However in the dipole formulation one has an extra term dependent on the scale ratio k_1/k_2 or in $\mathbf{b}$-space b_1/b_2, the initial relative dipole sizes. As with the earlier LO fixed α_S BFKL calculation, the choice of scale μ^2 is somewhat arbitrary. The dipole form of the BFKL amplitude has been used by a number of authors as the basis of models for both DIS at low x and diffractive DIS, e.g. [Bialas98, Nik97, Nik00].

7.5.4 Beyond the LO BFKL with fixed α_S

Taking the LO fixed α_S BFKL prediction for F_2 in DIS at face value, although the HERA data at low x does show a dramatic rise, the slope is not as steep as that predicted. This does not immediately show that the BFKL approach is wrong, it could be that the non-perturbative proton impact factor is obscuring the BFKL behaviour, maybe the scale in x reached at HERA is not small enough and NLO corrections are important and so on. Inclusive DIS may not be the cleanest test for the BFKL equation because of the large mismatch between the hard scale set by Q^2 at one end of the ladder and the soft scale from the proton wave-function at the other end. Processes with similar hard scales[9] at both ends of the ladder would avoid the need for non-perturbative terms. Examples are forward jets in DIS with $E_T^{jet} \approx Q^2$ [ZEU99r], forward π^0 production in DIS [H1 99r] and the total cross-section for $\gamma^* + \gamma^* \to X$ at high energies [L3 99]. Although the results are both intriguing and somewhat inconclusive, it is clear that the LO BFKL calculation gives too strong an energy dependence for the effects sought. In retrospect it is not surprising that the simplified LO calculation with fixed α_S does not agree with measurements. Apart from fixing α_S and the choice of scale for α_S, momentum conservation is not guaranteed and there are potentially large NLO corrections.

The running of α_S and NLO corrections to the BFKL equation are closely related and as both are still the subject of intense investigation only a summary overview will be given here. Although there had been a number of attempts to solve the LO BFKL equation with running α_S, the subject really came alive in 1998 with the publication of the NLO calculation in the fixed α_S framework by Fadin & Lipatov [Fad98] and Camici & Ciafaloni [Cam97,Cam98]. This was a highly non-trivial calculation and took nearly 10 years. In the context of the present discussion it may be considered

[9] In rather unfortunate terminology, these processes are known as 'single scale' and DIS with a large mismatch between scales as 'two scale'.

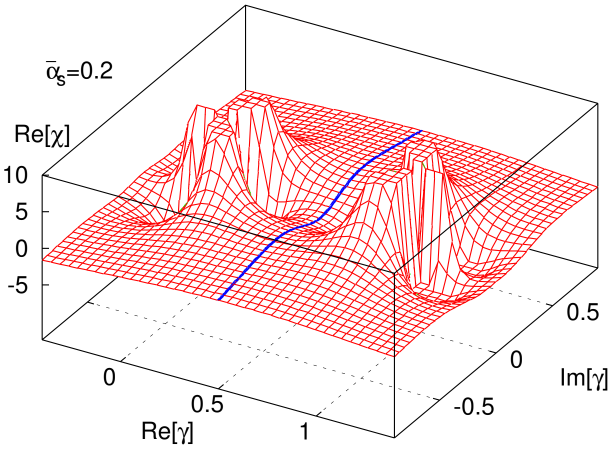

Fig. 7.15 Real part of the LO+NLO BFKL characteristic function χ in the complex γ plane and the contour for the Mellin inversion using the saddle point method at $Re(\gamma) = 1/2$ (from [Sal99]).

as the calculation of the next term in the expansion of the characteristic function of the BFKL kernel as a power series in α_S

$$\chi(\gamma) = \chi^{(0)}(\gamma) + \bar{\alpha}_S \chi^{(1)}(\gamma) + \cdots$$

where $\chi^{(0)} = \chi_0$ of the LO kernel. The surprising result is that the behaviour of χ near $\gamma = 1/2$ changes radically with

$$\chi(1/2) = \chi^{(0)}(1/2)[1 - 6.47\bar{\alpha}_S] \tag{7.32}$$

which in turn means that the exponent ω_0 of F_2 at small x may even change sign (e.g. for $\alpha_S = 0.2$ one finds the LO result of -0.53 becomes 0.13). There has been much discussion about the meaning of this result for the validity of the BFKL approach. The essence of the problem is to be seen by comparing Fig. 7.15, which shows $\mathrm{Re}(\chi)$ at LO+NLO, with Fig. 7.12 showing only the LO contribution. The shape of the function has changed completely and it calls into question the validity of the saddle point approximation around $Re(\gamma) = 1/2$ for evaluating the Mellin inversion at NLO. The fact that the single saddle point along the $\mathrm{Re}(\gamma) = 1/2$ integration contour at LO has become a complex conjugate pair, thus giving rise to oscillations in the BFKL cross-section as a function of $\ln(\mathbf{k}_1^2/\mathbf{k}_2^2)$ [Levin98,Ros99].

A number of approaches have been put forward to ameliorate the situation. They fall into two classes, those concentrating on the implications for BFKL as applied to DIS and those for the BFKL kernel more generally. For DIS what matters at low x is the behaviour of the kernel near $\mathrm{Re}(\gamma) = 0$. Although it has not been emphasised here, the general BFKL

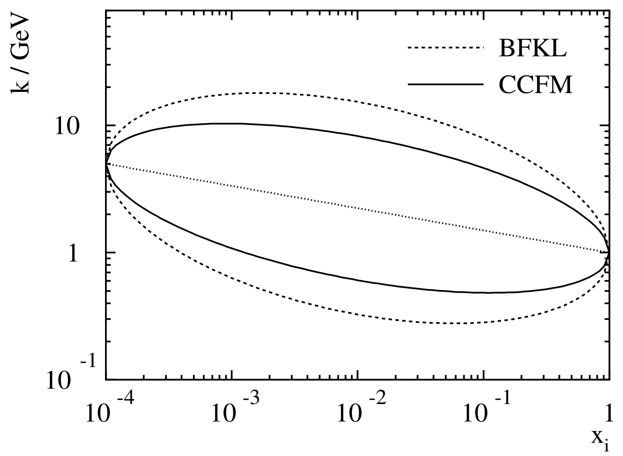

Fig. 7.16 The range over which the transverse momentum in a gluon ladder diffuses as a function of the intermediate x_i for the CCFM and BFKL equations. This plot, from [Sal97], is for $x = 10^{-4}$, $k = 5\,\mathrm{GeV}$ and $\alpha_S = 0.2$.

amplitude must have a symmetric structure with respect to the transverse momenta at either end of the gluon ladder ($\mathbf{k}_1$, $\mathbf{k}_2$) and this is reflected in the symmetry of $\chi(\gamma)$ about the line $\mathrm{Re}(\gamma) = 1/2$. For general studies of the kernel, this symmetry can be exploited. The following are among some of the many proposals that have been made.

Thorne [Tho00] argues that for 'two-scale' processes, such as DIS, the dominant effect is the running of α_S. Since one is working with the unintegrated gluon density of Eq. 7.29, the scale for running α_S is $\mathbf{k}^2$. This changes the nature of the LO BFKL equation considerably. In double Mellin transform space (see Eq. 7.25) the fixed α_S equation is an algebraic equation. When $\bar{\alpha}_S$ is replaced by $\bar{\alpha}_S(\mathbf{k}^2) = [\bar{b}_0 \ln(\mathbf{k}^2/\Lambda^2_{QCD})]^{-1}$ the equation becomes a first order differential equation in the Mellin variable γ (from the extra $\ln(\mathbf{k}^2/\Lambda^2)$ factors). Although the equation can be solved by use of an integrating factor, the singularity structure in complex γ spaced has changed. For fixed $\bar{\alpha}_S$ the leading singularity is a pole at $\bar{\alpha}_S\chi(\gamma) = \omega$, giving the LO result for $F_g(x, \mathbf{k})$ using the standard saddle point approximation at $Re(\gamma) = 1/2$. For LO running α_S, the leading singularity is now a cut at $\gamma = 0$ and the saddle point approximation gives slowly convergent or unstable results (which is in line with the results of earlier attempts to run α_S in the LO BFKL equation). To get around this Thorne makes use of the knowledge of the γ-space singularity structure to change the contour from parallel to the imaginary axis at $Re(\gamma) = 1/2$ to one that encloses the real axis for $Re(\gamma) < 0$. The other problem that has to be solved is that the BFKL kernel is no longer infra-red finite because $\mathbf{k}^2$ can diffuse

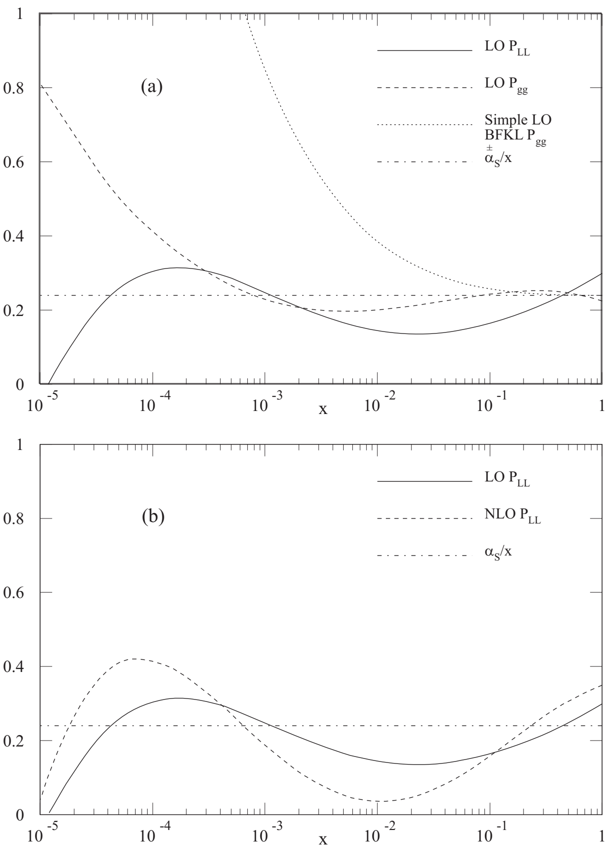

Fig. 7.17 The splitting function $xP_{gg}(x)$ as a function of x for $Q^2 \approx 8\,\mathrm{GeV}^2$ from the LO BFKL calculation with running α_S compared with that for fixed α_S. From [Tho00].

into the non-perturbative region (unlike the DGLAP case where the strong k_t ordering prevents this). An example of the scale of diffusion is shown in Fig. 7.16. This problem is finessed by renormalising the gluon density at some scale μ^2 and calculating only the change of $F_g(x, \mathbf{k})$ with $\ln(\mathbf{k}^2)$. Effectively what Thorne is doing is to use the BFKL equation to improve the calculation of the splitting functions P_{gg} and P_{LL} (for the longitudinal structure function) at low x. Some results are shown in Fig. 7.17(a), the steep rise given by the LO fixed α_S calculation for P_{gg} (shown as the dotted line) is moderated to the dashed line for his running α_S LO calculation. At low x and Q^2 in the HERA region the exponent of $xg(x, Q^2)$ would be changed from the 'classical' BFKL result of ~ 0.5 to something more like ~ 0.25. Finally he shows that if one starts from the running α_S LO result the NLO corrections are modest and under control, as shown in Fig. 7.17(b) for P_{LL}.

Altarelli *et al.* [**Alt00**] These authors also concentrate on improving the description of DIS at low x. They emphasise the importance of imposing momentum conservation and also make use of a 'duality relation' derived from the consistency of the large Q^2 large $1/x$ limits of the BFKL and DGLAP approaches. The duality relation ([Bal97]) relates the BFKL χ function to the moments of the gluon anomalous dimension in the OPE form of the DGLAP equations

$$\chi(\gamma_S(N, \alpha_S), \alpha_S) = N,$$

where $\gamma_S(N, \alpha_S)$ is the singlet anomalous dimension (given the subscript S to avoid confusion with the Mellin conjugate variable) and N is the moment index.[10] Momentum conservation requires $\gamma_S(1, \alpha_S) = 0$ (see Eqs. 4.22 and 4.51) and hence $\chi(0, \alpha_S) = 1$. Further use of the duality relation allows them to derive an improved expansion of χ near $\gamma = 0$ and also to translate this into an improved expansion of γ_S at low x. Because of the problem of singularities in the BFKL kernel at $\gamma = 1$ their procedure does not give a complete prescription of the splitting function and a parameter λ, related to the low x exponent of the splitting function, must be estimated from data.

Kovchegov & Mueller [**Kov98**] concentrate on the structure of the BFKL amplitude at NLO within the context of the dipole approach. They separate the NLO kernel into a conformally invariant part (as is the LO fixed α_S kernel[11]) and a part coming from the running of α_S and are able to resum both parts. As a consequence they find that the appropriate scale for α_S is $k_1 k_2$ and

$$G(Y, \mathbf{k}_1, \mathbf{k}_2) = \frac{e^{E(Y,k_1,k_2)}}{2\pi k_1 k_2 \sqrt{4\pi D Y}} \tag{7.33}$$

where

$$E(Y, k_1, k_2) = \omega Y - \ln^2(k_1/k_2)/4DY + \frac{D}{3}(\alpha_S \omega_0 b_0)^2 Y^3, \tag{7.34}$$

$$\omega = \omega_0 (1 - \frac{\alpha_S N_c}{\pi} \chi^{(1)}(1/2)), \quad Y = \ln\left(\frac{s}{k_1 k_2}\right),$$

and

$$\omega_0 = \frac{N_c \alpha_S}{\pi} \chi^{(0)}(1/2) = \frac{4\alpha_S(k_1 k_2)}{\pi} N_c \ln 2, \quad D = \frac{7\alpha_S}{2\pi} N_c \zeta(3).$$

The first term in Eq. 7.34 for the exponent of G corresponds to the NLO result given in Eq. 7.32 and comes from the conformally invariant part of the

[10] N corresponds to ω or $n - 1$.

[11] For details on the conformal invariance of the BFKL equation see [Nav97].

NLO kernel. The next term is the 'relative dipole size' factor found in the LO case. The last term is a new feature coming from the running coupling part. It shows a non-Regge form in the sense that it is $\alpha_S^5 Y^3$ rather than the $(\alpha_S Y)^j$ powers expected in the BFKL summation. However the coefficient of this term is small, so it is unlikely to affect present phenomenology.

Ciafaloni *et al.* [**Cia99a, Cia99b**] These authors argue that $\chi^{(1)}$ is dominated, to a good approximation, by a small number of 'collinear' contributions from the running of α_S, the non-singular piece of the splitting function and the choice of energy scale. In this collinear approximation $\chi^{(0)}(\gamma) = 1/\gamma + 1/(1-\gamma)$ and $\chi^{(1)}(\gamma) = A/\gamma^2 + B/(1-\gamma)^2 - 1/(2\gamma^3) - 1/(2(1-\gamma)^3)$, where A, B are known coefficients. The origin of the inverse cubic terms is from the choice of energy scale. In the double Mellin integral of Eq. 7.25 for $F(s, \mathbf{k}_1, \mathbf{k}_2)$ the scale $\mathbf{k}^2$ was used. However this choice does not respect the symmetry of the BFKL kernel between $\mathbf{k}_1$ and $\mathbf{k}_2$ and a better choice might be $k_1 k_2$. At LO one is summing terms of the form $(\bar{\alpha}_S \ln(s/s_0))^n$ and a change of scale s_0 can be absorbed in discarded higher order terms in $\bar{\alpha}_S$. This is not possible at NLO and above. Consider the scales as they appear in the Mellin integral

$$\left(\frac{s}{k_1 k_2}\right)^{\omega} \left(\frac{k_1^2}{k_2^2}\right)^{\gamma} = \left(\frac{s}{k_1^2}\right)^{\omega} \left(\frac{k_1^2}{k_2^2}\right)^{\gamma+\omega/2},$$

the change in energy scale is equivalent to a shift $\gamma \to \gamma - \omega/2$ in the 2nd Mellin integration variable. The scale on the LHS respects the symmetry of the BFKL kernel and the choice on the RHS is relevant for DIS 'two-scale' processes in which $k_1^2 >> k_2^2$. This gives a technique for resumming these 'energy scale' terms to all orders [Sal98, And96]. The technical implementation is somewhat tricky because after the first Mellin integration ω is a function of γ. The resulting function $\chi(\gamma, \omega)$ can then used to estimate the high energy LO+NLO (or small x) exponent as shown in Fig. 7.18. More precisely ω_s is the minimum value of $\bar{\alpha}_S \chi(\gamma, \omega)$ and is the power expected for $F(s, \mathbf{k}_1, \mathbf{k}_2)$ controlling high energy $\gamma^* \gamma^*$ cross-sections or DIS forward jets. ω_c is the position of the leading singularity in the anomalous dimension and gives the power growth at small x of the splitting functions. Both ω's vary slowly with α_S and lie between the LO result and the NLO result derived from Eq. 7.32.

To summarise the BFKL calculations. Over the last few years a lot of progress has been made in understanding why the LO fixed α_S calculation cannot be expected to describe DIS data directly, and probably other 'single scale' hard processes. It is too early to say which approach to the NLO BFKL will be the most successful, but it is clear that the running of α_S plays a key role. Finally it is interesting to note that preliminary results of both the approaches by Thorne and Altarelli *et al.* mentioned above when applied to fitting F_2 data appear to improve the χ^2 of the fit.

Maybe more on this in Chap. 10?

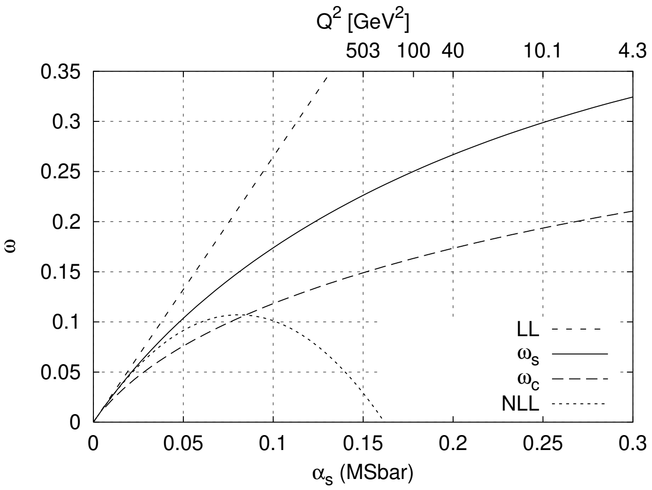

Fig. 7.18 BFKL exponent ω for various calculations: LO, NLO, resummed collinear approximation of Ciafaloni *et al.* (from [Sal99]).

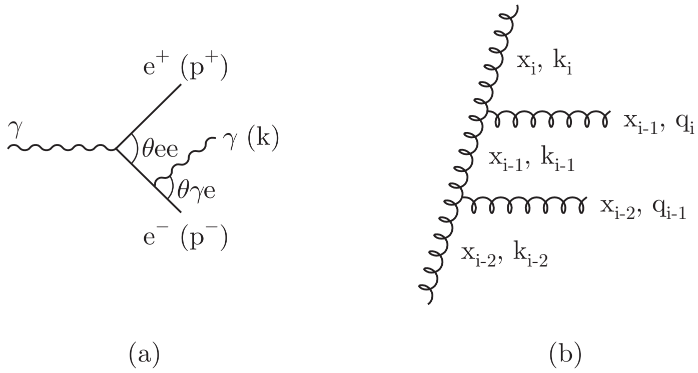

Fig. 7.19 Angular ordering: (a) soft photon emission in $\gamma \to e^+e^-$; (b) details of momenta in the CCFM gluon ladder.

7.6 Angular ordering and the CCFM equation

Angular ordering, or coherence of soft radiation, is a property of both QED and QCD. The basic idea may be understood by considering to what extent do the e^+ or e^- radiate independently after pair creation. Dokshitzer *et al.* [Dok91,Ch.4] give a heuristic picture based on the uncertainty principle. Consider the process shown in Fig. 7.19(a), the lifetime of the e^- virtual state before emission of the final state photon is given by

$$t_\gamma^- \sim \frac{1}{M_{\rm virt}}\frac{E}{M_{\rm virt}} = \frac{E}{(k+p^-)^2} \approx \frac{1}{k\theta_{\gamma e}^2},$$

where $M_{\rm virt}$ is the mass of the virtual state and the momenta and angles are defined in the figure. The lifetime has been estimated using $\Delta E \Delta t \sim 1$ and allowing for time dilation. During this time the e^+e^- pair will have separated a transverse distance $r_T^{ee} = \theta_{ee} t_\gamma^-$. Now $k\theta_{\gamma e} = k_T = \lambda_T^{-1}$, where λ_T is the transverse wavelength of the emitted photon. Using this one has

$$r_T^{ee} = \lambda_T \frac{\theta_{ee}}{\theta_{\gamma e}}$$

and for $\theta_{\gamma e} >> \theta_{ee}$ the charge separation at the time of emission is very much less than λ_T. Under these circumstances the emitted photon cannot resolve the separate charges only their sum (which is zero) and the radiation is strongly suppressed. Independent emission of photons only occurs for $\theta_{\gamma e} < \theta_{ee}$ for which $r_T^{ee} > \lambda_T$. This phenomena, under the name of the Chudakov effect was observed in 1950's in large cosmic ray air showers. Essentially the same phenomenon occurs for $\mathrm{g} \to \mathrm{q\bar{q}}$ in QCD with the modification that the wide angle soft gluon radiation is not zero (because the initial gluon carries a non-zero colour charge) but 'as if it were emitted from the parent gluon'. The details of the QCD calculation are given in Ellis *et al.* [Ell96,Sec.5.5]. The angular ordering constraint applies to all QCD branching processes involving both quarks and gluons and in particular $\mathrm{g} \to \mathrm{gg}$. Thus in a cascade the angles of the emitted particles must decrease as one proceeds down any one branch. This has important consequences for the emission of final state hadrons as well as providing the basis for an alternative approach to inclusive DIS.
The CCFM (Ciafaloni [Cia88]; Catani, Fiorani & Marchesini [Cat90,Mar95], equation is the application of angular ordering to the calculation of the gluon ladder. Figure 7.19b shows a section of the ladder with transverse momenta k_i of gluons between emissions and q_i of the emitted gluon. The x_i variables are the usual fractions of the initial longitudinal momentum. For a small angle emission of gluon i, $\theta_i \approx q_i/(x_{i-1}p)$ and angular ordering $\theta_i > \theta_{i-1}$ then gives the condition that $q_i > z_{i-1}q_{i-1}$ where $z_i = x_i/x_{i-1}$. The soft gluon emission probability takes the form

$$dP = \frac{d^2q_i}{\pi q_i^2} dz_i \frac{\bar{\alpha}_S}{z_i} \Delta(z_i, q_i, k_i) \Theta(q_i - z_{i-1}q_{i-1}),$$

where $z_i << 1$, the theta function reflects the angular ordering condition and the form factor Δ (which screens the $1/z$ singularity) is given by

$$\Delta(z_i, q_i, k_i) = \exp\left\{ -\int_{z_i}^{1} dz' \frac{\bar{\alpha}_S}{z'} \int \frac{dq'^2}{q'^2} \Theta(k_i - q')\Theta(q' - z'q_i) \right\}.$$

By considering successive emissions along the chain, an integral equation for $F(x, k, Q)$, the CCFM unintegrated gluon density, may be derived

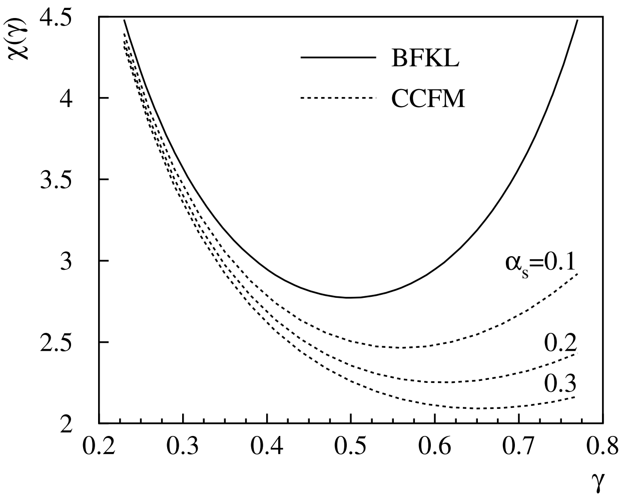

Fig. 7.20 The CCFM characteristic function in Mellin space for different values of α_S together with that for the LO BFKL equation. From [Sal97].

$$F(x,k,Q) = F^{(0)}(x,k,Q)+\bar{\alpha}_S \int_x^1 \frac{dz}{z} \int \frac{d^2q}{\pi q^2}\Delta(z,q,k)\Theta(Q-zq)F(x/z,k',Q),$$

where $k' = |\mathbf{k}+\mathbf{q}|$ and Q is the hard scale of the probe which sets the maximum angle for gluon emission. For larger x the singular part of the gluon splitting function $\bar{\alpha}_S/z$ is replaced by the full P_{gg} splitting function. One of the interesting features of the CCFM equation is that it 'interpolates' between the BFKL equation at small x and the DGLAP equation at moderate x. For small x, small z will dominate the integral and the $\Theta(Q-zq) \to 1$ which gives $F(x,k,Q)$ independent of Q as in the BFKL equation. For moderate to large x, $\Delta \to 1$, the variables $z_i \approx 1$ and the condition $q_i > z_{i-1}q_{i-1}$ becomes $q_i > q_{i-1}$, which is the strong ordering in transverse momentum of the DGLAP equation.

The CCFM equation cannot be solved analytically but it has been studied numerically, for example Kwiecinski *et al.* [Kwi95], Salam [Sal97]. Figure 7.20, from [Sal97], shows the characteristic function of the CCFM equation in Mellin space for different values of α_S together with that for the LO BFKL equation. The close similarity of all the curves for small values of γ demonstrates that solutions of the CCFM equation in this region approximate those of BFKL. At low x the CCFM equation exhibits BFKL like diffusion of transverse momentum along the gluon ladder, but the extent of the diffusion is not so large, as Fig 7.16 shows. The numerical study by [Kwi95] used an input function of the form $F^{(0)}(x,k,Q_0) = 3N(1-x)^5\exp(-k^2/Q_0^2)$ where $Q_0 = 1$,GeV and the normalisation N is chosen so that the gluon

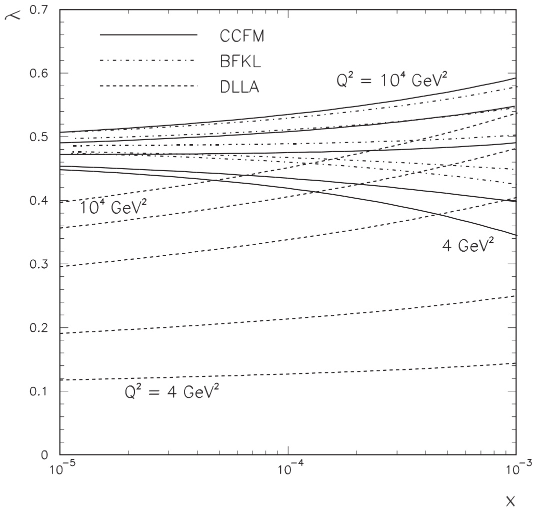

Fig. 7.21 A comparison of the small x exponents of the gluon density from the CCFM, LO BFKL and DLLA approaches (from [Kwi95]).

density integrated over k and x corresponds to half the proton's momentum. They compared the CCFM equation with the LO fixed α_S BFKL and the DLLA limit of the DGLAP equations. Fig. 7.21 shows the exponent $\lambda(Q^2)$ of the predicted gluon densities $(xg(x, Q^2) \sim x^{-\lambda(Q^2)})$. The results for the CCFM and BFKL are quite similar, but the CCFM does show a wider spread in values at larger x. Both give much larger exponents than the DLLA approach. Extending their CCFM model with a 'soft' Pomeron background for large x Kwiesinki *et al.* [Kwi96] were able to get a reasonable description of the then available HERA data at low x (H1 and ZEUS HERA 1993 data). However both the CCFM and more conventional DGLAP fits (GRV(94) and MRSA$'$) also give adequate descriptions of the data. In each case parameters in the models have to be fit to the F_2 data. The crucial test would be to compare with a different structure function at low x and in particular F_L where quite large differences are predicted.

The DIS final state may provide more sensitive measures for comparing the differences between the CCFM/BFKL approach and conventional DGLAP and a number of Monte Carlo codes based on the CCFM equation are available: SMALLX [Mar92] and CASCADE [Jun99]. For the latter, Jung emphasises the importance of a proper treatment of non-Sudakov form-factor $\Delta(z_i, q_i, k_i)$. In the paper cited and [Jun00] he demonstrates that the CCFM approach as realised in CASCADE is able to fit a wide range of HERA data including F_2, large E_T dijet data in photoproduction and forward jets in DIS. Final state topics are covered in Chap. 8.

7.7 Unitarity and saturation

Cross-sections are limited by unitarity which gives a non-linear constraint on the scattering amplitude. At low energies, where resonances dominate, this constraint is most easily realised using a partial-wave decomposition. At very high energies unitarity leads to the Froissart-Martin bound[12] on the total cross-section

$$\sigma_{tot}(s) < A \ln^2 s,$$

where s is the centre of mass energy squared and $A \sim 60\,\mathrm{mb}$ is a constant determined from the pion mass. All the models and approximations considered so far for the high energy (low x) behaviour of the structure function or $\sigma^{tot}_{\gamma^* p}$ have given high energy behaviours growing like powers of W^2 (or $1/x$) and thus will eventually violate the Froissart bound. For the simple Regge pole description of total cross-sections given by Donnachie and Landshoff the rate of increase with s is very gentle, $s^{0.08}$, which does not violate the Froissart bound until astronomically large energies are reached. The much larger effective exponents given by the DGLAP or BFKL equations are a different matter. Rather than attempt a summary of the more formal approaches, simple physical ideas will be used to give an outline of how unitarity and non-linear effects enter deep inelastic scattering.

In the language of the QCD improved parton model there are two related effects that need to be considered as the density of gluons increases at low x: the first is 'shadowing' in which the effective total cross-section is reduced because the 'target' partons overlap each other; the second is saturation in which gluon absorption tales place through the inverse of the $\mathrm{g} \to \mathrm{gg}$ splitting. Both of these effects get enhanced in nuclei but will also occur in nucleons. Another limit that will be touched on briefly is how the high energy behaviour of $\sigma^{tot}_{\gamma^* p}$ changes as $Q^2 \to 0$, that is as the wavelength of the probe $1/Q$ approaches and exceeds the size of the target nucleon.

To get a semi-quantitative feel for the problem remember that in the infinite momentum frame $xg(x, Q^2)$ gives the number of gluons per unit of rapidity ($\ln(1/x)$ or dx/x) and with a transverse size $\sim 1/Q$. So the transverse area occupied by the gluons is $\sim \pi xg/Q^2$. In the infinite momentum frame the photon probe interacts with a proton of momentum p contracted to a disk of thickness $2Rm_{\mathrm{p}}/p$ in the longitudinal direction and diameter $2R$. Thus one might expect geometrical shadowing when $\pi xg/Q^2 \sim \pi R^2$. With this very crude estimate, if R is taken to be 1 fm then at $Q^2 \sim 10\,\mathrm{GeV}^2$ shadowing would not occur until $xg \sim 250$. Such densities are not likely to be reached within the low x range of HERA. However in more realistic calculations, the effective areas may be considerably smaller in which case shadowing will occur at much lower densities. Levin [Lev97] and others have argued that this is the case and one of the reasons why it has not been possible to see BFKL effects clearly at HERA.

[12] See [Mar69] for a detailed account.

The gluon-gluon recombination or absorption cross-section is of order $\alpha_S(Q^2)/Q^2$ at a transverse scale Q^2, thus one should expect saturation effects when total effective gluon-gluon recombination cross-section in the proton approaches that of the size of the proton disk,

$$\frac{\alpha_S(Q^2)}{Q^2} xg(x,Q^2) \sim \pi R^2.$$

Gribov, Levin and Ryskin [Gri83] and later Mueller and Qiu [Mue86] extended the low x DLLA approximation to include the effect of saturation with the equation

$$\frac{\partial^2 xg(x,Q^2}{\partial \ln Q^2 \partial \ln(1/x)} = \frac{3\alpha_S}{\pi} xg(x,Q^2) - \frac{81\alpha_S^2}{16Q^2R^2}(xg(x,Q^2))^2. \tag{7.35}$$

In this equation the first term on the RHS gives essentially equation 7.5 of DLLA or DAS, while the second term is an estimate of gluon recombination. Note that this term will damp the growth of xg at low x, in fact giving zero growth when $xg(x,Q^2) = 48\pi Q^2R^2/(81\alpha_S)$, in agreement with the crude estimate above. However the above equation is itself an approximation that is not valid when the gluon density reaches these large values. Non-perturbative approaches have to be use, even though α_S is small. One such is that of Mclerran and Venugopalan [McL94] in which the high density gluons are replaced by a classical field. An interesting consequence is that the very low x high gluon density regime in hadrons may be 'universal'. This will not be pursued here but it may be of importance in the next generation of heavy ion experiments.

7.8 Dipole models - general formalism

Dipole models (e.g. [Fra88], [Nik90,Nik92,Nik94], [Mue94a,b], [Got99], [Gol99], [McD00], [Cap00]) provide a rather general framework for studying the approach to saturation at low x, the low Q^2 limit and as discussed in Sec. 7.5.3 they are related to the BFKL equation. Referring to Fig. 7.22 the dipole model can be given a very direct physical interpretation in the rest frame of the proton. The virtual photon, with 4-momentum q, splits into a $\mathrm{q\bar{q}}$ pair in which the q takes a fraction z of the initial momentum and the splitting occurs a 'long' time $\sim 1/(mx)$ before the pair interacts with the proton (see problem 3 at the end of the chapter). The $\mathrm{q\bar{q}}$ pair then scatters coherently from the proton in a time which is short in comparison to $\sim 1/(mx)$. The $\gamma^* \to \mathrm{q\bar{q}}$ process is described by QED and the strong interaction physics is then contained in the cross-section for the dipole-proton interaction. During the interaction it is assumed that the transverse size of the pair, r, remains constant.

Although the resulting formalism will have greater generality it is convenient to start from the BFKL $\mathbf{k}_T$ factorised form of Eq. 7.28 and 7.29, in which impact factors[13] were introduced. From the two equations the γ^*p

[13]The required γ^* impact factors are calculated in [For97, Ch.6].

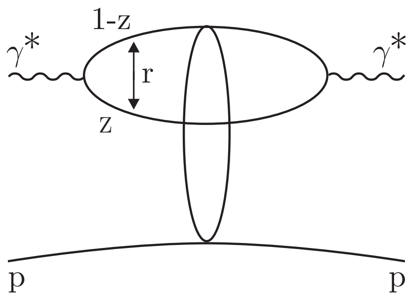

Fig. 7.22 The q$\bar{\text{q}}$ dipole model for DIS.

total cross-section for polarisation λ may be written as

$$\sigma_\lambda(x, Q^2) = \frac{1}{2\pi} \int \frac{d^2\mathbf{k}}{\mathbf{k}^4} \Phi_{\gamma,\lambda}(\mathbf{k}) F_g(x, \mathbf{k}). \tag{7.36}$$

For the longitudinal polarisation state $\lambda = L$, the $\gamma^* \to$ q$\bar{\text{q}}$ impact factor is

$$\Phi_{\gamma,L}(\mathbf{k}) = 32\alpha\alpha_S \sum_1^{n_f} e_f^2 \int_0^1 dz \int d^2\mathbf{r}(1 - e^{i\mathbf{k}\cdot\mathbf{r}}) Q^2 z^2 (1-z)^2 K_0^2(\epsilon r), \tag{7.37}$$

where Q^2 is the virtuality of the γ^*, $\epsilon = z(1-z)Q^2 + m_f^2$, n_f if the number of active quark flavours of mass m_f and charge e_f and K_0 is a Macdonald (or modified Bessel) function. Referring to Fig. 7.14, there are two types of coupling between the q$\bar{\text{q}}$ pair and the two gluons: in the first both gluons couple to the same quark (or antiquark); in the second one gluon couples to the quark and the other to the antiquark. In the above expression for $\Phi_{\gamma,L}$ the former coupling gives rise to the 1 and the latter to the $e^{i\mathbf{k}\cdot\mathbf{r}}$ in the factor $(1 - e^{i\mathbf{k}\cdot\mathbf{r}})$. Inserting the expression for $\Phi_{\gamma,L}$ into Eq. 7.36 and re-arranging gives

$$\sigma_L(x, Q^2) = \int_0^1 dz \int d^2\mathbf{r}\, |\Psi_L(z, \mathbf{r})|^2 \hat{\sigma}(x, r^2), \tag{7.38}$$

where

$$|\Psi_L(z, \mathbf{r})|^2 = \frac{6\alpha}{\pi^2} \sum_1^{n_f} e_f^2 Q^2 z^2 (1-z)^2 K_0^2(\epsilon r) \tag{7.39}$$

and the *dipole cross-section* is given in this case by

$$\hat{\sigma}(x, r^2) = \frac{8\pi\alpha_S}{3} \int \frac{d^2\mathbf{k}}{\mathbf{k}^4} F_g(x, \mathbf{k})(1 - e^{i\mathbf{k}\cdot\mathbf{r}}). \tag{7.40}$$

Starting from the impact factor $\Phi_{\gamma,T}$ for the transversely polarised γ^* states an equation of identical form to 7.39 may be deduced where

$$|\Psi_T(z,\mathbf{r})|^2 = \frac{3\alpha}{2\pi^2}\sum_1^{n_f} e_f^2 \left\{[z^2+(1-z)^2]\epsilon^2 K_1^2(\epsilon r) + m_f^2 K_0^2(\epsilon r)\right\}. \quad (7.41)$$

In these expressions $Q^2 = -q^2, x = Q^2/(Q^2+W^2), W^2 = (p+q)^2$ where p and q are the 4-momenta of the proton and γ^* respectively.

A number useful physical insights may already be gained from the forms of these expressions. The functions $K_0(x)$ and $K_1(x)$ are exponentially damped for large positive values of x and for purposes of approximating the integrals they may be replaced by

$$K_0(x) = c_0\Theta(1-x), \quad K_1(x) = \frac{c_1}{x}\Theta(1-x), \quad (7.42)$$

where c_i are constants. Note that there are two transverse scales involved $1/Q$, from the virtuality of the γ^* and R a typical hadron radius of about 1 fm at which the cross-section saturates. The following qualitative results may be obtained (see problems 4,5,6 at the end of the chapter):

- At small transverse separation, $\hat{\sigma}(x,r^2) \sim r^2$. At large $r \sim R$ some form of saturation mechanism must damp the cross-section to respect the unitarity limit.
- Contribution of 'large' sized $q\bar{q}$ pairs $r \sim R >> 1/Q$. The integrals are dominated by values of $\epsilon r < 1$ giving z or $1-z << 1/(Q^2R^2)$ and from the forms of $|\Psi_{T,L}(z,\mathbf{r})|^2$ it follows that

$$\sigma_T(x,Q^2) \sim 1/Q^2 \quad \sigma_L(x,Q^2) \sim m_f^2/Q^4.$$

- Contribution of 'small' sized $q\bar{q}$ pairs $r < 1/Q$. Now the constraint $\epsilon r < 1$ may be satisfied without any restriction on z and both transverse and longitudinal cross-sections 'scale', i.e.

$$\sigma_T(x,Q^2) \sim 1/Q^2 \quad \sigma_L(x,Q^2) \sim 1/Q^2.$$

This very simple analysis shows that small $q\bar{q}$ pairs will give rise to Bjorken scaling, but it also shows that there is another contribution of potentially similar importance at large Q^2 – the *aligned jet* configuration when either the q or $\bar{q}$ jet takes almost all the momentum of the incoming γ^*.

Interest in dipole models has been revitalised and extended by data at low x from HERA including the discovery of the relatively large (roughly 10%) contribution of diffractive events to the DIS cross-section. As shown, for example by Nikolaev and Zakharov [Nik92], the same photon wave-functions and the dipole cross-section also appear in the expression for the forward diffractive differential cross-section

$$\frac{d\sigma_{T,L}^D}{dt}|_{t=0} = \frac{1}{16\pi}\int_0^1 dz \int d^2\mathbf{r}\, |\Psi_{T,L}(z,\mathbf{r})|^2 |\hat{\sigma}(x,r^2)|^2. \quad (7.43)$$

It is thus natural to try to describe both total DIS and its diffractive component within the same model. This will not be pursued here as it is somewhat outside the main topic of this book – see Wüsthoff and Martin [Wue99] for a short review. One other use of the dipole formalism, that is evident from Eq. 7.40, is that it gives a handle on the unintegrated gluon density. This has been examined in detail recently by Ivanov and Nikolaev [Iva00]. To close this section the dipole model of Golec-Biernat & Wüsthoff is studied in somewhat more detail. It has been chosen for its simplicity, but it exhibits many of the features to be found in other models.

7.8.1 The Golec-Biernat-Wüsthoff model

The model ([Gol99]) is a compact realisation of the general features of the dipole formalism as outline above. It has a small number of parameters but appears to describe quite well a large range of F_2 data at low x ($x < 0.01$), both total and diffractive DIS contributions. It also allows a smooth extrapolation to the photoproduction limit and gives a qualitative description of recent data from HERA on F_2 at very low Q^2. It is a phenomenological model with saturation built in and although it is not unique it has an appealing simplicity. The key feature of the model is that the 'saturation radius', R_0, depends on x[14]

$$R_0(x) = \frac{1}{Q_0}\left(\frac{x}{x_0}\right)^{\lambda/2}, \tag{7.44}$$

where $Q_0 = 1\,\mathrm{GeV}$ sets the dimensions and λ and x_0 are parameters. $R_0(x)$ then scales the $\mathrm{q\bar{q}}$ transverse separation r in the dipole cross-section

$$\hat{\sigma}(x, r^2) = \sigma_0 g(\hat{r}^2), \quad \hat{r} = \frac{r}{2R_0(x)}, \tag{7.45}$$

and σ_0 is a constant. The function $g(\hat{r}^2)$ is constrained to vanish like $\hat{r}^2$ as $\hat{r} \to 0$ and it should tend to 1 as for $\hat{r} \geq 1$. The latter condition guarantees that saturation occurs and the total cross-sections calculated from $\hat{\sigma}$ will tend to a constant for small Q^2. The authors of the model choose a simple ansatz for g that is reminiscent of eikonalization

$$g(\hat{r}^2) = 1 - \exp(-\hat{r}^2). \tag{7.46}$$

In addition to the three parameters of the model (λ, x_0, σ_0) values have to be chosen for the quark masses. For the light quark masses 140 MeV is chosen as this gives a good description of data at very low Q^2. The charm quark mass is taken as 1.5 GeV. The model parameters were determined be fitting all (then) available DIS data with $x < 0.01$[15] with statistical and systematic errors added in quadrature. Two fits were done, one with three

[14] In the general discussion of dipole models the saturation radius R was taken to be fixed.

[15] The data set is essentially the HERA 1994 F_2 data from H1 and ZEUS together with shifted vertex and ZEUS BPC data at low Q^2, details are given in Chap. 5, Tab. 5.1.

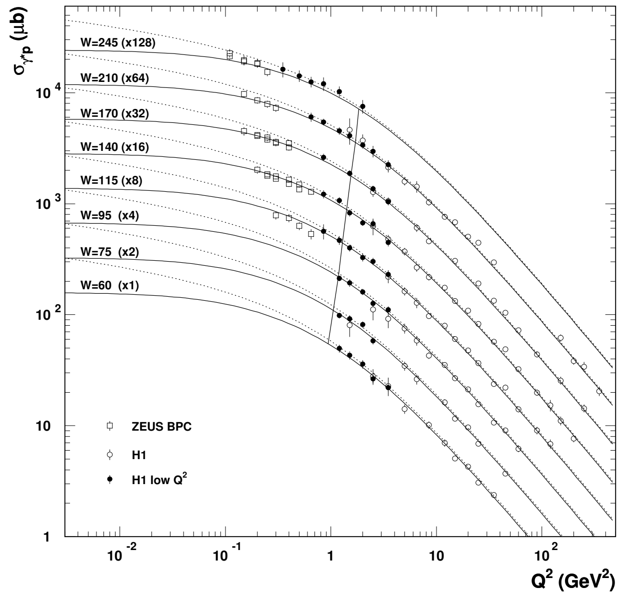

Fig. 7.23 The dipole model fit by Golec-Biernat & Wüsthoff to $\sigma_{\gamma^* p}$ with three light quarks. The solid lines show the fit with light quark mass of $m_f = 140\,\mathrm{MeV}$, the dotted line the effect of putting $m_f = 0$. The 'critical line' is shown as the almost vertical line (from [Gol99]).

light quarks only and one with four flavours (3 light quarks and charm). The values of the parameters for the two fits are: (no charm) $\sigma_0 = 23.03\,\mathrm{mb}$, $\lambda = 0.288$, $x_0 = 3.04 \cdot 10^{-4}$; (with charm) $\sigma_0 = 29.12\,\mathrm{mb}$, $\lambda = 0.277$, $x_0 = 0.41 \cdot 10^{-4}$. The importance of the choice of light quark mass in tuning the approach to the photoproduction limit is shown in Fig. 7.23 which shows the light quark only fit.

An important aspect of the model is the idea of a 'critical line' which indicates where saturation effects become important as function of x and Q^2. It is defined by the condition $R_0^2(x) = 1/Q^2$, so it depends on the fit parameters λ and x_0. Figure 7.24 shows the logarithmic slope $dF_2/d\ln Q^2$ from the model (light quark only fit) as functions of Q^2 and x for fixed W. In the perturbative region the logarithmic slope gives a very direct measure of scaling violations but it has also been advocated [Bar91] as a quantity sensitive to the onset of saturation or the transition from perturbative to non-perturbative regimes at low x and Q^2. This latter aspect is shown very clearly in the plots by the proximity of the critical line to the peak of the slope at a given value of W. The comparison of the model curves with

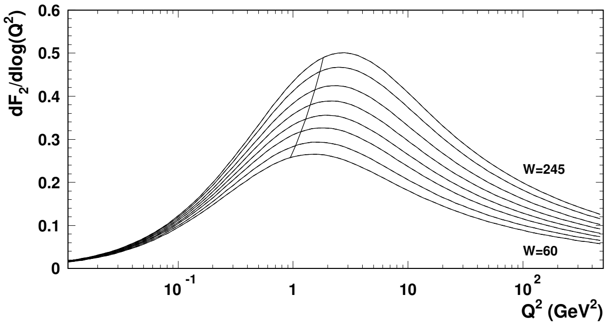

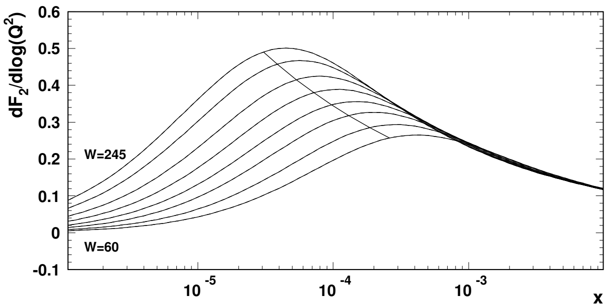

Fig. 7.24 The slope $dF_2/d\ln Q^2$ from the dipole model of Golec-Biernat & Wüsthoff shown as functions of Q^2 and x for fixed values of W. The 'critical line' is also shown running across the curves in each plot (from [Gol99]).

preliminary data from ZEUS shown in Fig. 7.25 is striking. The slopes have been calculated by fitting the high statistics HERA 1996/7 sample (including accurate small angle data measured with the ZEUS beam pipe tracker detector) and fixed target data from NMC and E665. The F_2 data at fixed x values were fitted with a form $F_2(x, Q^2) = A + B\log Q^2 + C\log^2 Q^2$ from which the logarithmic derivative is $B + 2C\log Q^2$. It is clear, that at least qualitatively, the model is predicting the general trend of the data. Both data and model also help the understanding of the first attempt by ZEUS to measure $dF_2/d\ln Q^2$ ([Cal97,ZEU99s]). Because of the lower precision and coverage of the data at that time the slope had to be averaged over all W values, thus obscuring the detail now available. The second fit by Golec-Biernat and Wüsthoff includes a massive charm quark in addition to the three light flavours. While the overall features are similar the position of the critical line relative to the peak changes somewhat and the peak in the charm component, $dF_2^c/d\ln Q^2$, occurs at larger values of both x and

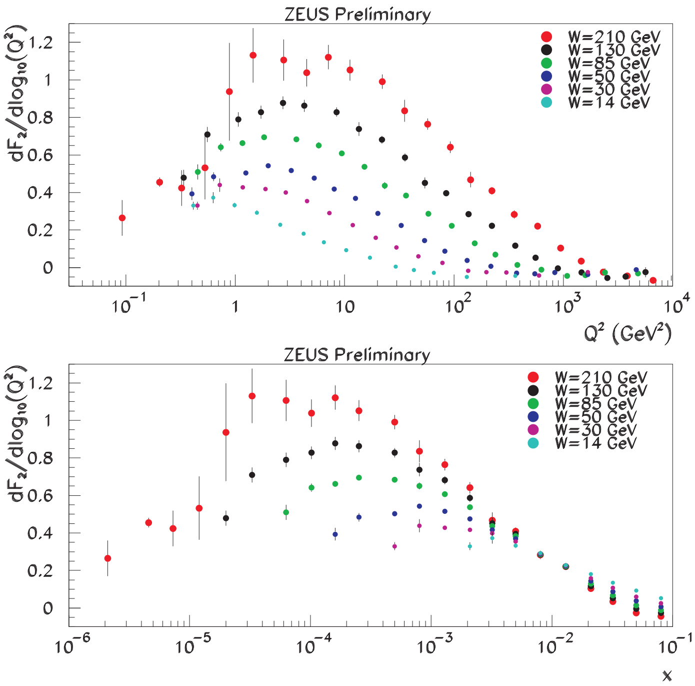

Fig. 7.25 Preliminary data from ZEUS on the slope $dF_2/d\ln Q^2$ from the high precision 96/97 data (including small angle data from the BPT).

Q^2. These predictions will be tested with the high luminosity data available after the HERA upgrade.

One needs to be somewhat careful before jumping to the conclusion that the Golec-Biernat-Wüsthoff model shows that saturation effects have been seen at HERA. As discussed at the beginning of this section, on fairly general grounds, one may not have the 'kinematic reach' at HERA to be sure of seeing such effects.Also, any model that fits all the low x and Q^2 F_2 data should reproduce the features of the slopes. However the simplicity of the GBW model, the fact that it is soundly based on physics arguments and its wide scope make it and others like it very appealing. One idea that will certainly be pursued further both theoretically and experimentally is the possible universality of the dipole cross-section.

7.9 Higher Twist at Low x

There have been a number of attempts to estimate higher twist contributions at low x. Martin and Ryskin [Mar98b] made an exploratory study based on contributions from vector meson dominance and absorptive corrections. They found that for F_2 the two contributions tended to cancel at low x. Ciafaloni *et al.* [Cia00] studied higher twist terms in the context

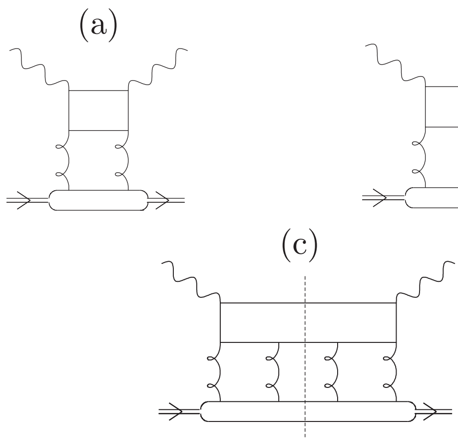

Fig. 7.26 The simplest QCD diagrams contributing to higher twist with 2, 3 or 4 gluons in the t-channel.

of the BFKL equation. Their conclusion was that higher twist terms are present at small x but have only a small effect on scaling violations.

The most systematic study has been made by Bartels and coworkers [Bar99a,Bar99b,Bar00]. The first two papers establishes the structure of twist-4 terms from the 2, 3 and 4 t-channel gluon exchange diagrams shown in Fig. 7.26. The calculation of the quark box at the top which connects the gluons to the γ^* is similar to that outlined in the previous section for $\gamma^* \to \mathrm{q\bar{q}}$ in the context of dipole models. The contributions are analysed separately for transverse and longitudinal photon polarisations and each splits into four terms:

$\Delta F^{(2)}$ From (a): these are the higher twist terms 'left over' from the diagram that gives the standard leading twist 2 contribution to DIS. This contribution is related to the BFKL equation.

$\Delta F^{(3)}$ From (b): these are higher order corrections to terms from (a) that are needed to complete the covariant derivative of the two gluon diagram.

$\Delta F^{R,I}$ From (c): the contributions split into two independent pieces: those labelled R can be Reggeised with two separate gluon ladders built on the two pairs of gluons on either side of the vertical dashed line; those labelled I are irreducible and cannot be Reggeised in the same way (for example a contribution to this class may involve a splitting from two to four gluons or gluon exchange across the centre line).

The total contribution to the structure function F_2 or $\sigma^{\gamma^* p}$ then takes the form

$$F_{T,L}(x,Q^2) = F_{T,L}^{(\tau=2)}(x,Q^2) + \Delta F_{T,L}(x,Q^2),$$

where

$$\Delta F_i(x,Q^2) = \Delta F_i^{(2)} + \Delta F_i^{(3)} + \Delta F_i^R + \Delta F_i^I \quad i = T, L. \tag{7.47}$$

The calculations are carried out in the double logarithmic approximation. As for the leading twist-2 case, pQCD allows one to calculate the Q^2 dependence of the higher twist terms but does not specify the form of the initial distributions in x. However the signs of the contributions can be determined and they are not all the same, the details are given in Tab. 7.1. Depending on the initial conditions cancellations can occur between the

Table 7.1 The signs of the higher twist contributions.

	$F_2^{(\tau=2)}$	$\Delta F^{(2)}$	$\Delta F^{(3)}$	ΔF^R	ΔF^I
L	+	−	+	−	+
T	+	+	−	+	−

terms and be different for the two polarisation states.The Q^2 evolution of the four contributions falls into two groups, the first three terms in Eq. 7.47 evolve in the same way as $\tau = 4$ 2-gluon operators whereas the last term evolves as a 4-gluon operator. The 4-gluon terms from diagram (c) are likely to be the most important at low x and indeed in the DLA, it can be shown that asymptotically ΔF^I rises twice as fast as the DAS limit for the leading twist 2-gluon term (Eq. 7.10). To be able to estimate the size of the twist-4 terms, assumptions have to be made about the starting functions. This is difficult to do at present. The 4-gluon exchange amplitude (Fig. 7.26(c)) can be related to diffractive q$\bar{\text{q}}$ production in DIS and this enables some limit to be put on a particular combination of the the terms $\Delta F^{R,I}$. For the other terms [Bar99a] make 'reasonable' assumptions about relating the terms to a standard global fit with both 'flat' and 'singular' behaviours at low x. They also consider different combinations of T and L contributions. Because of the uncertainties in the starting functions it is impossible to make firm predictions but some trends can be seen: significant cancellations occur for both the T and L structure functions; the twist-4 corrections are larger in the T than the L state; for flat input the total T twist-4 contribution is negative at small x but for a rising input it is positive.

To overcome the problem of insufficient information about the starting distributions, in [Bar00] Bartels *et al.* make use of the GBW dipole model described in the previous section. As the model describes the data for both F_2 down to $Q^2 = 0$ and DIS diffractive ${}_2^D$, it can play the role of ersatz data input for the higher twist analysis. In addition, as the model has a fairly simple mathematical structure it is possible to make a full higher twist expansion of it and study how the various higher twist components behave. It turns out a natural variable for the expansion is

$$\xi \equiv \frac{1}{Q^2 R_0^2(x)} = \frac{Q_0^2}{Q^2}\left(\frac{x_0}{x}\right)^{\lambda},$$

rather than Q_0^2/Q^2. The different regions of the model are also easily related to ξ: $\xi < 1$ is the perturbative (DGLAP) region of large Q^2 and not too small x; $\xi > 1$ is the Regge (Pomeron) region of small Q^2 and very small x; $\xi \approx 1$ marks the transition region. In the DGLAP region one expands in powers of ξ ($1/Q^2$ usual higher twist), in the Pomeron region in powers of $1/\xi$ (Q^2) and in the transition region both expansions will break down. The results of this study are shown in Fig. 7.27 (top plot for $\sigma_T + \sigma_L$, bottom for σ_L) and may be summarised as follows.

- Both the T and L higher twist terms become large as $\xi = 1$ is approached (from above), they have opposite signs T being positive and L negative.
- The magnitudes of the T and L terms are comparable, thus the complete higher twist contribution to the total cross-section (and hence F_2) is small. This is not the case for σ_L (or F_L).
- In more detail, the top plot shows that the twist-6 and twist-8 contributions in the total cross-section cancel almost completely, leaving only a small correction from the twist-4 term.
- The bottom plot shows that this is not the case for σ_L, where the leading twist-2 is almost a factor of 2 larger than the exact result for ξ just larger than 1.

While these results are clearly model dependent they are in line with phenomenological studies of higher twist (e.g. [Mar98c]) and results from global fits which have shown that standard DGLAP fits to F_2 can describe the data well down to the vicinity of $Q^2 \approx 1\,\mathrm{GeV}^2$ with either small higher twist terms at low x or none at all. However they also give a warning that this may be a false perception of the true location of the 'transition region'. Clearly accurate data on F_L is crucial for a complete understanding of these issues.

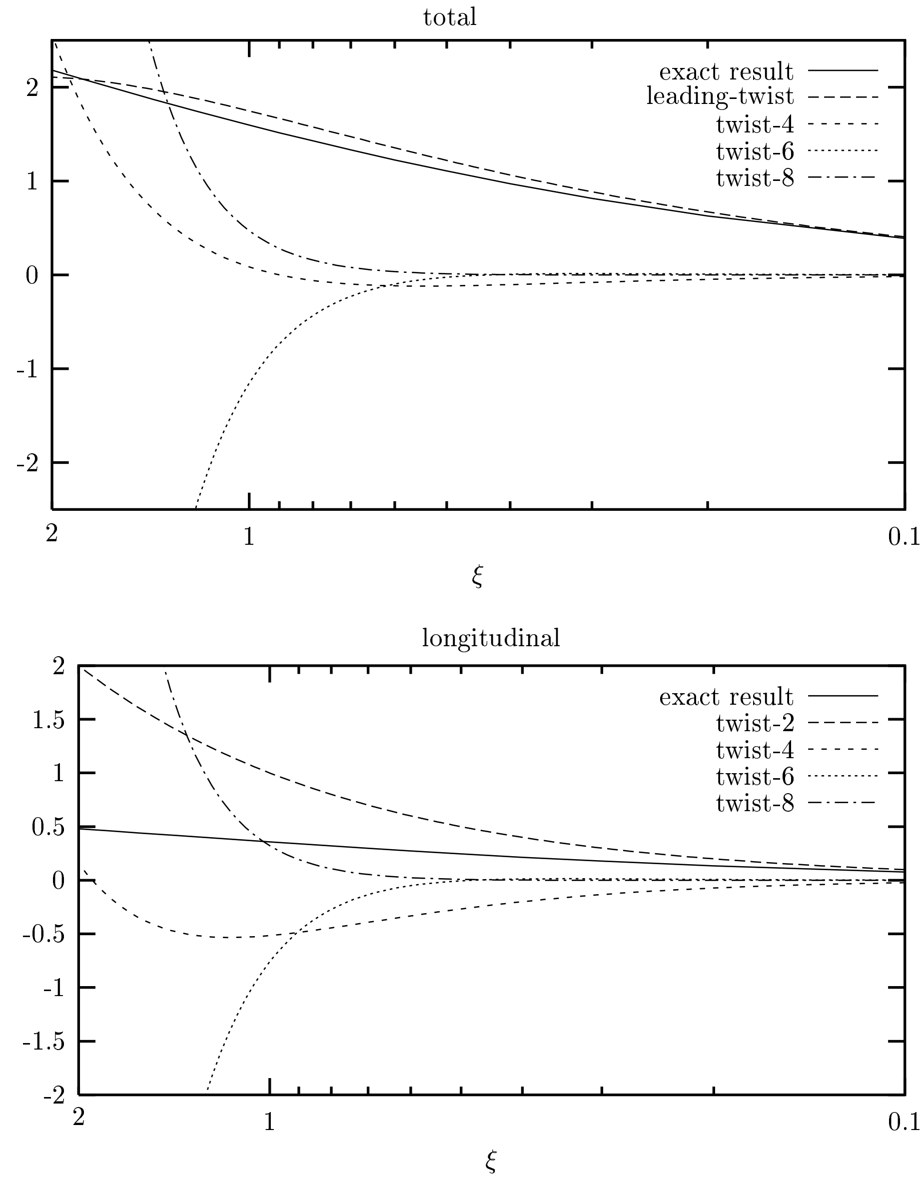

Fig. 7.27 Higher twist contributions in the GBW dipole model. Top: for the total cross-section $\sigma_T + \sigma_L$. Bottom: σ_L only. In both plots the contributions are renormalised by a common factor and the variable ξ is defined in the text..

7.10 Summary

The possible pQCD approaches to DIS at low x have been explained, with particular attention given to the seminal work by BFKL on low x dynamics. Much has been learnt about the limitations of the original fixed α_S calculation and work is continuing to understand how to best incorporate the large NLO corrections. At the very least it appears that the techniques will enable the calculation of gluon splitting functions to be 'improved' at low x. Low x physics is an active and rapidly developing field which has been strongly stimulated by the advent of HERA. One of the surprises is the good description of the HERA data (at least up and including the 1994/5 samples) down to rather low Q^2 and x values by the standard NLO DGLAP equations. There is now some understanding of why this might be based on a higher twist analysis of the Golec-Biernat Wüsthoff dipole model. However it is also possible to get a good description of the data by a variety of other approaches. Some incorporate aspects of the low x gluon dynamics inherent in the BFKL or CCFM equations, others are more phenomenological based loosely on the ideas of Regge theory or dipole pictures. There are hints that the high statistics 1996/7 HERA data and some of the recent theoretical advances going beyond NLO will lead to more decisive tests between the different approaches. It is certain that better data on observables other than inclusive F_2, such as F_2^c and particularly F_L would help enormously in this endeavour.

7.11 Questions

1. Writing Eq. 7.12 for the DAS limit in terms of x and Q^2, find an expression for the corresponding effective slope at small x, $\lambda_{eff} = d\ln F_2/d\ln(1/x)$.
2. The saddle point approximation to the integral

$$I = \int_{-\infty}^{+\infty} dx g(x) e^{-f(x)},$$

may be used when $g(x)$ is slowly varying around the minimum of the function $f(x)$. By expanding $f(x)$ around its minimum at x_0

$$f(x) = f(x_0) + \frac{1}{2} f''(x_0)(x - x_0)^2 + \ldots$$

show that

$$I \approx g(x_0) e^{-f(x_0)} \sqrt{\frac{2\pi}{|f''(x_0)|}}.$$

Using this result evaluate the integral 7.26 to give the LO BFKL result 7.27 for $F(s, \mathbf{k}_1, \mathbf{k}_2)$.
3. Justify the statement made at the start of Sec. 7.8 that in the proton rest frame the q$\bar{\text{q}}$ pair is produced a long time $\sim 1/(mx)$ before the interaction. Use light cone vectors introduced in Sec. 3.3.1:

$$q = (q^+, q^-, \mathbf{0}), \quad Q^2 = -2q^+q^-, \quad p = (m/\sqrt{2}, m/\sqrt{2}, \mathbf{0})$$

$$q_1 = \left(zq^+, \frac{\mathbf{k}_T^2}{2zq^+}, \mathbf{k}_T\right) \quad q_2 = \left((1-z)q^+, \frac{\mathbf{k}_T^2}{2(1-z)q^+}, -\mathbf{k}_T\right),$$

where m is the proton mass and q_1 and q_2 are the momenta of the q and $\bar{\text{q}}$ respectively. Consider the energy difference, $\Delta E = q_1^0 + q_2^0 - q^0$, between the q$\bar{\text{q}}$ pair and the γ^*. Show that

$$\Delta E \approx \frac{mx}{2}\left[1 + \frac{\mathbf{k}_T^2}{z(1-z)Q^2}\right],$$

and hence that the required result follows.
4. This and following two questions refer to the general considerations on dipole models in Sec. 7.8. By expanding the exponential factor $e^{i\mathbf{k}\cdot\mathbf{r}}$ in Eq. 7.40 and performing the angular integral, show that at small transverse separation, $\hat{\sigma}(x, r^2) \sim r^2$.
5. Verify the results that for 'large' sized q$\bar{\text{q}}$ pairs, that the integrals are dominated only by highly asymmetric configurations and

$$\sigma_T(x, Q^2) \sim 1/Q^2 \quad \sigma_L(x, Q^2) \sim m_f^2/Q^4.$$

6. Verify the result for 'small' sized $q\bar{q}$ pairs, that

$$\sigma_T(x, Q^2) \sim 1/Q^2 \quad \sigma_L(x, Q^2) \sim 1/Q^2.$$

These last two results can be deduced by appropriate approximation of the $\int dz$ integrals first, or by using the result that $\int d^2\mathbf{r}\sigma(r)K_i^2(\epsilon r) \propto \epsilon^{-4}$ on dimensional grounds. Further details are to be found in [For97,Ch.7].

8

Lepton induced DIS at high Q^2

Full formalism for μN, $\nu(\bar{\nu})N$ and $e^{\pm}p$ at high energies, both NC & CC. Give the general expressions for $d^2\sigma/dxdy$ for the various DIS processes in terms of the structure functions (F_2, F_L and xF_3). Give a careful account of how the structure functions for NC ($e^{\pm}p \to e^{\pm}X$ via γ^*, Z^0 exchange), CC ($e^{\pm}p \to \bar{\nu}(\nu)X$ via $W^{\pm}$ exchange) are related to the quark PDFs through the electroweak couplings. Include polarised $e^{\pm}$.

Discussion of which structure functions are important where.

Some discussion of radiative corrections?

Include data on high Q^2 cross-sections.

9

Aspects of the hadronic final state; α_S

Dijets - Discuss the QCD Compton and BGF singularities in the final state. Extension of kinematic variables from 2 to 5. Introduce x_p and z by analogy to x and y of eq scattering and mention ϕ dependence. Measurement of α_S. Forward jets as a handle on BFKL. QCD instantons and their hadronic final state characteristics. Introduce rapidity plateau in non-diffractive processes and exponential suppression of gaps. Inclusive diffractive processes and extension of formalism to $F_2^{D(4)}$ (+ mention ϕ dependence). Quasi-elastic processes such as vector meson production and relation to the gluon and the transition region.

The contents of this chapter are perhaps the most speculative.

10

Hadron induced DIS

The description of hard scattering in hadron-hadron interactions using the QCD enhanced parton model is a large subject. This chapter concentrates on those areas that are important for the determination of parton densities, or complement lepton induced DIS. Because of the very large momentum transfers involved, high E_T jet production in pp or p$\bar{\text{p}}$ interactions probes hadronic structure to very small distance scales. At the Tevatron with $\sqrt{s} = 1.8\,\text{TeV}$ one reaches a scale of around $10^{-4}\,\text{fm}$, comparable or even exceeding the scale reached in the highest Q^2 events at HERA. At the LHC one will be able to probe a couple of orders of magnitude smaller. It is in this sense that one may speak of hadron induced DIS.

The chapter starts with the basic idea and essential assumptions. The crucial result is factorisation, as this enables hard processes to be calculated using pQCD matrix elements and PDFs determined from other processes. Much of the initial discussion of detail is focused on Drell-Yan lepton-pair production. This then leads naturally to W and Z production at p$\bar{\text{p}}$ colliders. The core of the chapter concerns high E_T jet production in hadron-hadron collisions - a pure QCD process. High E_T isolated photon production is treated briefly and the chapter ends with a discussion of the importance of hadron induced DIS for LHC physics.

Written Summer 2001, revised Xmas 2001.

10.1 Rapidity

The majority of high energy hadron-hadron interactions, whether in fixed target or collider modes, produce final states with limited transverse momentum (with respect to the initial beam direction). Also in the parton model, the transverse momentum of the partons is assumed small in comparison to the longitudinal momentum. In these circumstances it is very convenient to use *rapidity*, $y = \dfrac{1}{2}\ln\left(\dfrac{E+p_z}{E-p_z}\right)$, together with transverse momentum, p_T and an azimuthal angle, ϕ to describe a particle's momentum. If

$$p = (E, p_T\cos\phi, p_T\sin\phi, p_z)$$

then, in terms of y,

$$p = (m_T \cosh y, p_T \cos\phi, p_T \sin\phi, m_T \sinh y), \tag{10.1}$$

where $m_T = \sqrt{m^2 + p_T^2}$ is the *transverse mass*. Rapidities are additive under Lorentz boosts along the beam direction and a rapidity difference is an invariant under the same transformation. At high energies, when masses can be ignored, the rapidity is often replaced by the pseudo-rapidity $\eta = -\ln\tan\frac{\theta}{2}$ (θ is the polar angle), as it is much easier to measure. Note that η has an infinite range $(-\infty, \infty)$ corresponding to $(-1 < \cos\theta < 1)$, whereas y always has a finite range, approximately $\left(\ln\frac{m}{2E}, \ln\frac{2E}{m}\right)$. The difference is usually only important in the regions close to the beam line where it is difficult, if not impossible, to measure particle momenta.
A useful relation following from the Jacobian of the transformation from Cartesian to rapidity momentum components is

$$\frac{d^3p}{E} = p_T dp_T d\phi dy \equiv d^2 p_T dy \to \pi dp_T^2 dy \approx \pi dp_T^2 d\eta, \tag{10.2}$$

where for the last expressions the azimuthal angle has been integrated out.

10.2 The cross-section for a hard hadronic process

The basic idea of using the QCD improved parton model to calculate the cross-section for a hard scattering process is summarised in Fig. 10.1. It is a natural extension of the approach used for lepton-induced DIS. The hadron-hadron cross-section is constructed from a convolution of the calculable parton-level cross-section for the hard process with the parton momentum densities for the incident hadrons. The new features are having two parton densities in the convolution and parton fragmentation or vector boson decay in the final state, depending on the process considered.

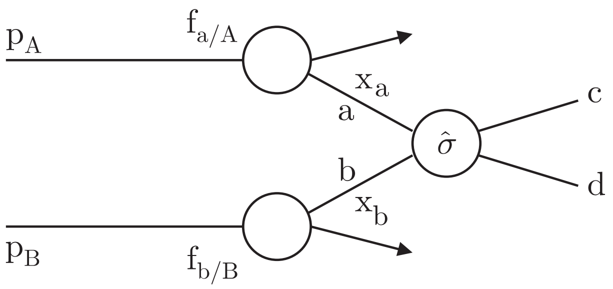

Fig. 10.1 The basic idea of the QCD improved parton model for a hard hadron-hadron interactions.

Formally one may write

$$d\sigma_{hard}(p_A, p_B, Q^2) = \sum_{ab} \int dx_a dx_b f_{a/A}(x_a, \mu^2) f_{b/B}(x_b, \mu^2) \times d\hat{\sigma}_{ab \to cd}(\alpha_S(\mu^2), Q^2/\mu^2)(1 + \delta_{had}) \quad (10.3)$$

where $d\hat{\sigma}_{ab\to cd}$ is the parton-parton cross-section at a hard scale Q^2 and $f_{a/A}$ is the parton momentum density of parton a in hadron A at a factorisation scale μ^2. The initial parton momenta are $p_a = x_a p_A$, $p_b = x_b p_B$ and the factor $(1 + \delta_{had})$ represents hadronisation corrections, which may be necessary if the final state of the hard process contains quarks and/or gluons fragmenting into jets. The hard scale will be provided by jet E_T or lepton-pair mass, for example. Strictly the scale involved in the definition of α_S in the cross-section (the renormalisation scale) could be different from the factorisation scale, but it is usual to set the two to be equal and indeed the choice $\mu^2 = Q^2$ is often made as well.[1] As before in any calculation at finite order in α_S, it will be important to ensure that the parton densities have been extracted at the same order as that used for the calculation of $d\hat{\sigma}_{ab\to cd}$.

The formal proof of factorisation is a difficult technical task involving the detailed analysis of the short and long distance singularities of classes of Feynman diagrams in the limit in which all scalar products of the external momenta are at scales $\sim Q^2$ very much larger than the external hadronic masses involved. In this limit one may treat the partons as massless and as one is dealing with a gauge theory QED provides useful analogies and insights. A good summary is given by Collins, Soper & Sterman [Col89]. A few qualitative remarks may help towards the underlying physics. At the simplest level one has the assumption of the parton model shown in the cartoon of Fig. 10.2(a), in which the two hadrons approaching each other at large equal and opposite momenta in the CM frame are Lorentz contracted. Time dilation ensures that during the instant of overlap, in which the partons a, b with momentum fractions x_a, x_b experience the hard scatter, the spectator partons in the two hadrons are 'frozen'.

The crucial difference between this process and that of leptonic DIS is the possibility that soft interactions between the colour fields of one hadron with the partons of the other may modify the calculation of the hard scattering cross-section $\hat{\sigma}_{ab\to cd}$, either before or after the hard interaction. In the equivalent problem in classical electrodynamics a relativistic charged particle passes close to a stationary charge and it is well known, e.g. [Jac75, p552], that the electric field of the moving particle is Lorentz contracted from spherical to disk with axis along the direction of motion. This means that the stationary test particle only feels a sizeable field around the instant of closest approach. The fact that partons are confined into colourless hadrons in QCD on the scale of 1 fm implies that the colour fields will decrease even more rapidly at large distances. In QED gauge invariance is cru-

[1] The choice $\mu^2 \approx Q^2$ avoids large $\ln(\mu^2/Q^2)$ terms appearing.

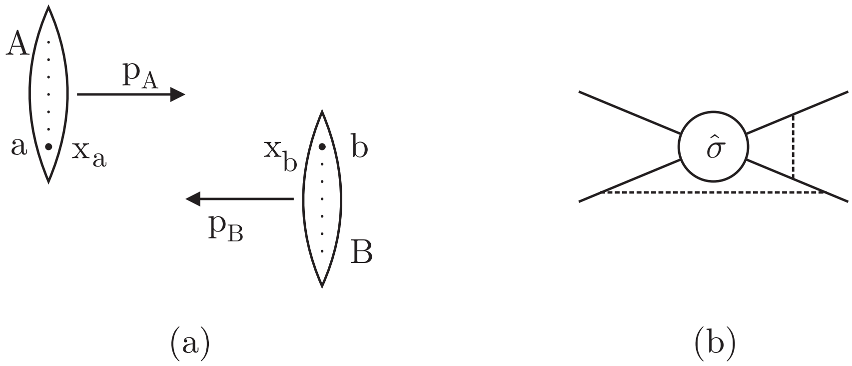

Fig. 10.2 (a) A cartoon of the Lorentz contracted hadrons in the CM frame at high energies showing the two partons with momentum fractions x_a, x_b that will be involved in the hard collision.(b) A two-body hard scattering diagram with soft photon or gluon insertions soft as the dashed lines.

cial in ensuring the cancellation of many apparent singularities that arise from collinear or infra-red divergences. For example consider a hard scattering between two electrons, as shown in Fig. 10.2(b), with two soft photon insertions. The QED Bloch-Nordsieck theorem ensures that when all diagrams required by gauge invariance are included the hard cross-section is not modified by the soft insertions. In the similar QCD diagram for the hard scattering between two coloured partons, the crucial insertions for factorisation are those connecting the initial and final states. Although QCD is a gauge theory, it has a more complicated non-abelian structure, and this means that not all soft cancellations can be guaranteed. In hadron-hadron scattering factorisation has been proved at leading twist (i.e. for the leading terms in the expansion of the cross-section in inverse powers of Q^2), but it has also been shown that factorisation is not exact beyond the single loop for higher twist terms. Explicit calculations for Drell-Yan production at two loops show factorisation breaking of the order m^4/Q^4, where m is the scale of the external hadron masses.[2] For the rest of this chapter factorisation will be assumed for leading twist QCD improved parton model calculations.

10.3 The Drell-Yan process

The Drell-Yan (D-Y) process [Dre70] of lepton pair production ($q\bar{q} \to \gamma^* \to \ell^+\ell^-$) was the first application of the parton model to a hard hadronic interaction. As it is the simplest such process and is also the basis for the calculation of W and Z boson production in hadron-hadron interactions,

[2]See [Col89] for references.

it will be discussed in some detail. The leading order diagram is shown in Fig. 10.3. The hard scale is set by the invariant mass of the lepton pair.

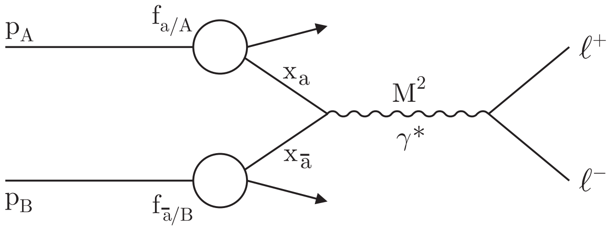

Fig. 10.3 Leading order, parton model, diagram for Drell-Yan lepton pair pair production in hadron-hadron scattering.

Although the D-Y cross-section is a tiny fraction of the total hadron-hadron cross-section, experimentally the presence of an energetic e^+e^- or $\mu^+\mu^-$ pair is a clean signature for the process. The success of the Drell-Yan model gave an important boost to the parton model generally and it allowed direct confirmation of the assumed limited parton transverse momentum. Because the D-Y process may be initiated by any pair of hadrons, it opens the possibility of studying parton momentum densities in hadrons other than the proton, e.g. the pion.

10.3.1 Kinematics and LO cross-section

Experimentally, for a fixed hadronic CM energy $\sqrt{s}$, three quantities may be reconstructed for the D-Y pair: the invariant mass (M), the rapidity (y) and the transverse momentum (p_T with respect to the incident hadron beam line). Ignoring p_T for the moment and referring to Fig. 10.3 the 4-momenta of the incident partons in the hadron-hadron CM frame are

$$p_a = \frac{\sqrt{s}}{2}(x_a, 0, 0, x_a), \qquad p_b = \frac{\sqrt{s}}{2}(x_b, 0, 0, -x_b),$$

where $s = (p_A + p_B)^2$ and parton masses have been ignored. Then

$$M^2 = (p_a + p_b)^2 = x_a x_b s, \quad y = \frac{1}{2}\ln\left(\frac{E + p_z}{E - p_z}\right) = \frac{1}{2}\ln(x_a/x_b),$$

where E, p_z are the energy and longitudinal momentum of the lepton pair. For D-Y, it is conventional to define $\tau = x_a x_b$ and as M is also the CM energy, $\sqrt{\hat{s}}$, of the $\mathrm{q\bar{q}} \to \ell^+\ell^-$ sub-process

$$\hat{s} = \tau s \quad \text{and} \quad \tau = M^2/s.$$

The parton momentum fractions, x_a, x_b, may also be written in terms of τ and y

$$x_a = \sqrt{\tau}\, e^{y}, \qquad x_b = \sqrt{\tau}\, e^{-y}. \tag{10.4}$$

An alternative to the variable y is the normalised longitudinal momentum of the lepton pair – Feynman x or x_F.

$$x_F = \frac{2}{\sqrt{s}}\,(p_{\ell+} + p_{\ell-}) \approx x_a - x_b \ \text{ ignoring } p_T,$$

where an obvious notation has been used for the lepton momenta. Sometimes the definition $x_F = x_a - x_b$ is used. In terms of τ and x_F one has

$$x_a = \frac{\sqrt{x_F^2 + 4\tau} + x_F}{2}, \quad x_b = \frac{\sqrt{x_F^2 + 4\tau} - x_F}{2}. \tag{10.5}$$

The cross-section for the sub-process is the same as that for $e^+e^- \to \mathrm{q\bar{q}}$ via a virtual photon

$$\hat{\sigma}(\mathrm{q}_a\bar{\mathrm{q}}_a \to \ell^+\ell^-) = \frac{Q_a^2}{3}\sigma_0, \quad \text{where} \quad \sigma_0 = \frac{4\pi\alpha^2}{3\hat{s}} \tag{10.6}$$

where Q_a is the electric charge of quark q_a. Note that both the quark flavour and colour have to match for the annihilation. This gives a factor 1/9 which is multiplied by 3 when summed over all colours, giving the overall colour factor of 1/3. Using the above expression in Eq. 10.3 gives the parton model expression for D-Y pair production

$$\begin{aligned} \frac{d\sigma_{DY}}{dM^2} &= \frac{\sigma_0}{3}\int_0^1 dx_a dx_b \delta(x_a x_b s - M^2) \\ &\times \sum_a Q_a^2\left[f_{a/A}(x_a) f_{\bar{a}/B}(x_b) + f_{\bar{a}/A}(x_a) f_{a/B}(x_b)\right], \end{aligned} \tag{10.7}$$

where $\hat{s} = M^2$ (the dilepton invariant mass) and the sum is only over quark flavours as the $\bar{\mathrm{q}}$ contributions are shown explicitly. Using the definitions of τ and σ_0 above the last equation may be rewritten as

$$M^4\frac{d\sigma_{DY}}{dM^2} = \frac{4\pi\alpha^2}{9}\tau F_0(\tau), \tag{10.8}$$

where

$$\begin{aligned} F_0(\tau) &= \int_0^1 dx_a dx_b \delta(x_a x_b - \tau) \\ &\times \sum_a Q_a^2\left[f_{a/A}(x_a) f_{\bar{a}/B}(x_b) + f_{\bar{a}/A}(x_a) f_{a/B}(x_b)\right]. \end{aligned} \tag{10.9}$$

At the parton level the PDF's $f_{a/A}(x_a)$ do not depend on M^2 and the above equations show that $M^4\dfrac{d\sigma_{DY}}{dM^2}$ is a function of τ only – it 'scales' in the same sense that $F_2(x, Q^2)$ in DIS scales at the parton level. The data does show approximate scaling and this was an important result for the model. The D-Y cross-section is also predicted to fall as M^{-4} at fixed τ. Starting from Eq. 10.7 and using Eq. 10.4 for x_a, x_b one finds

$$s\frac{d^2\sigma_{DY}}{d\tau dy} = \frac{4\pi\alpha^2}{9\tau}\sum_a Q_a^2\left[f_{a/A}(x_a)f_{\bar{a}/B}(x_b) + f_{\bar{a}/A}(x_a)f_{a/B}(x_b)\right] \quad (10.10)$$

for the double differential cross-section. At $y = 0$, the right-hand side of the above equation is also a function of τ only. Data is often presented with respect to M^2 and x_F rather than τ and y

$$\begin{aligned} M^4\frac{d^2\sigma_{DY}}{dM^2dx_F} &= \frac{4\pi\alpha^2}{9}\frac{\tau}{(x_a+x_b)} \\ &\times\sum_a Q_a^2\left[f_{a/A}(x_a)f_{\bar{a}/B}(x_b) + f_{\bar{a}/A}(x_a)f_{a/B}(x_b)\right], \end{aligned} \quad (10.11)$$

where x_a, x_b are given by Eq. 10.5 and the extra factor of $(x_a + x_b)$ comes from the Jacobian $dx_a dx_b \to dM^2 dx_F$.
Fig. 10.4 is taken from the review of McGaughey *et al.* [McG99] and shows approximate scaling of $M^4\dfrac{d^2\sigma_{DY}}{dM^2dx_F}$ from fixed target experiments on $pA \to \mu^+\mu^- X$ at 400 and 800 GeV incident proton momenta. At a fixed value of x_F the cross-section is a slowly varying function of τ and data from different CM energies lie on the same curve. The curves show the result of an $O(\alpha_S)$ calculation that will be described in more detail below. By measuring the double differential cross-section over a wide range of values of M^2 and y (or x_F) one has a direct constraint on the PDFs of the parent hadrons A and B. For example, the ratio of the D-Y rates for pp and pd scattering at high energy is sensitive to the $\bar{d}/\bar{u}$ ratio in the valence region. The E866 fixed target experiment [Haw98] measured the pd/pp ratio with 800 GeV incident protons. Since $x_F > 0$ and referring to Eq. 10.11, the PDF factor will be dominated by the first terms which are products of beam quark with target antiquark momentum distribution functions

$$\frac{\sigma_{DY}(pd)}{2\sigma_{DY}(pp)} \approx \frac{[4u(x_a)+d(x_a)][\bar{u}(x_b)+\bar{d}(x_b)]}{2[4u(x_a)\bar{u}(x_b)+d(x_a)\bar{d}(x_b)]}, \quad (10.12)$$

where strong isospin symmetry has been used to write the deuteron PDFs in terms of those for the proton. The ratio may be written as

$$\frac{\sigma_{DY}(pd)}{2\sigma_{DY}(pp)} \approx \frac{\left(1+\frac{1}{4}\frac{d_A}{u_A}\right)\left(1+\frac{\bar{d}_B}{\bar{u}_B}\right)}{2\left(1+\frac{1}{4}\frac{d_A}{u_A}\frac{\bar{d}_B}{\bar{u}_B}\right)} \approx \frac{1}{2}\left(1+\frac{\bar{d}_B}{\bar{u}_B}\right), \quad (10.13)$$

where the last approximation follows from the fact that $d < u$ in the valence region together with the numerical suppression. If $\bar{d} = \bar{u}$, as was often assumed for the $q\bar{q}$ nucleon sea, the measured ratio should be approximately

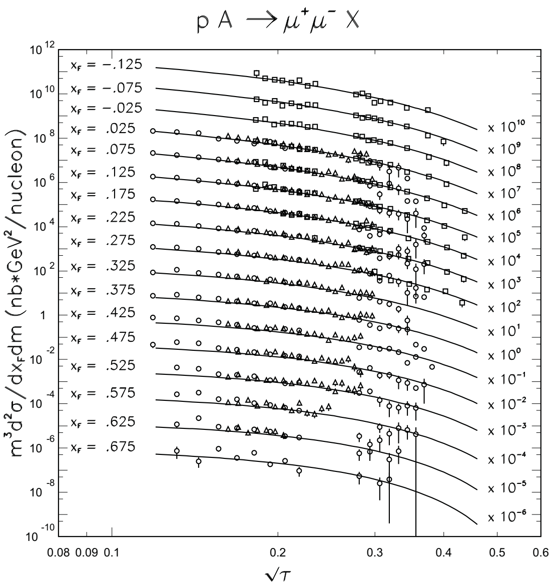

Fig. 10.4 Approximate scaling of the D-Y $pA \to \mu^+\mu^- X$ double differential cross-section at fixed values of x_F. Data are from NA3 at 400 GeV (triangles [Bad84]), E605 (squares [Mor91]) & E772 (circles [McG94]) at 800 GeV. The lines show an $O(\alpha_S)$ calculation of $pd \to \mu^+\mu^- X$. From McGaughey *et al.* [McG99].

independent of x_b. As Fig. 10.5 shows this is not the case and the experiment has provided important data for refining global PDF determination.

10.3.2 Transverse momentum and QCD corrections

There are two sources of transverse momentum corrections for the D-Y process. Firstly, the intrinsic transverse momentum of the q and $\bar{\text{q}}$ in the initial state hadrons. In the parton model this is assumed to be small (few hundred MeV) in comparison with both the longitudinal momentum scale and the dilepton mass scale. Secondly, the potentially larger transverse momenta introduced by QCD corrections such as gluon emission. The effect of the first source cannot be calculated perturbatively, but it can be measured and the parton model assumption of limited p_T is verified. Simple models for the intrinsic parton p_T, e.g. a Gaussian distribution, may be used to describe this part of the dilepton p_T spectrum. At larger p_T there is a non-gaussian tail and this is taken to be evidence for the QCD corrections. The other evidence of the need for corrections is that at fixed target energies in particular, although the parton model explains the approximate scaling seen in the data, it predicts a cross-section that is too low by as much as 50%.

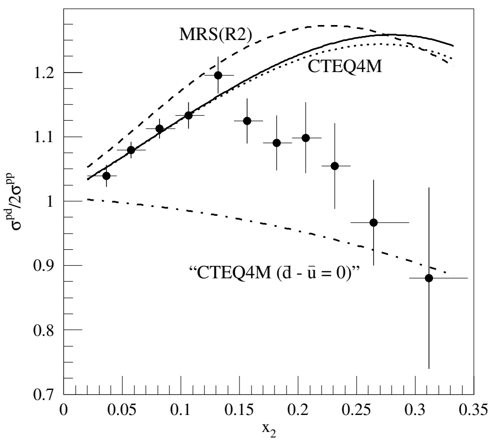

Fig. 10.5 Ratio of Drell-Yan rates $\sigma_{DY}(pd)/(2\sigma_{DY}(pp))$ as measured by the E866 experiment [Haw98]. The curves show a number of predictions calculated using PDFs available prior to this experiment.

The QCD diagrams for order α_S corrections to the D-Y process are shown in Fig. 10.6. There are three types: the two diagrams on the left are virtual

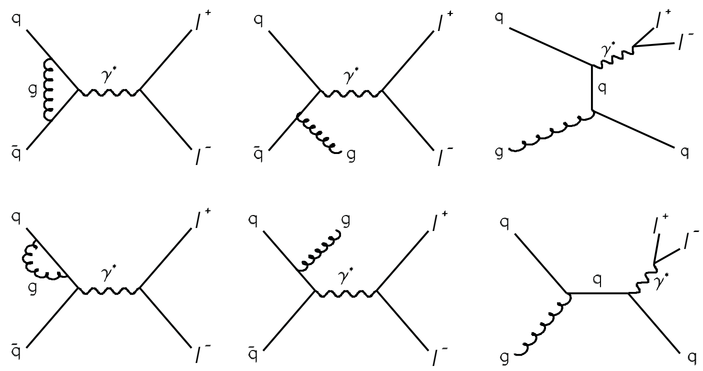

Fig. 10.6 Order α_S QCD corrections to Drell-Yan. (Figure from [McG99].)

gluon vertex and loop insertions; the next two come from $q\bar{q} \to \gamma^* g$ (inverse of photon-gluon fusion) and finally the two on the right are from $qg \to \gamma^* q$ (inverse QCD Compton scattering). It is no coincidence that the same diagrams occur in DIS (as can be seen by referring back to Figs**??** and **??** of Chapter 4.) The net effect of the QCD corrections is similar to that explained in detail in Chapter 4. The various divergences that arise from the loop integrals, collinear parton configurations and infra-red parton emission have to regularised by the introduction of 'renormalised' parton densities at a renormalisation scale μ^2. This introduces $\ln(M^2/\mu^2)$ scaling violations into the PDFs and explicit correction terms to the LO parton model cross-sections. Because the diagrams are intrinsically the same as in DIS, the renormalised parton densities are those governed by the DGLAP equations. At order α_S and in the $\overline{\mathrm{MS}}$ scheme with scale $\mu^2 = M^2$ the D-Y cross-section of Eq. 10.8 becomes

$$M^4 \frac{d\sigma_{DY}}{dM^2} = \frac{4\pi\alpha^2}{9}\tau\left[F_1(\tau, M^2) + G_1(\tau, M^2)\right], \tag{10.14}$$

where
The gluon part of the following needs to be checked! RD

$$\begin{aligned}
F_1(\tau, M^2) &= \int_0^1 dx_a dx_b dz \delta(x_a x_b z - \tau)\left(\delta(1-z) + \frac{\alpha_S(M^2)}{2\pi} D_q(z)\right) \\
&\quad \times \sum_a Q_a^2 \left[f_{a/A}(x_a, M^2) f_{\bar{a}/B}(x_b, M^2) + (a \leftrightarrow \bar{a})\right] \\
G_1(\tau, M^2) &= \int_0^1 dx_a dx_b dz \delta(x_a x_b z - \tau)\frac{\alpha_S(M^2)}{2\pi} D_g(z) \\
&\quad \times \sum_a Q_a^2 \left[f_{g/A}(x_a, M^2)\left(f_{a/B}(x_b, M^2) + f_{\bar{a}/B}(x_b, M^2)\right) + (a, \bar{a} \leftrightarrow g)\right],
\end{aligned}$$

and D_q and D_g are the D-Y coefficient functions

$$\begin{aligned}
D_q(z) &= C_F\left[4(1+z^2)\left(\frac{\ln(1-z)}{1-z}\right)_+ - 2\frac{1+z^2}{1-z}\ln z + \frac{2\pi^2 - 24}{3}\delta(1-z)\right] \\
D_g(z) &= T_R\left[(z^2 + (1-z)^2 \ln\frac{(1-z)^2}{z} + \frac{1}{2} + 3z - \frac{7}{2}z^2\right].
\end{aligned}$$

The first term, F_1, in the [] on the RHS of Eq. 10.14 is the modified $\mathrm{q\bar{q}}$ term corresponding to the LO F_0. The second term, G_1, is a new contribution which arises from the two diagrams on the right of Fig. 10.6 and depends explicitly on the gluon density. At fixed target energies the first term dominates and gives rise to a large positive correction. At the higher energies of collider experiments, corresponding to smaller values of τ, the qg terms (which are negative) are larger and the overall correction to the parton model result is smaller. With the order α_S corrections the calculation of the D-Y cross-section is in good agreement with the data in both shape and normalisation. The curves in Fig. 10.4 are $O(\alpha_S)$ calculations for $pd \to \mu^+\mu^- X$ at 800 Gev using the CETQ4M PDFs without any further normalisation adjustment (from [McG99]). $O(\alpha_S^2)$ corrections have also been calculated [Ham91] and are generally smaller than the α_S corrections.

10.4 W & Z boson production

The Drell-Yan process was one of the discovery channels for the J/ψ in 1974 and the discovery channel for the Υ family of heavy $\mathrm{Q\bar{Q}}$ vector mesons in 1977. Provided the detector components have sufficient resolution, the D-Y process enables a very wide range of dilepton invariant mass to be covered in a single experiment. At high enough energies the W and Z gauge bosons can be produced and once more the dilepton mode was crucial for their discovery in $\mathrm{p\bar{p}}$ collisions. To $O(\alpha_S)$ the hadronic part of the lepton-pair production cross-section for the W and Z is the same as that for a virtual photon, as the gluon coupling is flavour blind. At $O(\alpha_S^2)$ there is a numerically small difference for Z production.

10.4.1 Z boson production

The situation here is similar to that in high energy e^+e^- annihilation – diagrams for $\mathrm{q\bar{q}} \to Z \to \ell^+\ell^-$ must be added to those for $\mathrm{q\bar{q}} \to \gamma^* \to \ell^+\ell^-$. Eq. 10.6 for the sub-process cross-section becomes

$$\hat{\sigma}(\mathrm{q}_i\bar{\mathrm{q}}_i \to \ell^+\ell^-) = \frac{4\pi\alpha^2}{9\hat{s}}\left[Q_i^2 - 2Q_i v_i v_\ell \chi_1(\hat{s}) + (a_i^2+v_i^2)(a_\ell^2+v_\ell^2)\chi_2(\hat{s})\right],$$

where Q_i is the electric charge and v_i, a_i are the electroweak vector and axial couplings of quark q_i

$$v_i = T_i^3 - 2Q_i \sin^2\theta_W, \quad a_i = T_i^3, \quad \kappa = \frac{\sqrt{2}G_F M_Z^2}{16\pi\alpha}$$

T_i^3 is the 3rd component of the weak isospin and is $+1/2$ for ν_ℓ, u, c, t and $-1/2$ for ℓ^-, d, s, b.

$$\chi_1(\hat{s}) = \kappa\frac{\hat{s}(\hat{s}-M_Z^2)}{(\hat{s}-M_Z^2)^2+\Gamma_Z^2 M_Z^2}, \quad \chi_2(\hat{s}) = \kappa^2\frac{\hat{s}^2}{(\hat{s}-M_Z^2)^2+\Gamma_Z^2 M_Z^2}.$$

As in e^+e^- annihilation the angular distribution of the final state leptons contains sensitive information on the vector boson couplings through the vector-axial interference term. A resonance with pure vector or axial couplings gives an angular distribution of $(1+\cos^2\theta^*)$, where θ^* is the angle of ℓ^+ in the Z^0 rest frame with respect to the incident proton beam direction (in $\mathrm{p\bar{p}}$ interactions).[3] For a particle with both axial and vector couplings an asymmetric term in $\cos\theta^*$ is present as well. A direct measure of the interference term is given by the lepton forward-backward asymmetry $A_{FB} = \dfrac{\sigma(\theta^*>0)-\sigma(\theta^*<0)}{\sigma(\theta^*>0)+\sigma(\theta^*<0)}$. Most detectors cannot measure over the full solid angle, so A_{FB} must either be corrected for acceptance or the theory calculated over the measured angular range.

[3]To reduce the uncertainty introduced by the incident parton p_T, precision experiments measure the lepton angle in the Collins-Soper frame [Col77b].

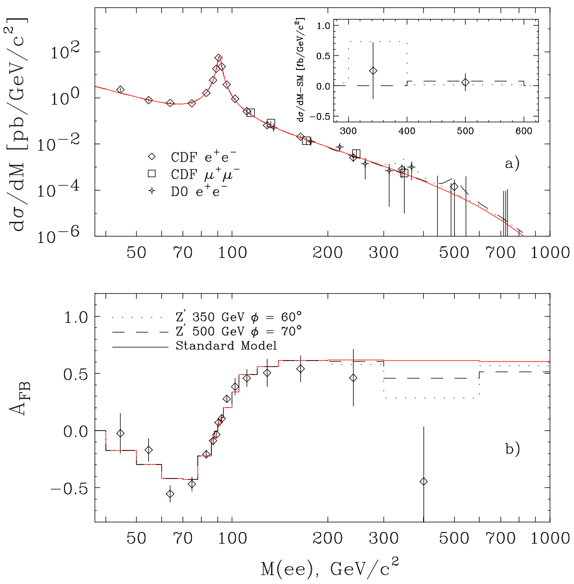

Fig. 10.7 Drell-Yan lepton pair production around the mass of the Z^0 boson from the CDF experiment [CDF01b]. (a) $d\sigma/dM$ together with an $O(\alpha_S^2)$ using MRST99 PDFs (full curve); (b) A_{FB} together with an $O(\alpha_S)$ standard model calculation.

Fig. 10.7 shows the cross-section $d\sigma/dM$ and A_{FB} for $\mathrm{p\bar{p}} \to \ell^+\ell^- X$ at $\sqrt{s} = 1.8\,\mathrm{TeV}$ with $M > 40\,\mathrm{GeV}$. The data are from the CDF experiment [CDF01b] and correspond to $108\,\mathrm{pb}^{-1}$. Electrons are measured in the range $|\eta| < 4.2$ and muons in $|\eta| < 1.1$. The curve shown in plot (a) is an $O(\alpha_S^2)$ calculation using the MRST99 PDFs normalised to the Z peak cross-section (factor 1.11). For A_{FB}, plot (b), the data are compared with an $O(\alpha_S)$ calculation. The calculations describe the shapes of both distributions around the position of the Z peak very well. The dashed curves show the sensitivity to a model with an additional Z' boson and indicate the continuing potential of D-Y for discovering new physics.

For studies of the properties of the Z^0 itself one integrates the data over the region of the resonance ($|M - M_Z| < \Delta$ where $\Gamma_Z << \Delta << M_Z$). The expression for the cross-section also simplifies as only the term involving χ_2 is important. To calculate the integrated cross-section it is enough to use the 'narrow resonance approximation'

$$\frac{1}{(\hat{s} - M_Z^2)^2 + \Gamma_Z^2 M_Z^2} \to \frac{\pi}{M_Z \Gamma_Z}\delta(\hat{s} - M_Z^2),$$

where the normalisation is given by the full area under the Breit-Wigner line shape. Using this gives

$$\hat{\sigma}(\mathrm{q}_i\bar{\mathrm{q}}_i \to Z \to \ell^+\ell^-) = \frac{4\pi^2\alpha^2}{9}\frac{M_Z}{\Gamma_Z}\kappa^2(a_i^2+v_i^2)(a_\ell^2+v_\ell^2)\delta(\hat{s}-M_Z^2). \quad (10.15)$$

Using the standard model expression, $B(Z \to \ell^+\ell^-) = \dfrac{G_F M_Z^3}{6\sqrt{2}\pi\Gamma_Z}(v_\ell^2 + a_\ell^2)$, one may write the above equation as

$$\hat{\sigma}(\mathrm{q}_i\bar{\mathrm{q}}_i \to Z \to \ell^+\ell^-) = \hat{\sigma}(\mathrm{q}\bar{\mathrm{q}} \to Z)B(Z \to \ell^+\ell^-),$$

where

$$\hat{\sigma}(\mathrm{q}\bar{\mathrm{q}} \to Z) = \frac{\pi}{3}\sqrt{2}G_F M_Z^2\frac{(a_i^2+v_i^2)}{16}\delta(\hat{s}-M_Z^2). \quad (10.16)$$

Note that this differs from ESW eqn 9.31 by 16 - check!! RD

10.4.2 W boson production

Since the width of the W is also small in comparison with its mass, one may use the narrow resonance approximation to calculate the sub-process production cross-section. The form is that of Eq. 10.16 for the Z, but with the electroweak coupling factor replaced by the appropriate CKM matrix element $|V_{ij}|$

$$\hat{\sigma}(\mathrm{q}_i\bar{\mathrm{q}}_j \to W) = \frac{\pi}{3}\sqrt{2}G_F M_W^2|V_{ij}|^2\delta(\hat{s}-M_W^2) \quad (i \neq j). \quad (10.17)$$

To calculate the rate for a leptonic final state one also needs

$$B(W \to \ell\nu_\ell) = \frac{G_F M_W^3}{6\sqrt{2}\pi\Gamma_W}.$$

Until the advent of high energy running at LEP, above the $e^+e^- \to W^+W^-$ threshold, precise measurement of the mass and width of the W was the preserve of p$\bar{\mathrm{p}}$ collider experiments via the D-Y process. Because of much higher rates at hadron machines such measurements will remain competitive.

Note that many experimental and theoretical uncertainties can be reduced by measuring the ratio of lepton pair production at the W and Z

$$\begin{aligned} R_{DY} &= \frac{N(W \to \ell\nu_\ell)}{N(Z \to \ell^+\ell^-)} = \frac{\sigma_W}{\sigma_Z}\frac{B(W \to \ell\nu_\ell)}{B(Z \to \ell^+\ell^-)} \\ &= \frac{\sigma_W\Gamma_Z}{\sigma_Z\Gamma_W}\frac{\Gamma(W \to \ell\nu_\ell)}{\Gamma(Z \to \ell^+\ell^-)}. \end{aligned} \quad (10.18)$$

These questions will not be followed any further here, but the possible use of W or Z production as a 'luminosity monitor' for next generation hadron colliders will be considered in Sec.10.7.2.

10.4.3 W decay asymmetry

The technique for calculating the rapidity distributions for W and Z production in hadron-hadron collisions follows that for D-Y production. For both the photon and Z, the rapidity distribution must be symmetric about $y = 0$ (this follows from CP invariance since they are both neutral particles). The same does not hold for $W^{\pm}$ and, as the charge of the W may be determined from its leptonic decay, one has a handle on the hadronic parton densities at very large mass scales. Define the positive z axis, and hence $y > 0$, to be along the direction of the incoming proton in a $p\bar{p}$ collision. Then W^+ will tend to be produced forward, $u\bar{d} \to W^+ \to \ell^+\nu_\ell$, as both u quarks tend to carry more momentum than d quarks. Conversely $\bar{u}d \to W^- \to \ell^-\nu_\ell$ will tend to produce W^- at $y < 0$. What is measured is the angular asymmetry of the decay $\ell^{\pm}$ (where ℓ is μ or e). Consider the production and decay of the W in its rest frame. Fig. 10.8(a) shows W^+

Fig. 10.8 Production and decay of W in its rest frame: (a) W^+; (b) W^-.

production and decay, with the polar axis defined to be along the incoming proton beam direction and θ^* the decay angle of ℓ^+ in the W rest frame. Neglecting parton transverse momenta the u and $\bar{d}$ are aligned along the z-axis and neglecting all masses the alignment of the initial and final spins are shown as the double arrows. The total spin is $J = 1$, with $J_z = -1$ in the initial state and $J_z = +1$ in the final state. The angular dependence of the matrix element is given by the rotation matrix $d^1_{1,-1}(\theta^*) = \frac{1}{2}(1 - \cos\theta^*)$. This shows that ℓ^+ is produced preferentially backwards. Similarly, diagram (b) shows the situation for W^-, now both initial and final state have $J_z = -1$ and the angular dependence of the matrix element is given by $d^1_{-1,-1}(\theta^*) = \frac{1}{2}(1 + \cos\theta^*)$. For W^- decay, ℓ^- is produced preferentially forwards. As the lepton tends to be produced in the opposite direction to the parent W for both charge states, the lepton decay asymmetry will be somewhat smaller than the W production asymmetry but it is nonetheless a useful quantity to measure. A typical example from the CDF experiment [CDF98] is shown in Fig. 10.9, together with predictions using a number of PDFs.

In the W rest frame, $E_\ell = |p_\ell| = M_W/2$, so $\cos^2\theta^* = 1 - \frac{4p_T^2}{M_W^2}$, where

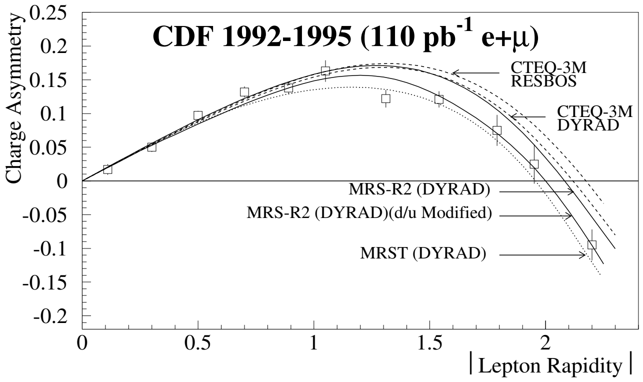

Fig. 10.9 W decay asymmetry as measured by CDF in $\mathrm{p\bar{p}}$ at $\sqrt{s} = 1.8\,\mathrm{TeV}$ [CDF98].

p_T refers to the decay $\ell^{\pm}$ and is invariant under boosts along the z-axis. Averaging the W decay angular distribution over both charge states gives

$$\frac{1}{\sigma}\frac{d\sigma}{d\cos\theta^*} \propto (1 + \cos^2\theta^*).$$

Changing variables from $\cos\theta^*$ to p_T^2 gives

$$\frac{1}{\sigma}\frac{d\sigma}{dp_T^2} \propto \frac{1}{M_W^2}\left(1 - \frac{4p_T^2}{M_W^2}\right)^{-1/2}\left(1 - \frac{2p_T^2}{M_W^2}\right).$$

When smeared over the finite width of the W, the cross-section shows a peak at $p_T \sim M_W/2$ – the Jacobian peak. This is one of the methods of measuring the W mass. The p_T distribution is also smeared by W transverse motion. Another method, which is less sensitive to this last effect, is based on the transverse mass

$$M_T^2 = |p_{T\ell}||p_{T\nu}|(1 - \cos\Delta\phi),$$

where $p_{T\nu}$ is identified with the missing transverse momentum in the event and $\Delta\phi$ is the difference in azimuthal angles between the charged lepton track and the missing momentum vector. Since M_T depends on $p_{T\ell}$ it will also exhibit a Jacobian peak and thus sensitivity to M_W. For more details on W mass measurement see [Ell96,Ch9] and for a recent measurement giving $M_W = 80.691 \pm 0.227\,\mathrm{GeV}$ see [DØ 00a]. For the most precise value of M_W, data from $\mathrm{p\bar{p}}$ at the Tevatron is combined with data from LEPII on $e^+e^- \to W^+W^-$ [PDG00, p249].
As in classic D-Y, the W and Z bosons produced at large transverse momenta correspond to QCD processes beyond the LO parton model, specifically $\mathrm{q\bar{q}} \to Vg$ and $\mathrm{q}g \to V\mathrm{q}$. There is a difference, however, in that there

are now two scales involved. For pQCD to give valid results $p_T >> \langle k_T \rangle$ (the typical intrinsic parton transverse momentum of $\sim$ 700 MeV), but the vector boson mass M_V also sets a scale giving rise to terms involving $\ln(M_V^2/p_T^2)$. For $\langle k_T \rangle << p_T << M_V$, it may be necessary to sum multiple 'soft' gluon emission. For leading logs this has been done, more detail is to be found in [Ell96, Sec.9.4], where further references are given.

10.5 High p_T jet production

So far, the hard parton processes that have been discussed involve electroweak couplings at the leading, parton model, order and QCD effects only enter as $O(\alpha_S)$ corrections. High p_T jet production in hadron-hadron scattering is a manifestation of an underlying hard two-parton interaction involving gluon or quark exchange at the leading order, giving cross-sections of $O(\alpha_S^2)$. More details on the leading order diagrams and matrix elements are given in the appendix to this chapter. At the high energies of $\mathrm{p\bar{p}}$ colliders, particularly the Tevatron, these processes give rise to spectacular events with two back-to-back high-p_T jets standing out from the remaining hadronic remnants nearer the beam line – an example is shown in Fig. 10.10. Higher order processes give rise to events with more than two jets.

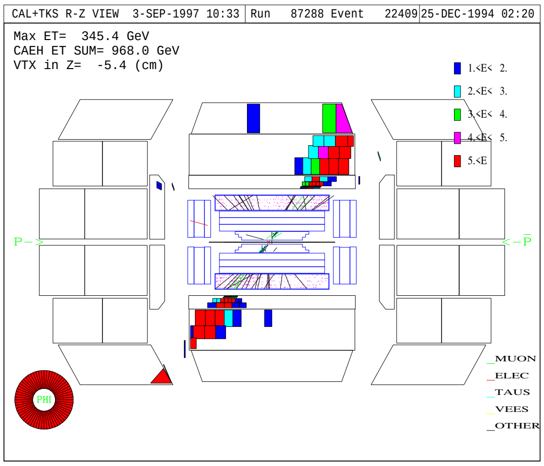

Fig. 10.10 A high E_T dijet event from $\mathrm{p\bar{p}}$ interactions at $\sqrt{s} = 1.8\,\mathrm{TeV}$ as measured by the DØ experiment.

Most of the published jet data from hadron-hadron colliders have been produced using a cone jet definition in η, ϕ space with cone radius, $R =$

$\sqrt{(\Delta\eta)^2 + (\Delta\phi)^2}$, typically of about 1 unit. However, it has been argued that cone algorithms are not 'infra-red' safe when measuring multi-jet events [Gie97,Sey00]. For the Tevatron RunII a k_T algorithm (*xref to jet chapter?*) is being used and some RunI data has been re-analysed using this method. Such concerns do not affect the present discussion which concentrates on the lowest order two-jet events. For a proper comparison of theory with data the efficiency of the jet finder must be taken into account, but 100% efficiency will be assumed here. At Tevatron energies and simple jet topologies this is a reasonable approximation to the truth.

10.5.1 Parton-parton kinematics

Fig. 10.11(a) shows the parton-parton hard sub-process $ab \to cd$, where the initial partons a, b are contained in the colliding hadrons A, B. The Mandelstam variables for the sub-process are

$$\hat{s} = (p_a + p_b)^2, \quad \hat{t} = (p_a - p_c)^2, \quad \hat{u} = (p_a - p_d)^2.$$

Assuming that all parton masses may be neglected, these may be approximated as

$$\hat{s} \approx 2p_a \cdot p_b, \quad \hat{t} \approx -2p_a \cdot p_c \quad \hat{u} \approx -2p_a \cdot p_d.$$

In the same approximation the following relations also hold

$$\hat{s} + \hat{t} + \hat{u} = 2E_a(E_a + E_b - E_c - E_d) = 0, \tag{10.19}$$

as there is overall conservation of 4-momentum in the hard sub-process. Diagram (b) shows the scattering angle, θ^*, in the parton-parton CM frame. Since masses are neglected all four partons have the same energy in the CM, $E^* = \sqrt{\hat{s}}/2$.

Fig. 10.11 Two body parton-parton kinematics: (a) definition of of sub-process variables $\hat{s}$ and $\hat{t}$; (b) the parton-parton CM frame and the definition of the CM scattering angle θ^*.

In terms of θ^*

$$\hat{t} = -\frac{\hat{s}}{2}(1 - \cos\theta^*), \quad \hat{u} = -\frac{\hat{s}}{2}(1 + \cos\theta^*).$$

The initial state sub-process momenta are given in terms of the hadron-hadron CM energy, $\sqrt{s}$ by

$$p_a = \frac{\sqrt{s}}{2}(x_a, 0, 0, x_a), \quad p_b = \frac{\sqrt{s}}{2}(x_b, 0, 0, -x_b),$$

where x_a, x_b are the fractions of the initial-state hadron beam momenta involved in the hard collision. As with other kinematic quantities of interest these have to be inferred from the final-state parton momenta which also cannot be measured directly, but are assumed to be those of the two jets. Ignoring any initial parton transverse momentum, one has

$$\begin{aligned} p_c &= p_T(\cosh y_c, \cos\phi, \sin\phi, \sinh y_c), \\ p_d &= p_T(\cosh y_d, -\cos\phi, -\sin\phi, \sinh y_d). \end{aligned}$$

Here the transverse mass $m_T = p_T$ as parton masses are being neglected. From these and using energy and longitudinal momentum conservation one finds

$$x_a = \frac{x_T}{2}\left(e^{y_c} + e^{y_d}\right), \quad x_b = \frac{x_T}{2}\left(e^{-y_c} + e^{-y_d}\right), \tag{10.20}$$

where $x_T = 2p_T/\sqrt{s}$ and y_c, y_d are the rapidities of the final state partons (jets). It is also convenient to have expressions in terms of parton CM quantities. Defining

$$y_{CM} = \frac{1}{2}(y_c + y_d), \quad y^* = \frac{1}{2}(y_c - y_d)$$

one finds

$$x_a = x_T e^{y_{CM}} \cosh y^*, \quad x_b = x_T e^{-y_{CM}} \cosh y^*.$$

Note that y^* is invariant under boosts along the beam direction and that $\cos\theta^* = \tanh y^*$. The sub-process CM energy, $\sqrt{\hat{s}}$, is also the invariant jet-jet mass, M_{JJ}. From the above relations one has

$$\hat{s} \equiv M_{JJ}^2 = x_a x_b s = 4p_T^2 \cosh^2 y^*. \tag{10.21}$$

10.5.2 Single jet inclusive cross-section

For the two-body parton-parton scattering sub-process shown in Fig. 10.11 the cross-section is given by the standard expression

$$d\hat{\sigma} = \frac{1}{32\pi^2\hat{s}}\hat{\sum}|M|^2 \frac{d^3p_c}{E_c}\frac{d^3p_d}{E_d}\delta^4(p_a + p_b - p_c - p_d), \tag{10.22}$$

where $\hat{\sum}|M|^2$ is the final spin summed and initial spin averaged squared matrix element (details given in the appendix at the end of the chapter). Using one of final state momentum integrals to eliminate $\delta^3(\mathbf{p})$ gives

$$d\hat{\sigma} = \frac{1}{16\pi^2\hat{s}}\hat{\sum}|M|^2 \frac{d^3p_c}{E_c}\delta(\hat{s} + \hat{t} + \hat{u}), \tag{10.23}$$

where Eq. 10.19 has been used. Inserting the above into the master equation (10.3) gives an expression for the single-jet inclusive cross-section

$$\frac{Ed^3\sigma}{d^3p} = \frac{1}{16\pi^2 s}\sum_{a,b,c,d}\int_0^1 \frac{dx_a}{x_a}\frac{dx_b}{x_b} f_{a/A}(x_a, \mu^2) f_{b/B}(x_b, \mu^2)$$

$$\times \hat{\sum} |M(ab \to cd)|^2 \frac{1}{1+\delta_{cd}} \delta(\hat{s}+\hat{t}+\hat{u}), \tag{10.24}$$

where E and p are the total energy and momentum of the jet and the sum on the RHS is over all valid quark and gluon two-body processes. The $1/(1+\delta_{cd})$ term accounts for cases that have identical partons in the final state. For comparison with experimental data it is usual to use the transformation given in Eq. 10.2 to get the inclusive jet cross-section in terms of jet E_T and η. Fig. 10.12 shows the inclusive jet E_T spectrum from $\mathrm{p\bar{p}}$ interactions at $\sqrt{s} = 1.8\,\mathrm{TeV}$ as measured by the DØ experiment [DØ 99a]. Jets were defined by an iterative $\Delta\eta, \Delta\phi$ cone algorithm with radius $R = 0.7$. The cross-section is averaged over $|\eta| < 0.5$ and is for $E_T > 60\,\mathrm{GeV}$. The two curves indicate the $\pm 1\sigma$ systematic error band, the largest contribution to which is the energy scale uncertainty. The data are compared with the NLO calculation from JETRAD [Gie94] with scale $\mu = E_T/2$ and CTEQ3M PDFs [Lai95]. There is good agreement over seven orders of magnitude in cross-section. The DØ experiment has also

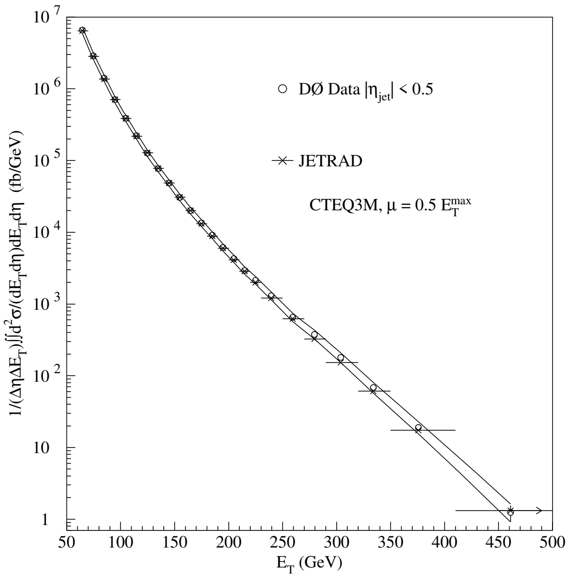

Fig. 10.12 Inclusive jet E_T spectrum in $\mathrm{p\bar{p}}$ collisions at $\sqrt{s} = 1.8\,\mathrm{TeV}$ as measured by DØ [DØ 99a].

measured inclusive jet cross-sections using a k_T algorithm for events with $|\eta| < 0.5$ and $p_T > 60\,\mathrm{GeV}$ [DØ 01]. Reasonable agreement is found with the NLO QCD prediction using JETRAD except at the lowest p_T values. While the measurements using the k_T algorithm are consistent with those using a cone algorithm, the former are consistently above the latter. Some of the difference may be understood in the details of how the hadronisation process affects jet reconstruction by the two algorithms.

How reliable are the NLO calculations? The agreement between data and theory just demonstrated for the inclusive jet cross-section is impressive, but a number of choices have been made. The calculations are performed at NLO using the $\overline{\mathrm{MS}}$ renormalisation scheme and with a 'standard choice' of $\mu = E_T/2$ for the factorisation scale. Ultimately one would like to have the calculations at NNLO, but this is a very large project and although progress is being made it will be some years before it is complete [Glo01]. Within a given renormalisation scheme one way to estimate the effect of higher orders is to vary the renormalisation and factorisation scales – giving the so-called scale dependence. In an extensive investigation Anandam & Soper [Ana00] have studied the simultaneous dependence on scale and renormalisation scheme at NLO. Two parameters are introduced, λ which allows the renormalisation scheme to be changed ($\lambda = 0, 1$ for the $\overline{\mathrm{MS}}$ and DIS schemes respectively) and μ varies the factorisation scale. The renormalisation scale is fixed at $\mu_{UV} = E_T/2$ and CTEQ4 PDFs are used. The changes in the inclusive jet cross-section $d\sigma/dE_T$ are then calculated as μ and λ vary over the ranges $E_T/8 < \mu < 2E_T$ and $-2 < \lambda < 2$. Results for $E_T = 50, 400\,\mathrm{GeV}$ are shown in Fig. 10.13, the contours representing 1% change in $d\sigma/dE_T$. The plots show that $\mu = E_T/2$ is indeed a good choice of factorisation scale, as the dependence on λ is then weak. The authors use these calculations to estimate the overall uncertainty in the NLO calculation as a function of E_T for two choices of parameter change: 'minimum' $[\Delta \log_2(\mu) = \pm 1, \Delta\lambda = \pm 1]$; 'conservative' $[\Delta \log_2(\mu) = \pm 2, \Delta\lambda = \pm 2]$. For the minimum change the errors vary from 3% to 7% as E_T varies from 50 to 400 GeV and for the conservative case the variation is from 9% to 32%.

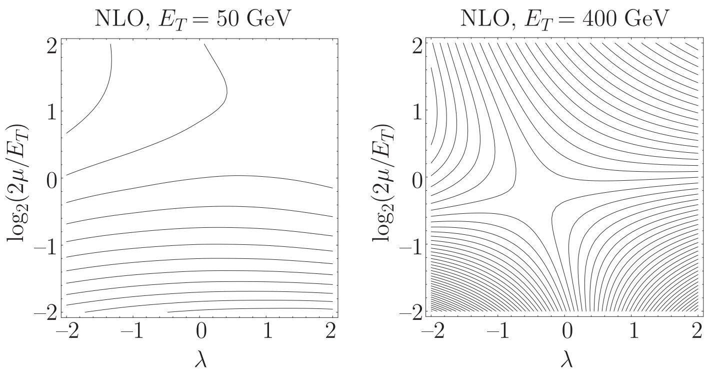

Fig. 10.13 Contour plots showing 1% changes in the inclusive jet cross-section $d\sigma/dE_T$ as the scale (μ) and scheme (λ) parameters are varied. From [Ana00].

10.5.3 Dijet cross-sections

With enough data more information on the hard processes is available from measurement of various dijet cross-sections. Start from the differential form of the hadron-hadron master equation, Eq. 10.3,

$$\frac{d\sigma(AB \to jjX)}{dx_a dx_b d\cos\theta^*} = \sum_{ab} f_{a/A}(x_a, \mu^2) f_{b/B}(x_b, \mu^2) \frac{d\hat{\sigma}_{ab\to cd}}{d\cos\theta^*},$$

where the parton-parton CM scattering angle θ^* is defined in Fig. 10.11(b). In the CM frame Eq. 10.22 for the sub-process cross-section gives

$$\frac{d\hat{\sigma}}{d\cos\theta^*} = \frac{1}{32\pi\hat{s}} \hat{\sum} |M|^2.$$

Inserting this into the previous equation and using the Jacobian $dp_T^2 dy_c dy_d \to \frac{s}{2} dx_a dx_b d\cos\theta^*$, the dijet cross-section is given by

$$\begin{aligned} \frac{d^3\sigma}{dy_c dy_d dp_T^2} &= \frac{1}{16\pi s^2} \sum_{a,b,c,d} \frac{f_{a/A}(x_a, \mu^2)}{x_a} \frac{f_{b/B}(x_b, \mu^2)}{x_b} \\ &\quad \times \hat{\sum} |M(ab \to cd)|^2 \frac{1}{1+\delta_{cd}}. \end{aligned} \tag{10.25}$$

Usually for comparison with experimental data

$$\frac{d^3\sigma}{dy_c dy_d dp_T^2} \to \frac{d^3\sigma}{d\eta_1 d\eta_2 dE_T^2},$$

where E_T is the transverse energy of the leading (highest E_T) jet and $\eta_{1,2}$ are the pseudo-rapidities of the two jets, now taken to represent those of the scattered partons c and d. In terms of the jet variables the initial momentum fractions are given by

$$x_a = \frac{E_T}{\sqrt{s}}(e^{\eta_1} + e^{\eta_2}) \quad x_b = \frac{E_T}{\sqrt{s}}(e^{-\eta_1} + e^{-\eta_2}).$$

The CDF collaboration [CDF01c], Fig 10.14, have used data from 86 pb^{-1} of p$\bar{\text{p}}$ collisions at $\sqrt{s} = 1.8$ TeV to measure the dijet cross-section as a function of the leading jet E_T with $0.1 < |\eta_1| < 0.7$ for four bins of pseudo-rapidity of the second jet in the range $0.1 < |\eta_2| < 3.0$. Jets are defined using a cone algorithm in $\Delta\eta$, $\Delta\phi$ with radius 0.7. The NLO QCD calculation describes both the E_T and rapidity dependence of the data.

Apart from establishing the underlying quark and gluon dynamics, dijet measurements give sensitive measures for new phenomena. At the highest E_T, the single inclusive jet cross-section measured by the CDF experiment showed a small excess over the standard NLO QCD prediction

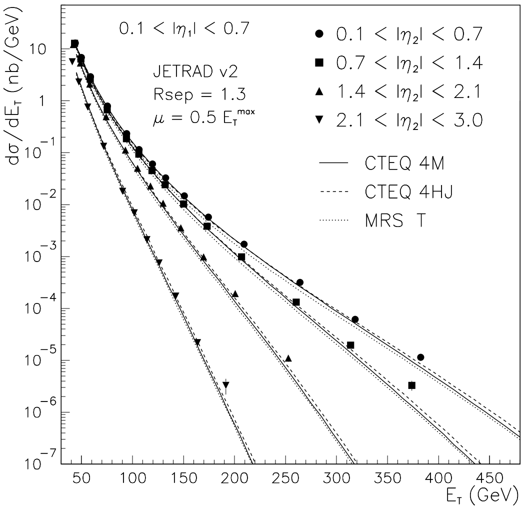

Fig. 10.14 Dijet $d^3\sigma/d\eta_1 d\eta_2 dE_T$ as measured by CDF [CDF01c] is plotted for four bins of 2nd jet pseudo-rapidity η_2 as a function of the leading jet E_T with $0.1 < |\eta_1| < 0.7$. The QCD predictions are from JETRAD with three choices of PDFs.

[CDF96,CDF01a].[4] The CDF excess may be studied in more detail by using dijet data. Fig. 10.15 shows the comparison of the dijet data and NLO QCD in more detail. The excess of events over the standard model prediction is clearly seen in all rapidity bins at the highest E_T values. The shaded band shows the correlated systematic errors, which are dominated by the energy scale uncertainty. The best description of the excess is given by the CTEQ4HJ PDFs, in which the gluon density was enhanced at large x specifically to accommodate the excess. More details are given in [Lai96,CDF01a].

Rather than characterising the dijet events in terms of rapidities, another useful choice of variables is the jet-jet invariant mass M_{JJ} and CM scattering angle θ^*. Either by a change of variables from Eq. 10.25 or by analogy with the D-Y cross-section, Eq. 10.7, the double differential cross-section takes the form

$$\frac{d^2\sigma}{dM_{JJ}^2 d\cos\theta^*} = \frac{1}{32\pi M_{JJ}^2} \sum_{a,b,c,d} \int_0^1 dx_a dx_b f_{a/A}(x_a,\mu^2) f_{b/B}(x_b,\mu^2)$$

[4]The excess was not seen by the DØ experiment, but given the quite large systematic errors at large E_T, the data from the two experiments are not inconsistent.

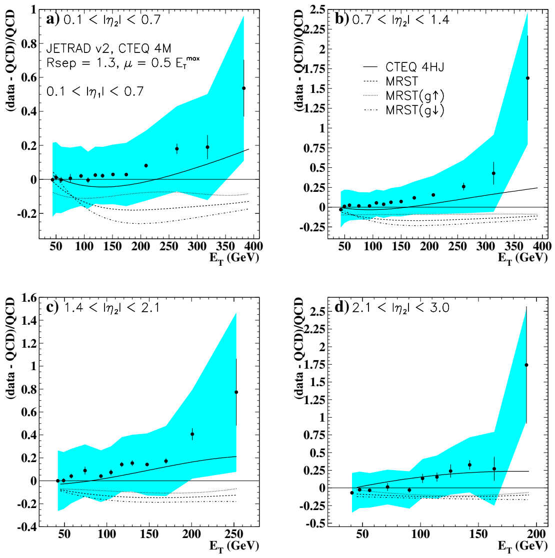

Fig. 10.15 The dijet data shown in the previous figure are plotted as (Data-QCD)/QCD are plotted using the same binning. The reference QCD prediction is from JETRAD with CTEQ4M PDFs and predictions using different PDFs are shown as curves. The error bars show statistical errors and the shaded band the correlated systematic errors.

$$\times \delta(x_a x_b s - M_{JJ}^2) \hat{\sum} |M(ab \to cd)|^2 \frac{1}{1+\delta_{cd}}, \quad (10.26)$$

where $\cos\theta^* = \tanh(|\Delta\eta|/2)$ and $M_{JJ}^2 = 2E_1^T E_2^T(\cosh\Delta\eta - \cos\Delta\phi)$. Massless jets are assumed with $E_{1,2}^T$ the jet transverse energies. $\Delta\eta = \eta_1 - \eta_2$ and $\Delta\phi$, the differences in jet pseudo-rapidities and azimuthal angles respectively.

The angular dependence of the squared matrix elements given in the appendix may be expressed conveniently in terms of $\chi = \dfrac{\hat{u}}{\hat{t}} = \dfrac{(1+\cos\theta^*)}{(1-\cos\theta^*)}$. For example the angular factor for $qq' \to qq'$ is $\dfrac{4}{9}(2\chi^2 + 2\chi + 1)$. The dominant terms for dijet production are $gg \to gg$, $gq \to gq$ and for $\mathrm{p\bar{p}}$, $q\bar{q} \to q\bar{q}$ (see problem 6). All of these processes involve gluon exchange in the $\hat{t}$-channel, giving rise to the characteristic $\sin^{-4}(\theta^*/2)$ angular behaviour at small θ^*. It is often convenient to remove this rapid angular variation by plotting $\dfrac{d\sigma}{d\chi}$ rather than $\dfrac{d\sigma}{d\cos\theta^*}$, since $\dfrac{d\sigma}{d\chi} \sim$ constant for small angles (large χ). For two-jet final states, there is usually no way of identifying quark or gluon jets so the cross-sections are symmetrised over

$\hat{t}$ and $\hat{u}$ exchanges, which means that the data are presented in terms of $\chi' = \dfrac{(1 + |\cos\theta^*|)}{(1 - |\cos\theta^*|)}$.

The dijet invariant mass and angular distributions also give sensitive tests of standard QCD and competitive limits on new phenomena such as composite quarks and new contact interactions. Fig. 10.16 shows $d^3\sigma/dM_{JJ}d\eta_1 d\eta_2$

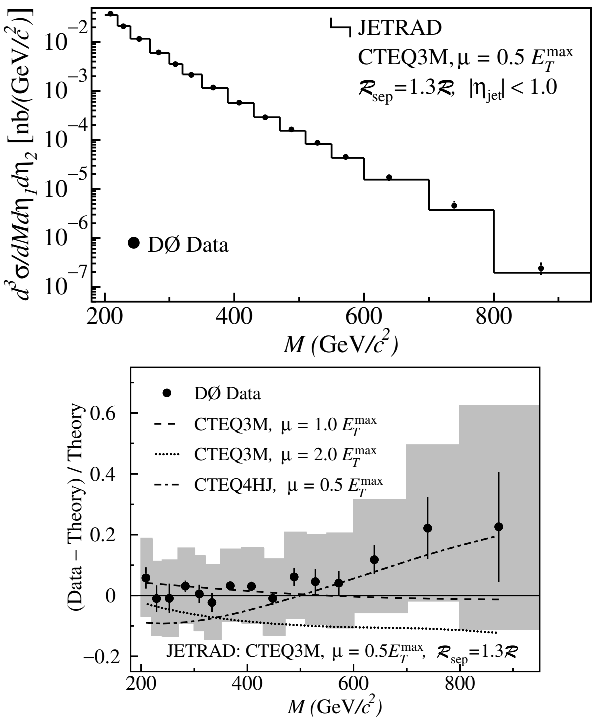

Fig. 10.16 Dijet invariant mass distribution as measured by the DØ experiment in $p\bar{p}$ at $\sqrt{s} = 1.8$ TeV [DØ 99b]. The upper plot shows $d^3\sigma/dM_{JJ}d\eta_1 d\eta_2$ with $|\eta_i| < 1.0$; the lower plot shows (Data-QCD)/QCD, with a number of alternative choices of PDFs and scales. The standard QCD prediction is from JETRAD with CTEQ3M PDFs and renormalisation factorisation scales $\mu = 0.5E_T^{max}$.

with $|\eta_i| < 1.0$ as measured by DØ in $p\bar{p}$ collisions at $\sqrt{s} = 1.8$ TeV [DØ 99b]. The upper plot shows the jet mass spectrum compared to the NLO QCD prediction from JETRAD with CTEQ3M PDFs, the agreement between theory and data is good over the whole range of M_{JJ} shown from 300 to 850 GeV. The lower plot shows (Data-QCD)/QCD with a number of alternative choices of PDFs and scales. The shaded region shows the

$\pm 1\sigma$ systematic uncertainty on the data, the largest contribution comes from the jet energy scale uncertainty which rises from 7% at 200 GeV to around 30% at the highest energies. A change of scale from $\mu = 0.5E_T^{max}$ to $\mu = 2.0E_T^{max}$ produces a roughly 10% change in the prediction independent of jet mass.

As discussed above, $d\sigma/d\chi'$ should be fairly flat as a function of χ' if gluon exchange diagrams dominate the hard parton-parton interaction. Deviations from this behaviour could signal new effects. The dijet angular dis-

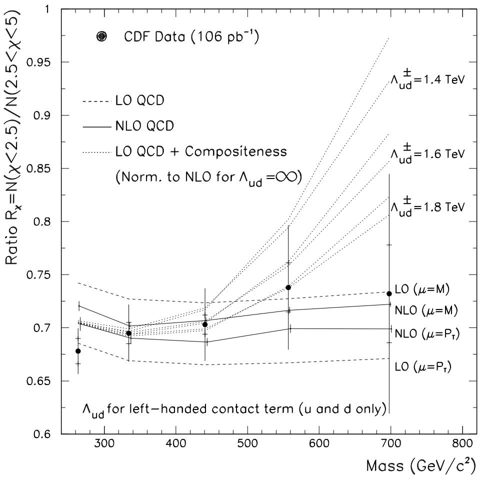

Fig. 10.17 Dijet angular ratio R_χ as a function of dijet mass, M_{JJ}. $R_\chi = N(\chi' < 2.5)/N(2.5 < \chi' < 5.0)$ where χ' is defined in the text. From the CDF experiment [CDF96].

tribution $d\sigma/d\chi'$ is indeed found to be flat in the range $2 < \chi' < 5$ rising by about 30% between 1 and 2. An isotropic angular distribution (in θ^*) would give a very rapidly rising distribution at small χ' values. The ratio of events $R_\chi = N(\chi' < 2.5)/N(2.5 < \chi' < 5.0)$ is therefore a useful number to quantify the shape of the dijet angular distribution. Fig. 10.17 shows R_χ as a function of M_{JJ} as measured by the CDF experiment from dijet events with $E_T > 50$ GeV, $|\eta_{1,2}| < 2$ and $\chi' < 5$. The ratio shows little variation with M_{JJ} and the level is reasonably well described by NLO QCD with either $\mu = M_{JJ}$ or $\mu = p_T$ as choice of renormalisation scale. The other curves refer to models with additional contact interactions which will be discussed in Chap.12.

The overall conclusion on inclusive and dijet physics from p$\bar{\text{p}}$ interactions at high energies (particularly the Tevatron data) is that NLO QCD gives a very good description. Apart from direct support for the QCD enhanced parton model and the dominance of gluon exchange diagrams, the jet data can provide useful constraints on parton momentum densities. The limitations come primarily from the large systematic uncertainty in the jet energy scale at large E_T and to a lesser extent from the renormalisation and factorisation scale uncertainties.

10.6 Isolated photon production

The production of isolated[5], high E_T, photons in hadron-hadron collisions offers, in principle, a clean approach to parton dynamics. The leading order processes are $\mathrm{q}\bar{\mathrm{q}} \to \gamma^* g$ (annihilation) and $\mathrm{q}g \to \gamma^* \mathrm{q}$ (QCD Compton), diagrams for which are shown in Fig. 10.18(a),(b). Expressions for the squared matrix elements are given in the appendix. Similar diagrams are also relevant for the production of high E_T vector bosons.

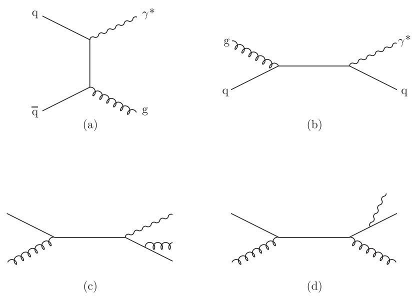

Fig. 10.18 Diagrams for high E_T isolated photon (or vector boson) production: (a) annihilation; (b) QCD Compton; (c),(d) NLO diagrams.

The advantages of direct photons over high E_T jets are: no complications from parton fragmentation and jet algorithms; generally much better energy resolution for EM calorimeters. The disadvantages are: the smaller rate, $O(\alpha\alpha_S)$ rather than $O(\alpha_S^2)$; the potentially large background from π^0 and η decays; the problems of intrinsic k_T and soft gluon radiation. Using Eq. 10.20, for photons produced centrally ($y \approx 0$), the initial state partons are probed at $x \approx 2E_T^\gamma/\sqrt{s}$. Generally for hadron-hadron scattering with moderate E_T^γ the Compton process dominates, which implies a sensitivity to the gluon density. At very large E_T^γ in $\mathrm{p}\bar{\mathrm{p}}$ the annihilation diagram is most important. In principle the prompt photon process allows study of the gluon density at larger x values than those accessible through scaling violations in DIS. QCD calculations have been performed to NLO. Fig. 10.18(c),(d) shows a couple of NLO diagrams and (d) – with

[5] Also known as direct or prompt photon production.

a photon radiated from the final quark line – requires the introduction of a non-perturbative photon fragmentation function, D_q^γ, for its complete evaluation. D_q^γ obeys an evolution equation analogous to the DGLAP equations and is similar to hadron fragmentation functions familiar from e^+e^- applications (see e.g. [Ell96,Ch.6] for details). In a similar way to the renormalisation of parton densities, D_q^γ absorbs the collinear singularity which arises when the momenta of the quark and photon are parallel. There is an important difference due to the point-like coupling of the photon which gives an inhomogeneous but calculable addition to the evolution equations. The effect of this addition is to enhance the numerical importance of the contribution of D_q^γ in the NLO corrections.

For p$\bar{\text{p}}$ at Tevatron energies of $\sqrt{s} = 1.8\,\text{TeV}$, direct photon production has been measured to E_T^γ of well over 100 GeV. Fig. 10.19 shows the cross-section $d^2\sigma/dE_T^\gamma d\eta$ for two ranges of pseudo-rapidity, central $|\eta| < 0.9$ and forward $1.6 < |\eta| < 2.5$. In both cases the NLO calculation, with a scale E_T^{max} (the larger of the photon or leading jet E_T) and CTEQ4M PDFs, agrees well with the data for $E_T^\gamma > 40\,\text{GeV}$. At lower E_T^γ the measured data points lie above the NLO calculation. A similar excess of data over

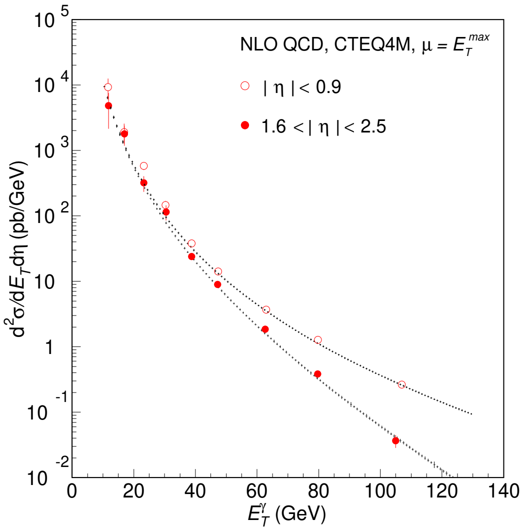

Fig. 10.19 The cross-section for isolated photon production in two rapidity ranges as measured by the DØ experiment [DØ 00b]. The curves show an NLO QCD calculation using CTEQ4M PDFs..

the NLO calculation has been seen at lower energy pp and pA direct photon fixed-target experiments. The reason for the excess is not completely clear and various suggestions have been put forward:

- an incorrect experimental determination of the background from the $\gamma\gamma$ decays of π^0 and η;
- intrinsic parton k_T;
- soft gluon emissions.

Some authors have attempted to include the effect of intrinsic k_T by allowing a Gaussian smearing with an additional fit parameter. The mean value $\langle k_T \rangle$ has been estimated from a number of processes, fixed target D-Y muon pair production from pion and proton beams, direct gamma production from pp($\bar{\text{p}}$) interactions at both fixed target and collider energies and direct gamma production in high energy γp interactions at HERA. It is found that the measured $\langle k_T \rangle$ increases with CM energy W, as shown in Fig. 10.20 from Chekanov *et al.* [ZEU01b]. The introduction of intrinsic

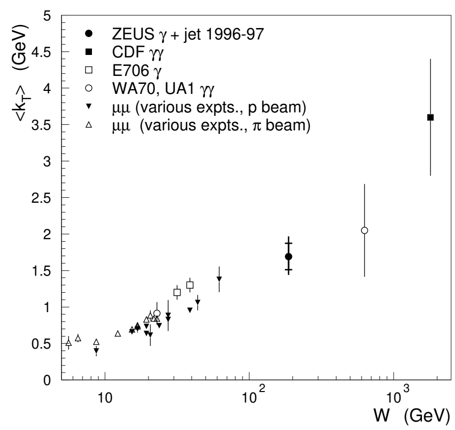

Fig. 10.20 Mean intrinsic parton transverse momentum $\langle k_T \rangle$ from D-Y and direct photon processes as a function of CM energy W. Summary plot from [ZEU01].

partonic k_T does improve the description of prompt photon data at low E_T^γ and allowing $\langle k_T \rangle$ to increase with W does provide a reasonably consistent picture across a wide range of energies and experiments [Lae00]. However, at the relatively low values of E_T^γ where the discrepancy between data and theory (without explicit addition of intrinsic k_T) is worse, other factors may be as important and are not yet included in the calculations.

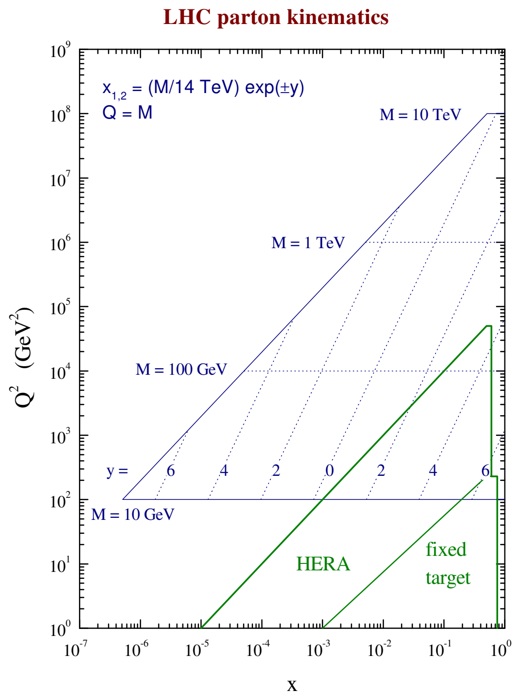

Fig. 10.21 The LHC kinematic plane for producing a state of mass M and rapidity y in terms of DIS variables x, Q^2. The kinematic regions covered by HERA and the fixed target experiments are shown for comparison. Figure courtesy of W J Stirling.

Also it is possible that not all prompt photon experiments give completely consistent results. More details are given in the critical study by Aurenche *et al.* [Aur99]. Work is underway to include the effect of soft gluon emissions by resummation techniques and there is some optimism that this may lead to a resolution of the problem [Lae00,Ste00]. Until this problem is understood, the use of low E_T^γ direct photon data as a constraint on the gluon density is suspect. As an alternative the global fitting teams are using high E_T jet data from the Tevatron.

10.7 Hadronic DIS at the LHC

The methods described so far in this chapter will be essential for calculating many standard model and beyond the standard model processes at the LHC. Accurate prediction of the former will often be a prerequisite to claims of a discovery of the latter. To produce a state of mass M with rapidity y requires[6]

$$x_a = \frac{M}{\sqrt{s}} e^{+y}, \quad x_b = \frac{M}{\sqrt{s}} e^{-y} \tag{10.27}$$

where $\sqrt{s}$ is the pp CM energy (14 TeV for the LHC) and x_a, x_b are the fractions of the incident beam momenta involved in the hard collision. For states with masses less than 500 GeV, this means that at least one of the interacting partons will have an $x < 10^{-3}$ and thus be well into the $q\bar{q}$ sea region. This is shown graphically in Fig. 10.21 which shows the LHC kinematic plane in terms of DIS variables x, Q^2 with the HERA and fixed target regions for comparison. It can be seen from the figure that the HERA x range is well matched to the regions required for 'low mass' LHC physics, but the parton densities will have to be evolved over two or three orders of magnitude in Q^2. The precise determination of the $q\bar{q}$ sea and gluon densities from global analyses using HERA, Tevatron and fixed target data will be very important.

10.7.1 Jet Physics at the LHC

With an increase in CM energy and luminosity of an order of magnitude between the Tevatron and the LHC, jet physics will be still be systematics limited at E_T scales in excess of 3 TeV. At 'low' luminosity ($10^{33}\,\mathrm{cm^{-2}s^{-1}}$), the integrated luminosity for one year is estimated to be $10\,\mathrm{fb^{-1}}$, at the full design luminosity the figure is a factor 10 larger. Fig. 10.22 shows the inclusive jet E_T distributions at $\sqrt{s} = 14$ TeV for three bins of pseudo-rapidity. The data points are from a study for the ATLAS detector (reported by [Sta01]) and correspond to an integrated luminosity of $30\,\mathrm{fb^{-1}}$. There are roughly 0.4M events with $E_T > 1$ TeV and to match the statistical precision, the ATLAS collaboration are hoping to control systematics to 1% at 1 TeV and about 10% at 3 TeV. Another study for ATLAS (also reported by [Sta01]) looked at $300\,\mathrm{fb^{-1}}$ of dijet daa with a threshold jet $E_T > 180$ GeV. The events span a region in the (x, Q^2) plane corresponding to $4 \times 10^4 < Q^2 < 4 \times 10^7\,\mathrm{GeV^2}$ and $0.002 < x < 0.6$. As discussed in Sec. 10.5.3, the dijet angular distribution is a sensitive tool for discovering new physics and Fig. 10.23 shows the relative deviation of the χ distribution calculated at NLO for composite quarks compared to the point-like standard model. $(N_{\mathrm{composite}} - N_{\mathrm{SM}})/N_{\mathrm{SM}}$ is plotted for three values of compositeness scale $20, 30, 40$ TeV. With these data, a limit of the order of 40 TeV at 95% CL could be set on the scale of quark substructure.

10.7.2 Collider Luminosity

Apart from needing to know the parton densities accurately for the prediction of standard model rates, there is also the vital question of how the collider luminosity will be determined. The traditional approach to luminosity determination has been to measure a process with high rate and

[6] The kinematics are those of the D-Y process discussed in sec. 10.3.1.

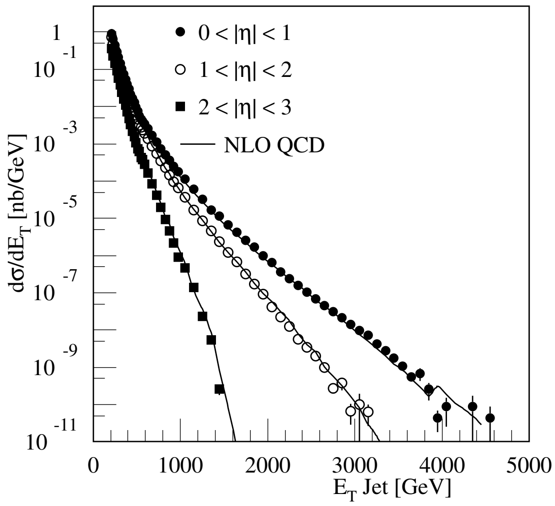

Fig. 10.22 Jet E_T at the LHC for three bins of η from a study for the ATLAS experiment [Sta01].

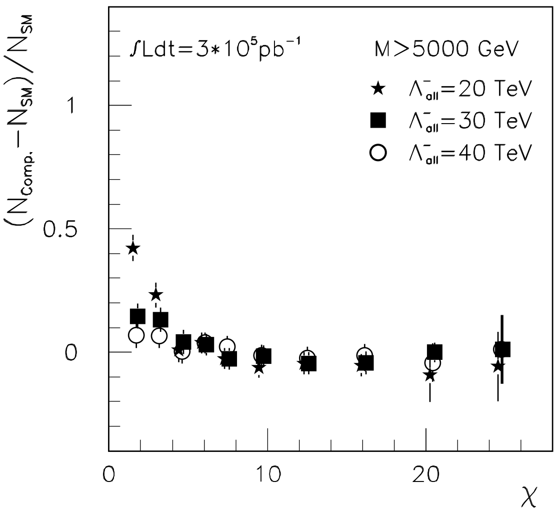

Fig. 10.23 LHC dijet χ distribution, deviations from the SM expectation for three values of quark compositeness scales. From [Sta01].

accurately known cross-section. In colliders with an electron beam (e^+e^-, ep) this means a QED process. In p$\bar{\text{p}}$ or pp scattering QED processes tend to be too small or too difficult to measure in a collider geometry, so an alternative is to measure the total pp rate N_{tot} and the forward elastic rate N_{el}. Using the optical theorem and assuming that the real part of the elastic amplitude is small,

$$\left.\frac{d\sigma_{el}}{dt}\right|_{t=0} \approx \frac{\sigma_{tot}^2}{16\pi}.$$

Assuming that acceptances can be determined accurately, one has $N_{tot} = L\sigma_{tot}$ and $N_{el} = L\sigma_{tot}^2$, from which both the luminosity L and σ_{tot} can be determined. Apart from the very high rates at small angles to the beam line, one has the problem of extrapolating the elastic cross-section or rate from the measured region at small t to $t = 0$. These considerations have led a number of authors to consider W and Z production as an alternative luminosity monitor [Dit97, Kho01, Gie01b].

The leptonic decay modes of the W and Z give clean experimental signatures. The parton sub-processes are known to NNLO and, as has been discussed in Chap.4, the DGLAP coefficient functions are also known to NNLO and there are reasonable approximations to the full NNLO splitting functions. The MRST team have investigated the predictions for $\sigma \cdot B$ for W and Z production at the Tevatron and LHC at different orders but with the same input data determining the parton densities. The results are shown in Fig. 10.24. The data points are recent measurements from the DØ and CDF Tevatron experiments. The large jump from LO to NLO is the large $O(\alpha_S)$ correction to the parton model D-Y prediction that was discussed in Sec. 10.3.2. The convergence between NLO and the NNLO estimate is good. However it is not enough to consider only one set of PDFs. No estimate has been made of PDF errors from the statistical and systematic errors of the input data and from other assumptions used in the global fitting procedure. This is a topical and rapidly developing subject, which is addressed in more detail in Chap.10. Khoze *et al.* [Kho01] have made an attempt to estimate some of the uncertainties by using a number of different sets of PDFs produced by the MRST team. The results for $\sigma \cdot B$ are shown in Fig. 10.25. From this study they estimate better than $\pm 5\%$ uncertainty at the LHC. One of the largest factors contributing to the uncertainty is the normalisation of the HERA F_2 measurements – around 2.5%.

Giele & Keller [Gie01b] have also considered the problem of estimating the accuracy of the $\sigma \cdot B$ predictions for W and Z production. They have used the PDFs from an extensive study by Giele *et al.* [Gie01a], in which the choice of input data sets to the global fit is varied. They also attempt to quantify the statistical consistency of the input data. Depending on the choice, the one sigma variation in the predictions for $\sigma \cdot B$ varies between 1 and 8%. They also make another important observation on the advantages of using W and Z production. The ratio of W to Z production (R_{DY} defined

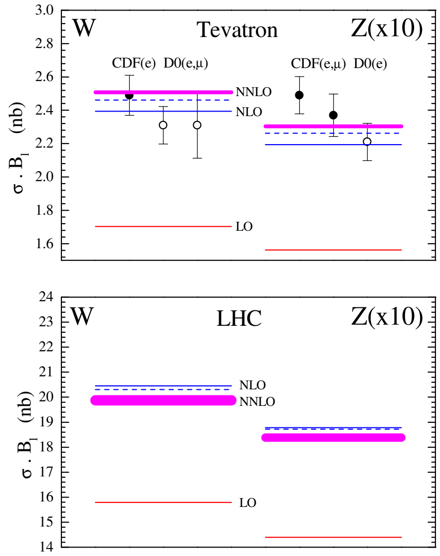

Fig. 10.24 Predictions for $\sigma \cdot B$ for W and Z production at the Tevatron and LHC colliders as a function of the order of calculation with fixed parton input. The band and dashed line indicate the uncertainty in present NNLO calculations. From [Kho01].

in Eq. 10.18) is independent of the collider luminosity and thus gives an observable that may be used to check how well a particular PDF set actually describes W and Z production. Using PDFs from their favoured set of input data (H1-94+BCDMS+E665) they estimate a RunIb luminosity for DØ of $80.3^{+2.3}_{-2.8}\,\mathrm{pb}^{-1}$ to be compared with the quoted DØ number of $84.5 \pm 3.6\,\mathrm{pb}^{-1}$.

10.7.3 Parton-parton luminosity

Dittmar *et al.* [Dit97] make the point that for many hard processes at the LHC it is actually the parton-parton luminosity[7] that is needed, rather than that for the complete pp interaction. For W and Z production the basic processes are

$$u\bar{d} \to W^+ \to \ell^+\nu; \quad d\bar{u} \to W^- \to \ell^-\nu; \quad u\bar{u}(d\bar{d}) \to Z^0 \to \ell^+\ell^-.$$

So by measuring the rapidity distribution (through that of the decay $\ell^\pm$) one may constrain the luminosity of the u and d quarks and anti-quarks.

[7]The concept of parton-parton luminosity is intuitively obvious but more details and examples are given in [Ell96,Chap.7].

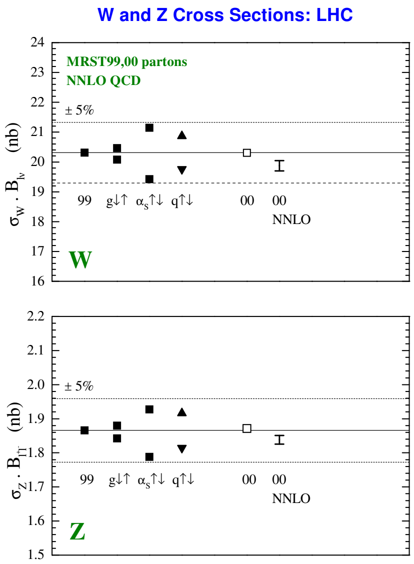

Fig. 10.25 Predictions for $\sigma \cdot B$ for W and Z production at the Tevatron and LHC colliders by the MRST team using a number of different PDFs. The filled points use the NLO PDFs of MRST99, the open points are NLO and NNLO calculations using MRST00 PDFs. The differences in the MRST99 set are from different assumptions about the input parton densities and α_S. From [Kho01].

At the LHC one is dealing with pp collisions rather than the p$\bar{\text{p}}$ process already discussed in Sec. 10.4.3 and the CM energy is an order of magnitude larger. For small y values $x_a \approx x_b \sim 10^{-3}$, both well into the region of the q$\bar{\text{q}}$ sea. For medium to large rapidities, x_a will be in the valence region with $x_b << 10^{-3}$. So only in the latter case will there be a substantial difference in W$^\pm$ rates, with W^+ larger because of the two u-valence quarks in the proton. For an actual observable process, one must fold in the decay kinematics (also discussed in Sec. 10.4.3). The event distributions in rapidity for W$^\pm$ production and decay corresponding to $100\,\text{pb}^{-1}$ of pp interactions at the LHC energy of $\sqrt{s} = 14\,\text{TeV}$ are shown in Fig. 10.26. The idea is that by measuring the rate of decay leptons in small fixed intervals Δy_i one will eventually be able to constrain the corresponding q and $\bar{\text{q}}$ densities over an x range of something like $(5 \times 10^{-4}, 0.1)$ at a $Q^2 \approx 10^4\,\text{GeV}^2$. Statistical precision will not be a problem. Other processes that are initiated by the same q$\bar{\text{q}}'$ combinations may now be calculated accurately, without the uncertainty from the extrapolation of parton densities from lower energies. The paper contains more detail on experimental problems in the context of a realistic model of an LHC detector, concluding that of the order of 1% accuracy in the measurement of the lepton pseudo-rapidity distribu-

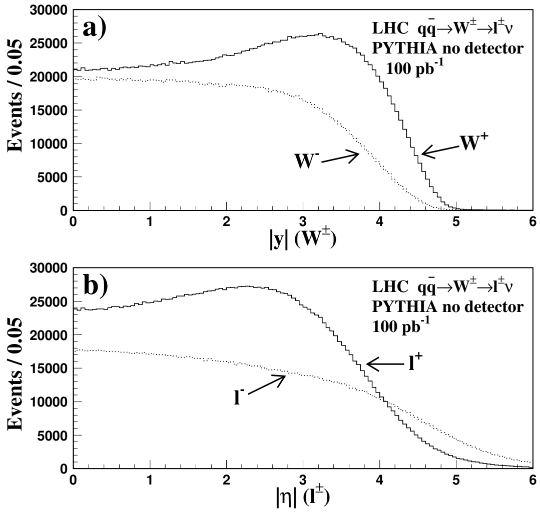

Fig. 10.26 Predictions for the $W^\pm$ asymmetry and the $W^\pm \to \ell^\pm \nu$ decay asymmetry at the LHC using MRSA PDFs. From [Dit97].

tion could be achieved. The authors also consider, but in less detail, how the same ideas might be extended to constraining the gluon momentum density using direct processes of the sort discussed in Sec. 10.6.

10.8 Summary

This chapter has shown the power of the QCD enhanced parton model, which relies on pQCD calculations at NLO and the universality of parton momentum density functions. At least at leading twist, one has a well defined framework, supported by proofs of factorisation, in which to perform the calculations. The early success of the parton model predictions of scaling in the Drell-Yan process helped consolidate the parton approach. The later QCD calculation of corrections to D-Y gave impressive agreement between data and theory in both shape and normalisation. The D-Y process is central to understanding how to use the QCD enhanced parton model in hadron-hadron processes, because of its simplicity and its importance as a discovery channel for high mass states such as the W and Z. The calculation of these processes is described briefly. More extensive discussion is devoted to the important topic of jet production in high energy $p\bar{p}$ and pp colliders. Generally the overall agreement at NLO between jet data and theory is good. There is a need for NNLO calculations to reduce the scale uncertainties at the highest E_T and there is a problem with a complete understanding of soft gluon emission effects at low E_T. The latter affects, in particular, the reliability of predictions for direct photon production. Despite these problems data from hadron-hadron DIS are an important and complementary ingredient to global fits to determine hadron PDFs. Finally the chapter ends with a brief discussion of the importance of these topics for physics at the LHC.

10.9 Problems

1. Calculate the Jacobian of the transformation from Cartesian to rapidity momentum components given in Eq. 10.2.

2. Check the kinematics of D-Y lepton pair production at the start of Sec. 10.3.1 and, in particular, Eqs 10.4, 10.5.

3. Consider the Drell-Yan process for $\pi - \mathrm{C}$ scattering. The carbon nucleus has an equal number of protons and neutrons and thus also an equal number of u and d quarks. Using Eq. 10.10 with $y \approx 0$, show that in the quark-parton model, the ratio

$$r = \frac{\sigma(\pi^+ \mathrm{C} \to \mu^+\mu^- X)}{\sigma(\pi^- \mathrm{C} \to \mu^+\mu^- X)}$$

equals 1/4 when τ approaches 1. What value does r have for small τ?

4. Derive the expression given in Eq. 10.15 for $\hat{\sigma}(\mathrm{q}_i\bar{\mathrm{q}}_i \to Z \to \ell^+\ell^-)$ using the narrow resonance approximation.

5. Check the parton-parton kinematics of Sec. 10.5.1 in the hadron-hadron and parton-parton frames. Show that the Jacobian $\dfrac{\partial(x_a, x_b, \cos\theta^*)}{\partial(y_c, y_d, p_T^2)}$ has the value $2/s$.

6. Estimate the relative sizes of the parton-parton squared matrix elements of the appendix as follows. Express each in terms of the variable χ (defined in Sec. 10.5.3), for example the gg term is

$$\frac{9}{2}\left(3 - \frac{\chi}{(\chi+1)^2} + \chi + \chi^2 + \frac{1}{\chi^2} + \frac{1}{\chi}\right).$$

Then evaluate each term at $\chi = 1$ ($\theta^* = 90°$).

7. Use Eq. 10.25 and the squared matrix element given in the appendix for gluon-gluon scattering to estimate the dijet cross-section at central rapidities and jet $E_T = 200\,\mathrm{GeV}$ at $\sqrt{s} = 1.8\,\mathrm{TeV}$. Repeat the calculation for the LHC energy of $\sqrt{s} = 14\,\mathrm{TeV}$. Explain why the LHC cross-section is larger.
[Parton densities may be found at www-spires.dur.ac.uk/HEPDATA/.]

10.10 Appendix: $\sum|M|^2$ for tree-level sub-processes

Process	$\hat{\sum}\|M\|^2/(4\pi\alpha_S)^2$	Fig. 10.27
$qq' \to qq'$	$\frac{4}{9}\frac{\hat{s}^2+\hat{u}^2}{\hat{t}^2}$	a
$q\bar{q}' \to q\bar{q}'$	$\frac{4}{9}\frac{\hat{s}^2+\hat{u}^2}{\hat{t}^2}$	a
$qq \to qq$	$\frac{4}{9}\left(\frac{\hat{s}^2+\hat{u}^2}{\hat{t}^2}+\frac{\hat{s}^2+\hat{t}^2}{\hat{u}^2}\right)-\frac{8}{27}\frac{\hat{s}^2}{\hat{u}\hat{t}}$	a, b
$q\bar{q} \to q'\bar{q}'$	$\frac{4}{9}\frac{\hat{t}^2+\hat{u}^2}{\hat{s}^2}$	c
$q\bar{q} \to q\bar{q}$	$\frac{4}{9}\left(\frac{\hat{s}^2+\hat{u}^2}{\hat{t}^2}+\frac{\hat{t}^2+\hat{u}^2}{\hat{s}^2}\right)-\frac{8}{27}\frac{\hat{u}^2}{\hat{s}\hat{t}}$	a, c
$q\bar{q} \to gg$	$\frac{32}{27}\frac{\hat{t}^2+\hat{u}^2}{\hat{t}\hat{u}}-\frac{8}{3}\frac{\hat{t}^2+\hat{u}^2}{\hat{s}^2}$	d, e, f
$gg \to q\bar{q}$	$\frac{1}{6}\frac{\hat{t}^2+\hat{u}^2}{\hat{t}\hat{u}}-\frac{8}{3}\frac{\hat{t}^2+\hat{u}^2}{\hat{s}^2}$	d, e, f reversed
$gq \to gq$	$-\frac{4}{9}\frac{\hat{s}^2+\hat{u}^2}{\hat{s}\hat{u}}+\frac{\hat{s}^2+\hat{u}^2}{\hat{t}^2}$	g, h, i
$gg \to gg$	$\frac{9}{2}\left(3-\frac{\hat{t}\hat{u}}{\hat{s}^2}-\frac{\hat{s}\hat{u}}{\hat{t}^2}-\frac{\hat{t}\hat{s}}{\hat{u}^2}\right)$	j, k, l
	$\hat{\sum}\|M\|^2/(16\pi^2\alpha_S\alpha e_q^2)$	Fig. 10.18
$q\bar{q} \to \gamma^* g$	$\frac{8}{9}\frac{\hat{t}^2+\hat{u}^2+2\hat{s}(\hat{s}+\hat{t}+\hat{u})}{\hat{t}\hat{u}}$	a
$qg \to \gamma^* q$	$-\frac{1}{3}\frac{\hat{s}^2+\hat{u}^2+2\hat{t}(\hat{s}+\hat{t}+\hat{u})}{\hat{s}\hat{u}}$	b

$\sum|M|^2$ is summed over final state and averaged over the initial state spins and colours. The Mandelstam variables for the sub-processes, $\hat{s}, \hat{t}, \hat{u}$, are defined at the start of Sec. 10.5.1. The original calculations are to be found in [Com77, Owe78, Duk82] and a useful summary together with plots of angular dependences are given by [Tym92].

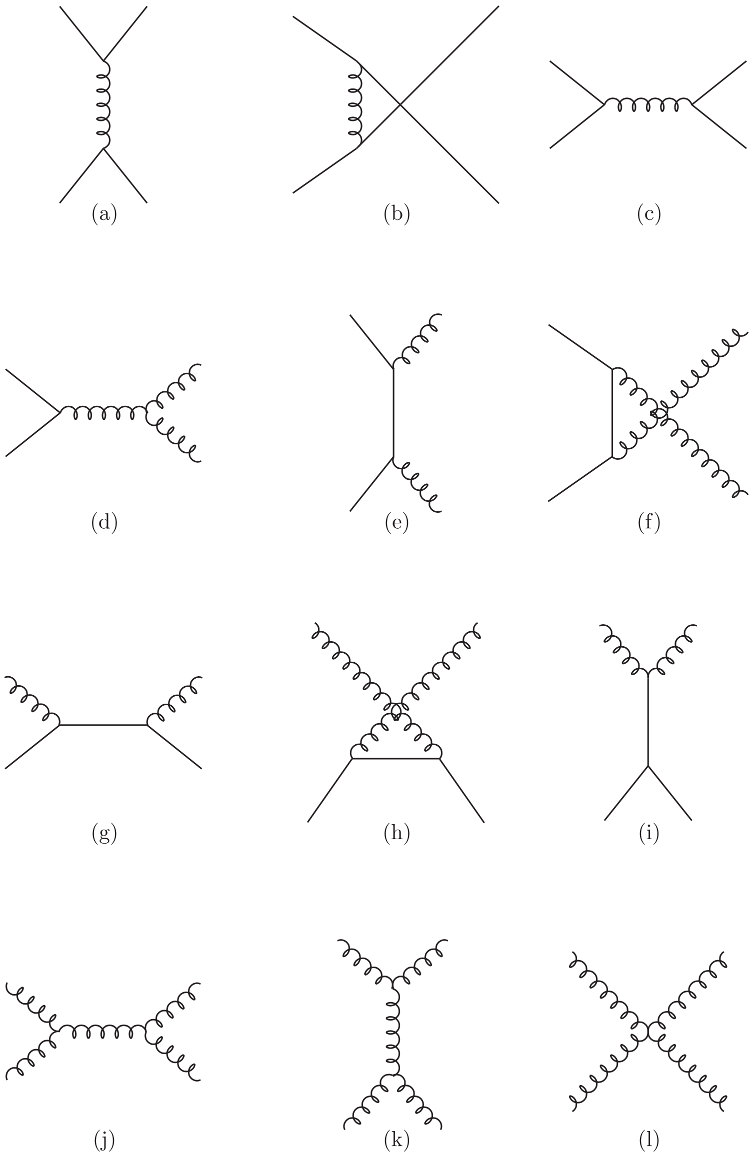

Fig. 10.27 Leading order QCD diagrams for quark and gluon scattering sub-processes as indicated in the table.

11

Polarised DIS and nucleon spin

Brief account of the formalism and definition of polarised PDFs for virtual photon exchange. Outline of the SLAC, SMC and HERMES experiments and data. The enigma of what is carrying the nucleon's spin. DGLAP evolution for polarised PDFs. Summary of NLO fits - lack of knowledge of gluon - problem of extrapolation to small x. Sum rules. Semi-inclusive measurements. Prospects for future experiments, including an outline of the formalism needed for a fully polarised HERA ep collider (*well maybe!*).

12

Beyond the Standard Model

Start with the SM. Separate uncertainties on EW parameter and pdf extraction. Accuracy of cross-section predictions at high Q^2 and large x. Discussion of eq contact interactions and input from $e^+e^- \to$ hadrons, Tevatron, Drell Yan and atomic parity violation experiments - how they affect the cross-sections. Ditto leptoquarks. Sensitivity to TeV scale extra space-time dimensions...

13
Appendices

13.1 Appendix A: Dirac equation and some other conventions

The conventions followed here are those of many recent books (Halzen & Martin [Hal84], Aitchison & Hey [Ait89], Renton [Ren90]).

Units

Throughout most of this book 'natural units' with $\hbar = c = 1$ are used. This means that energies, momenta and masses have the same units and dimensions of $[\text{length}]^{-1}$. The conversation factor to 'real' units is then $\hbar c = 0.197\,\text{GeV fm}$ or $(\hbar c)^2 = 0.389\,\text{Gev}^2\,\text{mb}$.
The electromagnetic fine structure constant is $\alpha \equiv \frac{e^2}{4\pi\epsilon_0 \hbar c} = \frac{e^2}{4\pi} = \frac{1}{137}$.

Lorentz 4-vectors and metric

The basic (contravariant) space-time and energy-momentum 4-vectors are

$$x^\mu = (t, \mathbf{x}) \quad p^\mu = (E, \mathbf{p}) \qquad \text{with scalar product}$$

$$p \cdot x = p^\mu g_{\mu\nu} x^\nu = Et - \mathbf{p}\cdot\mathbf{x}, \quad \text{where} \quad g_{\mu\nu} = \begin{pmatrix} 1 & 0 & 0 & 0 \\ 0 & -1 & 0 & 0 \\ 0 & 0 & -1 & 0 \\ 0 & 0 & 0 & -1 \end{pmatrix}$$

is the metric tensor. The covariant 4-vector is $p_\mu = g_{\mu\nu} p^\nu$ so that a scalar product may also be written $p^\mu p_\mu = E^2 - \mathbf{p}^2 = m^2$.

Derivates, note the signs!

$$\partial^\mu = \frac{\partial}{\partial_\mu} = \left(\frac{\partial}{\partial t}, -\nabla\right), \quad \partial_\mu = \frac{\partial}{\partial^\mu} = \left(\frac{\partial}{\partial t}, \nabla\right)$$

Dirac equation

The algebra of 4×4 Dirac matrices is defined by

$$\gamma^\mu = (\gamma^0, \boldsymbol{\gamma}), \quad \gamma\gamma^\mu\gamma^\nu + \gamma^\nu\gamma^\mu = 2g^{\mu\nu}, \quad \gamma^{\mu\dagger} = \gamma^0\gamma^\mu\gamma^0$$

$$\gamma^{0\dagger} = \gamma^0, \quad \gamma^0\gamma^0 = I, \quad \gamma^{k\dagger} = -\gamma^k, \quad k = 1, 2, 3$$

$$\gamma^5 = i\gamma^0\gamma^1\gamma^2\gamma^3, \quad \gamma^5\gamma^\mu + \gamma^\mu\gamma^5 = 0, \quad \gamma^{5\dagger} = \gamma^5$$

The slash notation is

$$\not{p} = \gamma \cdot p = \gamma^0 E - \boldsymbol{\gamma}\cdot\mathbf{p}, \quad \text{but note that} \quad \not{\partial} = \gamma\cdot\partial = \gamma^0 \frac{\partial}{\partial t} + \gamma\cdot\nabla.$$

The Dirac equation in coordinate space for a spin 1/2 particle of mass m and momentum p $(E > 0)$ is

$$(i\hbar\not{\partial} - mc)\psi(x) = 0, \quad \text{or with} \quad \psi(x) = e^{-ip\cdot x}u(p): \quad (\not{p} - m)u(p) = 0,$$

where $u(p)$ is the 4-component spinor. The conjugate spinor is

$$\overline{u} \equiv u^\dagger \gamma^0, \quad \text{satisfying} \ \ \overline{u}(\not{p} - m) = 0.$$

The normalisation is

$$u^{(r)\dagger} u^{(s)} = 2E\delta_{rs}, \ \ \overline{u}^{(r)} u^{(s)} = 2m\delta_{rs}, \ \text{with completeness} \ \sum_{s=1,2} u^{(s)}\overline{u}^{(s)} = \not{p} + m.$$

The negative energy or antiparticle solutions satisfy ($E > 0$):

$$\psi(x) = e^{+ip\cdot x} v(p), \quad (\not{p} + m)v(p) = 0, \ \ \overline{v}v = -2m, \quad \sum v\overline{v} = \not{p} - m.$$

The standard representation of the γ matrices is used.

$$\gamma^0 = \begin{pmatrix} I & 0 \\ 0 & -I \end{pmatrix}, \ \ \boldsymbol{\gamma} = \begin{pmatrix} 0 & \boldsymbol{\sigma} \\ -\boldsymbol{\sigma} & 0 \end{pmatrix}, \ \ \gamma^5 = \begin{pmatrix} 0 & I \\ I & 0 \end{pmatrix}$$

$$\sigma_1 = \begin{pmatrix} 0 & 1 \\ 1 & 0 \end{pmatrix}, \ \ \sigma_2 = \begin{pmatrix} 0 & -i \\ i & 0 \end{pmatrix}, \ \ \sigma_3 = \begin{pmatrix} 1 & 0 \\ 0 & -1 \end{pmatrix}$$

The standard form of solution for the particle and antiparticle spinors is

$$u(p) = \sqrt{E+m} \begin{pmatrix} \xi_\pm \\ \frac{\boldsymbol{\sigma}\cdot\mathbf{p}}{E+m}\xi_\pm \end{pmatrix}, \quad v(p) = \sqrt{E+m} \begin{pmatrix} \frac{\boldsymbol{\sigma}\cdot\mathbf{p}}{E+m}\eta_\pm \\ \eta_\pm \end{pmatrix}, \quad \text{where}$$

$$\xi_+ = \begin{pmatrix} 1 \\ 0 \end{pmatrix}, \quad \xi_- = \begin{pmatrix} 0 \\ 1 \end{pmatrix}, \quad \eta_+ = \begin{pmatrix} 0 \\ 1 \end{pmatrix}, \quad \eta_- = \begin{pmatrix} 1 \\ 0 \end{pmatrix}.$$

States of definite helicity are

$$u_R = \frac{1+\gamma^5}{2}u, \quad u_L = \frac{1-\gamma^5}{2}u, \quad v_R = \frac{1-\gamma^5}{2})v, \quad v_L = \frac{1+\gamma^5}{2}v$$

and for the standard solutions

$$u_R(p) = \frac{\sqrt{E+m}}{2} \begin{pmatrix} (1 + \frac{\boldsymbol{\sigma}\cdot\mathbf{p}}{E+m})\xi_\pm \\ (1 + \frac{\boldsymbol{\sigma}\cdot\mathbf{p}}{E+m})\xi_\pm \end{pmatrix}, \ \ u_L(p) = \frac{\sqrt{E+m}}{2} \begin{pmatrix} (1 - \frac{\boldsymbol{\sigma}\cdot\mathbf{p}}{E+m})\xi_\pm \\ -(1 - \frac{\boldsymbol{\sigma}\cdot\mathbf{p}}{E+m})\xi_\pm \end{pmatrix}$$

$$v_R(p) = \frac{\sqrt{E+m}}{2} \begin{pmatrix} -(1 - \frac{\boldsymbol{\sigma}\cdot\mathbf{p}}{E+m})\eta_\pm \\ (1 - \frac{\boldsymbol{\sigma}\cdot\mathbf{p}}{E+m})\eta_\pm \end{pmatrix}, \ \ v_L(p) = \frac{\sqrt{E+m}}{2} \begin{pmatrix} (1 + \frac{\boldsymbol{\sigma}\cdot\mathbf{p}}{E+m})\eta_\pm \\ (1 + \frac{\boldsymbol{\sigma}\cdot\mathbf{p}}{E+m})\eta_\pm \end{pmatrix}$$

At high energies $E >> m$ these solutions tend to

$$u_R \to \sqrt{E} \begin{pmatrix} \xi_+ \\ \xi_+ \end{pmatrix}, \ u_L \to \sqrt{E} \begin{pmatrix} \xi_- \\ -\xi_- \end{pmatrix}, \ v_R \to \sqrt{E} \begin{pmatrix} -\eta_+ \\ \eta_+ \end{pmatrix}, \ v_L \to \sqrt{E} \begin{pmatrix} \eta_- \\ \eta_- \end{pmatrix}$$

Some trace theorems

$$\mathrm{Tr}(\not{a}\not{b}) = 4a.b, \quad \mathrm{Tr}(\not{a}\not{b}\not{c}) = 0, \text{ and for any odd number of } \gamma\text{'s}$$

$$\gamma_\mu \not{a} \gamma^\mu = -2\not{a}, \quad \gamma_\mu \not{a}\not{b} \gamma^\mu = 4a \cdot b, \quad \gamma_\mu \not{a}\not{b}\not{c} \gamma^\mu = -2\not{c}\not{b}\not{a}$$

$$\mathrm{Tr}(\not{a}\not{b}\not{c}\not{d}) = 4((a \cdot b)(c \cdot d) + (a \cdot d)(b \cdot c) - (a \cdot c)(b \cdot d)$$

$$\mathrm{Tr}(\gamma^\mu \not{a} \gamma^\nu \not{b})\,\mathrm{Tr}(\gamma_\mu \not{c} \gamma_\nu \not{d}) = 32((a \cdot c)(b \cdot d) + (a \cdot d)(b \cdot c))$$

$$\mathrm{Tr}(\gamma^\mu \not{a} \gamma^\nu \gamma^5 \not{b})\,\mathrm{Tr}(\gamma_\mu \not{c} \gamma_\nu \gamma^5 \not{d}) = 32((a \cdot c)(b \cdot d) - (a \cdot d)(b \cdot c))$$

$$\mathrm{Tr}(\gamma^5 \not{a}\not{b}\not{c}\not{d}) = 4i\epsilon_{\mu\lambda\nu\sigma} a^\mu b^\lambda c^\nu d^\sigma,$$

where $\epsilon_{\mu\lambda\nu\sigma}$ is the totally antisymmetric tensor of rank 4 with value $+1$ (-1) according as $\mu\lambda\nu\sigma$ is an even (odd) perm of 0123 and 0 otherwise. A useful contraction of two ϵ's is:

$$\epsilon^{\mu\nu\alpha\beta}\epsilon_{\mu\nu\gamma\sigma} = -2(\delta^\alpha_\gamma \delta^\beta_\sigma - \delta^\alpha_\sigma \delta^\beta_\gamma)$$

13.2 Appendix B: Feynman rules for QED and QCD

13.3 Appendix C: Phase space and cross-sections

Units are such that $\hbar = c = 1$.

General cross-section formula

The state of a particle with 4-momentum $p = (E, \mathbf{p})$ and spin (or helicity) λ has normalisation

$$\langle p', \lambda' | p, \lambda \rangle = 2E\delta_{\lambda\lambda'}\delta^3(\mathbf{p} - \mathbf{p}').$$

This corresponds to $2E$ particles per unit volume and a Lorentz invariant phase space factor $d^3p/(2E(2\pi)^3)$. A useful identity is

$$\frac{d^3p}{2E} = d^4p\,\theta(E)\delta(p^2 - m^2).$$

The scattering operator S is written as $S = 1 + iT$, and the reduced matrix element, $M(B : A)$, for a scattering process $A \to B$ is defined by

$$S_{fi} = \langle B|iT|A\rangle = i(2\pi)^4\delta^4(p_A - p_B)M(B : A),$$

where p_A, p_B are the total 4-momenta of states A and B respectively.

To calculate the total cross-section for a collider process $a + b \to X$ one starts from the Fermi golden rule

$$\text{flux} \times \sigma(ab \to X) = \int w_{fi} \times [\text{final state phase space}]$$

where $w_{fi} = |S_{fi}|^2/VT$ is the transition rate and VT is the total space-time volume. In a colliding beam experiment the initial state particle flux is $2E_a 2E_b|\mathbf{v}_a - \mathbf{v}_b|$, where $\mathbf{v}_i$ are the particle velocities. Inserting the expression for S_{fi} in terms of the reduced matrix element into the above equation gives rise to the square of the overall 4-momentum conservation delta function. Formally this is handled by using the identity

$$(2\pi)^4\delta^4(p_f - p_i) = \int e^{ix(p_f - p_i)}d^4x$$

to replace one of the $\delta^4()$, then performing the integration with $p_f = p_i$ on account of the other $\delta^4()$ to give $\int d^4x = VT$. The VT factors then cancel to give

$$\sigma(ab \to X) = \frac{1}{2E_a 2E_b|\mathbf{v}_a - \mathbf{v}_b|}\int \mathrm{dLips}(s : X)|M(X : ab)|^2$$

where dLips is the Lorentz invariant phase space, which for a final state with n_X particles is

$$\mathrm{dLips}(s : X) = (2\pi)^4\delta^4(p_X - p_a - p_b)\prod_{i=1}^{n_X}\frac{d^3k_i}{(2\pi)^3 2k_i^0},$$

where $s = (p_a + p_b)^2$ and $p_X = \sum_i k_i$. For a total cross-section to all final states X an additional $\sum_X$ is performed. For the unpolarised cross-section for particles with spin, final spin states are summed and initial states averaged. This gives an additional term, $1/[(2S_a+1)(2S_b+1)]$, on the righthand side, where S_a, S_b are the spins of particles a and b. If a differential cross-section is required then the relevant variables are excluded from the phase space integral.

Flux factor

The flux factor $2E_a 2E_b|\mathbf{v}_a - \mathbf{v}_b|$ is a Lorentz invariant and may be written in a number of ways. In the lab frame, with b at rest, it is $2E_a 2m_b|\mathbf{v}_a|$. The following relations are also true:

$$2E_a 2E_b|\mathbf{v}_a - \mathbf{v}_b| = 4\left[(p_1.p_2)^2 - m_1^2 m_2^2\right]^{\frac{1}{2}} = 2\lambda^{\frac{1}{2}}(s, m_a^2, m_b^2),$$
$$\text{where} \quad \lambda(s, m_a^2, m_b^2) = (s - m_a^2 - m_b^2)^2 - 4m_a^2 m_b^2.$$

Two-body scattering

Consider the special case of two-body scattering $\mathbf{a} + \mathbf{b} \to \mathbf{a}' + \mathbf{b}'$ with 4-momenta $p_a = p_1,\ p_b = p_2,\ p_{a'} = p_3,\ p_{b'} = p_4$. The cross-section in the lab frame (particle b at rest) is given by:

$$d\sigma = \frac{|M|^2}{2E_1 2m_2|\mathbf{v_1}|}(2\pi)^4\delta^4(p_3 + p_4 - p_1 - p_2)\frac{d^3p_3}{2E_3(2\pi)^3}\frac{d^3p_4}{2E_4(2\pi)^3}. \quad (13.1)$$

In this case

$$\mathrm{dLips}(s; p_3, p_4) = (2\pi)^4\delta^4(p_3 + p_4 - p_1 - p_2)\frac{d^3p_3}{2E_3(2\pi)^3}\frac{d^3p_4}{2E_4(2\pi)^3}$$

where $s = (p_3 + p_4)^2 = (p_1 + p_2)^2$. It may be evaluated by using the $\delta^4()$ to integrate over 4 of the 6 variables $d^3p_3 d^3p_4$ and doing this in the CM frame gives:

$$\frac{d\sigma}{d\Omega} = \frac{1}{(8\pi w)^2}|M|^2\frac{p'}{p} \quad (13.2)$$

where $w = \sqrt{s}$ is the total CM energy, p and p' the magnitudes of the initial and final CMS 3-momenta respectively.

Optical theorem

The unitarity of the S matrix, $S^\dagger S = 1$, is a consequence of the conservation of the overall probability flux in a scattering process. It may also be written in terms of the T matrix as

$$-i(T - T^\dagger) = T^\dagger T.$$

Taking matrix elements of this expression and inserting a complete set of states on the RHS gives:

$$2\mathrm{Im}\Big[\langle B|T|A\rangle\Big] = \sum_X\left(\prod_{i=1}^{n_X}\int\frac{d^3k_i}{(2\pi)^3 2k_i^0}\right)\langle B|T^\dagger|X\rangle\langle X|T|A\rangle.$$

Using the relationship $\langle B|T|A\rangle = (2\pi)^4\delta^4(p_A - p_B)M(B : A)$ and cancelling the overall 4-momentum conservation $(2\pi)^4\delta^4(p_A - p_B)$ then gives

$$2\mathrm{Im}[M(B:A)] = \sum_X \left(\prod_{i=1}^{n_X} \int \frac{d^3k_i}{(2\pi)^3 2k_i^0}\right) \times (2\pi)^4\delta^4(p_A - p_X)M^\dagger(B:X)M(X:A).$$

Putting $B = A = a + b$, the RHS of the above expression is essentially that for the total cross-section for $a + b \to X$ apart from the flux factor. Thus one has the *optical theorem*

$$\sigma(ab \to X) = \frac{\mathrm{Im}[M(ab:ab)]}{\sqrt{\lambda(s, m_a^2, m_b^2)}}, \tag{13.3}$$

where $\mathrm{Im}[M(ab : ab)]$ is the imaginary part of the forward ($\theta_{CM} = 0$) scattering amplitude for elastic $\mathbf{a} + \mathbf{b} \to \mathbf{a} + \mathbf{b}$. For the unpolarised total cross-section for particles with spin there is an additional

$$\frac{1}{(2S_a + 1)(2S_b + 1)} \sum_{ss'}$$

on the RHS from the summing and averaging over spin states.

Crossing symmetry

Crossing symmetry states that the matrix element for a process containing an antiparticale of 4-momentum p_μ in the initial (final) state is identical with the matrix element for the *crossed* process which contains the corresponding particle of 4-momentum $-p_\mu$) in the final (initial) state. As crossing symmetry requires the continuation to negative energies, it is intimately connected with the analytic properties of the matrix element and more generally with the theory of dispersion relations. This subsection gives a brief summary of crossing relations for $2 \to 2$ scattering.

Consider the process $a + b \to c + d$ with reduced matrix element $M_{ab:cd}(s, t, u)$ where

$$s = (p_a + p_b)^2, \quad t = (p_a - p_c)^2, \quad u = (p_a - p_d)^2$$

are the usual Mandelstam kinematic invariants. This defines the 's-channel' with $s > 0$, $t < 0$, $u < 0$. The 't-channel' corresponds to the process $a + \overline{c} \to \overline{b} + d$ with

$$\overline{s} = (p_a + \overline{p_c})^2 = (p_a - p_c)^2 = t,\ \overline{t} = (p_a - \overline{p_b})^2 = (p_a + p_b)^2 = s,\ \overline{u} = u,$$

where $\overline{s} = t > 0$, $\overline{(t)} = s < 0$, $\overline{u} = u < 0$ and

$$M_{a\overline{c}:\overline{b}d}(\overline{s}, \overline{t}, \overline{u}) = M_{ab:cd}(t, s, u).$$

Similarly for the 'u-channel' $a + \overline{d} \to c + \overline{b}$

$$\overline{s} = (p_a + \overline{p_d})^2 = (p_a - p_d)^2 = u, \ \overline{t} = t, \ \overline{u} = (p_a - \overline{p_b})^2 = (p_a + p_b)^2 = s,$$

where $\overline{s} = u > 0, \ \overline{(}t) = t < 0, \ \overline{u} = s < 0$ and

$$M_{a\overline{d}:c\overline{b}}(\overline{s}, \overline{t}, \overline{u}) = M_{ab:cd}(u, t, s).$$

Crossing symmetry may be used to relate the $|M|^2$ appearing in the cross-section formluae for, say, $a + b \to c + d$ and $a + \overline{c} \to \overline{b} + d$. Note however that crossing symmetry does not apply to the flux and phase-space terms nor to colour factors. One final note of caution about the application of crossing symmetry to processes involving fermions. When the $\sum_{spins} |M|^2$ is performed it will involve taking traces over the spinor operators

$$u(p)\overline{u}(p) = \not{p} + m \text{ (fermions)}, \quad v(p)\overline{v}(p) = \not{p} - m \text{ (antifermions)}.$$

When p is crossed to $-p$, on the LHS of the above

$$u(p)\overline{u}(p) \to u(-p)\overline{u}(-p) = v(p)\overline{v}(p),$$

whereas on the RHS $\not{p} + m \to -\not{p} + m$. This is a consequence of the sign conventions chosen for the fermion and antifermion spinors, $\overline{u}u = 2m$ and $\overline{v}v = -2m$. It means that when $\sum_{spins} |M|^2$ is crossed it picks up a factor of (-1) for each fermion crossed, thus for

$$e^+e^- \to \mu^+\mu^- \quad \text{and} \quad \mu^-e^- \to e^-\mu^- \quad \text{factor } (-1)^2$$

whereas

$$e^-\gamma \to e^-\gamma \quad \text{and} \quad e^+e^- \to \gamma\gamma \quad \text{factor } (-1).$$

13.4 Appendix D: DIS cross-sections

General

In the lab frame (target proton at rest) the double differential cross-section for inelastic scattering, $e(k) + p(p) \to e(k') + X(p_X)$, mediated by virtual photon exchange only can be written as;

$$\frac{d^2\sigma}{d\Omega dE'} = \frac{\alpha^2}{q^4}\frac{E'}{mE}\mathrm{L}\cdot\mathrm{W} \tag{13.4}$$

where α is the fine structure constant, m the proton mass, $q = k - k'$ the 4-momentum transfer, E and E' the energies of the incident and scattered electron and L·W is the contraction of the leptonic and hadronic tensors.

The leptonic tensor $L_{\mu\nu}$ has the form

$$L_{\mu\nu} = 2[k'_\mu k_\nu + k'_\nu k_\mu - k\cdot k' g_{\mu\nu}].$$

The hadronic tensor $W_{\mu\nu}$ is defined formally in terms of matrix elements of the hadronic EM current j_μ

$$W_{\mu\nu} = \frac{1}{4\pi}\sum_X\left(\prod_{i=1}^{n_X}\int\frac{d^3k_i}{(2\pi)^3 2k_i^0}\right)(2\pi)^4\delta^4(p+q-p_X) \times\left(\frac{1}{2}\sum_s\right)\langle p,s|j_\mu^\dagger(0)|X\rangle\langle X|j_\nu(0)|p,s\rangle, \tag{13.5}$$

but it is more useful to use the form in terms of the structure functions W_i

$$W_{\mu\nu} = W_1(-g_{\mu\nu} + \frac{q_\mu q_\nu}{q^2}) + \frac{W_2}{m^2}(p_\mu - \frac{p\cdot q}{q^2}q_\mu)(p_\nu - \frac{p\cdot q}{q^2}q_\nu). \tag{13.6}$$

The W_i are real scalar functions of two variables, E', θ in the lab or any two of the invariant variables, x, y, Q^2 (to be defined below). Note that both $L_{\mu\nu}$ and $W_{\mu\nu}$ are symmetric under the interchange $\mu \leftrightarrow \nu$ and gauge invariance requires

$$q_\mu L^{\mu\nu} = 0, \quad L^{\mu\nu}q_\nu = 0, \quad q_\mu W^{\mu\nu} = 0, \quad W^{\mu\nu}q_\nu = 0.$$

[The hadronic weak current has a similar structure, but there is an additional term $i\varepsilon_{\mu\nu\alpha\beta}p^\alpha p^\beta W_3/(2m^2)$ coming from the parity violating piece.]

Using the above constraints from gauge invariance, the contraction $L\cdot W$ reduces to

$$L\cdot W = 4(k\cdot k')W_1 + 2[(p\cdot k)(p\cdot k') - (k\cdot k')m^2]\frac{W_2}{m^2}.$$

In the lab frame the cross-section then takes the form

$$\frac{d^2\sigma}{d\Omega dE'} = \frac{\alpha^2}{4mE^2\sin^4\frac{\theta}{2}}(W_2\cos^2\frac{\theta}{2} + 2W_1\sin^2\frac{\theta}{2}) \tag{13.7}$$

where θ is the scattering angle of the electron. This form was used for the early fixed target experiments.

It is convenient to have the cross-section expressed in terms of scaling variables $x = \dfrac{-q^2}{2p \cdot q}$, $y = \dfrac{p \cdot q}{p \cdot k}$ and $Q^2 = -q^2$. Also at this point it is conventional to replace the W_i by their 'scaling limit' equivalents $F_1 = W_1$, $F_2 = \nu W_2/m^2$ where $\nu = (p \cdot q)$. The Jacobian for the transformation $d\Omega dE' \to dxdy$ is given by $2\pi/J$ where

$$J = \frac{\partial(x, y)}{\partial(u, E')} = \frac{E'}{m(E - E')}, \quad u = \cos\theta.$$

Then at large $s = (k + p)^2$ when mass terms may be ignored

$$\frac{d^2\sigma}{dxdy} = \frac{4\pi\alpha^2 s}{Q^4}\Big[xy^2 F_1(x, y) + (1 - y)F_2(x, y)\Big]. \tag{13.8}$$

Another usual form, derived from this using $Q^2 = sxy$ and the longitudinal structure function $F_L = F_2 - 2xF_1$, is

$$\frac{d^2\sigma}{dxdQ^2} = \frac{2\pi\alpha^2}{xQ^4}\Big[Y_+ F_2(x, Q^2) - y^2 F_L(x, Q^2)\Big], \tag{13.9}$$

where $Y_+ = 1 + (1 - y)^2$.

For completeness the expression for $d^2\sigma/dxdQ^2$ including the mass terms (which may be necessary at low Q^2 and moderate x) is

$$\frac{d^2\sigma}{dxdQ^2} = \frac{2\pi\alpha^2}{xQ^4}\left[1 - y - \frac{m^2x^2y^2}{Q^2} + \frac{y^2}{2}\frac{1 + 4m^2x^2/Q^2}{1 + R}\right] F_2(x, Q^2), \tag{13.10}$$

where $R \equiv \sigma_L/\sigma_T = F_L/2xF_1$ and $F_L = F_2(1+4m^2x^2/Q^2) - 2xF_1$ (σ_L, σ_T are the $\gamma^* p$ total cross-sections for longitudinal and transverse polarisations respectively, see below).

Note that there are a number of different definitions of the W_i structure functions. In this book, following recent convention (e.g. [Ynd99]), the W_i and F_i are both defined to be dimensionless. In older books the factor $1/m$ appearing here as $1/(mE)$ (from the flux factor) in the first equation of this subsection, is absorbed in the definition of $W_{\mu\nu}$. Also here $\nu = (p \cdot q)$ rather than $\nu = (p \cdot q)/m$.

Elastic electron-muon scattering

It is useful to have various forms of the cross-section for the EM elastic scattering of two point-like spin 1/2 particles, specifically the process $e(k) + \mu(p) \to e(k') + \mu(p')$, where the electron mass is ignored and m is the muon mass. Start from the formulae in the 'two-body scattering' subsection above with $p_3 = k'$, $p_4 = p'$ and

$$|M|^2 \to \frac{1}{4}\sum_{spins} |M(s's : \sigma'\sigma)|^2,$$

$$M(s's:\sigma'\sigma) = \frac{-ee'}{q^2}[\bar{u}(k',\sigma')\gamma_\mu u(k,\sigma)][\bar{u}(p',s')\gamma^\mu u(p,s)].$$

When squared and summed this reduces to a contraction of two leptonic tensors

$$\frac{1}{4}\sum_{spins}|M|^2 = \frac{(4\pi)^2\alpha^2 e'^2}{q^4} L^{(e)}_{\alpha\beta} L^{(\mu)\alpha\beta}.$$

Ignoring the electron mass

$$L^{(e)} \cdot L^{(\mu)} = 8\Big[(k'\cdot p')(k\cdot p) + (k'\cdot p)(k\cdot p') - m^2(k\cdot k')\Big].$$

Evaluating this in the lab frame gives

$$L^{(e)} \cdot L^{(\mu)} = 16m^2 EE'\left[\cos^2\frac{\theta}{2} + \frac{Q^2}{2m^2}\sin^2\frac{\theta}{2}\right],$$

where $E,\ E'$ are the lab energies of the incident and scattered electron. In evaluating the two-body final state phase space it is convenient not to integrate out all the delta functions. Writing $d^3p'/(2p'^0) = d^4p'\,\theta(p'^0)\delta(p'^2 - m^2)$, the $\int d^4p'$ gives overall 4-momentum conservation leaving $\delta(p'^2 - m^2)$. Now

$$\delta(p'^2 - m^2) = \delta(q^2 + 2\nu) = \frac{1}{2}\delta(\nu - Q^2/2)$$

where $\nu = p\cdot q = m(E - E')$, giving

$$\mathrm{dLips} = \frac{E'dE'd\Omega}{4(2\pi)^2}\delta(\nu - Q^2/2).$$

Taking these results together with the flux factor of $4mE$ gives

$$\frac{d^2\sigma}{d\Omega dE'} = \frac{4\alpha^2 e'^2}{Q^4} mE'^2\left[\cos^2\frac{\theta}{2} + \frac{Q^2}{2m^2}\sin^2\frac{\theta}{2}\right]\delta(\nu - Q^2/2). \qquad (13.11)$$

At high energies when all mass terms may be ignored, the summed matrix element squared takes a simple form:

$$\frac{1}{4}\sum_{spins}|M|^2 = \frac{e^2e'^2}{t^2}2[s^2 + u^2],$$

where $s = 2k\cdot p,\quad t = -2k\cdot k',\quad u = -2p\cdot k'$. Using this and Jacobian $J' = Q^2E'/(my^2E)$ for the $dxdQ^2 \to d\Omega dE'$ change of variables gives

$$\frac{d^2\sigma}{dxdQ^2} = \frac{2\pi}{J'}\frac{d^2}{d\Omega dE'} = \frac{\pi\alpha^2 e'^2}{t^2}\frac{y^2s^2}{Q^2}\left[1 + \frac{u^2}{s^2}\right]\delta(\nu - Q^2/2).$$

Since $x = Q^2/(2\nu)$, $\delta(\nu - Q^2/2) = \delta(1-x)/\nu$ and using $t^2 = Q^4$, $u/s = -(p\cdot k')/(p\cdot k) = -(1-y)$ and $Q^2 = sxy$ this last results may be written

$$\frac{d^2\sigma}{dxdQ^2} = \frac{2\pi\alpha^2 e'^2}{Q^4}[1 + (1-y)^2]\frac{1}{x}\delta(1-x). \qquad (13.12)$$

Finally if the $\delta(1-x)$ is integrated out out gets a high energy invariant form of the elastic cross-section

$$\frac{d\sigma}{dQ^2} = \frac{2\pi\alpha^2 e'^2}{Q^4}[1 + (1-y)^2].$$

A closely related form may be deduced easily from the formula for a two-body cross-section in the CM frame (with all delta functions integrated out)

$$\frac{d\sigma}{d\Omega} = \frac{1}{(8\pi)^2 s}\frac{1}{4}\sum_{spins}|M|^2,$$

(as in this case the initial and final 3-momenta are identical). Inserting the high energy form for $|M|^2$ gives

$$\frac{d\sigma}{d\Omega} = \frac{\alpha^2 e'^2}{2st^2}[s^2 + u^2], \text{ or since } dt = d(\cos\theta)/2, \ \frac{d\sigma}{dt} = \frac{2\pi\alpha^2 e'^2}{t^2}[1 + u^2/s^2].$$

γ^*p total cross-section

Both for theoretical and phenomenological studies it is often convenient to think of EM DIS as virtual photon proton scattering. In this section the relationship between $\sigma^{tot}_{\gamma^* p}$ and structure functions will be established.

Using the optical theorem (Eq. 13.3) $\sigma^{tot}_{\gamma^* p}$ is given by $\mathrm{Im}[M(\gamma^* p : \gamma^* p)]$, the forward $\gamma^* p$ scattering amplitude and this latter is $e^2 T_{\mu\nu}$, the time ordered product of the hadronic EM current operators as shown in Eq. 3.42. The imaginary part of $T_{\mu\nu}$ is $2\pi W_{\mu\nu}$ and and to form $\mathrm{Im}[M(\gamma^* p : \gamma^* p)]$ this is contracted with the γ^* polarisation vector ε_μ. Thus, for a γ^* with polarisation $\lambda = \pm 1, 0$

$$\sigma^{tot}_{\gamma^* p}(\lambda) = \frac{8\pi^2\alpha}{W^2 - m^2}\varepsilon^\dagger_\mu(\lambda) W^{\mu\nu}\varepsilon_\nu(\lambda), \qquad (13.13)$$

where W is the $\gamma^* p$ CM energy. This expression is for unpolarised protons, the spin averaging is included in the definition of $W^{\mu\nu}$. The reader may wonder why $W^2 - m^2$ appears in the denominator rather than $\sqrt{\lambda(W^2, m^2, -Q^2)}$ as a literal application of Eq. 13.3 would imply. The reason is that as the γ^* is a virtual particle there is a certain amount of freedom in the definition of the γ^* flux factor. Here the convention of Hand [Han63] is followed in which the flux is given by the energy that a real photon would require to create the final state. An alternative is that of Gilman [Gil68] in which the flux is given by the momentum of the γ^*. In this case $W^2 - m^2$ is replaced by $\sqrt{\lambda(W^2, m^2, -Q^2)}$.

To evaluate Eq. 13.13 take the z-axis to be along the direction of $\mathbf{q}$, the γ^* 3-momentum. The γ^* has energy ν/m and mass $-Q^2$. With these choices the polarisation vectors are

$$\varepsilon(\pm 1) = \frac{1}{\sqrt{2}}(0, 1, \pm i, 0), \quad \varepsilon(0) = \frac{1}{\sqrt{Q^2}}\left(\sqrt{(\nu/m)^2 + Q^2}, 0, 0, \nu/m\right),$$

using these and Eq. 13.6 gives[1]

$$\begin{aligned}
\sigma_T &\equiv \frac{1}{2}(\sigma(+) + \sigma(-)) = \frac{8\pi^2\alpha}{W^2 - m^2} W_1 \\
\sigma_L &\equiv \sigma(0) = \frac{8\pi^2\alpha}{W^2 - m^2}\left[\frac{(\nu/m)^2 + Q^2}{Q^2} W_2 - W_1\right]
\end{aligned}$$

From these a third relation, obtained by adding them, is often used

$$\sigma_T + \sigma_L = \frac{8\pi^2\alpha}{W^2 - m^2}\frac{(\nu/m)^2 + Q^2}{Q^2} W_2.$$

Using $F_1 = W_1$ and $F_2 = \nu W_2/m$, one may also write

$$\sigma_T = \frac{8\pi^2\alpha}{W^2 - m^2} F_1 \tag{13.14}$$

$$\sigma_T + \sigma_L = \frac{8\pi^2\alpha}{W^2 - m^2}\left[\frac{\nu}{Q^2} + \frac{m^2}{\nu}\right] F_2. \tag{13.15}$$

There are two simplified forms of these last two relations:

- For $W^2 >> m^2$ ignore the m^2 in common overall factor, replace ν/Q^2 by $1/(2x)$ and drop the 2nd term $(m^2/\nu = 2m^2/(W^2 y))$ in the expression for F_2 to give

$$\sigma_T = \frac{4\pi^2\alpha}{W^2} 2F_1 \tag{13.16}$$

$$\sigma_T + \sigma_L = \frac{4\pi^2\alpha}{W^2}\frac{F_2}{x}. \tag{13.17}$$

- The second form is appropriate for large W^2 and small Q^2. Use the relation $W^2 - m^2 = Q^2(1-x)/x \approx Q^2/x$ for the overall factor and make the same approximation as before for the F_2 term to give

$$\sigma_T = \frac{4\pi^2\alpha}{Q^2} 2xF_1 \tag{13.18}$$

$$\sigma_T + \sigma_L = \frac{4\pi^2\alpha}{Q^2} F_2. \tag{13.19}$$

[1] An obvious shorthand is used for $\gamma^* p$ cross-sections.

Since real photons have only transverse polarisation states, as $Q^2 \to 0$ $\sigma_L \to 0$ and $F_2/Q^2 \to \sigma_T$ (constant independent of Q^2. Using the two relations one may also write

$$\sigma_L = \frac{4\pi^2\alpha}{Q^2}\Big[F_2 - 2xF1\Big] = \frac{4\pi^2\alpha}{Q^2}F_L, \tag{13.20}$$

which implies $F_L/Q^2 \sim Q^2$ as $Q^2 \to 0$.

The double diffential cross-section for $e + p \to X$ is related to the $\gamma^* p$ cross-sections by

$$\frac{d^2\sigma}{dxdQ^2} = \Gamma\big(\sigma_T + \varepsilon\sigma_L\big), \tag{13.21}$$

where Γ and ε are the flux and polarisation of the virtual photon respectively. Comparing the above equation to Eq. 13.9 and using the relations 13.19, 13.20 one finds

$$\Gamma = \frac{\alpha[1 + (1-y)^2]}{2\pi x Q^2} \tag{13.22}$$

$$\varepsilon = \frac{2(1-y)}{1 + (1-y)^2}. \tag{13.23}$$

These are approximations valid for $W^2 >> m^2$, the full expressions including the discarded small mass terms may be found in [Rob90,p13] or [Ren90,p305].

13.5 Appendix E: DIS event generators

Summary of MC event generators

13.6 Appendix F: Data sources

Data sources - HEPDATA - experiments

13.7 Appendix G: Parton Parameterisations

CTEQ, MRS(T), GRV and exp. partons

Bibliography

Abr99 Abramowicz, H. & Caldwell, A. (1999), *Rev. Mod. Phys.* **71** 1275.

Ada90 Adams, M.R. *et al.* (1990), *Nucl. Instr.. Meth.* A **291** 533.

Ade97 Adel K, Barreiro F & Yndurain F J (1997), *Nucl. Phys.* B **495** 221.

Adl66 Adler S L (1966), *Phys. Rev.* **143** 1144.

Ait98 Aitchison I J R & Hey A J G (1989), *Gauge Theories in Particle Physics*, 2nd ed, Adam Hilger.

Aiv94 Aivazis M et al (1994), *Phys. Rev.* D **50** 3085,3102.

Alt77 Altarelli G & Parisi G (1977), *Nucl. Phys.* B **126** 298.

Alt78 Altarelli G & Marinelli G (1978), *Phys. Lett.* B **76** 89.

Alt82 Altarelli G (1982), *Phys. Rep.* **81** 1.

Alt00 Altarelli G, Ball R D & Forte S (2000), *Nucl. Phys.* B **575** 313, [hep-ph/9911273].

Ana00 Anandam P & Soper D E (2000), *Phys. Rev.* D **61** 094003.

And96 Andersson B *et al.* (1996), *Nucl. Phys.* B **467** 443.

And98 Andersson, B. (1998), *The Lund Model*, CUP.

Arn94 Arneodo M (1994), *Phys. Rep.* **240** 301.

Aub83 Aubert J J *et al.* EMC (1983), *Nucl. Phys.* B **(** 213)31.

Aub87 Aubert *et al.* (1987), *Nucl. Phys.* B **293** 740.

Aur99 Aurenche P *et al.* (1999), *isol g critique*, *Eur. Phys. J.* C **9** 107.

Bad84 Badier J *et al.* NA3 (1984), *isol g* , *Z. Phys.* C **26** 489.

Bal78 Balitsky Ya Ya & Lipatov L N (1978), *Sov. J. Nucl. Phys.* **28** 822.

Bal94 Ball R D & Forte F (1994), *Phys. Lett.* B **335** 77.

Bal95 Ball R D & Forte F (1995), *Act. Phys. Polon.* **B26** 2097, [hep-ph/9512208].

Bal97 Ball R D & Forte F (1997), *Phys. Lett.* B **405** 317, [hep-ph/9703417].

Bar91 Bartels J, Charchula K & Feltesse J (1991), *Proc. of the Workshop on HERA Physics*, eds W Buchüller & G Ingelman, Vol.I, 193.

Bar99a Bartels J & Bontus C (1999), *Phys. Rev.* D **61** 034009, [hep-ph/9906308].

Bar99b Bartels J, Bontus C & Spiesberger H (1999), Preprint [hep-ph/9908411].

Bar00 Bartels J, Golec-Biernat K & Peters K (2000), Preprint [hep-ph/0003042].

Bas95 Bassler, U. and Bernardi, G. (1995), *Nucl. Instr.. Meth.* A **361** 197.

Bas99 Bassler, U. and Bernardi, G. (1999), *Nucl. Instr.. Meth.* A **426** 583.

Baz95 Bazarko, A.O. *et al.* (1995), *Z. Phys.* C **65** 189.

Ben89 Benvenuti, A. *et al.* (1989), *Phys. Lett.* B **223** 485.

Ben90 Benvenuti, A. *et al.* (1990), *Phys. Lett.* B **237** 592.

Ben91 Bentvelsen, S. *et al.* (1991), *Proc. of the Workshop on Physics at HERA, DESY 1991*, eds W. Buchmüller & G. Ingelman, Vol I, 23.

Ber83 Bernreuther W (1983), *Ann.Phys.*, **151**, 127.

Bernreuther W & Wetzel W (1981), *Nucl. Phys.* B **197** 228.

Bia98 Bialas A, Peschanski R & Royon C (1998), *Phys. Rev.* D **57** 6899.

Bjo64 Bjorken J D & Drell S D (1964), *Relativistic Quantum Mechanics*, McGraw Hill.

Bod98 Bodek A & Yang U K (1998), *Phys. Rev. Lett.* **82** 2467, [hep-ph/9809480].

Bot97 Botje M (1997), *QCDNUM16, a fast QCD evolution code,* ZEUS Note 97-066 (unpublished).

Bot00 Botje M (2000), *Eur. Phys. J.* C **14** 285, [hep-ph/9912439].

Bot01 Botje M (2001), *pdf errors*, [hep-ph/0110123].

Bow90 Bowler M (1990), *Femtophysics*, Pergamon Press.

Bro73 Brosky S J & Farrar G (1973), *Phys. Rev. Lett.* **31** 1153.

Bro75 Brosky S J & Farrar G (1975), *Phys. Rev.* D **11** 1309.

Bro80 Brock, R. *et al.* (1997), *Phys. Rev. Lett.* **44** 1027.

Buz96 Buza M *et al.* (1996), *Nucl. Phys.* B **472** 611.

Cal97 Caldwell A (1997), Invited talk at the DESY Theory Worshop on 'Recent Developments in QCD' (unpublished).

Cam97 Camici G & Ciafaloni M (1997), *Phys. Lett.* B **412** 396; Erratum *Phys. Lett.* B **417** 390.

Cam98 Camici G & Ciafaloni M (1998), *Phys. Lett.* B **430** 349, [hep-ph/9803389].

Cap00 Capella A *et al.* (2000), [hep-ph/0006233].

Cat90 Catani F, Fiorani F & Marchesini G (1990), *Phys. Lett.* B **234** 339.

CDF96 Abe F *et al.* CDF (1996), *Inclusive jet excess*, *Phys. Rev. Lett.* **77** 438.

CDF98 Abe F *et al.* CDF (1998), *W decay asymm.*, *Phys. Rev. Lett.* **81** 5754.

CDF01a Affolder T *et al.* CDF (2001), *Inclusive jets and pdfs*, *Phys. Rev.* D **64** 032001.

CDF01b Affolder T *et al.* CDF (2001), *D-Y around Z0*, [hep-ex/0106047], *Phys. Rev. Lett.* **87** 131802.

CDF01c Affolder T *et al.* CDF (2001), *dijet double diff xsec*, [hep-ex/0012013], *Phys. Rev.* D **64** 012001.

Cia88 Ciafaloni M (1988), *Nucl. Phys.* B **296** 49.

Cia99a Ciafaloni M & Colferai D (1999), *Phys. Lett.* B **452** 372, [hep-ph/9812366].

Cia99b Ciafaloni M, Colferai D & Salam G P (1999), *Phys. Rev.* D **60** 114036, [hep-ph/9905566].

Cia00 Ciafaloni M, Colferai D & Salam G P (1999), Preprint [hep-ph/0007240].

Clo79 Close F E (1979), *Introduction to Quarks and Partons*, Academic Press.

Col77a Collins P D B (1977), *Introduction to Regge Theory and High Energy Physics*, CUP.

Col77b Collins J C & Soper D (1977), *Phys. Rev.* D **16** 2219.

Col89 Collins J C *et al.* (1989), *Factorisation of Hard Processes in QCD* in Perturbative Quantum Chromodynamics, ed. A H Mueller, World Scientific.

Com77 Combridge B L, Kripfganz J & Ranft J (1977), *Phys. Lett.* B **70** 234.

Coo88 Cooper-Sarkar A M *et al.* (1988), *Z. Phys.* C **39** 281.

Coo98 Cooper-Sarkar A M, De Roeck A & Devenish R C E (1998), IJMPA 13 (3385).

Cud97 Cudell J R *et al.* (1997), Preprint [hep-ph/9712235].

DØ 99a Abbott B *et al.* DØ (1999), *Inclusive jets*, *Phys. Rev. Lett.* **82** 2451.

DØ 99b Abbott B *et al.* DØ (1999), *Dijet mass spectrum*, *Phys. Rev. Lett.* **82** 2457.

DØ 00a Abbott B *et al.* DØ (2000), *W mass*, *Phys. Rev. Lett.* **84** 222.

DØ 00b Abbott B *et al.* DØ (2000), *Isolated photons*, *Phys. Rev. Lett.* **84** 2786.

DØ 01 Abazov V M *et al.* DØ (2001), *Inclusive jets* k_T, [hep-ex/0109041], PLB to be published.

Das96 Dasgupta M & Webber B R (1996), *Phys. Lett.* B **382** 273.

DeR74 De Rujula A *et al.* (1974), *Phys. Rev.* D **10** 1649.

DeR93 De Roeck, A.D. (1993), *J. Phys.* G. **19** 1549.

Dev72 Devenish R C E & Lyth D H (1972), *Phys. Rev.* D **5** 47.

Dit97 Dittmar M, Pauss F & Zürcher D (1997), *Lumi at LHC*, *Phys. Rev.* D **56** 7284.

Dok77 Dokshitzer Yu. L (1977), *Sov. Phys. JETP* **46** 641.

Dok91 Dokshitzer Yu. L *et al.* (1991), *Basics of Perturbative QCD*, Editions Frontiers.

Don92 Donnachie A & Landshoff P V (1992), *Phys. Lett.* B **296** 227.

Don93 Donnachie A & Landshoff P V (1993), *Z. Phys.* C **61** 139.

Don98 Donnachie A & Landshoff P V (1998), *Phys. Lett.* B **437** 408.

Dre70 Drell S D & Yan T M (1970), *Phys. Rev. Lett.* **25** 316.

Duk82 Duke D W & Owens J F (1982), *Phys. Rev.* D **26** 1600.

Eic97 Eichler, R. *et al.* (1997), [hep-ex/9712011].

Ell83 Ellis R K, Furmanski W & Petronzio R (1983), *Nucl. Phys.* B **212** 29.

Ell94 Ellis R K *et al.* (1994), *Nucl. Phys.* B **420** 517.

Ell96 Ellis R K, Stirling W J & Webber B R (1996), *QCD and collider physics*, CUP.

Esk99 Eskola K J, Kolhinen V J & Salgado C A (1999), *Eur. Phys. J.* C **9** 61, [hep-ph/9807297].

Fad98 Fadin V S & Lipatov L N (1998), *Phys. Lett.* B **429** 127, [hep-ph/9802290].

Fey69 Feynman R P (1969), *Phys. Rev. Lett.* **23** 1415,*Photon Hadron Interactions* Benjamin NY, 1972.

Fis82 Fisk H E & Sciulli F (1982), *Ann. Rev. Nuc. Part.* **32** 499.

Fol63 Foldy L F & Peierls R F (1963), *Phys. Rev.* **130** 1585.

For95 Forshaw J R & Roberts R G (1995), *Phys. Lett.* B **351** 308.

For97 Forshaw J R & Ross D A (1997), *Quantum Chromodynamics and the Pomeron*, CUP.

Fra88 Frankfurt L L & Strikman M (1988), *Phys. Rep.* **160** 235.

Fre90 Freudenreich K (1990), *Intl. J. Mod. Phys.* A **5** 3643.

Fri91 Friedman J I, Kendall H W & Taylor R E (1991), *Rev. Mod. Phys.* **63** 573,597,615.

Fur82 Furmanski W & Petronzio R (1982), *Z. Phys.* C **11** 293.

Gal97 Gallo, E. *et al.* (1997), [hep-ex/9710013].

Gie94 Giele W T, Glover E W N & Kosower D A (1994), *Phys. Rev. Lett.* **73** 2019.

Gie97 Giele W T & Kilgore W B (1997), *Phys. Rev.* D **55** 7183.

Gie01a Giele W T, Keller S A & Kosower D A (2001), *optim. pdfs*, [hep-ph/0104052].

Gie01b Giele W T & Keller S A (2001), *Lumi at LHC*, [hep-ph/0104053].

Glo01 Glover E W N (2001), Contribution to the 36th Recontres de Moriond in QCD & Hadronic Interactions, Les Arcs France March 2001, [hep-ph/0106069].

Gil68 Gilman F J (1968), *Phys. Rev.* **167** 1366.

Glu94 Glück M, Reya E & Stratmann M (1994), *Nucl. Phys.* B **422** 37.

Gol99 Golec-Biernat K & Wüsthoff M (1999), *Phys. Rev.* D **59** 014017, *Phys. Rev.* D **60** 114023.

Got67 Gottfried K (1967), *Phys. Rev. Lett.* **18** 1154.

Got99 Gotsman E *et al.* (1998), *Nucl. Phys.* B **539** 535.

Gri72 Gribov V N & Lipatov L N (1972), *Sov. J. Nucl. Phys.* **15** 438.

Gri83 Gribov L V, Levin E M & Ryskin M G (1983), *Phys. Rep.* **100** 1.

Gro69 Gross D J & Llewellyn-Smith C H (1969), *Nucl. Phys.* B **14** 337.

Gru98 Gruppen K (1998), *Particle Detectors* CUP.

H1 95a H1 Collab., Aid *et al.* (1995), *Phys. Lett.* B **354** 494.

H1 96a H1 Collab., Aid *et al.* (1996), *Nucl. Phys.* B **470** 3.

H1 97 H1 Collab., Adloff, C. *et al.* (1997), *Phys. Lett.* B **393** 452, [hep-ex/9611017].

H1 99r H1 collab., C Adloff *et al.* (1999), *Phys. Lett.* B **462** 440, [hep-ex/9907030].

H1 00h H1 Collab., Adloff, C. *et al.* (2000), *Eur. Phys. J.* C **13** 609.

H1 01a H1 Collab., Adloff, C. *et al.* (2001), *Eur. Phys. J.* C **21** 33, *Low* x, F_L, α_S, [hep-ex/0012053].

H1 01b H1 Collab., Adloff, C. *et al.* (2001), *Phys. Lett.* B **xx** yy, D^* F_2^c, [hep-ex/0108039].

Hal84 Halzen F & Martin A D (1984), *Quarks and Leptons*, Wiley.

Ham91 Hamberg R *et al.* (1991), *Nucl. Phys.* B **359** 343; Van Neerven W L & Zijlsrtra E B (1992), *Nucl. Phys.* B **382** 11.

Han63 Hand L N (1963), *Phys. Rev.* **129** 1834.

Har98 Harris, B.W. and Smith, J. (1998), *Phys. Rev.* D **57** 2806.

Haw98 Hawker E H *et al.* E866 (1998), *Phys. Rev. Lett.* **80** 3715.

Iva00 Ivanov I P & Nikolaev N N (2000), [hep-ph/0004206].

Jac75 Jackson J D (1975), *Classical Electrodynamics* 2nd ed, Wiley.

Jac79 Jacquet, F. and Blondel, A. (1979), *Proc. of the Study of an ep facility for Europe*, ed U Amaldi, DESY 79/48, p391.

Jau76 Jauch J M & Rohrlich F (1976), *The theory of photons and electrons*, 2nd Ed, Springer Verlag.

Jun99 Jung H (1999), *Proc. Workshop on Monte Carlo generators for HERA physics*, Eds A Doyle *et al.* , DESY Hamburg, [hep-ph/9908497].

Jun00 Jung H (2000), *Proc. XXXVth Recontre de Moriond*, Ed J Tran Than Van, [hep-ph/0006082].

Jun01 Jung H & Salam G P (2001), *Eur. Phys. J.* C **19** 351, [hep-ph/0012143].

Kho01 Khoze V A *et al.* (2001), *lumi monitor for LHC*, *Eur. Phys. J.* C **19** 313.

Kin91 King, B.J. *et al.* (1991), *Nucl. Instr.. Meth.* A **302** 254.

Kle00 Klein, M. (2000), *Proc. Int'l Symp. on Lepton & Photon Interactions*, Stanford 1999, [hep-ex/0001059].

Kle99 Kleinknecht K (1999), *Detectors for Particle Radiation* 2nd ed., CUP.

Kot95 Kotwal, A.V. (1995), *Proton and deuteron structure functions in muon scattering at 470 GeV*, Harvard University Ph.D. thesis.

Kov98 Kovchegov Y V & Mueller A H (1998), *Phys. Lett.* B **439** 428, [hep-ph/9805208].

Kra00 Krämer M *et al.* , Edinburgh preprint [hep-ph/0003035].

Kur77 Kuraev E A *et al.* (1977), *Sov. Phys. JETP* **45** 199.

Kwi95 Kwiecinski *et al.* (1995), *Phys. Rev.* D **52** 1445.

Kwi96 Kwiecinski *et al.* (1996), *Phys. Rev.* D **53** 6094.

L3 99 L3 collab., M Acciarri *et al.* (1999), *Phys. Lett.* B **453** 333.

Lan72 Landshoff P V & Polkinghorne J C (1972), *Phys. Rep.* **5C** 1).

Lae92 Laenen, E. *et al.* (1992), *Nucl. Phys.* B **291** 325.

Lae93 Laenen, E. *et al.* (1993), *Nucl. Phys.* B **392** 162,229.

Lea96 Leader E & Predazzi E (1996), *Introduction to gauge theories and modern particle physics* (2 vols), CUP.

Lae00 Laenen E, Oderda G & Sterman G (2000), *soft g resums*, *Phys. Rev. Lett.* **84** 4296.

Lai95 Lai H L *et al.* CTEQ3 (1995), *Phys. Rev.* D **51** 4763.

Lai96 Lai H L *et al.* CTEQHJ (1996), *Phys. Rev. Lett.* **77** 44.

Lai97 Lai H L *et al.* CTEQ4 (1997), *Phys. Rev.* D **55** 1280.

Lev97 Levin E M (1997), Talk given at the RIKEN-BNL Workshop, [hep-ph/9709226].

Lev98 Levin E M (1998), Preprint [hep-ph/9806228], unpublished.

Lip75 Lipatov L N (1975), *Sov. J. Nucl. Phys.* **20** 95.

Lip80 Lipatov L N (1980), *Sov. J. Nucl. Phys.* **63** 904.

Lop80 Lopez C & Yndurain F J (1980), NPB **171** 231.

Lop96 Lopez C *et al.* (1996), *Z. Phys.* C **72** 561.

McD00 McDermott M *et al.* (2000), Prprint [hep-ph/9912547v2].

McG94 McGaughey P L *et al.* E772 (1994), *isol g* , *Phys. Rev.* D **50** 3038.

McG99 McGaughey P L, Moss J M & Peng J C (1999), *Ann. Rev. Nuc. Part.* **49** 217.

McL94 McLerran L & Venugopalan R (1994), *Phys. Rev.* D **49** 2233, 3352, *ibid* **50** 2225.

Mar69 Martin A (1969), *Scattering Theory, Unitarity, Analyticity & Crossing*, Lecture Notes in Physics No. 3, Springer.

Mar92 Marchesini G & Webber B R (1992), *Nucl. Phys.* B **386** 215.

Mar95 Marchesini G (1995), *Nucl. Phys.* B **445** 49.

Mar98a Martin A D *et al.* (1998), *Eur. Phys. J.* C **2** 287.

Mar98b Martin A D & Ryskin M G (1998), *Phys. Lett.* B **431** 395, [hep-ph/9802366].

Mar98c Martin A D *et al.* (1998), *Phys. Lett.* B **443** 301.

Mat73 Matveev V A, Muradyan R M & Tavkhelidze A N (1973), Lett. Nuovo Cim.**77**19.

Moc00 Moch S & Vermaseren J A M (2000), Talk at *Loops and Legs in QFT*, Bastei, Germany, April 2000, [hep-ph/0006053].

Mor91 Moreno G *et al.* E605 (1991), *isol g* , *Phys. Rev.* D **43** 2815.

Mue86 Mueller A H & Qiu J (1986), *Nucl. Phys.* B **260** 427.

Mue94a Mueller A H (1994), *Nucl. Phys.* B **415** 373.

Mue94b Mueller A H & Patel B (1994), *Nucl. Phys.* B **425** 471, [hep-ph/9403256].

Mut98 Muta T (1998), Foundations of QCD, 2nd Ed, World Sci.

NMC92 NMC Collab., Amaudruz, P. *et al.* (1992), *Phys. Lett.* B **295** 159.

NMC93 NMC Collab., Arneodo, M. *et al.* (1993), *Phys. Lett.* B **309** 222.

NMC97a NMC Collab., Arneodo M *et al.* (1997), F_2^p *&* F_2^d *data Nucl. Phys.* B **483** 3.

NMC97b NMC Collab., Arneodo M *et al.* (1997), F_2^n/F_2^p *data Nucl. Phys.* B **487** 3.

Nav97 Navelet H & Peschanski R (1997), *Nucl. Phys.* B **507** 353, [hep-ph/9703238].

Nik90 Nikolaev N N & Zakharov B G (1990), *Z. Phys.* C **49** 607.

Nik92 Nikolaev N N & Zakharov B G (1992), *Z. Phys.* C **53** 331.

Nik94 Nikolaev N N, Zakharov B G & Zoller V R (1994), *JETP Lett.* **59** 6, [hep-ph/9312268].

Nik97 Nikolaev N N, Zakharov B G & Zoller V R (1994), *JETP Lett.* **66** 138, [hep-ph/9707463].

Nik00 Nikolaev N N, Speth J & Zoller V R (2000), *Phys. Lett.* B **473** 157, [hep-ph/9911433].

Oku56 Okun L B & Pomeranchuk I Y (1956), *Sov. Phys. JETP* **3** 307.

Owe78 Owens J F, Reya E & Glück M (1978), *Phys. Rev.* D **18** 1501.

PDG00 Groom D E *et al.* Particle Data Group (2000), EPJC **15** 1.

PDG02 PDG, Groom D E *et al.* (2002), *Eur. Phys. J.* C **xx** yy.

Pen83 Pennington M R (1983), *Rep. Prog. Phys.* **46** 393.

Pes95 Peskin M E & Schroeder D V (1995), *An introduction to quantum field theory*, Addison Wesley.

Pry93 Prytz K (1993), *Phys. Lett.* B **311** 286.

Ren90 Renton R (1990), *Electroweak Interactions - An introduction to the physics of quarks and leptons*, CUP.

Rie95 Riemersma, S. *et al.* (1995), *Phys. Lett.* B **347** 143.

Rob90 Roberts R G (1990), *The structure of the proton*, CUP.

Rob98a Roberts R G & Thorne R (1998), *Phys. Lett.* B **421** 303.

Rob98b Roberts R G & Thorne R (1998), *Phys. Rev.* D **57** 6871.

Ros98 Ross D A (1998), *Phys. Lett.* B **431** 161, [hep-ph/9804332].

Sak90 Sakumoto, W.K. *et al.* (1990), *Nucl. Instr.. Meth.* A **294** 179.

Sal97 Salam G P (1997), Talk at the Ringberg Workshop, [hep-ph/9707383].

Sal98 Salam G P (1998), JHEP **9807** 19.

Sal99 Salam G P (1999), Lectures at the XXXIX Cracow School of Theoretical Physics, [hep-ph/9910492].

Sel97 Seligman W G *et al.* , CCFR (1997), *Phys. Rev. Lett.* **79** 1213.

Sey00 Seymour M H (2000), *Jet defn. for hadron colliders*, [hep-ph/0007051].

Smi99 Smirnov G I (1999), *Eur. Phys. J.* C **10** 239, [hep-ph/9901422].

Smi00 Smith J, Proc. of DIS2000 (to be published) and [hep-ph/0005242].

Sta01 Stavropoulos G D (2001), *LHC QCD studies*, [hep-ph/0111420].

Ste00 Sterman G & Vogelsang W (2000), *soft g resums*, [hep-ph/0002132].

Sti93 Stirling J & Whalley M R (1993), *J. Phys.* G. **19** D1.

tHo72 't Hooft G & Veltman M (1972), *Nucl. Phys.* B **44** 189.

Tho00 Thorne R S (2000), *Phys. Lett.* B **474** 372, [hep-ph/9912284].

Tho01 Thorne R S (2000), *Phys. Rev.* D **64** 074005.

Tym92 Tymieniecka T & Zarnecki A F (1992), DESY 92-137 (unpublished).

vNne00a van Neerven W L & Vogt A (2000), Talk at *Loops and Legs in QFT*, Bastei, Germany, April 2000, [hep-ph/0006230].

vNne00b van Neerven W L & Vogt A (2000), [hep-ph/0007362].

Vel94 Veltman M (1994), *Diagrammatica*, CUP.

Vir92 Virchaux M & Milsztajn A (1992), *Phys. Lett.* B **274** 221.

Vog99 Vogt A (1999), *Phys. Lett.* B **471** 97.

Wei95 Weinberg S (1995), *Quantum Theory of Fields I & II*, CUP.

Whi90 Whitlow, L.W. *et al.* (1990), *Phys. Lett.* B **250** 193.

Wil69 Wilson K G (1969), *Phys. Rev.* **179** 1499.

Wue99 Wüsthoff M & Martin A D (1999), *J. Phys.* G. **25** R309.

Yan01 Yang U K *et al.* , CCFR (2001), *Phys. Rev. Lett.* **86** 2742, [hep-ex/0009041].

Ynd99 Yndurain F J (1999), *The theory of quark and gluon interactions* 3rd ed, Springer.

ZEU96 ZEUS collab., M. Derrick *et al.* (1996), *Z. Phys.* C **72** 399.

ZEU99r ZEUS collab., J. Breitweg *et al.* (1999), *Eur. Phys. J.* C **6** 239, [hep-ex/9805016].

ZEU99s ZEUS collab., J. Breitweg *et al.* (1999), *Eur. Phys. J.* C **7** 609, F_2 *Phenom. + SVX*.

ZEU00a ZEUS Collab., Breitweg, J. *et al.* (2000), *Eur. Phys. J.* C **12** 35.

ZEU00b ZEUS Collab., Breitweg, J. *et al.* (2000), *Eur. Phys. J.* C **12** 411.

ZEU00c ZEUS Collab., Breitweg, J. *et al.* (2000), *Phys. Lett.* B **487** 53, *BPT data*, [hep-ex/0005018].

ZEU01a ZEUS Collab., Breitweg, J. *et al.* (2001), *Eur. Phys. J.* C **21** 443, [hep-ex/0105090].

ZEU01b Chekanov S *et al.* ZEUS (2001), *prompt g kt*, *Phys. Lett.* B **511** 19.